

Virtual Fixtures for Bilateral Telemanipulation

by

Jake J. Abbott

A dissertation submitted to The Johns Hopkins University in conformity with the requirements for the degree of Doctor of Philosophy.

Baltimore, Maryland

August, 2005

© Jake J. Abbott 2005

All rights reserved

Abstract

This dissertation addresses three related topics in the application of virtual fixtures to bilateral telemanipulation systems. Bilateral telemanipulation is the direct human control of a remote robot, with force and/or tactile feedback, and virtual fixtures are guidance modes, implemented in software, that assist the user in accomplishing a telemanipulated task. The first topic addressed in this dissertation is the design of functional and stable forbidden-region virtual fixtures, which prevent robot motion into forbidden-regions of the workspace. Metrics are defined to evaluate the effectiveness of forbidden-region virtual fixtures, and a human-factors experiment uses these metrics to quantify how users interact with various combinations of forbidden-region virtual fixtures and telemanipulation control system. A method to predict system stability that incorporates an explicit model of the telemanipulator and bounding models of human users is created and experimentally verified. Next, a new condition is presented for the passivity of a virtual wall with sampling, sensor quantization, and friction effects, for an impedance-type robot. This condition is experimentally verified to correspond to recognizable physical behaviors. It is then shown that virtual fixtures and bilateral telemanipulators can be designed indepen-

dently under passivity considerations, and then coupled to create a stable systems. The method presented generalizes to all types of virtual fixture and to robots with any mechanical characteristics. Finally, a novel bilateral telemanipulation control method called Pseudo-admittance is presented, and its stability properties are analyzed. This controller mimics admittance control on an impedance-type robot, and has many desirable properties, such as tremor attenuation, quasi-static transparency, and the ability to include guidance virtual fixtures that help the robot move along desired paths or surfaces in the workspace. The properties of Pseudo-admittance Bilateral Telemanipulation, with and without guidance virtual fixtures, are verified through experiment and simulation. The research in this dissertation is particularly relevant to robot-assisted surgical tasks – which require safety as well as precision – but it is also applicable to a broad range of telemanipulated tasks. The dissertation concludes with interesting topics for future work that build upon the results presented.

Dissertation Advisor: Assistant Professor Allison M. Okamura

Dissertation Readers: Professor Gregory D. Hager, Professor Wilson J. Rugh,
Professor Louis L. Whitcomb

Acknowledgements

First and foremost I would like to thank my advisor Dr. Allison Okamura. She created a supportive environment where ideas were given the time, freedom, and resources needed to flourish. Her advice was always welcome, she always looked out for my current and future success, and she did the best thing an advisor can do – she made me feel appreciated and respected.

I would like to thank Panadda “Nim” Marayong for her help collecting data for Chapter 2. She was very generous with her time, and accepted her moniker of “worst-case human” with good humor. I would also like to thank Dr. Robert Howe at Harvard University for permission to use his finger impedance data.

I would like to thank Dr. Wilson Rugh and Dr. Joel Spruck for their helpful suggestions on the passive-virtual-wall proof of Chapter 3. Dr. Rugh helped me avoid abuse of the calculus of variations in my original derivation, and Dr. Spruck first suggested that I consider the Cauchy-Schwarz Inequality, which I went on to use in my final derivation.

I would like to thank Lawton Verner for the many hours of his time devoted to helping me with problems with the PHANToM robots used in Chapter 5.

I would like to thank (in alphabetical order) Dr. Greg Chrikjian, Dr. Noah Cowan, Sommer Gentry, Dr. Greg Hager, Dr. Pablo Iglesias, Dr. Mohsen Mahvash, Panadda Marayong, Todd Murphy, Tabish Mustufa, Dr. Wilson Rugh, Chad Schneider, Lawton Verner, Robert Webster, and Dr. Louis Whitcomb for any and all discussions and suggestions over the years that found their way into this dissertation. I would also like to thank the anonymous reviewers of the conference and journal papers that constitute the bulk of this dissertation. Their comments led to improvements in the work that might not have occurred otherwise.

I would like to thank KEXP and NPR for improving the large portion of my waking hours that were spent sitting at my computer and in my car. I would also be remiss in not giving some amount of credit to the mind-expanding combination of *café latté* and foosball; while the benefits of this duo may be intangible, it would be difficult to prove that they did not improve my productivity.

Finally, I would like to thank my family (both in blood and in law), and especially my wife Katie, for their love, encouragement, and understanding. I will miss the time that was spent away from them. Earning a Ph.D. requires sacrifices be made by the student, but the friends and family of the student are asked to sacrifice as well.

This work is supported by National Science Foundation grants #ITR-0205318 and #IIS-0347464.

Contents

Abstract	ii
Acknowledgements	iv
List of Figures	ix
1 Introduction	1
1.1 Motivation	1
1.2 Dissertation Contributions	4
1.3 Prior Work	5
1.3.1 Robots of the Impedance and Admittance Type	6
1.3.2 Bilateral Telemanipulation	8
1.3.3 Haptic Virtual Environments	14
1.3.4 Virtual Fixtures	18
1.4 Dissertation Overview	21
2 Design Considerations for Forbidden-Region Virtual Fixtures	23
2.1 Introduction	23
2.2 System Model	24
2.3 Evaluation of Forbidden-Region Virtual Fixture Architectures	26
2.3.1 Telemanipulator Controller Architectures	29
2.3.2 Master and Slave FRVFs	31
2.3.3 Experiment	37
2.3.4 Results and Discussion	43
2.3.5 Conclusions for Human Factors Experiment	48
2.4 Stability of Forbidden-Region Virtual Fixtures	49
2.4.1 Equilibrium Stability Analysis	53
2.4.2 Experimental Validation	61
2.4.3 Discussion	75
2.4.4 Conclusions for Stability	78
2.5 Conclusions	79

3	Effects of Position Quantization and Sampling Rate on Virtual-Wall Passivity	81
3.1	Introduction	82
3.2	Passivity	85
3.3	System Model	85
3.4	Virtual-Wall Passivity	88
3.4.1	Approach	89
3.4.2	Sufficiency	90
3.4.3	Necessity	99
3.4.4	Discussion	102
3.5	Experimental Verification	107
3.5.1	Experimental Haptic Device	107
3.5.2	Experimental Results	109
3.6	Conclusions	116
4	Passively Combining Bilateral Telemanipulators and Virtual Environments	117
4.1	Introduction	117
4.2	Passive Virtual Environments	119
4.3	Unconditionally Stable Bilateral Telemanipulators	120
4.4	Combining Bilateral Telemanipulation and Virtual Environments	124
4.4.1	Impedance-Type Devices	125
4.4.2	Admittance-Type Devices	127
4.5	Experimental Demonstration	128
4.5.1	Unconditional Stability	129
4.5.2	Results	133
4.6	Discussion	136
4.7	Conclusions	141
5	Pseudo-admittance Bilateral Telemanipulation with Guidance Virtual Fixtures	142
5.1	Introduction	142
5.2	Pseudo-admittance Bilateral Telemanipulation	145
5.2.1	Control System	146
5.2.2	Stability	150
5.2.3	System Characteristics	155
5.3	Guidance Virtual Fixtures	159
5.3.1	Implementation	161
5.3.2	Attractivity	164
5.3.3	Parameter Selection	168
5.4	Experimental Verification	170
5.4.1	System	170
5.4.2	Pseudo-admittance Bilateral Telemanipulation	172
5.4.3	Guidance Virtual Fixtures	180
5.5	Conclusions	183

6	Conclusions and Future Work	185
A	Haptic Paddles	193
A.1	Electromechanical Device	193
A.2	Device Models	195
A.2.1	Mass with Viscous Friction	195
A.2.2	Mass with Coulomb-Plus-Viscous Friction	197
A.3	Ideal Actuator Assumptions	199
B	Discrete State-Space Model	205
C	Trajectories That Minimize Energy Losses Due to Friction	210
C.1	Monotonic Trajectories	210
C.2	No Resting	212
D	Linearizing and Decoupling Control	215
E	Adaptive Identification of PHANToM Parameters	218
E.1	PHANToM Model	219
E.2	Adaptive Algorithm	223
E.3	Adaptive Algorithm Applied to PHANToMs	226
	Bibliography	233
	Vita	249

List of Figures

1.1	A ruler assists in drawing a line straighter and faster than freehand.	3
1.2	Robots of the (a) impedance and (b) admittance types. $F(t)$ is the externally-applied force, and $V(t)$ is the resulting robot velocity. For the impedance-type robot, $F_a(t)$ is the actuator force.	7
1.3	Two-port network representation of a telemanipulator. The human and the environment are both one-port networks.	9
2.1	Telemanipulation Controller Architectures (Two-Port Circuit Representations): (a) position forward (PF), (b) position exchange (PE), (c) position forward/force feedback (PFFF), and (d) position exchange/force feedback (PEFF).	30
2.2	Forbidden-Region Virtual Fixtures (FRVFs): Impedance-type FRVF at master with (a) impedance-type FRVF at slave and (b) proxy-based FRVF at slave. The forbidden region is left of the virtual fixture.	34
2.3	Equilibrium position vs. FRVF stiffness for an unmeasured environmental disturbance force pushing slave into forbidden region, with $F_e = -5\text{ N}$, $F_h = 0\text{ N}$, $K_{pm} = K_{ps} = 1000\text{ N/m}$, and FRVF stiffnesses originally set at $K_{mVF} = K_{sVF} = 100\text{ N/m}$. Note that the master positions coincide.	35
2.4	Equilibrium position vs. FRVF stiffness for user attempting to move device into forbidden region, with $F_h = 5\text{ N}$, $F_e = 0\text{ N}$, $K_{pm} = K_{ps} = 1000\text{ N/m}$, and FRVF stiffnesses originally set at $K_{mVF} = K_{sVF} = 100\text{ N/m}$. Note that the slave positions coincide.	36
2.5	Experimental 1-DOF impedance-type bilateral telemanipulation system based on modified Haptic Paddles.	37
2.6	Visualization of Submittance: (a) Impedance-type FRVF at slave (high level of submittance) and (b) Infinite FRVF at slave (low level of submittance). The forbidden region is left of the virtual fixture.	39

2.7	Experimental data from a single subject with the PE controller for three trials of the <i>Touch</i> task with no FRVFs (master (- ·), slave (··)), and for three trials of the <i>Touch</i> task with a hard master FRVF and an infinite slave FRVF (master (—) and slave (- -)). The FRVF and the surface of the environment are located at 0 mm. (Top) The subject moves the system forward and touches the surface/FRVF as instructed, and then withdraws. (Bottom) Close-up near FRVF/environment surface, showing clear differences between methods.	44
2.8	Statistical Results using Tukey’s Method of Pairwise Comparisons. FRVF pairs are listed in descending order (best performance in each category is at the top of the list) for the nine combinations of hard (H), soft (S), infinite (I), and no (0) master and slave FRVF. Vertical bars indicate FRVF pairs that are not significantly different from one another ($p = 0.05$).	45
2.9	General three-channel telemanipulator implemented with a digital computer.	52
2.10	Experimental data showing slave manipulator interacting with an unstable FRVF. The equilibrium position, based on the master position and the system gains, is also shown. Vibrations do not occur on the surface of the FRVF, but rather, around an unstable equilibrium. The system shown is implementing PF control, with $K_{ps} = 600$ N/m, $K_{vs} = 2$ Ns/m, $K_{sVF} = 3000$ N/m, and $T = 0.002$ seconds.	54
2.11	Human index finger mass-spring-damper values for five users [32], with simple bounding lines added. Original data courtesy Robert D. Howe.	63
2.12	Algorithm for determining system stability.	65
2.13	The clouds of eigenvalues show how the system eigenvalues vary based on possible human users, for a system with $T = 0.002$ seconds, $K_{pm} = K_{ps} = 800$ N/m, and $K_{dm} = K_{ds} = 6$ Ns/m. Arrows indicate how the eigenvalues move as the FRVF stiffness is increased from $K_{sVF} = 500$ N/m to $K_{sVF} = 5500$ N/m. Eventually, the eigenvalues reach the imaginary axis, indicating possible instability for the worst-case user.	66
2.14	Predicted and experimental stability bounds for slave FRVFs vs. sampling rate, with $K_p = 600$ N/m and $K_d = 2$ Ns/m. Experimental data is shown for large ($user_L$) and small ($user_S$) users.	67
2.15	Predicted and experimental stability bounds for slave FRVFs, at 500-Hz sampling rate. Data is shown for large ($user_L$) and small ($user_S$) users.	69
2.16	Predicted and experimental stability bounds for slave FRVF, at 1000-Hz sampling rate. Data is shown for large ($user_L$) and small ($user_S$) users.	69

2.17	Predicted and experimental stability bounds for slave FRVFs vs. sampling rate for unilateral telemanipulation, with $K_{ps} = 1000$ N/m and $K_{ds} = 6$ Ns/m. A unilateral telemanipulator models saturation of the master actuator.	70
2.18	Predicted and experimental stability bounds for master FRVFs vs. sampling rate, with $K_p = 600$ N/m and $K_d = 2$ Ns/m. Experimental data is shown for large ($user_L$) and small ($user_s$) users.	71
2.19	Predicted and experimental stability bounds for master FRVFs, at 500-Hz sampling rate. Data is shown for large ($user_L$) and small ($user_s$) users.	73
2.20	Predicted and experimental stability bounds for master FRVFs, at 1000-Hz sampling rate. Data is shown for large ($user_L$) and small ($user_s$) users.	73
2.21	Predicted and experimental stability bounds for master FRVFs vs. sampling rate for unilateral telemanipulation, with $K_{ps} = 1000$ N/m and $K_{ds} = 6$ Ns/m (simple virtual wall). Experimental data is shown for large ($user_L$) and small ($user_s$) users. Requiring passivity of the FRVF gives a very conservative result.	74
3.1	Closed-loop system consisting of a human coupled with a virtual-wall system. Passivity of the individual blocks is sufficient for coupled stability.	83
3.2	Haptic device implementing a virtual wall. This is a sampled-data system, with device dynamics, sensor quantization, sampling, and zero-order hold considered explicitly.	86
3.3	Quantization mapping of encoder with resolution Δ falls somewhere between two extremes. Assume without loss of generality that the solid line represents quantization mapping.	88
3.4	Worst-case J^* for virtual-wall compression and release for a nominal system, with $\alpha > 0$ and $f_c \geq \beta$. Linear-worst-case lines are shown. $ J^*(\lambda) \geq J^*(-\lambda) $ and $ J_{lwc}^*(\lambda) \geq J_{lwc}^*(-\lambda) \forall \lambda$	97
3.5	Worst-case J^* for virtual-wall compression and release for a nominal system, with $\alpha < 0$. Due to the quadratic nature of the curves, regardless of the sign of β , there will exist a closed kinematic trajectory that will result in net energy generation ($J^* < 0$ for compression and release).	100
3.6	Friction containing stiction and nonlinear viscous friction, modeled as Coulomb-plus-viscous friction.	104
3.7	The modified Haptic Paddle used for virtual-wall passivity experiments.	108
3.8	Experimental data resulting from typical and malicious touch with $K = 300$ N/m. Positive values correspond to virtual-wall penetration. This plot supports passivity.	110

3.9	Experimental data resulting from typical and malicious touch with $K = 770$ N/m, and from a malicious touch with a wooden dowel for the same stiffness. Positive values correspond to virtual-wall penetration. The human finger can not exploit the active behavior at this stiffness.	111
3.10	Experimental force data, measured by the load cell, resulting from malicious touch with three virtual-wall stiffness values. The user touched the virtual wall very softly at approximately the 2-second mark. This virtual wall behaves passively only for $K = 80$ N/m.	113
3.11	Experimental force data, measured by the load cell, resulting from malicious touch with $K = 90$ N/m. The user touched the virtual wall very softly at approximately the 2-second mark. This stiffness value appears to be the passivity limit for our system – it is difficult for the user to generate non-passive behavior. Position data confirms that non-passive behavior occurs when straddling an encoder pulse.	114
4.1	Two-port network. The instantaneous power flow into the network is given by $F_1V_1 + F_2V_2$	122
4.2	Network models for (a) passive VEs overlayed on an unconditionally stable telemanipulator, and (b) passive device/VEs combined with an unconditionally stable telemanipulation controller. These models assume impedance-type ports.	126
4.3	Parallel connection of impedance elements in (a) block diagram and (b) equivalent circuit notations.	126
4.4	Under the assumptions of admittance control, the telemanipulator and the virtual environments are considered as one system. Unconditional stability of the entire admittance-type system is the appropriate design goal.	128
4.5	A master device passively implementing a virtual wall, coupled to an unconditionally stable two-port network consisting of the slave device and the telemanipulation controller. This system is stable when coupled to any passive human and environment.	129
4.6	Unconditional stability criteria for two-port network consisting of slave device and telemanipulation controller with $K_{ds} = K_{dm} = 2$ Ns/m, $K_{ps} = K_{pm} = 3990$ N/m, and $T = 0.001$ seconds. Criteria 1-3 correspond to (4.5)-(4.7), respectively. This system is unconditionally stable.	132
4.7	Unconditional stability criteria for two-port network consisting of slave device and telemanipulation controller with $K_{ds} = K_{dm} = 2$ Ns/m, $K_{ps} = K_{pm} = 4000$ N/m, and $T = 0.001$ seconds. Criteria 1-3 correspond to (4.5)-(4.7), respectively. This system is not unconditionally stable.	133

4.8	Interaction with a master-side FRVF with $K_{mVF} = 300$ N/m, $K_{ds} = K_{dm} = 2$ Ns/m, $K_{ps} = K_{pm} = 3990$ N/m, and $T = 0.001$ seconds. (top) A typical interaction where the user applies a moderate force to the FRVF with a finger through the finger loop. (middle) A malicious interaction where the user attempts to create non-passive behavior by applying a force low on the master device. (bottom) A malicious interaction where the slave is pulled into the forbidden region, saturating the slave actuators, and the master is then impulsively disturbed at approximately the 1.7-second mark. No non-passive behavior was demonstrated with this system.	134
4.9	Interaction with a master-side FRVF with $K_{mVF} = 900$ N/m, $K_{ds} = K_{dm} = 2$ Ns/m, $K_{ps} = K_{pm} = 3990$ N/m, and $T = 0.001$ seconds. (top) A typical interaction where the user applies a moderate force to the FRVF with a finger through the finger loop. (bottom) A malicious interaction where the slave is pulled into the forbidden region, saturating the slave actuators, and the master is then impulsively disturbed at approximately the 2.9-second mark. This disturbance results in a demonstration of non-passive behavior.	135
4.10	Master side of Fig. 4.2(b), with energy generation/dissipation explicitly considered.	138
4.11	(a) An impedance-type port of a sampled-data n-port network, (b) separated into its (passive-by-design) LTI n-port network, and an NLTV impedance that captures the difference between the LTI force F_{LTI} expected from the velocity V , and the actual sampled-data force F . Plot (c) shows an F associated with a typical F_{LTI} , and (d) shows F_{NLTV} . The instantaneous power entering the NLTV impedance is found by the inner product of F_{NLTV} and V	139
4.12	(a) An admittance-type port of a sampled-data n-port network, (b) separated into its (passive-by-design) LTI n-port network, and an NLTV admittance that captures the difference between the LTI velocity V_{LTI} expected from the applied force F , and the actual velocity V	140
5.1	A geometrical view of guidance virtual fixtures when (a) there is a component of the applied force in the preferred direction, and (b) when there is no component of the applied force in the preferred direction. The virtual fixture maps the input force F_{PDm} into the virtual fixture force F_{vf} , which is then used as a command to the proxy.	163
5.2	The user applies a unit-magnitude force \hat{F}_{PDm} , and the VF maps the applied force into the force F_{vf} . (a) If the angle ϕ is sufficiently small, the VF tends to be attractive. (b) If the angle ϕ is too large, the proxy is commanded away from the VF.	165
5.3	Visualization of the quadratic function (5.54), when (a) $(1 - \gamma_{vf})^2 - 4\gamma_{vf}t^2\phi < 0$, and when (b) $(1 - \gamma_{vf})^2 - 4\gamma_{vf}t^2\phi \geq 0$. A positive f''_{vf} tends to increase e_{vf}	168

5.4	An experimental demonstration of the steady-hand behavior seen in Pseudo-admittance control ($k_a = 30$ mm/(Ns)). Master (—) and proxy (⋯) trajectories are shown. At approximately the 5-second mark, the user releases the master, and the system stays in place.	173
5.5	Effects of slow update rate in proxy dynamics ($k_a = 30$ mm/(Ns)). Normalized force F_{PDm}/k_a (—) and proxy velocity (⋯) are shown.	174
5.6	Simulated interactions with viscous environments with damping b_e , $\gamma_f = 1$, and varying values of admittance gain k_a . Master (- -), slave (—), and proxy (⋯) trajectories are shown. The user applies a constant force F_h for the first three seconds, and then releases the master.	176
5.7	Simulated interactions with viscous environments with damping b_e , $\gamma_f = 5$, and varying values of admittance gain k_a . Master (- -), slave (—), and proxy (⋯) trajectories are shown. The user applies a constant force F_h for the first three seconds, and then releases the master.	177
5.8	Simulated interactions with an elastic environment with spring constant $k_e = 500$ N/m, with $\gamma_f = 1$ and varying values of admittance gain k_a . Master (- -), slave (—), and proxy (⋯) trajectories are shown. The user applies a constant force F_h for the first two seconds, and then releases the master.	178
5.9	Simulated interactions with an elastic environment with spring constant $k_e = 500$ N/m, with $\gamma_f = 5$ and varying values of admittance gain k_a . Master (- -), slave (—), and proxy (⋯) trajectories are shown. The user applies a constant force F_h for the first two seconds, and then releases the master.	179
5.10	Guidance virtual fixtures for the vertical plane defined by $x = 0$. Master (—) and proxy (⋯) trajectories are shown. All data is shown for $k_a = 40$ mm/(Ns), with other GFV parameters varying.	182
A.1	Current amplifier.	194
A.2	Plot showing that the r^2 metric is appropriate for a mass-damper model of the Haptic Paddle. Data is shown for master device.	198
C.1	The dynamic portion of $x_1(t)$ is stretched in time to create $x_2(t)$, containing no resting region.	213
E.1	Kinematic model of PHANToM robot. (a) Zero configuration. (b) Definition of angles and frames.	220
E.2	Inertial model of the PHANToM.	224

To my lovely wife Katie

Chapter 1

Introduction

1.1 Motivation

Telem Manipulation is the direct human control of a robotic manipulator, where the operator and the manipulator are at different locations. Telem Manipulation can be used to accomplish a great number of tasks that are too remote, highly scaled, or hazardous for direct human manipulation. It is particularly advantageous in unstructured environments where completely autonomous robotic systems cannot be used due to the limitations of artificial intelligence, sensor-data interpretation, and environment modeling. Telem Manipulation has current and potential benefits in diverse applications such as space, undersea, hazardous nuclear, chemical, and biological environments, surgery, construction, mining, military, firefighting and life-saving, warehousing, and entertainment [92].

“Bilateral” telem Manipulation typically refers to a system where a human operator manipulates a master robotic device, and a slave device emulates the behavior

of the master, with some form of haptic (force and/or tactile) feedback to the operator. Although haptic feedback can improve performance of telemanipulated tasks, traditional telemanipulation systems are not able to provide any intelligent assistance to the human operator. In addition, the accuracy and precision of even a perfectly designed telemanipulator is still ultimately limited by the accuracy and precision of the human user. Thus, we are developing novel human-machine collaborative control laws, called “virtual fixtures,” which bridge the gap between strictly autonomous and strictly teleoperated systems.

The term “virtual fixture” refers to a general class of guidance modes, implemented in software, that help a human-machine collaborative system perform a task by limiting movement into restricted regions and/or influencing movement along desired paths. The potential benefit of virtual fixtures is safer and faster operation. Virtual fixtures attempt to capitalize on the accuracy of robotic systems, while maintaining a degree of operator control. To help visualize the benefits of virtual fixtures, consider Fig. 1.1, where a ruler is used to assist in drawing a straight line. A line drawn with the ruler is straighter than a line drawn without a ruler, and it can also be drawn faster. A virtual fixture could be used to accomplish this same sort of task, but without the need for physical fixturing hardware.

Virtual fixtures can be used to prevent the slave manipulator from entering into forbidden regions of the workspace. A virtual fixture can be designed to act as an absolute barrier to any slave movement into the forbidden region. Or, a virtual fixture can act as guidance for the human user – preventing unintentional incursions

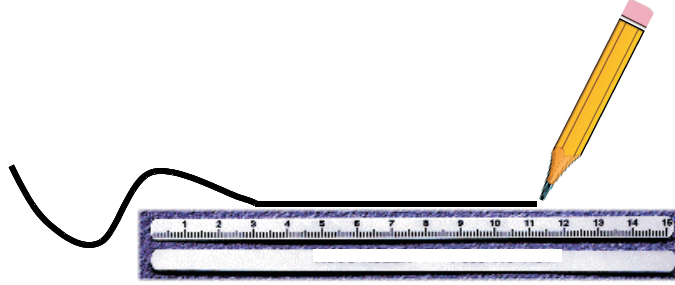


Figure 1.1: A ruler assists in drawing a line straighter and faster than freehand.

into the forbidden region, while making the user aware of the slave's precarious location. Virtual fixtures can also be used to constrain the slave manipulator to certain paths and surfaces in the workspace. A virtual fixture can be designed to rigidly constrain the slave to a path, much like a train on a track, so the user is only able to control the position of the robot along the path. Or, a virtual fixture can act as guidance to the user, creating preferred directions in the workspace that the user can choose to either follow or reject.

Virtual fixtures are particularly well suited for application in robot-assisted minimally invasive surgery (MIS). Telemanipulation has the potential to improve precision, dexterity, and visualization for the surgeon [31]. Bilateral telemanipulation systems can also decrease operation time and forces applied to the environment [105]. Virtual fixtures can further enhance robot-assisted MIS by ensuring that the remote manipulator does not enter forbidden areas of the workspace, such as organ surfaces that should not be cut or delicate tissue structures. They can also provide guidance in MIS tasks that require better-than-human levels of precision. We seek to develop virtual-fixture control laws that can be safely (stably) implemented on bi-

lateral telemanipulators, with special consideration given to environments relevant to MIS tasks.

1.2 Dissertation Contributions

We briefly summarize the major contributions of this dissertation as follows:

- We present a novel method for stability analysis of forbidden-region virtual fixtures implemented on bilateral telemanipulators. The method may be applied directly to a large class of common telemanipulation control architectures. The method is experimentally verified. To the best of the author's knowledge, this work represents the first rigorous stability analysis of forbidden-region virtual fixtures for telemanipulation.
- We present a necessary and sufficient condition for passivity of haptic virtual environments that is the first to explicitly consider not only the effects of sampling rate and friction, but also quantization resulting from measuring position with an optical encoder. This condition is experimentally verified.
- We present a framework for analysis of virtual-fixture stability that relies on passivity of individual system components. We show that stable virtual fixtures can be created by combining passive virtual environments with unconditionally stable telemanipulators. To the best of the author's knowledge, this represents the first attempt at generalizing the analysis of virtual-fixture stability to include any type of virtual fixtures and robot hardware.

- We present a novel bilateral telemanipulation control law for the performance of delicate tasks with the assistance of guidance virtual fixtures. The telemanipulation control law also shows promise for use with telemanipulation systems that are typically run under rate control. The salient features of the control law, both with and without guidance virtual fixtures, are shown through experiment and simulation.

1.3 Prior Work

The following is a review of the prior work that is relevant to this dissertation. We begin by reviewing robots of the impedance and admittance type. These terms will be used throughout this dissertation. Prior work in bilateral telemanipulation under both position and rate control is reviewed in Section 1.3.2. The work on position control is relevant background for the dissertation as a whole, which considers telemanipulation under position control, while the work on rate control is particularly relevant to Chapter 5, where elements from rate control are incorporated into a novel bilateral telemanipulation controller. Next, prior work on stable/passive virtual environments is discussed in Section 1.3.3, and we introduce two concepts – the “proxy” and the “virtual coupling” – that are used throughout this dissertation. The work on virtual-environment passivity is relevant to Chapters 3 and 4, where passive virtual environments are used as virtual fixtures. Finally, prior work on virtual fixtures (under various aliases) is discussed in Section 1.3.4. This prior work is shown to be largely *ad hoc*, motivating the generalizations used in this dissertation.

1.3.1 Robots of the Impedance and Admittance Type

In general, bilateral telemanipulators are constructed as one of four possible combinations of impedance-type and admittance-type master and slave robots [37]. Robots of the impedance type are backdrivable and have force-source actuators. They are also typically characterized by low inertia and friction. A linear impedance-type device is modeled by

$$F(s) - F_a(s) = Z(s)V(s) \quad (1.1)$$

where F and F_a are the externally-applied force and the force applied by the actuator, respectively, V is the velocity of the device, and Z is the (typically-low) impedance of the device, containing inertial and frictional properties.

Robots of the admittance-type are nonbackdrivable and have velocity-source actuators. The nonbackdrivability typically comes from large friction and gearing in electromechanical systems, and from valves and fluid incompressibility in hydraulic systems. The velocity is controlled with a high-bandwidth servo controller, and is assumed to be independent of applied external forces, due to nonbackdrivability. A linear admittance-type device is modeled by

$$V(s) = Y(s)F(s) \quad (1.2)$$

where F is the measured externally-applied force and Y is the controlled device admittance. The admittance Y is generated in software (nonbackdrivability assumes a device admittance $Y = 0$), as opposed to the impedance Z of an impedance-type device, which actually does represent the mechanical properties of the device. Figure

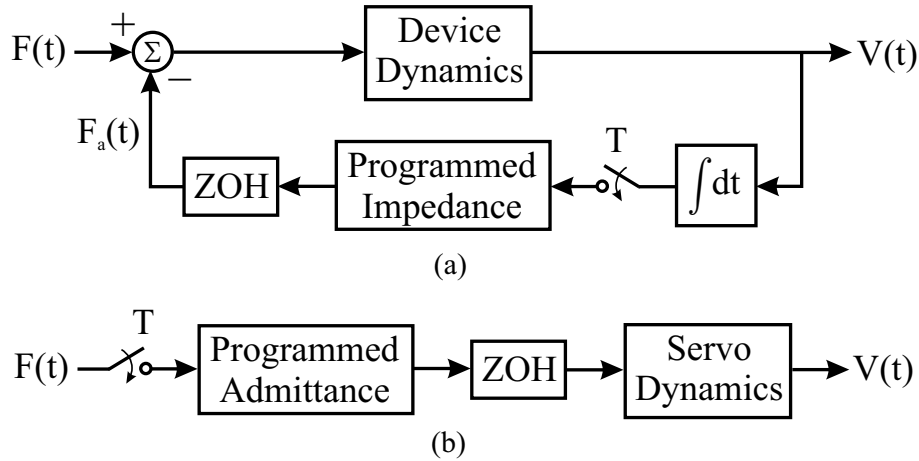


Figure 1.2: Robots of the (a) impedance and (b) admittance types. $F(t)$ is the externally-applied force, and $V(t)$ is the resulting robot velocity. For the impedance-type robot, $F_a(t)$ is the actuator force.

1.2 illustrates typical devices of the impedance and admittance types. With either type of device, the instantaneous power flow from the human to the system is given by $F(t) \cdot V(t)$.

Both impedance-type and admittance-type devices have desirable characteristics. Because of the backdrivability of impedance-type devices, they tend to interact well with a variety of environments, and they allow the stable haptic display of environments with very low impedance. They can also often be overpowered by a human in the event of failure, providing a degree of safety. Admittance-type devices have the desirable characteristics associated with traditional industrial robots – accuracy, strength, and good disturbance rejection. Admittance-type haptic devices are also able to stably generate virtual environments with very low admittance (high impedance).

1.3.2 Bilateral Telemanipulation

As discussed above, bilateral telemanipulation refers to a system where a slave device emulates the behavior of a human-controlled master device, with some form of haptic (force and/or tactile) feedback to the operator. Bilateral telemanipulation can be accomplished under position control (where the position of the slave manipulator corresponds to the position of the master), rate control (where the velocity of the slave manipulator corresponds to the position of the master), or force control (where the force applied by the slave corresponds to either the force applied by the user, or the position of the master). Scaling is possible in all three modes.

Position Control

Prior research on bilateral telemanipulation has focused largely on position control. Much of this research has worked towards creating systems that are both stable and transparent, where a *transparent* telemanipulator is often defined by having perfect position correspondence between the master and slave while perfectly presenting the slave/environment interaction force to the human user.

Early work in bilateral telemanipulation by Raju *et al.* [79] and Hannaford [33] led to the two-port-network representation of a telemanipulator, shown in Fig. 1.3. Recent work on analysis and design of telemanipulation controllers has used the two-port representation almost exclusively; it allows some analysis of the telemanipulator to be conducted independently from the human user and the environment.

Increasing transparency in a bilateral telemanipulator while retaining stability



Figure 1.3: Two-port network representation of a telemanipulator. The human and the environment are both one-port networks.

is a common research topic. This is important because transparency and stability are conflicting design goals [56]. Hannaford [34] developed a frequency-domain “loop gain” for a closed-loop telemanipulation system, based on the two-port parameters. This loop gain can then be used with traditional loop-shaping methods. Yokokohji and Yoshikawa [110] achieved perfect telepresence in a system that can be exactly modeled, but their technique requires accurate acceleration measurements, not available in practice. Sherman *et al.* [93] and Çavuşoğlu *et al.* [16] worked towards increasing transparency in a way that would assist the user in discriminating between different environmental impedances during palpation tasks. Speich *et al.* [96] increased transparency over the frequency range of human capability, while maintaining robust stability of the closed loop, using frequency-domain loop-shaping techniques. Hashtrudi-Zaad and Salcudean [37] provide guidelines for increasing transparency, while using the “absolute stability criteria” to guarantee stability. Ryu *et al.* [86] use the Passivity Observer/Passivity Controller (PO/PC) to maintain stability in a nonconservative way.

Topics from robust control have also been applied to bilateral telemanipulators. Sherman *et al.* [93] and Çavuşoğlu *et al.* [16] consider unstructured multiplicative uncertainties in the plant. Colgate [17] analyzed the structured singular values of

the telemanipulator’s scattering matrix. Kazerooni *et al.* [47], Leung *et al.* [58], and Yan and Salcudean [108] apply \mathcal{H}_∞ techniques, essentially designing for the worst-case exogenous input, sacrificing fidelity for stability robustness.

A large body of work has considered stability and transparency in the presence of time delays in the communication channel. Time delays are very important for certain telemanipulation applications, such as space and undersea. Kim *et al.* [49] use “shared compliant control,” where the slave robot uses a local compliant control system to interact well with an environment, even with delays. Leung *et al.* [58] consider time delays as a perturbation to the system. Yan and Salcudean [108] approximate the time delay with a Padé approximation. Hashtrudi-Zaad and Salcudean [38] broaden the definition of “transparency” for delayed systems. Anderson and Spong [8,9], Lawrence [56], and Niemeyer and Slotine [72,73] create stable systems through the use of scattering matrices and wave variables, essentially ensuring the passivity of the communication channel. Similarly, Stramigioli *et al.* [98] use a geometrical port-Hamiltonian method to create passivity, even in the presence of time delays. Yokokohji *et al.* [109] extended wave-variable techniques to improve feel at the expense of stability robustness.

Very little work has explicitly considered sampling and sensor-quantization effects in telemanipulation. Secchi *et al.* explicitly consider sampling effects [91], and consider sensor-quantization effects by modeling the quantization as a bounded error in the measurement [90]. Sampling and sensor quantization are likely to be significant limiting effects in robot-assisted surgical systems.

Rate Control

In recent years, researchers have worked towards providing force feedback on telemanipulators under rate control. Rate control has benefits when the workspace of the slave is much larger than the workspace of the master, such as with heavy hydraulic equipment [57,77]. If position control is used on such systems, hand tremor and other undesirable movements of the user are amplified at the slave. Similarly, rate control could potentially be beneficial even without position scaling, when the precision required at the slave manipulator is beyond the limits of the human user. An additional benefit of rate control is that the master device is typically a simple joystick with a very compact workspace.

It is not obvious how best to add force feedback to rate-controlled systems, due to the kinematic discrepancies between the master and the slave. Salcudean *et al.* [88] present a method to create transparent rate-controlled bilateral telemanipulation, where “transparency” is defined as accurately presenting the environment impedance to the human user. This was accomplished by feeding back the time derivative of the slave/environment interaction force. Their method makes certain idealizing assumptions that make it nonrobust in practice. In an attempt to increase robustness, Mobasser *et al.* [69, 70] continued with this definition of transparency, by estimating the impedance properties of the environment, and then presenting this impedance to the user.

Williams *et al.* [107] created Naturally-Transitioning Rate-to-Force Control, which acts like rate control when the slave is moving in free space, and acts like force control

when the slave is constrained by an environment. Their method works by creating an input to the rate controller that is a combination of the applied user force and the measured environmental force. They termed the controller “natural” in that it requires no switching between controllers – the method seamlessly handles coming in and out of contact with the environment.

Position Control vs. Rate Control

A body of research exists comparing position and rate control in virtual environments, and that research has parallels in telemanipulation. Zhai and Milgram [112] compared isotonic and isometric input devices for position and rate control. Isotonic devices are position input devices that require very little applied force; an example is a computer mouse. Isometric devices are force input devices with very little resulting position displacement; an example is a stiff load cell mounted on a rigid stationary platform. Isotonic devices are related to impedance-type master devices – as the actuation (force) on an impedance-type device is reduced, the device approaches an isotonic device. Isometric devices are related to admittance-type master devices – as the actuation (velocity) on an admittance-type device is reduced, the device approaches an isometric device. Zhai and Milgram found that rate control (in virtual environments) is best accomplished with an isometric input device, and position control is best accomplished with an isotonic input device. Elastic devices lie somewhere between isotonic and isometric devices; an example is a spring-centered joystick. Elastic devices can be thought of as either position or force input devices, since position and force are proportional through the elastic spring constant.

Zhai [111] found that elastic input devices are better for rate control than isometric input devices.

Returning to telemanipulation, Kim *et al.* [50] found that, when the workspace of the slave is smaller than or comparable to the workspace of the master, position control is always preferable to rate control. But, they found that the superiority of position control disappears if the slave is a slow-moving, low-bandwidth device. They essentially found that positioning tasks are most intuitively accomplished using position control. Researchers have worked to create position-control methods that have some of the benefits of rate control. Casals *et al.* [14] introduce a workspace-deformation position-control method that increases precision at key locations in the workspace (at the expense of reducing precision elsewhere). Abbott and Okamura [2] and Kontz and Book [52] present methods that provide alternatives to rate control, in applications where rate control might typically be used. Both are position control methods that make use of a slow-moving proxy to retain some of the benefits of rate control. Both systems are, roughly speaking, impedance-type masters implementing admittance-type controllers, through the use of a “virtual coupling” (defined below). Some of the noted benefits of this type of control is desirable “steady-hand” properties [2], as well as the ability to switch between position and rate control [52].

1.3.3 Haptic Virtual Environments

Stability and Passivity

Creating virtual environments (VEs) that behave stably has been an active area of research in the field of haptics. Colgate and Brown [18] catalogue the limiting factors in stably generating stiffness with a haptic display. They cite sample-and-hold, device dynamics, position sensor quantization, and velocity filtering as factors that limit the achievable stiffness of a virtual environment. They give a description of the errors incurred from obtaining a velocity estimate by differentiating a position measurement that was obtained with an encoder.

Many haptic VEs are created from fundamental building blocks known as “virtual walls.” A virtual wall is typically an impedance surface (such as a spring or spring-damper) accompanied by a unilateral constraint, where the impedance surface displays a force that is a function of the position (and its time derivatives) of the haptic device, and the unilateral constraint is a nonlinear switching condition that determines if the user is or is not in contact with the virtual wall. The majority of prior work on virtual environment stability has explicitly considered the virtual wall; this simplifies and generalizes the research, but it also assumes an impedance-type haptic device.

Much of the research in VE stability has worked towards creating passive VEs, under the assumption that humans interact stably with passive objects [40]. Creating passive VEs has the benefit of not relying on any specific model of the human user (other than passivity) in the stability analysis. However, creating passive

sampled-data systems is not trivial. Colgate *et al.* [19] give a description of how a virtual wall, implemented as a virtual spring, can become non-passive, even though a physical spring is passive. Gillespie and Cutkosky [29] enumerate “energy leaks” through which the virtual wall can generate energy, such as zero-order hold and asynchronous switching times associated with a sampled unilateral constraint.

We now summarize the major results in VE stability/passivity, in chronological order. Love and Book [61] use the Jury stability criterion to analyze contact instability. They assume the user can be modeled as an exogenous force input, thereby neglecting the dynamics of the user. Gillespie and Cutkosky [29] eliminate contact instability for a user modeled as a known, constant mass-spring-damper system. Colgate and Schenkel [20] present a simple condition on virtual-wall stiffness that is a function of the viscous friction in the system, as well as the sampling rate. Their result is a stiffness bound, below which the energy generated by “energy leaks” is dissipated by viscous friction in the haptic device, creating a system that appears passive to the user. Madill *et al.* [63] develop a nonlinear observer to estimate the position and velocity of the haptic device, as a way to deal with the effects of sensor quantization and Coulomb friction. However, their observer requires an accurate measurement of the force applied by the user. Goldfarb and Wang [30] implement a hysteresis coupled with a virtual spring as a way of ensuring virtual-wall passivity. They propose that one way to counter “energy leaks” is to simulate a dissipative system (rather than a lossless passive system). Adams and Hannaford [6] use a “virtual coupling” to ensure stable interaction with a VE. This method essentially filters

the impedance of the VE, limiting the range of stiffness presented to the user. Hanaford and Ryu [36] introduce a Passivity Observer/Passivity Controller (PO/PC) that keeps track of the net energy generated by the virtual wall, and actively dissipates this excess energy. Ryu *et al.* [85] continue the PO/PC work by removing the previous assumption that the velocity of the haptic device remains constant between samples. The PO/PC idea is also extended to allow the dissipation of excess energy to take place over prolonged time periods, with the goal of reducing induced high-frequency vibration [84]. Stramigioli *et al.* [97] use a port-Hamiltonian approach to explicitly keep track of energy as it moves through the system. Miller *et al.* [68] give conditions such that a quantifiable excess of passivity in a haptic device can be used to guarantee that a VE will appear passive to the user. Finally, Mahvash and Hayward [64] use a dual-rate system that maintains passivity and fidelity when interacting with deformable VEs.

Worthy of special note is the recent work by Diolaiti *et al.* [25], because their main result is the same as our main result of [5] and Chapter 3. Their work was completed in parallel to ours, and is listed here as prior work in the sense that it was presented before the completion of this dissertation. The presentation of [25] came after the submission of [5]. They arrived at their result using different methods than ours, and they give a different interpretation of the results. We believe that their work is complementary to ours.

The Proxy and the Virtual Coupling

Two important concepts will be referred to throughout this dissertation – they are the “proxy” and the “virtual coupling.” The proxy (as it is typically now referred to) was introduced by Zilles and Salisbury [113] as the “god-object.” The proxy is an object that exists entirely in software, created for the purpose of haptic interaction with VEs via an impedance-type haptic device. The idea is simple: the proxy position exactly coincides with the position of the haptic device when the haptic device is not interacting with a VE. When the haptic device enters into a VE, the proxy is constrained to remain on the surface of the VE. If the haptic device then servos to the proxy position, the user can haptically interact with the VE in an intuitive way. The idea of the proxy has been elaborated on since its introduction – this will be seen in Section 1.3.4, and in the remainder of this dissertation.

The “virtual coupling” was introduced by Colgate *et al.* [21], but greatly expanded upon by Adams and Hannaford [6]. The virtual coupling plays multiple roles. For visualization, a virtual coupling can be thought of as a software spring-damper attached to the end effector of a haptic device interacting with a VE (this visualization assumes an impedance-type haptic device). When designing stable virtual environments, traditionally the VE and the haptic device’s control system have been one and the same. This makes VE design specific to a given device. The virtual coupling acts as an intermediary between the haptic device and the VE – the impedance felt by the user is the impedance of the VE and the impedance of the virtual coupling in parallel (visualize two springs in series). In the limit as the

VE approaches a perfectly rigid object, the impedance felt by the user approaches the virtual coupling. In this way, the virtual coupling can be designed for a specific system, to guarantee stable interaction with any VE, designed without consideration of the haptic device.

The virtual coupling also plays another important role. Just as robots can be of the impedance or admittance type, so can VEs. An impedance-type VE is one that measures position (and its time derivatives) and outputs an appropriate force. Admittance-type VEs measure a force, and respond with the appropriate dynamics. Impedance-type VEs are typically implemented on impedance-type devices, and admittance-type VEs are typically implemented on admittance-type devices, but Adams and Hannaford [6] showed that it is possible to mix device/VE causalities (*i.e.*, impedance/admittance or admittance/impedance), but it requires the use of a virtual coupling to connect the device to the VE.

1.3.4 Virtual Fixtures

“Virtual fixtures” [1, 54, 75, 76, 78, 80] (also appearing under the name of “synthetic fixtures” [89], “virtual mechanisms” [45, 66], “virtual tools” [43], and “haptically augmented teleoperation” [102]) have been applied to telemanipulators using a variety of methods, though they can generally be categorized as either forbidden-region virtual fixtures (FRVFs) [78] or guidance virtual fixtures. As their name implies, forbidden-region virtual fixtures help keep the slave manipulator out of forbidden regions. Alternatively, guidance virtual fixtures help keep the slave on

desired paths or surfaces.

Rosenberg [80] implemented FRVFs as impedance surfaces on the master device to assist in peg-in-hole tasks. Joly *et al.* [45] introduced a proxy-based method where the proxy is constrained to move on the virtual fixture, and the master and slave both servo to the proxy position and affect its movement along the virtual fixture. Micaelli *et al.* [66] extended this method to allow for multiple proxies, each on its own virtual fixture and with its own dynamics. Itoh *et al.* [43] developed a task-assistance tool that connects admittance-type robots to virtual fixtures with impedance control methods. Park *et al.* [75] implemented FRFVs on the remote slave by rejecting master commands into the forbidden region. There is a proxy-based method, where the slave manipulator servos to the proxy, and the proxy follows the master when outside the FRVF, but will not follow the master into the forbidden region. Turro and Khatib [102] implemented guidance virtual fixtures on a system with an impedance-type master and admittance-type slave. The master is bound to a proxy, which is constrained to move on the virtual fixture, and the slave then tracks either the master or the proxy, depending on the desired level of user control. Payandeh and Stanisic [78] implemented virtual fixtures on both the master and slave manipulators, using a variety of geometries, to help guide the remote manipulator in a predetermined task. Kuang *et al.* [54] then applied this research to difficult assembly tasks. The virtual fixtures above were implemented with penalty-based or potential-field methods. These are impedance-type VEs that act in an active way, in that stored potential energy in the virtual fixture may

potentially be released in an undesirable fashion.

Virtual fixtures have also been implemented on passive cooperative robotic systems (where the human and robot simultaneously act on a single end-effector) known as Cobots [71]. Park *et al.* [76] extended these methods to telemanipulation systems where the master device is a Cobot, for assistance in nuclear deactivation and decommissioning tasks. These virtual fixtures act in a passive way (as compared to those created by potential fields) in the sense that the virtual fixtures are only able to restrict, and not generate, motion. These so-called *passive* virtual fixtures work much like methods developed for autonomous robots, such as “passive velocity field control” [60]. It is also possible to implement *passive* virtual fixtures using admittance-type systems. Since these nonbackdrivable robots move in a highly-controlled fashion (limited in practice by the bandwidth of the servo controller, as well as flexibility in the joints and links), one can passively restrict movement in any given direction by simply not commanding any movement in that direction. This type of virtual fixture has been implemented on the Johns Hopkins University Steady-Hand Robot [101] (which is an admittance-type cooperative manipulator) by Bettini *et al.* [11]. Research on this type of virtual fixture has also been recently been extended to admittance-type telemanipulators by Aarno *et al.* [1].

A topic of interest at Johns Hopkins University is how humans interact with virtual fixtures. Li and Okamura [59] used Hidden Markov Models to determine when a user wanted help from the virtual fixture, and adapted the virtual fixture to assist in the task. Kragic *et al.* [53] broke a complex microsurgical task into

subtasks, each of which benefited from different types of virtual-fixture assistance. They also explored the use of Hidden Markov Models for automatic detection of human intent. Marayong and Okamura [65] analyzed the effects of virtual fixtures on the performance of specific tasks. They asked the question: “How much guidance is best?” All of the above work used the JHU Steady-Hand Robot and was based on the virtual fixtures of [11].

1.4 Dissertation Overview

In this chapter, we presented the motivation for our research in virtual fixtures for bilateral telemanipulation, and presented the pertinent prior work for this topic. We defined what is meant by “impedance-type” and “admittance-type” robots and virtual environments, and we introduced the “proxy” and the “virtual coupling.” All of these concepts will be used throughout this dissertation.

Chapter 2 considers the design of forbidden-region virtual fixtures for bilateral telemanipulators where both the master and slave are impedance-type robots. Various virtual-fixture architectures are compared, using some common telemanipulation control systems, and metrics are defined to quantify the effectiveness of these systems. We then develop a stability analysis technique to assess the stability of these various telemanipulation control architectures combined with impedance-type forbidden-region virtual fixtures. The method makes use of a sampled-data model of the system, and explicitly considers the properties of the human user in the analysis. We experimentally verify our result.

We then apply passivity techniques to virtual-fixture analysis and design. In Chapter 3, we present a necessary and sufficient condition on virtual-wall passivity that considers sampling, quantization, and friction effects in impedance-type devices. This condition is experimentally verified. Next, Chapter 4 considers the use of passivity in the design of stable systems containing bilateral telemanipulators, virtual fixtures, human users, and unknown environments. We present a method to combine an unconditionally stable (passive) bilateral telemanipulator with passive virtual environments, resulting in stable virtual fixtures. This method generalizes to telemanipulation systems with master and slave devices of the impedance or admittance type, and to virtual fixtures of the impedance or admittance type.

In Chapter 5 we present a novel bilateral telemanipulation control system called Pseudo-admittance, which mimics admittance control on systems where the master device is of the impedance type, and has desirable properties for slow, precise tasks. It generalizes to systems where the slave manipulator is of the impedance or admittance type. Pseudo-admittance control lends itself to the implementation of guidance virtual fixtures, which are pursued in Chapter 5 as well. The desirable properties of the Pseudo-admittance controller and the guidance virtual fixtures are demonstrated through simulation and experiment.

We summarize our main results in Chapter 6. We also present some interesting topics for future work that build upon the ideas presented in this dissertation.

Chapter 2

Design Considerations for Forbidden-Region Virtual Fixtures

2.1 Introduction

Prior research in virtual fixtures for bilateral telemanipulation has been largely *ad hoc*, focusing on specific virtual fixtures applied to specific telemanipulation systems, with little or no rigorous stability analysis. In this chapter, we consider forbidden-region virtual fixtures (FRVFs), which prohibit the motion of a robot manipulator into a forbidden region of the workspace, for systems where the master and slave devices are of the impedance type. In Section 2.3 we define metrics to evaluate the effectiveness of FRVFs, and we statistically compare various FRVF/telemanipulation architectures using a human-factors study. In Section 2.4, we consider the stability of impedance-type FRVFs for a class of bilateral telemanipulation control systems

that includes many common control architectures. This is accomplished through a sampled-data system analysis, with explicit modeling of the human user.

2.2 System Model

We will adopt a system model similar to that of Lawrence [56]. The human is modeled with a linear time-invariant (LTI) model

$$F_h^*(s) - F_h(s) = Z_h(s)X_m(s) \quad (2.1)$$

F_h is the human/master interaction force. F_h^* is defined as the exogenous human input; this does not represent an actual force in the system, but rather the input that acts to change the equilibrium point of the system. The assumption that position and force control in the human limb is achieved by simultaneously modifying the system's impedance and equilibrium point is known as equilibrium-point control [12]. F_h^* simply acts to change the coordinates of the system, without affecting the dynamic properties of the human. X_m is the position of the master device (which is equivalent to the position of the human when they are in contact), and X_s is the position of the slave. Without loss of generality, we assume $X_m = X_s$ represents perfect position tracking (a scaling factor could be included, but that does not affect our approach). The human impedance Z_h is modeled as an LTI mass-spring-damper system:

$$Z_h(s) = m_h s^2 + b_h s + k_h \quad (2.2)$$

Modeling a human as a mass-spring-damper is a fairly common approximation [110], and there is evidence that this is an accurate model over short time intervals [32].

The master and slave device dynamics are approximated by linear models:

$$F_h(s) - F_{am}(s) = Z_m(s)X_m(s) \quad (2.3)$$

$$F_{as}(s) - F_e(s) = Z_s(s)X_s(s) \quad (2.4)$$

where Z_m and Z_s are the master and slave device impedances, respectively, F_{am} and F_{as} are the master and slave actuator forces, respectively, and F_e is any external environmental load on the slave. We will assume that the slave only interacts with passive environments. The master and slave impedances are modeled as LTI mass-damper systems:

$$Z_m(s) = m_m s^2 + b_m s \quad (2.5)$$

$$Z_s(s) = m_s s^2 + b_s s \quad (2.6)$$

The impedances above are often written in terms of velocities V_m and V_s rather than positions X_m and X_s . This simply scales the impedances by a factor of s . Working in terms of velocity often simplifies the analysis of telemanipulator stability (since the multiplication of force and velocity defines an instantaneous power flow), but we consider positions here to explicitly keep track of the positions of the master and slave with respect to their FRVFs, and also to acknowledge that position is the quantity that is typically sensed and used in the digital controller.

2.3 Evaluation of Forbidden-Region Virtual Fixture Architectures

The performance of a bilateral telemanipulation system is typically judged by three criteria: stability, tracking, and transparency. As with any control system, *stability* is a fundamental property that is essential for any viable telemanipulation system. The stability of the telemanipulator is affected by the human operator and the slave's environment. Stability is defined by bounded F_h^* resulting in bounded telemanipulator signals (V_m, V_s) [56]. Ideally, a telemanipulator would remain stable regardless of how the human operator behaves, the properties of the slave's environment, and noise and modeling errors in the system. In practice, telemanipulators often exhibit limit cycles as a mode of instability (although the limit cycles themselves may be considered as stable [48]). Limit cycles often result from unmodeled nonlinearities in systems whose linearizations are unstable. We will consider a telemanipulator exhibiting limit cycles as unstable, even though the signals in the system are bounded.

Tracking refers to the geometric correspondence between the master and slave devices (allowing for the possibility of position scaling). Good tracking is needed to translate movement generated by the user at the master device into movement at the slave device. Specifically, we want to minimize the position error between the master and slave; perfect tracking is given by $X_m(t) = X_s(t) \forall t$. A reasonable quantitative measure of tracking is the norm of $X_m(t) - X_s(t)$, where the norm of a

function of time $u(t)$ is defined as

$$\|u(t)\|_p = \begin{cases} (\int_0^\infty |u(t)|^p dt)^{1/p} & : 1 \leq p < \infty \\ \sup_{t \geq 0} |u(t)| & : p = \infty \end{cases} \quad (2.7)$$

Details on \mathcal{L}_p norms can be found in Khalil [48] or van der Schaft [104]. Perfect tracking then corresponds to $\|X_m(t) - X_s(t)\|_p = 0$, regardless of p .

Transparency is traditionally a measure of how well the impedance felt at the slave is reflected to the user. *Impedance* refers to the relationship between position (and its time derivatives) and force. The impedance of the environment is typically defined, using a linear model, as:

$$Z_e(s) = \frac{F_e(s)}{V_s(s)} \quad (2.8)$$

and the impedance felt by the user is

$$Z_{\text{felt}}(s) = \frac{F_h(s)}{V_m(s)} \quad (2.9)$$

Perfect transparency is achieved if $Z_{\text{felt}}(s) = Z_e(s)$, but a simple quantitative measure of transparency is not obvious. This topic was explored by Yokokohji and Yoshikawa [110]. A telemanipulator may have either good tracking or good transparency without necessarily having both. If a system does have both good tracking and transparency, it is sometimes described as creating “telepresence,” meaning that movements of the slave correspond to those of the master, and forces experienced at the slave are reflected to the user, creating a sensation of haptic immersion in the task.

The goals of telemanipulator design all revolve around giving the user the highest possible control over the slave. In contrast, the goal of virtual-fixture design is

to remove some control from the user. Because these goals generally conflict with one another, it is not obvious how to best implement FRVFs on a telemanipulation system. To the best of the author's knowledge, no previous research on telemanipulation with virtual fixtures investigates whether implementing virtual fixtures on the master or slave side (or both) leads to the most desirable system behavior. Also, no research has compared how a given virtual-fixturing method works with multiple telemanipulation control architectures.

The aim of this section is to compare different combinations of master and slave FRVFs, with common telemanipulation control architectures, and to determine which combinations lead to the most desirable system behavior. The controller architecture used with a given telemanipulator is usually dictated by hardware (actuators and sensors available). Thus, it is desirable to know which FRVF architecture should be used with a given control architecture. To quantify the effectiveness of FRVFs, we qualitatively and quantitatively define three metrics (tracking, safety, and submittance), which are then analyzed in a human-factors experiment. The research in this section was presented in part in [3]. Since this section culminates in a psychophysical study conducted to determine the effects of FRVFs when performing tasks at the threshold of human perception, we only consider stable and well-behaved telemanipulators, and neglect any sampled-data effects that are beyond the perception of a human user. Stability issues associated with sampled-data effects are addressed in Section 2.4.

2.3.1 Telemanipulator Controller Architectures

Four common telemanipulation control architectures are considered in this experiment. These four controllers are shown in Fig. 2.1, using a two-port circuit representation. For each of these four telemanipulation control systems, the master actuation scheme varies, but the slave is always controlled by a position servo controller of the form:

$$F_{as} = K_{ps}(X_m - X_s) - K_{vs}\dot{X}_s \quad (2.10)$$

The first controller we consider is the position-forward (PF) controller. In this control mode the slave tracks the master with a simple position servo, and the master is not actuated:

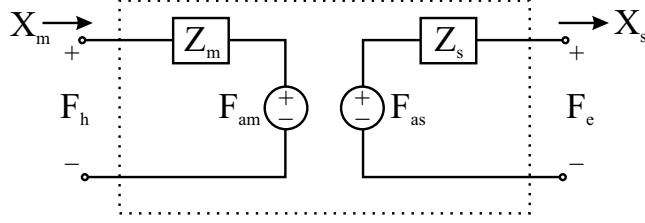
$$F_{am} = 0 \quad (2.11)$$

The PF controller is the only unilateral controller considered (no haptic feedback to the master). This controller can be thought of as a traditional feedback control system, since the master position acts as an exogenous input (excluding the effects of visual feedback to the operator).

Next we consider the position-exchange (PE) controller. Here, the slave servos to the master's position, and the master simultaneously servos to the slave's position:

$$F_{am} = K_{pm}(X_m - X_s) + K_{vm}\dot{X}_m \quad (2.12)$$

With this controller, all forces fed back to the master are generated from the position error between the master and slave. Variations of the PE controller have appeared



	Master Actuator Force	Slave Actuator Force
(a)	$F_{am} = 0$	$F_{as} = K_{ps}(X_m - X_s) - K_{vs}\dot{X}_s$
(b)	$F_{am} = K_{pm}(X_m - X_s) + K_{vm}\dot{X}_m$	
(c)	$F_{am} = F_e$	
(d)	$F_{am} = K_{pm}(X_m - X_s) + K_{vm}\dot{X}_m + F_e$	

Figure 2.1: Telemanipulation Controller Architectures (Two-Port Circuit Representations): (a) position forward (PF), (b) position exchange (PE), (c) position forward/force feedback (PFFF), and (d) position exchange/force feedback (PEFF).

under the names “classical” [33], “position-position” [37, 56], and “position error” [16, 93] control.

Next we consider the position-forward/force-feedback (PFFF) controller. The slave serves to the master’s position, and the force measured between the slave and its environment is fed back to the master actuator:

$$F_{am} = F_e \quad (2.13)$$

This is accomplished by commanding the appropriate voltage to the master actuator to create the desired force between the master and the human operator in a static situation. This controller theoretically reflects slave/environment forces perfectly to the master, limited in practice by the resolution of the load cells and D/A card, the calibration of the load cells, and any static friction in the actuated joint. The

PFFF controller feels identical to the PF controller when the slave interacts with a compliant environment of impedance $Z_e = 0$ (that is, when the slave is free), but provides better telepresence than the PF controller when $Z_e \neq 0$. Variations of the PFFF controller have appeared under the names “forward flow” [33], “position-force” [56], “kinesthetic force feedback” [16,93], and “force-position” [37] control.

The final controller we consider is the position-exchange/force-feedback (PEFF) controller. In this control mode, the slave servos to the master’s position, while the actuation of the master is the sum of a servo to the slave’s position, as well as the reflected force felt between the slave and its environment:

$$F_{am} = K_{pm}(X_m - X_s) + K_{vm}\dot{X}_m + F_e \quad (2.14)$$

This controller combines the features of the PE and the PFFF controllers. The PEFF feels like the PE controller when $Z_e = 0$, but gives additional force feedback when $Z_e \neq 0$. A variation on the PEFF controller has appeared under the name “position and force feedback” [16,93] control.

2.3.2 Master and Slave FRVFs

There are a number of ways to implement FRVFs on a telemanipulation system, and it is not obvious which FRVF method is the best to use, given all the characteristics a viable system must possess. For clarity, when mathematically describing these FRVF methods, we will consider a one-degree-of-freedom (1-DOF) system, where the FRVF is located at $X_m = X_s = 0$, and positive X_m and X_s define the forbidden region.

The first method is to implement the FRVFs with impedance methods. Here the FRVF is represented by a hyperplane with a specified stiffness, and movement through the hyperplane results in an actuator force F_a that is linearly proportional to the normal distance of movement through the hyperplane. For a slave-side impedance-type FRVF:

$$F_{am} = 0 \quad (2.15)$$

$$F_{as} = \begin{cases} -K_{sVF}X_s & : X_s \geq 0 \\ 0 & : X_s < 0 \end{cases} \quad (2.16)$$

where K_{sVF} is the positive slave FRVF stiffness. For a master-side impedance-type FRVF:

$$F_{am} = \begin{cases} K_{mVF}X_m & : X_m \geq 0 \\ 0 & : X_m < 0 \end{cases} \quad (2.17)$$

$$F_{as} = 0 \quad (2.18)$$

where K_{mVF} is the positive master FRVF stiffness. The actuator forces of (2.15)-(2.18) are in addition to any other actuator forces due to the underlying telemanipulation control system.

A second method to implement a FRVF is to disallow the slave to follow any movements of the master that are normal to the FRVF hyperplane when the master is in the forbidden region. This is accomplished through the use of a proxy [113] – a kinematic object that exists only in software but is used in the control system. The slave servos to the proxy, rather than the master, and the proxy typically coincides

with the master, but will not follow the master into the forbidden region:

$$F_{as} = K_{ps}(X_p - X_s) - K_{vs}\dot{X}_s \quad (2.19)$$

$$X_p = \begin{cases} X_m & : X_m < 0 \\ 0 & : X_m \geq 0 \end{cases} \quad (2.20)$$

The master actuator force is simply defined by the underlying telemanipulation control architecture.

A third method to implement a FRVF is to scale down the movements of the master normal to the virtual fixture by a scaling gain γ , where $0 \leq \gamma \leq 1$. This is also accomplished with a proxy, but the now the proxy's kinematic properties are a function of the master position and the FRVF position whenever the master enters into the forbidden region:

$$F_{as} = K_{ps}(X_p - X_s) - K_{vs}\dot{X}_s \quad (2.21)$$

$$X_p = \begin{cases} X_m & : X_m < 0 \\ \gamma X_m & : X_m \geq 0 \end{cases} \quad (2.22)$$

The second virtual-fixturing method discussed is a special case of this third method, where the normal components are scaled down to zero ($\gamma = 0$). The first two FRVF methods are illustrated in Figure 2.2(a) and Figure 2.2(b), respectively.

To motivation the potential need for both master-side and slave-side FRVFs, we consider the equilibrium position of the telemanipulator due to constant disturbance loads on either the slave or master device, when implementing impedance-type FRVFs. We consider a PE telemanipulator, with impedance-type FRVFs on both the master and slave sides. The equilibrium positions associated with constant hu-

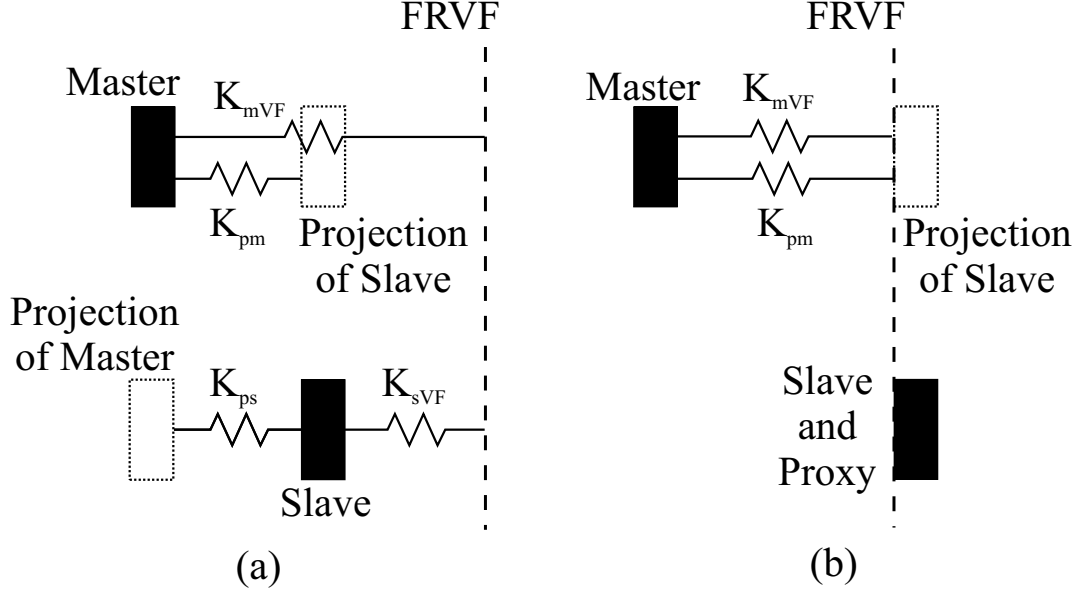


Figure 2.2: Forbidden-Region Virtual Fixtures (FRVFs): Impedance-type FRVF at master with (a) impedance-type FRVF at slave and (b) proxy-based FRVF at slave. The forbidden region is left of the virtual fixture.

man and environmental forces are found by solving the following algebraic equation:

$$\begin{bmatrix} F_h \\ F_e \end{bmatrix} = \begin{bmatrix} K_{pm} + K_{mVF} & -K_{ps} \\ K_{ps} & -K_{ps} - K_{sVF} \end{bmatrix} \begin{bmatrix} X_m \\ X_s \end{bmatrix} \quad (2.23)$$

This equation assumes $F_h > F_e$ (*i.e.*, that the forces result in the system engaging with the FRVFs). In Fig. 2.3, we observe the ability of the FRVF to reject disturbances that try to push the slave device into the forbidden region. This plot shows the effect of increasing the FRVF stiffness on the slave (K_{sVF}) or the master (K_{mVF}) independently, for a nominal system. It is clear that increasing either FRVF stiffness helps prevent the slave from entering into the forbidden region, but increasing K_{sVF} is more effective for this type of disturbance rejection. In addition, increasing K_{mVF} tends to create a larger position error between the master and slave devices than would increasing K_{sVF} , which harms the user's sense of telepresence.

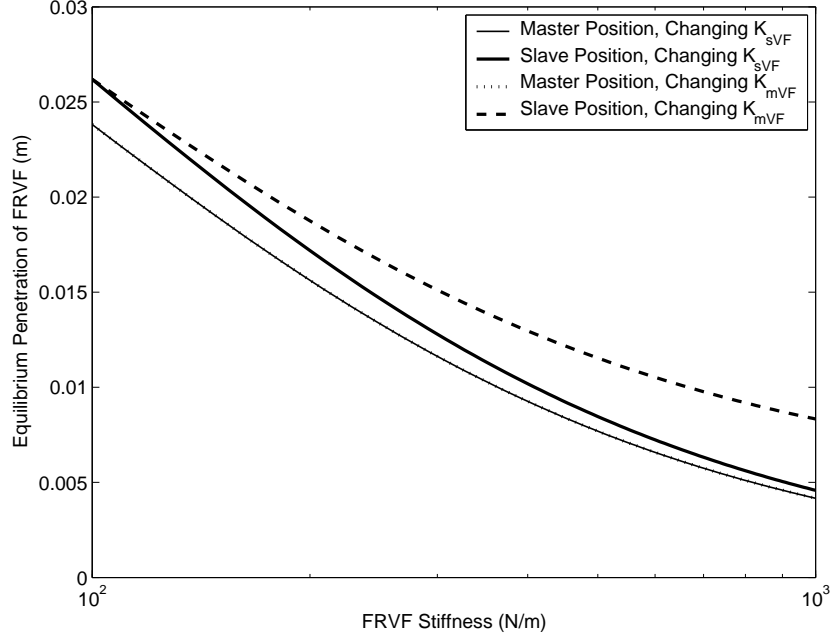


Figure 2.3: Equilibrium position vs. FRVF stiffness for an unmeasured environmental disturbance force pushing slave into forbidden region, with $F_e = -5\text{ N}$, $F_h = 0\text{ N}$, $K_{pm} = K_{ps} = 1000\text{ N/m}$, and FRVF stiffnesses originally set at $K_{mVF} = K_{sVF} = 100\text{ N/m}$. Note that the master positions coincide.

On the other hand, Fig. 2.4 shows that when the disturbance force occurs on the master side (*i.e.*, when the user attempts to move the device into the forbidden region), both types of FRVF prevent the slave from entering the forbidden region, but increasing K_{mVF} is actually better for maintaining a good sense of telepresence. Clearly, both types of FRVF have benefits and drawbacks, and both should be explored for possible use.

In this study, four levels of FRVF will be considered: soft, hard, infinite, and none (the control case). A *soft* FRVF is implemented as an impedance-type FRVF with $K_{iVF} = 1400\text{ N/m}$ ($i = m, s$). The soft FRVF gives a compliant feel as the virtual fixture is penetrated. The *hard* FRVF is also an impedance-type FRVF, with $K_{iVF} = 7200\text{ N/m}$. Qualitatively, the hard FRVF appears to the user to have

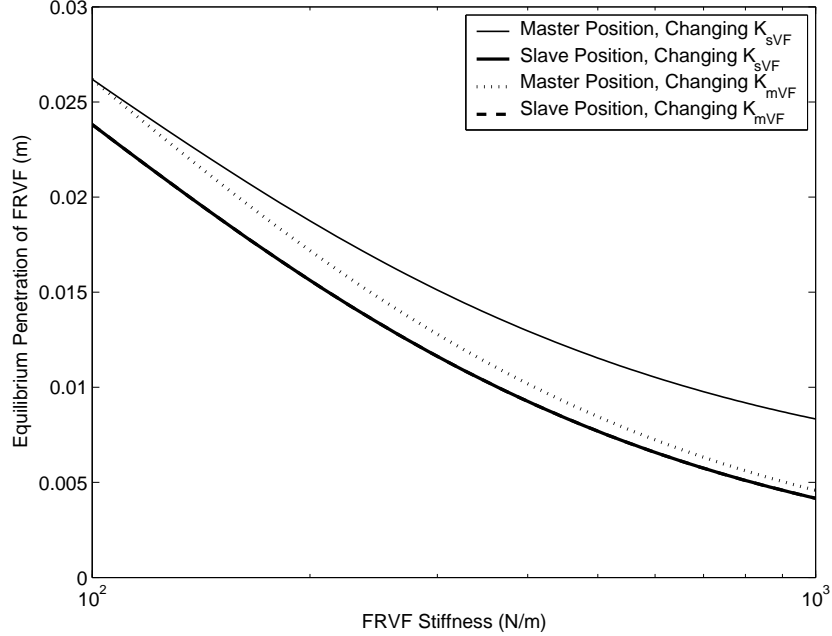


Figure 2.4: Equilibrium position vs. FRVF stiffness for user attempting to move device into forbidden region, with $F_h = 5 \text{ N}$, $F_e = 0 \text{ N}$, $K_{pm} = K_{ps} = 1000 \text{ N/m}$, and FRVF stiffnesses originally set at $K_{mVF} = K_{sVF} = 100 \text{ N/m}$. Note that the slave positions coincide.

almost no compliance. For the *infinite* FRVF, a proxy-based method is used, where the master motion through and normal to the FRVF hyperplane is scaled by $\gamma = 0$ before being commanded to the slave, disallowing any commanded movement of the slave through the FRVF. The control case of no FRVF and the soft FRVF are implemented on both the master and slave. The infinite FRVF is only implemented on the slave, by definition. The hard FRVF is only implemented on the master, because initial trials showed that the hard FRVF implemented on the slave could lead to unstable vibrations of the slave (this topic is explored in detail in Section 2.4). Three types of FRVF on the slave and three types on the master give a total of nine FRVF combinations used in this study.

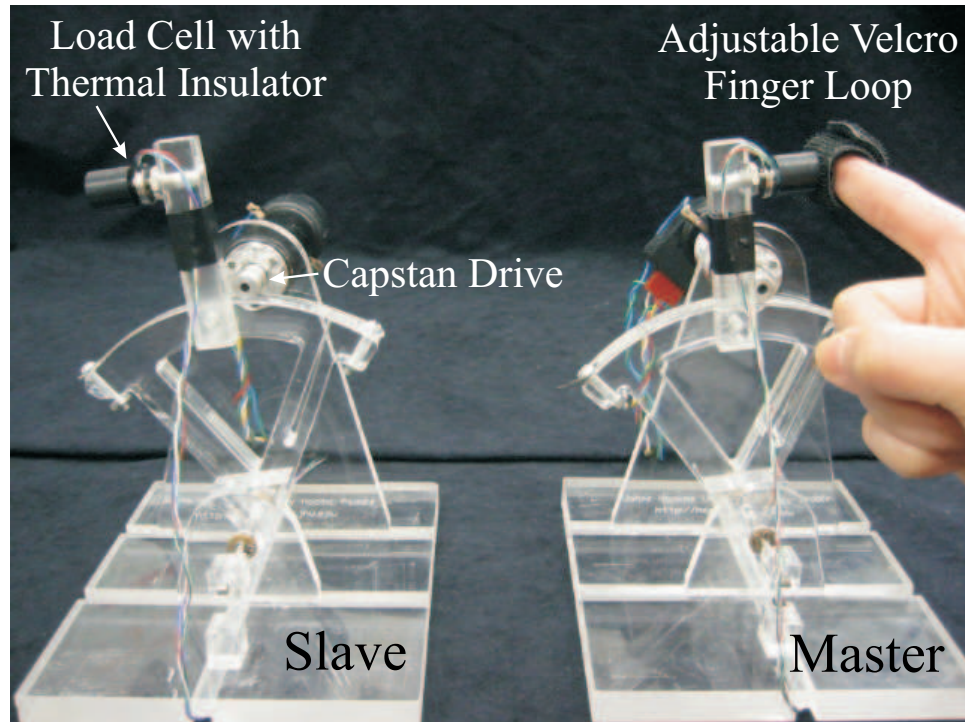


Figure 2.5: Experimental 1-DOF impedance-type bilateral telemanipulation system based on modified Haptic Paddles.

2.3.3 Experiment

Experimental Setup

The experimental setup used in this research is a 1-DOF bilateral telemanipulator consisting of two modified Haptic Paddles [74] (Fig. 2.5). The modified Haptic Paddles are impedance-type devices, with high backdrivability, low mass, and low friction. Details on the system are given in Appendix A.

A compliant environment is used in the experiment. The compliant environment is built from a soft sponge bound with a thick rubber band on its surface. This gives an environmental stiffness of approximately $K_e = 400$ N/m.

Metrics

In this section, we qualitatively define three metrics with which we can determine the effectiveness of FRVFs. These metrics are also defined quantitatively for use in the statistical study that follows. The three metrics we define are tracking, safety, and submittance.

To make the user feel that his or her movements are being directly recreated at the slave device, we would like the absolute value of the position error between the master and slave to be as small as possible, leading to good tracking. *Tracking* is quantified here by the largest-magnitude position error measured between the master and slave devices, $\|X_m(t) - X_s(t)\|_\infty$.

The purpose of the FRVF is to prevent the slave device from entering a forbidden region. From a safety perspective, it is inconsequential if the master device enters into a projection of the same forbidden region in its workspace. For this reason, *safety* is quantified here by the maximum penetration of the FRVF hyperplane by the slave device ($\|\max(X_s(t) - X_{VF}, 0)\|_\infty$, assuming that $X_s(t) - X_{VF} > 0$ corresponds to FRVF penetration). No negative penetrations are considered here, so two systems that never penetrate the FRVF on the slave side are both considered to have perfect safety, regardless of which system came closest to the forbidden region.

We define the final metric, *submittance*, to quantify the ability of the user to move the slave to any desired position outside of the forbidden region. When implementing FRVFs on a telemanipulation system, certain combinations of master and slave

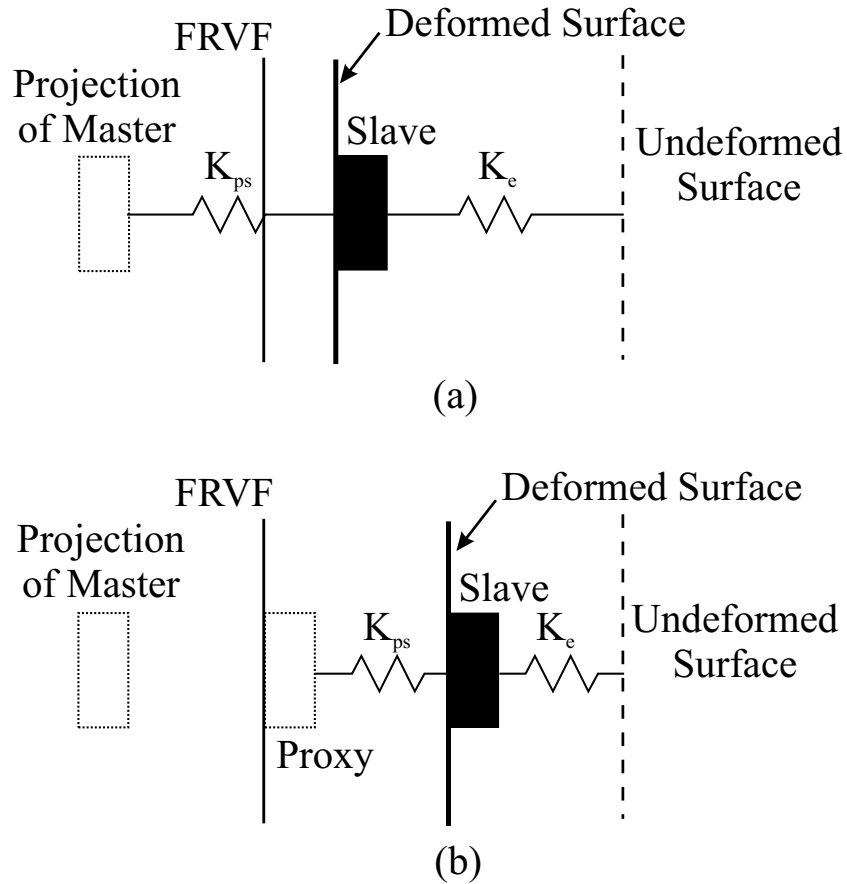


Figure 2.6: Visualization of Submittance: (a) Impedance-type FRVF at slave (high level of submittance) and (b) Infinite FRVF at slave (low level of submittance). The forbidden region is left of the virtual fixture.

FRVFs, designed to prevent movement into a forbidden region, can actually prevent the slave from ever reaching the forbidden region. This phenomenon is only seen when there is a disturbance load on the slave. There may be some circumstances where reaching the FRVF is necessary, such as when a FRVF is used to limit as well as act as a guide for depth of cutting, and a system with good submittance will allow this. Figure 2.6 illustrates how a system can have poor submittance. In Fig. 2.6(a), the slave serves to the master. The slave is also interacting with a compliant environment with stiffness K_e , and this environmental force tends to increase the

error between the master and the slave as the slave moves into the compliant environment. If the master and slave FRVFs are both of the impedance type, and the master FRVF is not too stiff, it is possible to command the slave up to the depth of the FRVF by moving the master past the FRVF. In Fig. 2.6(b), an infinite (proxy-based) FRVF is implemented on the slave side as previously described. Regardless of the type of FRVF on the master, the slave can never reach the forbidden region. To quantify this phenomenon, in our experiment *submittance* is quantified by the minimum distance between the slave and its FRVF when the slave fails to reach its FRVF ($X_{VF} - \min(X_{VF}, \sup_{t \geq 0} X_s(t))$, assuming that $X_s(t) - X_{VF} > 0$ corresponds to FRVF penetration). Any system where the slave is able to reach its FRVF is said to have perfect submittance.

An alternative definition of submittance would be as a measure of the user’s ability to command the slave to move anywhere in the workspace, including inside the forbidden region. There may be cases when it is desirable for the FRVF to act as a warning and guide to prevent the human user from unintentionally moving the slave into a forbidden region, while leaving the ultimate control with the user. We will not pursue this definition of submittance here.

ANOVA Experiment

An experiment was conducted to quantitatively compare the performance of systems with varying control architectures and FRVF methodologies, using the three metrics described above. The experiment was designed to simulate a scenario where the user knows the location of forbidden regions, and test how well FRVFs help the

user perform tasks safely. A mixed-effects analysis of variance (ANOVA) experiment was conducted [51]. Four control architectures, nine FRVF combinations, and two tasks (described below) give a total of 72 levels of the fixed-effect factor, representing all possible combinations. Six subjects were used in the experiment, giving six levels to the random-effect factor.

The user is asked to perform two different tasks. The first task, *Touch*, simulates the user attempting to work near a forbidden region without entering it. In this task, the subject was asked to move the slave forward and touch the surface of the compliant environment with the slave device, but to not depress the environment at all. The subject was instructed to stop and retract the slave when it was determined that the surface had been touched, using all visual and haptic information available.

The second task, *Depress*, simulates a FRVF to limit depth of cutting, needle insertion, etc. In this task, the subject was asked to move the slave forward and depress the surface of the compliant environment to a depth of 4 mm , where the FRVF was placed. This distance is equivalent to half of the threaded portion of the load cell on the slave (the Delrin cap was not present on the slave during this experiment). The subject was also shown an example of the slave depressing the surface to the correct depth. The subject was instructed to stop and retract the slave when it was determined that the slave had depressed the surface to the correct depth, using all visual and haptic information available.

In both the *Touch* and the *Depress* tasks, the subjects were told that if the slave device did not reach the desired position the trial would be repeated. The trial was

actually only repeated if the master device failed to reach the position of the FRVF. This was done because some FRVF combinations forbid the slave from reaching the correct depth. In these cases, haptic cues to the user prematurely indicate that the correct depth has been reached.

Each subject was asked to perform each of the 72 control/FRVF/task combinations three times, giving a total of 216 data runs assigned randomly to each subject, with 1296 data sets in total for the experiment. The average time to complete all the trials was approximately 40 minutes per subject. Subjects were allowed rest at any time. From each of the data sets, the tracking and safety metrics were calculated; the submittance metric was only calculated for the *Depress* task, because it only becomes an issue when the slave is loaded.

For reduced complexity, only one set of position, velocity-feedback, and force gains is used for each control architecture, but steps were taken to make these systems somewhat equivalent. First, the same local velocity-feedback was used on the master and slave for every controller ($K_v = 2.9 \text{ Ns/m}$). Second, whenever position information is used, a position gain of $K_p = 720 \text{ N/m}$ is used. The choice of identical position gains makes the PE and PEFF controllers feel more sluggish than the PF and PFFF controllers, but it creates systems that have identical steady-state position errors due to loads on the slave. The position and velocity gains chosen were tuned to give good position tracking, while still generating a stable system with a smooth feel. Finally, whenever force-feedback is used, it is unity force-feedback. This means that the proper voltage is given to the master motor to

make the force seen at the master load cell equal that seen at the slave load cell (in a static situation). The controller runs at 1000 Hz.

2.3.4 Results and Discussion

Figure 2.7 shows a sample of the original data recorded in the experiment and used in the statistical analysis. The figure shows multiple trials of a single subject performing the *Touch* task with the PE controller, with two FRVF schemes. From each of the trials shown, two quantities were recorded for the statistical analysis, corresponding to the tracking and safety metrics. The data shown is typical. From 1296 trials such as these, we conducted the ANOVA.

Figure 2.8 shows the results of Tukey’s Method of Pairwise Comparisons [51] – a test to determine if two data sets are significantly different from one another – for each of the four control architectures. Although forbidding any negative distances for the safety and submittance metrics slightly harms the normal distribution of the data, ANOVA is robust to this [51]. For each controller, the results are shown for the tracking and safety metrics for both the *Touch* and *Depress* tasks, and the submittance metric for the *Depress* task. The vertical bars indicate FRVF pairs that statistically are not significantly different from one another, with $p = 0.05$. Any FRVF pair that belongs to multiple groupings indicates a questionable result. For these cases, a more sensitive test is needed to sufficiently differentiate the groupings.

The results for tracking were the same across all four controllers. They indicate that an infinite slave FRVF with no master FRVF gives undesirable tracking, and

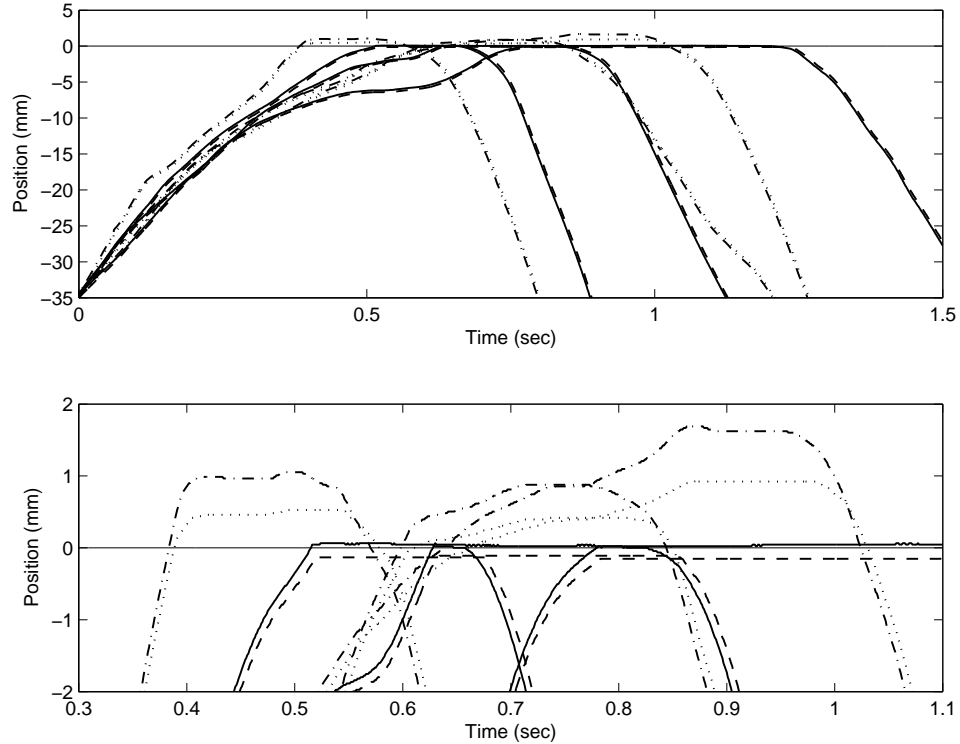


Figure 2.7: Experimental data from a single subject with the PE controller for three trials of the *Touch* task with no FRVFs (master (-·-), slave (···)), and for three trials of the *Touch* task with a hard master FRVF and an infinite slave FRVF (master (—) and slave (- -)). The FRVF and the surface of the environment are located at 0 mm. (Top) The subject moves the system forward and touches the surface/FRVF as instructed, and then withdraws. (Bottom) Close-up near FRVF/environment surface, showing clear differences between methods.

all other FRVF pairs give equally good tracking. This is most clearly seen in the PF and PFFF controllers, indicating that position feedback to the master can improve tracking with an infinite slave FRVF and no master FRVF. This makes sense; in the limit as the position gain of the master becomes very large, the master's position is unable to deviate from the slave's, regardless of the FRVF used at the slave.

The results for safety are the same for the PF, PE, and PFFF controllers. They indicate that for improved safety, a FRVF should be used at the master side if

<i>Touch Tracking</i>	<i>Depress Tracking</i>	<i>Touch Safety</i>	<i>Depress Safety</i>	<i>Depress Submittance</i>
FRVF	FRVF	FRVF	FRVF	FRVF
Master/Slave	Master/Slave	Master/Slave	Master/Slave	Master/Slave
H/0	H/0	S/I	S/I	0/S
S/S	H/S	H/S	H/S	0/0
S/I	H/I	H/I	H/I	S/S
0/0	S/0	0/I	H/0	S/0
H/S	S/S	H/0	0/I	H/0
H/I	S/I	S/S	S/S	H/S
S/0	0/0	S/0	S/0	H/I
0/S	0/S	0/S	0/S	0/I
0/I	0/I	0/0	0/0	S/I

(a) Position-Forward Control Architecture

<i>Touch Tracking</i>	<i>Depress Tracking</i>	<i>Touch Safety</i>	<i>Depress Safety</i>	<i>Depress Submittance</i>
FRVF	FRVF	FRVF	FRVF	FRVF
Master/Slave	Master/Slave	Master/Slave	Master/Slave	Master/Slave
H/I	H/0	S/I	S/I	0/0
H/0	H/S	H/S	H/S	0/S
0/0	H/I	H/I	H/I	S/S
0/I	S/S	H/0	H/0	S/0
S/0	S/0	0/I	0/I	H/S
0/S	S/I	S/S	S/S	H/0
S/I	0/0	S/0	S/0	0/I
S/S	0/S	0/S	0/S	S/I
H/S	0/I	0/0	0/0	H/I

(b) Position-Exchange Control Architecture

<i>Touch Tracking</i>	<i>Depress Tracking</i>	<i>Touch Safety</i>	<i>Depress Safety</i>	<i>Depress Submittance</i>
FRVF	FRVF	FRVF	FRVF	FRVF
Master/Slave	Master/Slave	Master/Slave	Master/Slave	Master/Slave
S/S	H/0	S/I	S/I	0/0
S/0	H/S	H/S	H/S	0/S
S/I	S/S	H/I	H/I	S/0
H/0	H/I	H/0	H/0	S/S
H/S	S/0	0/I	0/I	H/S
0/0	S/I	S/S	S/S	H/0
0/S	0/0	S/0	S/0	S/I
H/I	0/S	0/S	0/S	H/I
0/I	0/I	0/0	0/0	0/I

(c) Position-Forward/Force-Feedback Control Architecture

<i>Touch Tracking</i>	<i>Depress Tracking</i>	<i>Touch Safety</i>	<i>Depress Safety</i>	<i>Depress Submittance</i>
FRVF	FRVF	FRVF	FRVF	FRVF
Master/Slave	Master/Slave	Master/Slave	Master/Slave	Master/Slave
S/0	H/I	0/I	S/I	0/0
H/0	S/0	H/0	S/S	0/S
S/S	H/S	S/I	H/I	S/0
0/0	H/0	H/S	H/S	S/S
0/I	S/I	H/I	S/0	H/0
H/I	S/S	S/S	0/I	H/S
S/I	0/0	S/0	H/0	0/I
0/S	0/S	0/S	0/S	S/I
H/S	0/I	0/0	0/0	H/I

(d) Position-Exchange/Force-Feedback Control Architecture

Figure 2.8: Statistical Results using Tukey's Method of Pairwise Comparisons. FRVF pairs are listed in descending order (best performance in each category is at the top of the list) for the nine combinations of hard (H), soft (S), infinite (I), and no (0) master and slave FRVF. Vertical bars indicate FRVF pairs that are not significantly different from one another ($p = 0.05$).

an impedance-type FRVF is being implemented at the slave. Otherwise, all other FRVF schemes are equally safe. This is because a master with no FRVF can easily pull the slave through an impedance-type FRVF some finite distance before the FRVF generates enough actuator force to stop the slave. The results for the PEFF controller indicate that all FRVFs are equally safe. This is probably due to the large amount of haptic cues given to the user.

The results for safety are somewhat counter-intuitive. The statistics show that a system with an infinite slave FRVF is not significantly safer than many other systems, even though the only way to guarantee that the slave never crosses into a forbidden region is with an infinite slave FRVF. The results for a hard master FRVF are questionable for similar reasons. The reason for this result is that the *Touch* and *Depress* tasks did not capture every scenario the telemanipulator may experience. Recall that the experiment was designed to simulate a situation where the user knows where the forbidden regions are. In the *Touch* experiment, the user was instructed to touch the surface of the compliant environment, but to not depress the surface at all. Because of this instruction, the user used visual cues to help the slave approach the environment slowly, so almost any FRVF scheme worked to create a safe system. This experiment did not test scenarios where either the user did not have good visual cues or did not realize the slave was nearing a forbidden region. In these two scenarios, the user could move quickly into a FRVF, and an infinite slave FRVF and/or a hard master FRVF would probably give safer results than other FRVF schemes.

To determine if the infinite slave FRVF and/or the hard master FRVF are significantly safer than other FRVF schemes, additional experiments must be conducted. Two possibilities would be to modify the *Touch* experiment by obstructing the user's visual cues from the slave, or to instruct the user to do the *Depress* experiment, but put the FRVF at the surface of the environment. These tests may reveal that the infinite and/or hard slave FRVF are safer overall, but they could possibly also change the tracking and submittance results for these FRVFs. In fact, intuitively, these two FRVF schemes should give the worst submittance of any of the FRVF architectures.

A quick glance at the submittance results indicate that safety and submittance are inversely related to one another. This is intuitive, since submittance is a measure of user control, while safety is a measure of the lack of user control. The submittance results are the same for all controllers. A FRVF architecture with no master FRVF and an impedance-type slave FRVF gives the most submittance. A FRVF architecture with a soft master FRVF and an impedance-type slave FRVF gives the next-highest level of submittance. Finally, any FRVF scheme with either a hard master FRVF or infinite slave FRVF leads to equally poor submittance. In addition, there is also a distinction between the two schemes with the highest submittance for the PFFF controller. Here, no FRVFs appear to give better submittance than a FRVF scheme with no master FRVF and a soft slave FRVF.

Because the safety and submittance metrics are inversely related, no single FRVF method is obviously the best overall for use with a given control architecture. The final choice of FRVF method should be made with a specific application in mind,

as a balance of tracking, safety, and submittance.

2.3.5 Conclusions for Human Factors Experiment

Thirty-six different systems (consisting of nine FRVF methods and four control architectures) were implemented on a 1-DOF telemanipulation system. A six-subject ANOVA experiment was conducted to quantify the performance of the systems during two tasks that simulate a user working near a known forbidden region, with the intent of finding the best FRVF architecture for a given controller.

The experimental results show that performance is generally the same across all control architectures. They indicate that for good tracking, a telemanipulator should not use a FRVF architecture that has an infinite FRVF at the slave with no FRVF at the master. For safe operation, any telemanipulator that has an impedance-type FRVF at the slave should also have a FRVF at the master. For the best submittance, a system should be configured with an impedance-type FRVF at the slave, and no FRVF (or possibly a soft FRVF) at the master. Rather than making a conclusion on the best FRVF architecture overall, the desired application of the telemanipulator should be taken into account when choosing how to balance the system's tracking, safety, and submittance. The proper choice of FRVF architecture is likely to be highly task-dependent.

2.4 Stability of Forbidden-Region Virtual Fixtures

In this section, we consider the stability of a particular type of FRVF – an impedance surface, or “virtual wall.” This type of virtual fixture was discussed in Section 2.3.2. This is a method commonly used in haptic interfaces for virtual environments, where the position (velocity, acceleration) of the device in relation to the impedance surface is used to generate an actuator force on the device.

The maximum stiffness of a virtual surface that can be implemented is limited by the sampling rate of the computer, the resolutions of the position sensor and actuator, and the impedance of the mechanical device [18]. Many researchers have investigated stability of virtual walls for haptic display (as discussed in Section 1.3.3), but analyzing impedance-type FRVFs on a telemanipulator has added complexity because the system has more degrees of freedom (because there are two manipulators). They are also more difficult to stabilize because the slave manipulator does not have the additional damping provided by the human operator. Also, it may be desirable to implement virtual fixtures on both the master and slave devices simultaneously. In the experiment of Section 2.3, we found that implementing an impedance-type FRVF on the slave of a telemanipulator can lead to unwanted vibrations as the slave manipulator is pulled into the forbidden region by the master. These vibrations are not predicted by simple LTI models, and are most likely the manifestation of an unstable system, with nonlinearities that cause a limit cycle. Regardless of the reason, any sustained vibration is unwanted.

This section considers a general system where the master and slave devices can

each have FRVFs of different stiffness but at the same position (in their respective workspaces). We consider the underlying telemanipulation control architecture to have any combination of proportional-derivative (PD), velocity-feedback, and force-feedforward control. We assume that we begin with an existing telemanipulation system that is designed to be well behaved for the desired MIS task, and that we would like to overlay stable FRVFs on this system. We ask the question: “If a user attempts to apply a constant force to the master manipulandum of a bilateral telemanipulator, where the master and/or slave manipulator is interacting with a FRVF, will the system reach a static equilibrium or will it vibrate, and can this system behavior be predicted without simulating or physically implementing the system?” The results of this research indicate that these unwanted vibrations can be predicted given an accurate model of the master and slave devices and relatively simple bounds on human operator parameters.

As noted in Section 1.3.4, there has been recent interest in forbidden-region virtual fixtures for telemanipulation assistance, but to the best of the author’s knowledge, this work represents the first control-theoretic analysis of the stability of these FRVFs. To accomplish the stability analysis, we make use of a set of observations and assumptions that are different from previous work in this field of research in several ways. First, preliminary experiments show that, when implementing a telemanipulation controller on a digital computer, the sampling rate of the system is very important in determining system stability (which should come as no surprise), but it is also significantly more important than other system nonlinearities (such as

quantization from measuring position with optical encoders). While many previous works consider pure time delays in the system, or frequency-domain approximations of the zero-order hold (ZOH), in this section we explicitly consider the sampling rate of the sampled-data system to accurately account for this important system parameter. Second, a human operator is often modeled as time-varying, which is true in general, but possibly unnecessary. Experience tells us that when a malicious user attempts to drive a haptic system unstable, the user will adapt his or her hand properties until the perfect set of properties are found to make the system go unstable, but then the adaptation stops, and the constant malicious user allows the limit cycle to continue. In this section we consider a worst-case time-invariant human, which simplifies the analysis. Finally, many previous works model the human as passive, which, along with telemanipulator passivity, is a sufficient condition for system stability. In practice, when a human is attempting to act passively, he or she will actually behave dissipatively. In this section, we account for the dissipation in the human user, resulting in a stability analysis that is potentially less conservative than one based on passivity methods.

Figure 2.9 shows the general telemanipulator system we consider in this section; it is often referred to as a three-channel architecture. It is similar to that in [56], but we explicitly consider the discrete nature of the controller; continuous systems are written in s -domain, and discrete systems are written in z -domain. Each discrete block is preceded by a sampler and succeeded by a ZOH. The ZOHs result in actuator forces that are continuous-time staircase signals.

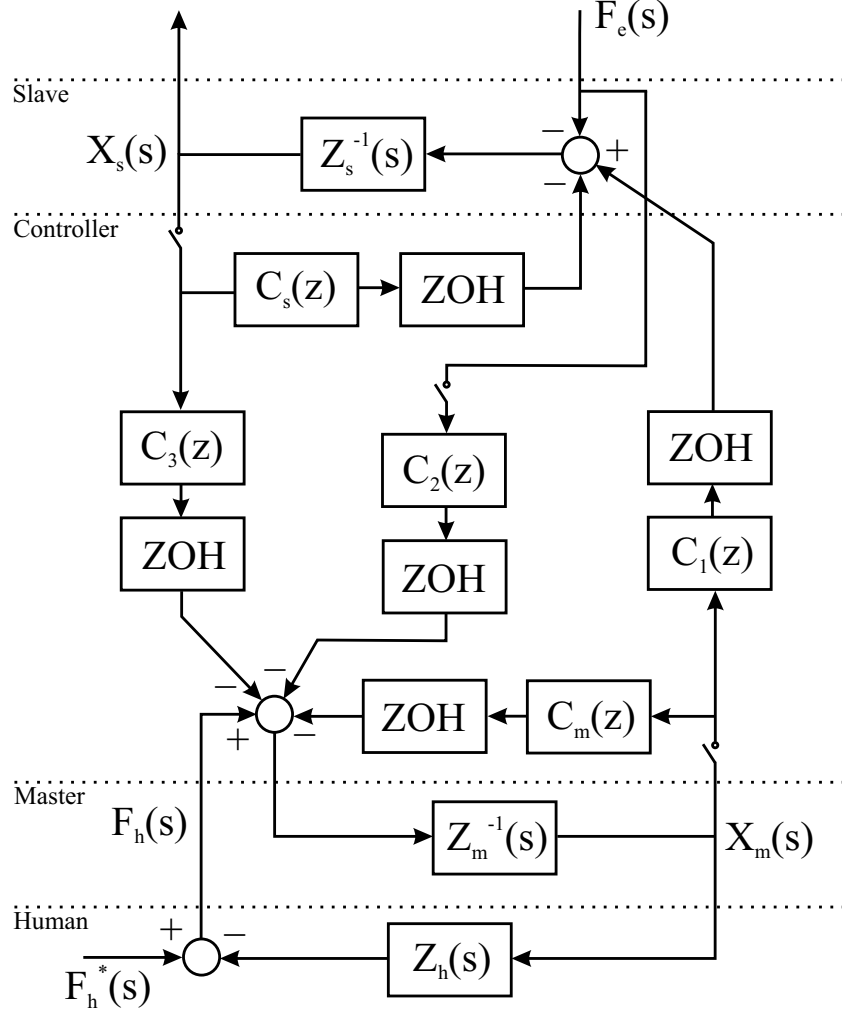


Figure 2.9: General three-channel telemanipulator implemented with a digital computer.

We implement a FRVF, at sample k , as a simple spring with a unilateral constraint:

$$F_{iVF}(k) = \begin{cases} K_{iVF}X_i(k) & : X_i(k) > 0 \\ 0 & : X_i(k) \leq 0 \end{cases} \quad (2.24)$$

where K_{iVF} is the stiffness of the FRVF, and $i = \{m, s\}$ for master and slave, respectively. The FRVF force is held constant over the sample by a ZOH. We assume, without loss of generality, that the FRVF is located at $X_m = X_s = 0$, since the underlying telemanipulator behavior will be independent of the zero position.

We consider the general class of telemanipulation control architectures that can be described by the equations (in time domain):

$$F_{am} = K_{pm}(X_m - X_s) + K_{dm}(\dot{X}_m - \dot{X}_s) + K_{vm}\dot{X}_m + K_{fm}F_e + F_{mVF} \quad (2.25)$$

$$F_{as} = K_{ps}(X_m - X_s) + K_{ds}(\dot{X}_m - \dot{X}_s) - K_{vs}\dot{X}_s - F_{sVF} \quad (2.26)$$

where K_{pm} and K_{ps} are the position gains of the master and slave, K_{dm} and K_{ds} are the derivative gains of the master and slave, K_{vm} and K_{vs} are additional velocity feedback gains of the master and slave, and K_{fm} is the force feedforward gain. This general class includes many common telemanipulation control architectures (including all of those introduced in Section 2.3.1). We will only explicitly discuss this class of controllers, but the methods presented in this section could be applied to other control architectures as well.

The unilateral constraints of the FRVFs make even the continuous-time idealization of the control blocks C_m and C_s nonlinear – this motivates the equilibrium stability analysis of the next section. This is followed by a discrete-time implementation of the idealized continuous-time controller.

2.4.1 Equilibrium Stability Analysis

When a slave device interacts with a stable impedance-type FRVF, the slave continues to move forward if the master moves forward, establishing an equilibrium point that balances the effects of the telemanipulation control system, the FRVF, and any external loads. Experiments show that when the slave device vibrates due to an unstable FRVF (that is, one that generates a limit cycle), the center of the

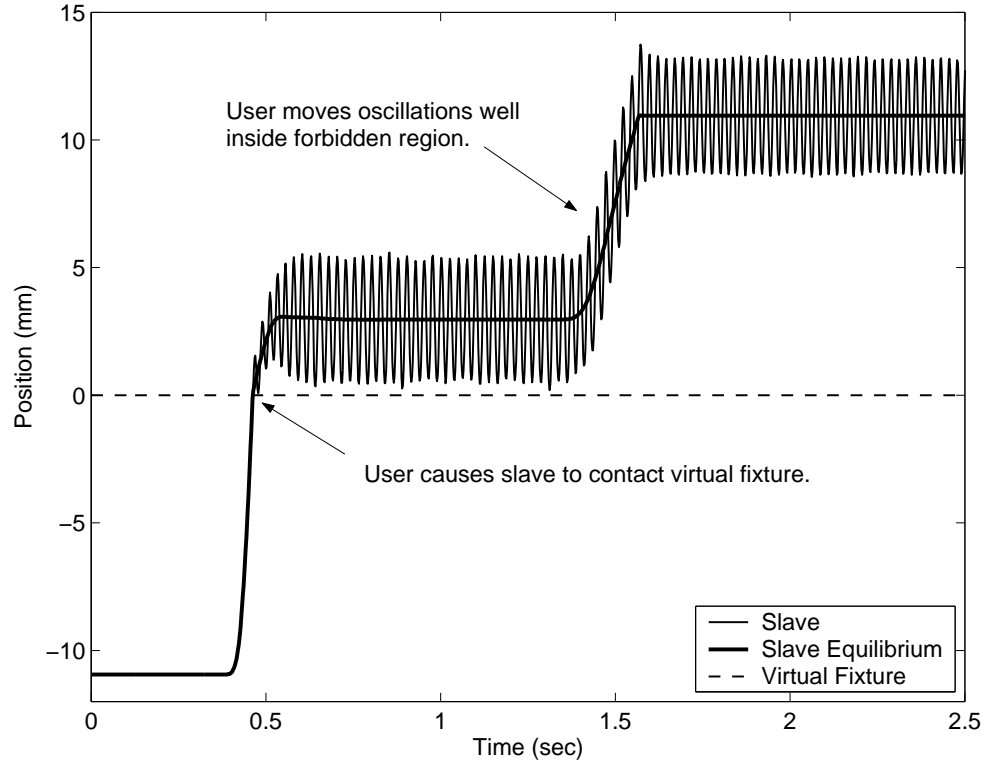


Figure 2.10: Experimental data showing slave manipulator interacting with an unstable FRVF. The equilibrium position, based on the master position and the system gains, is also shown. Vibrations do not occur on the surface of the FRVF, but rather, around an unstable equilibrium. The system shown is implementing PF control, with $K_{ps} = 600$ N/m, $K_{vs} = 2$ Ns/m, $K_{sVF} = 3000$ N/m, and $T = 0.002$ seconds.

vibration moves forward if the master moves forward, as seen in Fig. 2.10. Note that it is also possible to generate vibrations that exist entirely within the forbidden region. This is evidence that the vibrations occur not on the surface of the FRVF, but rather, around an unstable equilibrium below the surface of the FRVF (as was observed in [87]). This phenomenon is also present when a master device vibrates against an unstable FRVF, though it is not as easy to observe. Slave-side FRVFs tend to become unstable at much lower stiffness values than those on the master side (due to human damping on the master side), but Section 2.3 motivated the

possible need for both master- and slave-side FRVFs in MIS tasks.

The unilateral constraint of the FRVF represents a significant nonlinearity in the system, and techniques such as hybrid system theory could be used to analyze the unilateral constraint of the FRVF. However, behavior such as that in Fig. 2.10 leads us to believe that other tools could be used to effectively predict instability. It appears that instability results from a divergence from an unstable equilibrium (notice the beginnings of the instability in Fig. 2.10). We hypothesize that analysis of the equilibrium associated with a constant F_h^* will provide accurate results using relatively simple techniques. Also, we would not like to consider a limit cycle as a stable mode for our system when interacting with a FRVF, so equilibrium-point stability is a natural choice for a characterization of FRVF stability that corresponds to our intuition of well-behaved systems.

Preliminary experiments show that the condition when instabilities are most likely to occur is when the slave is in free space (*i.e.*, $F_e = 0$). Any contact of the slave with an environment only seems to destroy potential limit cycles. This even includes the case when the slave vibrates against a rigid environment. From an energy standpoint, each of these collisions is likely to provide a net dissipation. One can imagine a pathological case where a malicious exogenous F_e is perfectly constructed to create a limit cycle, but we assume here that the telemanipulator will only be interacting with passive environments. In addition, we are interested in applying FRVFs that are significantly stiffer than the relatively soft environments in MIS tasks. For these reasons, we will explicitly study the stability of the system

when $F_e = 0$.

Equilibrium Dual System

We consider the case where the human operator is trying to apply a constant positive force \bar{F}_h to the master manipulandum – this is accomplished with a constant F_h^* . The actual force felt between the human and master will be a function of the feedback system, and will deviate from the desired force by \hat{F}_h :

$$F_h(t) = \bar{F}_h + \hat{F}_h(t) \quad (2.27)$$

Let \bar{X}_m and \bar{X}_s be the equilibrium positions of the system. They will be defined by the relationships

$$X_m(t) = \bar{X}_m + \hat{X}_m(t) \quad (2.28)$$

$$X_s(t) = \bar{X}_s + \hat{X}_s(t) \quad (2.29)$$

and will be functions of \bar{F}_h and the control system gains. It is easy to verify that a unique equilibrium point exists, given any human impedance and F_h^* . At the equilibrium position, the master and slave devices are in static force equilibrium governed by the equations

$$\bar{F}_h + K_{pm}(\bar{X}_s - \bar{X}_m) = K_{mVF}\bar{X}_m \quad (2.30)$$

$$K_{ps}(\bar{X}_m - \bar{X}_s) = K_{sVF}\bar{X}_s \quad (2.31)$$

We would like to analyze the stability of the system around the equilibrium point associated with a given \bar{F}_h . By substituting the equations developed in this section

into the original system equations of Section 2.2, and making use of the fact that Z_m and Z_s are mass-damper systems with no spring terms (which results in $F_h = F_{am}$ and $F_{as} = 0$ at equilibrium), the system can be rewritten as

$$Z_h(s)\hat{X}_m(s) = -\hat{F}_h(s) \quad (2.32)$$

$$Z_m(s)\hat{X}_m(s) = \hat{F}_h(s) - \hat{F}_{am}(s) \quad (2.33)$$

$$Z_s(s)\hat{X}_s(s) = \hat{F}_{as}(s) \quad (2.34)$$

where

$$\begin{aligned} \hat{F}_{am}(s) = & (K_{pm} + K_{mVF})\hat{X}_m(s) - K_{pm}\hat{X}_s(s) \\ & + K_{dm}s(\hat{X}_m(s) - \hat{X}_s(s)) + K_{vm}s\hat{X}_m(s) \end{aligned} \quad (2.35)$$

$$\begin{aligned} \hat{F}_{as}(s) = & K_{ps}\hat{X}_m(s) - (K_{ps} + K_{sVF})\hat{X}_s(s) \\ & - K_{ds}s(\hat{X}_m(s) - \hat{X}_s(s)) + K_{vs}s\hat{X}_s(s) \end{aligned} \quad (2.36)$$

(2.32)-(2.36) represent a dual system to the one introduced in Section 2.2. The dual system is written in terms of positions and forces around the equilibrium, and the master and slave FRVFs are lumped with local master and slave controllers.

By considering the system in this way, there is a neighborhood around the equilibrium where the unilateral constraint of the FRVF is nonexistent (the size of the neighborhood has a “radius” of \bar{X}_s on the slave side, and \bar{X}_m on the master side), so for small deviations away from the equilibrium, the system will appear linear. Because this dual system, which includes virtual fixtures, can be written as a linear system around an equilibrium position, the stability of this equilibrium can be analyzed using a relatively simple technique – analysis of the system eigenvalues. Note

that this dual system has no exogenous force inputs (compare (2.32) and (2.34) to (2.1) and (2.4), respectively). A constant exogenous force influences the equilibrium position, but not the behavior around that equilibrium.

To analyze the stability of the above system, in the next section we create a linear state-space model of the system of Section 2.2 that does not include any unilateral constraints, but instead allows for the FRVFs to be included as in (2.35) and (2.36).

Discrete State-Space Model

In this section, we develop a discrete state-space representation of the original system introduced in Section 2.2. The state-space model will consider the control system of (2.25) and (2.26), without explicit consideration of the virtual fixtures. In the previous section we established that analyzing the stability of this system will reveal stability information about the system that includes FRVFs.

We assume that no sensor is available to measure velocity directly, so the control system will use a backwards-difference method to compute velocity

$$\dot{X}_m(k) = \frac{X_m(k) - X_m(k-1)}{T} \quad (2.37)$$

where T is the sampling period of the computer. $\dot{X}_s(k)$ is computed in the same way.

Including this backwards-difference in the state-space model is not an approximation if it is actually the way the controller measures velocity, which is common in practice.

The individual control blocks are

$$C_1(z) = \frac{K_{ds}}{T}(1 - z^{-1}) + K_{ps1} \quad (2.38)$$

$$C_2(z) = K_{fm} \quad (2.39)$$

$$C_3(z) = -\frac{K_{dm}}{T}(1 - z^{-1}) - K_{pm3} \quad (2.40)$$

$$C_m(z) = \frac{K_{dm} + K_{vm}}{T}(1 - z^{-1}) + K_{pmm} \quad (2.41)$$

$$C_s(z) = \frac{K_{ds} + K_{vs}}{T}(1 - z^{-1}) + K_{pss} \quad (2.42)$$

Using a structure of this form will allow us to incorporate virtual fixtures into the state-space model, by setting $K_{pm3} = K_{pm}$ and $K_{pmm} = K_{pm} + K_{mVF}$, and by setting $K_{ps1} = K_{ps}$ and $K_{pss} = K_{ps} + K_{sVF}$.

In creating a discrete state-space model, we first find a discrete model for the continuous subsystems. By combining (2.1) and (2.3), we get

$$F_h^*(s) - F_{am}(s) = Z_{hm}(s)X_m(s) \quad (2.43)$$

where $Z_{hm}(s) = Z_h(s) + Z_m(s)$. F_{am} is the master actuator force being generated by the controller, that is held constant between samples with a ZOH. We assume that F_h^* varies slowly relative to the sampling frequency, and can be modeled as constant over a sampling period. This is a reasonable assumption since F_h^* represents voluntary human action, which is very slow relative to computer speeds [106]. Because the force input of this subsystem can be considered constant throughout the sampling period, the discrete transfer function from force to position can be found using

$$Z_{hm}^{-1}(z) = (1 - z^{-1})\mathcal{Z}\left[\frac{Z_{hm}^{-1}(s)}{s}\right] \quad (2.44)$$

where $\mathcal{Z}[\mathcal{Y}(s)]$ is the z -transform of the time series represented by the Laplace transform $\mathcal{Y}(s)$ [28]. This transfer function is exact at the samples. The transfer function $Z_s^{-1}(z)$ is calculated in an analogous way from (2.4). This assumes that

F_e can be modeled as constant between samples, which will be reasonable if the sampling rate of the system is fast and the environment that the system interacts with is compliant, which should be the case for MIS tasks. This assumption is discussed further in Section 2.4.3. The z -transforms of transfer functions of the form of (2.2) and (2.6) can be found precomputed in [28].

Using the modeling assumptions above, we developed an LTI discrete state-space model

$$\mathbf{x}(k+1) = \mathbf{A}\mathbf{x}(k) + \mathbf{B}\mathbf{u}(k) \quad (2.45)$$

where the state vector and input vector of the system are given by

$$\mathbf{x}(k) = \begin{bmatrix} X_m(k) \\ X_m(k-1) \\ X_m(k-2) \\ X_s(k) \\ X_s(k-1) \\ X_s(k-2) \\ F_h^*(k-1) \\ F_e(k-1) \end{bmatrix}, \quad \mathbf{u}(k) = \begin{bmatrix} F_h^*(k) \\ F_e(k) \end{bmatrix} \quad (2.46)$$

The algorithm for numerically generating this model is given as Appendix B. This discrete state-space model was designed as a discrete system from the beginning, and is not simply a discrete-time approximation of a continuous-time state-space model. The model has eight eigenvalues, but two of them are identically equal to zero in the z -plane, due to the structure of the \mathbf{A} matrix. The location of the

remaining eigenvalues reveal stability and transient properties of the system. Any eigenvalue lying outside the unit circle in the z -plane would indicate an unstable equilibrium [28]. If an equilibrium is deemed stable, characteristics of eigenvalues in the z -plane are related to those in the s -plane by

$$z = e^{sT} \tag{2.47}$$

We use the fact that for eigenvalues in the s -plane, the damping ratio is found by

$$\zeta = \sin \left(\tan^{-1} \left(\frac{-\Re\{s\}}{|\Im\{s\}|} \right) \right) \tag{2.48}$$

The term “damping ratio” is only explicitly defined for second-order systems, but we apply the term analogously here to quantify the relationship between decay and oscillation in the components of the system’s time response. By using knowledge of damping, we can require a more stringent condition than stability on our system; we can limit the magnitude and duration of decaying oscillations in the stable system. This leads to a more informative analytical result than passivity analysis (which is explored in Chapters 3 and 4).

2.4.2 Experimental Validation

In this section we validate our proposed method on a real system that contains many unmodeled effects (quantization, unmodeled friction, actuator bandwidth and saturation, and unmodeled dynamics), and show that the proposed method is a good predictor of stability in real, non-ideal systems.

Because the real system measures a quantized position signal, obtaining a velocity through a backward difference results in a noisy velocity signal. To mitigate

this effect, a digital first-order low-pass filter with a bandwidth of 200 Hz is used to smooth the velocity measurement before it is used by the control system. Neither the quantization of the encoders nor this filter is included in the state-space model, but the experimental results show that the method is robust to these small unmodeled effects.

Human Users

It is well known that the properties of the human user are important in determining the stability of bilateral telemanipulators [35]. For our method, we are interested in obtaining a worst-case LTI mass-spring-damper model of the human index finger (where the worst-case is that which is most likely to make the system unstable). Rather than obtain new data that is specific to our system and human users, we chose to use previous data acquired by Hajian and Howe [32]. Figure 2.11 shows finger impedance data for five users. The data was taken at varying nominal force levels (corresponding to \bar{F}_h in this chapter). We have modified the plot by adding simple bounding lines which are meant to represent possible worst-case user parameters at each force level. We note that Hajian and Howe make no claim about these five subjects being fully representative of the population as a whole or about the model's validity when $\bar{F}_h < 2$ N.

Two human users were used to verify the method presented here. One user was large (100 kg, 1.91-m tall) and one user was small (49 kg, 1.55-m tall). These two users have index fingers with distinct mechanical properties (length, mass, strength), and are meant to represent the extremes of users that may interact with the system.

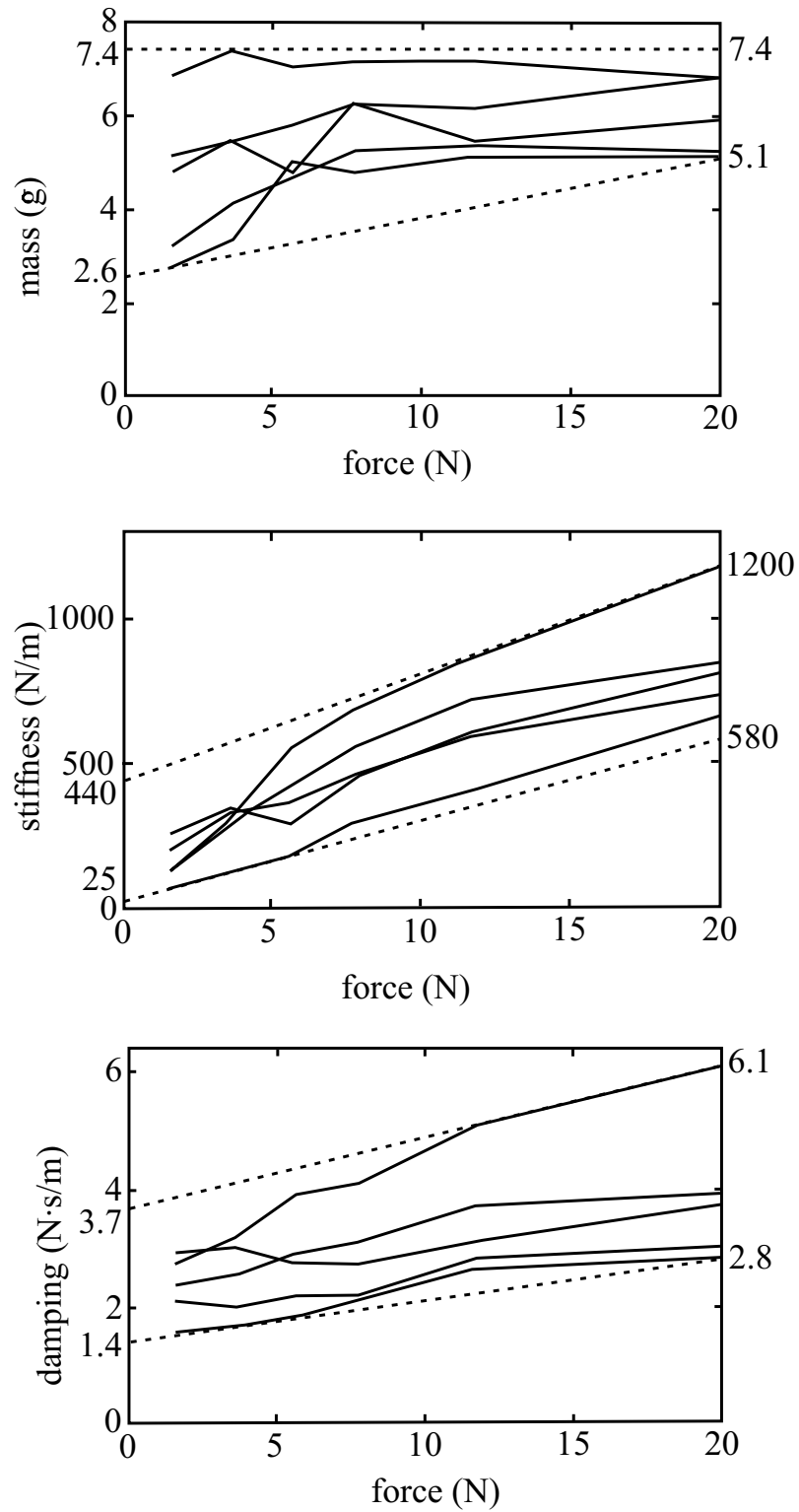


Figure 2.11: Human index finger mass-spring-damper values for five users [32], with simple bounding lines added. Original data courtesy Robert D. Howe.

Both users were very experienced with the use of haptic devices.

For each of the experimental data that follow, the users attempted to make the system go unstable in any way possible, such that the index finger was through the Velcro finger loop, and their elbow was resting. The goal was to determine the maximum FRVF stiffness at which he or she was unable to make the system go unstable (that is, generate a sustained limit cycle). For the purpose of this paper, a limit cycle that simply switched back and forth between two neighboring encoder counts was not considered unstable, since no better performance can be expected with quantization effects. This type of limit cycle may make the wall feel active (as discussed in Chapter 3), but does not necessarily result in the gross instability that we are concerned with here.

Humans are adept at learning how to drive haptic systems to instability [18], and our users had as much time as necessary to experiment with the system, slowly lowering the FRVF stiffness level, until they were confident that they could not drive the system unstable. Many different strategies were learned and adopted, such as pushing hard, pushing soft, relaxing the hand, clenching the hand, fast movement into the FRVF, holding the device at the surface of FRVF, and impulsively disturbing the slave. The users were also allowed to iterate, raising and lowering the FRVF stiffness as many times as was necessary to determine the limits of stability.

Algorithm

The algorithm used to determine if a possible instability exists is given as Fig. 2.12. It generates an LTI human by using the simple bounding lines from Fig. 2.11;

```

input telemanipulator parameters
input human model
for each user force level
  for each user mass at force level
    for each user damping at force level
      for each user stiffness at force level
        generate discrete state-space model
        convert eigenvalues to s-plane
        find minimum damping ratio  $\zeta$ 
        if current  $\zeta <$  lowest  $\zeta$ 
          lowest  $\zeta =$  current  $\zeta$ 
          worst-case user = current user
          worst-case force = current force
return lowest  $\zeta$ 
return worst-case user
return worst-case force
if lowest  $\zeta < 0$ 
  return "system is unstable"

```

Figure 2.12: Algorithm for determining system stability.

at each force level, it creates many possible combinations of m_h , b_h , and k_h that could exist between the upper and lower bounding lines at that force level. This process is repeated for many possible force levels. For each LTI human user, the discrete state-space model is generated, and the eigenvalues are analyzed. Rather than simply returning if the eigenvalues are stable ($|z| < 1$ or $\Re\{s\} < 0$), the damping ratios of the eigenvalues are returned, as previously discussed, to give more information about the system's transient behavior.

Figure 2.13 shows the result of this algorithm run at two different values of K_{sVF} , with all other system parameters constant. The results of the two runs were

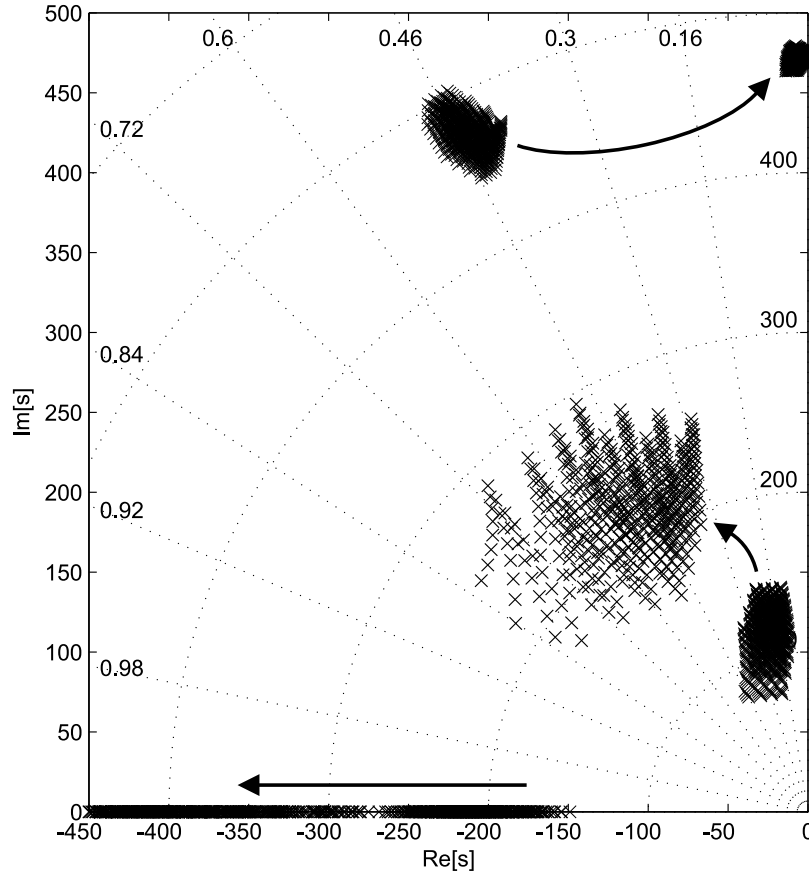


Figure 2.13: The clouds of eigenvalues show how the system eigenvalues vary based on possible human users, for a system with $T = 0.002$ seconds, $K_{pm} = K_{ps} = 800$ N/m, and $K_{dm} = K_{ds} = 6$ Ns/m. Arrows indicate how the eigenvalues move as the FRVF stiffness is increased from $K_{sVF} = 500$ N/m to $K_{sVF} = 5500$ N/m. Eventually, the eigenvalues reach the imaginary axis, indicating possible instability for the worst-case user.

superimposed to create the figure, and arrows were added to show how the clouds of eigenvalues (continuously) move as K_{sVF} is increased. Each cloud of eigenvalues was generated from 512 different human users that could exist between the bounding lines in Fig. 2.11, and shows how the system eigenvalues could vary based on the human user for a given system.

We now proceed by comparing the results predicted by the discrete state-space model with those actually observed in our real system. Because the possible combi-

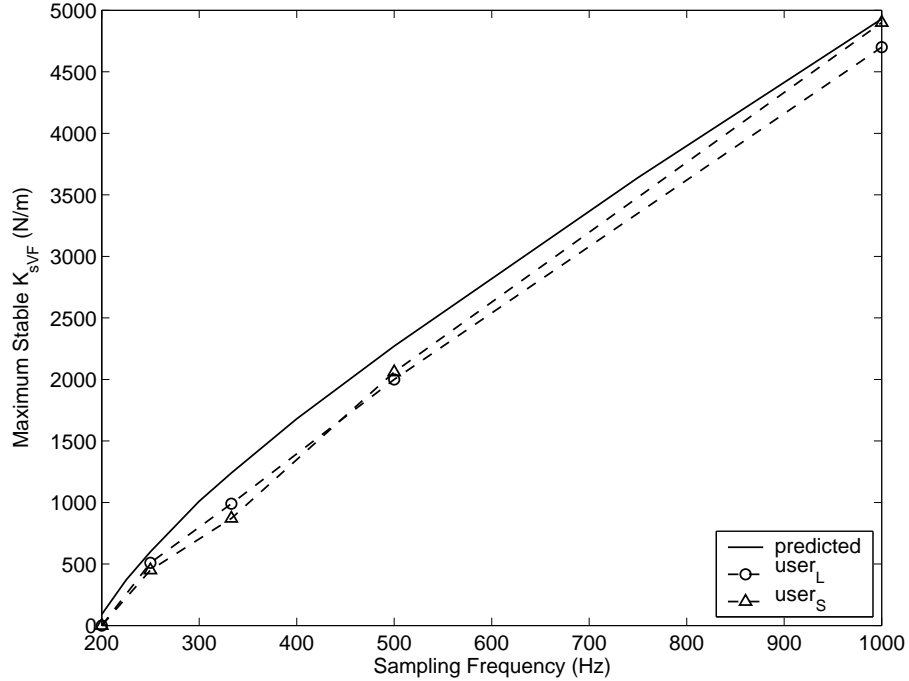


Figure 2.14: Predicted and experimental stability bounds for slave FRVFs vs. sampling rate, with $K_p = 600$ N/m and $K_d = 2$ Ns/m. Experimental data is shown for large ($user_L$) and small ($user_s$) users.

nations of controller gains are limitless, for the remainder of this section we limit our discussion to symmetric position-position telemanipulation controllers (with one exception where noted). That is, $K_{pm} = K_{ps} \equiv K_p$, $K_{dm} = K_{ds} \equiv K_d$, $K_{vm} = K_{vs} = 0$, and $K_{fm} = 0$.

Slave FRVF Results

We first consider the FRVF on the slave side. Figure 2.14 shows the effect of sampling rate on the maximum stable FRVF that can be implemented on a typical telemanipulator. The experimental data was collected as described in the previous discussion of the human users. As is expected, the stiffness of the FRVF goes up with sampling rate. This figure indicates that the discrete state-space model is a

good predictor of experimental data across sampling rates. It also appears that the stability of the slave FRVF is independent of the user – that is, both users were able to generate the finger properties necessary to maintain a limit cycle for roughly the same set of FRVF stiffnesses.

We now look in more detail at the effects of the underlying telemanipulation controller gains on the stability of the FRVF. Figure 2.15 shows how the maximum stable slave FRVF changes as K_p and K_d are changed independently, for a system running at 500 Hz. This data shows that K_p has a small effect on the stability, while K_d has a large effect. The small effect of K_p is likely due to the fact that, for stable telemanipulators, the value of K_p is small relative to K_{sVF} . It is also again evident that there is little difference between users. Figure 2.16 shows the same type of plot for a system running at 1000 Hz. This data shows the same trends, with an even better fit between the actual and the predicted stability.

We briefly leave the symmetric telemanipulator to consider the problem of saturation of the master actuators. In practice, the master device of a telemanipulation system may be designed to be light and very backdrivable, but a consequence of this design may be that the master actuators are small and saturate at relatively low force values. When the user applies enough force to saturate the master actuators, small changes in the system on the slave side lead to no changes in the master actuator’s output, basically taking the master “out of the loop.” This typically makes the slave device vibrate easier than when the master is “in the loop,” so it is a problem that must be addressed.

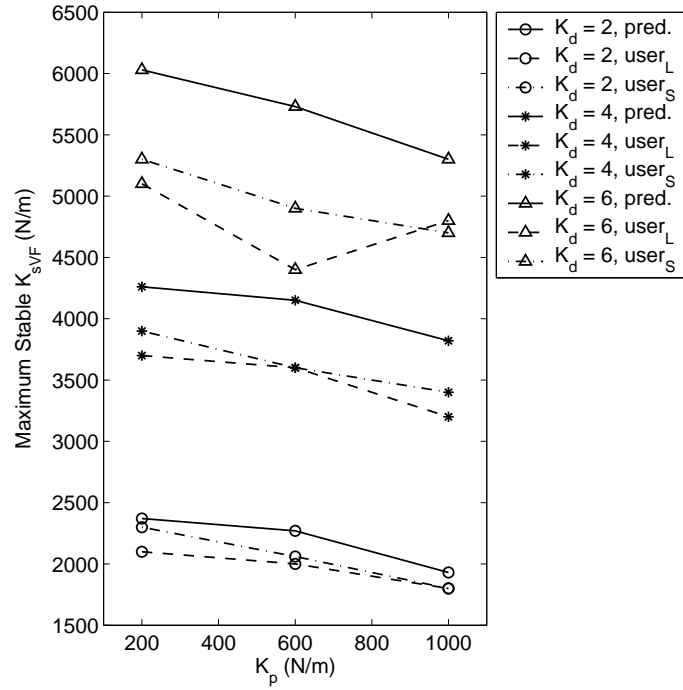


Figure 2.15: Predicted and experimental stability bounds for slave FRVFs, at 500-Hz sampling rate. Data is shown for large ($user_L$) and small ($user_S$) users.

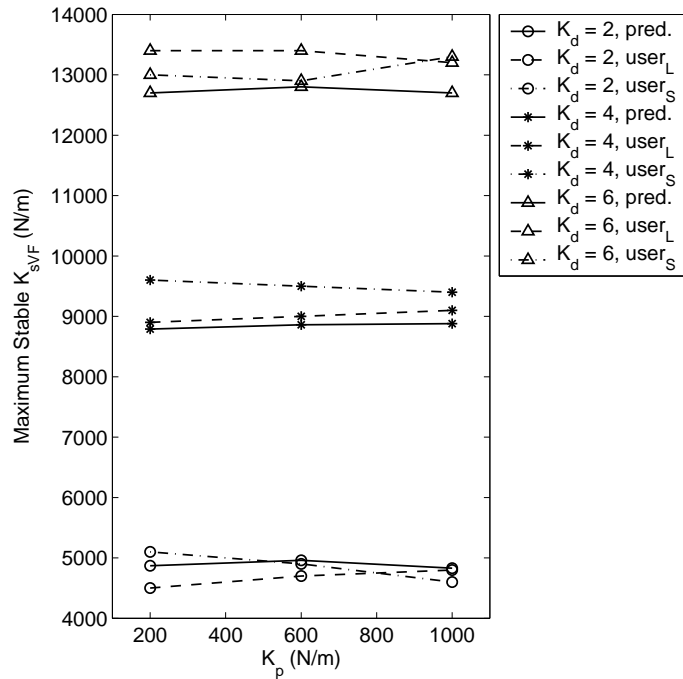


Figure 2.16: Predicted and experimental stability bounds for slave FRVF, at 1000-Hz sampling rate. Data is shown for large ($user_L$) and small ($user_S$) users.

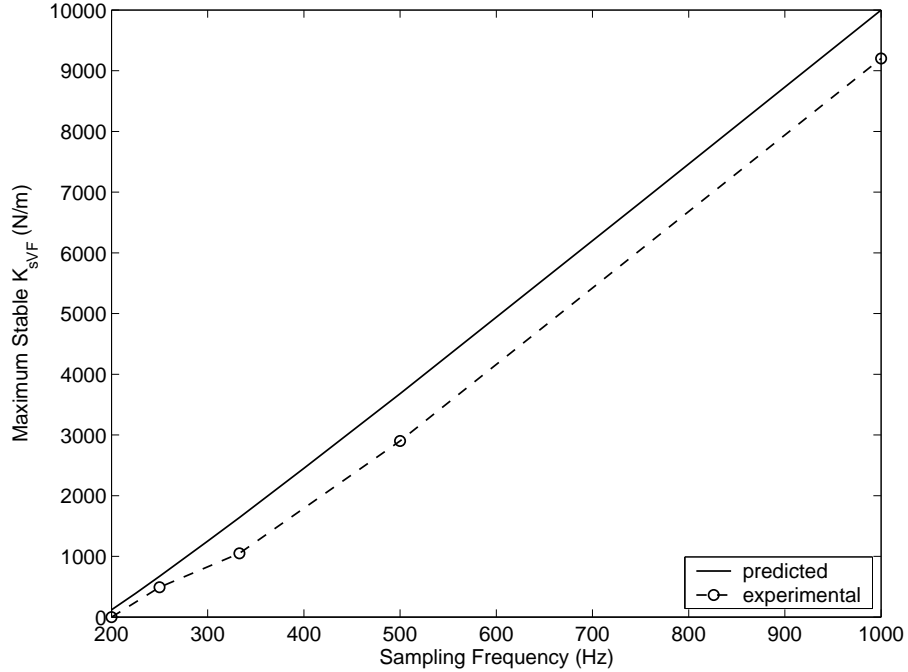


Figure 2.17: Predicted and experimental stability bounds for slave FRVFs vs. sampling rate for unilateral telemanipulation, with $K_{ps} = 1000$ N/m and $K_{ds} = 6$ Ns/m. A unilateral telemanipulator models saturation of the master actuator.

To analyze saturation of the master actuators, we simply consider the system as a unilateral telemanipulator. The discrete state-space formulation is general enough to handle this case (using an equilibrium-point control model of the human results in the existence of an equilibrium point for a constant F_h^* , even when the master is completely unactuated). Figure 2.17 shows, across sampling rates, that the predictions match the observed data roughly as well as they did for the bilateral case. Of course, the user's properties have no effect of the performance of the unilateral system.

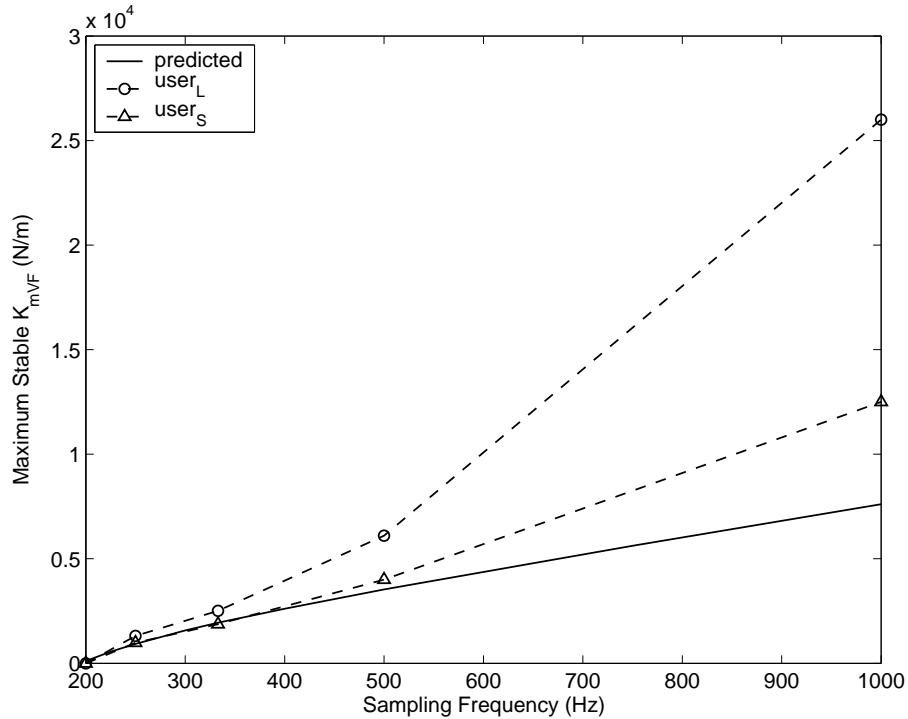


Figure 2.18: Predicted and experimental stability bounds for master FRVFs vs. sampling rate, with $K_p = 600$ N/m and $K_d = 2$ Ns/m. Experimental data is shown for large (user_L) and small (user_S) users.

Master FRVF Results

We now consider the FRVF on the master side. Figure 2.18 shows the effect of sampling rate on the maximum stable FRVF that can be implemented on a typical telemanipulator. Again, as expected, the stiffness of the FRVF goes up with sampling rate. This figure shows significant differences from Fig. 2.14, though. First, there are significant differences between users, and the differences appear to grow as the sampling rate increases. The small user was able to generate finger impedances that the large user just could not, due to the inherent mechanical properties of the finger, making the system go unstable at lower stiffness values. Second, the prediction method appears to be conservative at high sampling rates.

To understand the effects of the underlying telemanipulator gains on FRVF stability, we first consider Fig. 2.19. This figure shows how the maximum stable FRVF changes as K_p and K_d are changed independently, for a system running at 500 Hz. As before, the value of K_d has a large effect on the maximum FRVF stiffness, while the value of K_p has little effect. From this data, it is clear that the prediction is close to the data gathered for the small user, but is conservative for the large user. The fact that the prediction is conservative for one user and not for the other is exactly what would be expected if there is a discrepancy between users. The algorithm looks for the worst-case user, which in this case is a very small finger, and the prediction for all other users would necessarily be conservative.

Figure 2.20 shows the case where the sampling rate of the system has increased to 1000 Hz. For this case, the prediction is conservative for the small user, and very conservative for the large user. In fact, the large user was never able to make the system go unstable in the same mode as the other instabilities presented in this chapter. For the large user, the FRVF stiffness was eventually turned up so high that the system went unstable due to the noise in the velocity signal, and not from the sampling rate. The instability felt different (very high frequency and low amplitude), and the figure indicates that the maximum stable FRVF stiffness actually decreases as K_d increases, which is expected for this type of instability.

We now return to the case of the unilateral telemanipulator. A unilateral telemanipulator interacting with a master-side FRVF is essentially the same as a haptic device interacting with a virtual wall – the slave manipulator has no effect on the

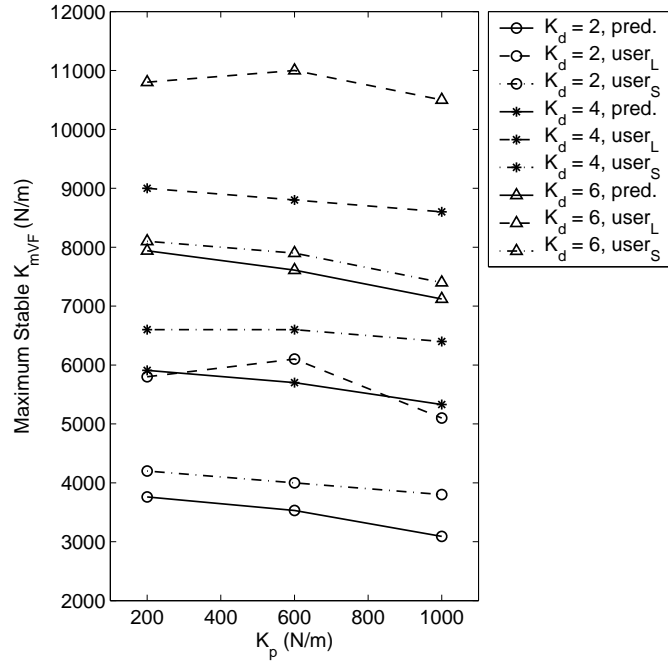


Figure 2.19: Predicted and experimental stability bounds for master FRVFs, at 500-Hz sampling rate. Data is shown for large ($user_L$) and small ($user_S$) users.

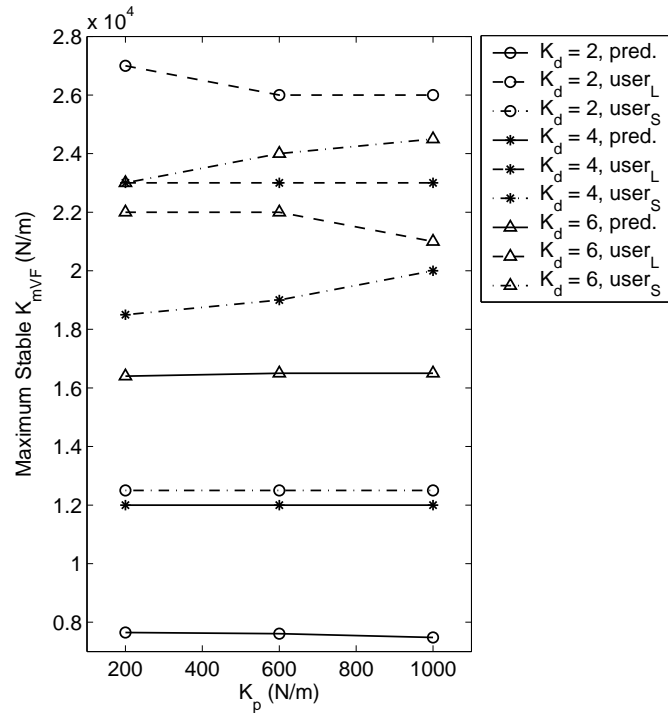


Figure 2.20: Predicted and experimental stability bounds for master FRVFs, at 1000-Hz sampling rate. Data is shown for large ($user_L$) and small ($user_S$) users.

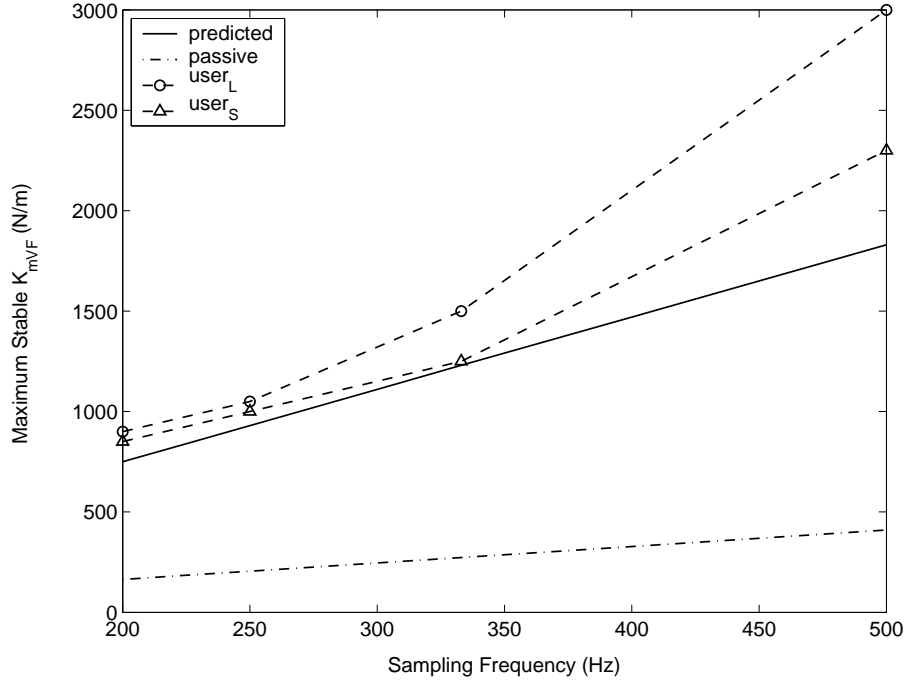


Figure 2.21: Predicted and experimental stability bounds for master FRVFs vs. sampling rate for unilateral telemanipulation, with $K_{ps} = 1000$ N/m and $K_{ds} = 6$ Ns/m (simple virtual wall). Experimental data is shown for large ($user_L$) and small ($user_S$) users. Requiring passivity of the FRVF gives a very conservative result.

master. Thus, this is an opportunity to directly compare our algorithm to previous work on virtual-wall stability. Figure 2.21 shows that, across sampling rates, our method is slightly conservative on the master side, but not nearly as conservative as requiring that our FRVF be passive (using a standard passivity result [20]). The work on virtual-wall passivity presented in Chapter 3 indicates that requiring passivity may be even more conservative, once position sensor quantization is considered.

2.4.3 Discussion

In the previous section we showed that it is possible to accurately predict instabilities that result from telemanipulators interacting with stiff FRVFs, even though the closed-loop system contains an element as complex as a human. We obtained accurate predictions by explicitly considering sampling effects, and we showed that we need not consider the unilateral constraint of the FRVF explicitly. In addition, we showed that useful analytical results can be obtained with only rough LTI models of the human user. The experimental results of the previous section demonstrate that our method is an effective tool in determining the limits on FRVF stiffness that can be safely implemented, without the need for extensive simulation in the design process.

The method presented here is in some sense trial and error (choose system gains and then analyze system stability), but the system behavior and eigenvalue locations change in a way that should be expected (e.g., increasing position gains tends toward instability). Our method explicitly considers a 1-DOF system, but the results are likely to translate to systems with higher degrees of freedom. Telemanipulators are typically implemented using Cartesian-based control (as opposed to direct joint control), and techniques such as the computed-torque method are available to decouple and linearize the Cartesian degrees of freedom [22]. With controllers such as this, the degree of freedom considered in our paper would simply correspond to the direction normal to the FRVF at the point of contact. Also, we explicitly considered the index finger of the human user here, but other system-appropriate human mod-

els could be used. For example, it has been shown that the human wrist can also be accurately modeled as an LTI mass-spring-damper [55]. As a proof of concept, the idea that the human user can be modeled as a worst-case LTI model, rather than as a more general time-varying model, was shown to be accurate in predicting system stability bounds.

It should be noted that actually implementing a FRVF stiffness just below the stability limit would probably not be desirable for real robot-assisted surgical tasks – sustained vibration may be impossible to generate, but a slowly-decaying, large-amplitude vibration would be undesirable as well. A benefit of considering the location of the eigenvalues of the system as a measure of stability is that it is not a binary test, simply returning “stable” or “unstable.” The damping in the eigenvalues can be used as an additional source of information about the system’s transient response. In addition, the damping in the worst-case eigenvalue can be used as a rough measure of stability robustness (in second-order systems, the damping ratio is highly correlated to the phase margin in the system).

The method presented here was shown to be accurate in determining system stability when the slave is not in contact with any environment (which was determined to be the most likely scenario to result in instabilities). One assumption used in creating the discrete state-space model in Section 2.4.1 is the assumption that F_e is constant between samples. Our method was developed specifically for MIS applications, where the environment will be soft tissues with relatively low stiffness values. If the system interacts with stiff environments (relative to the sampling rate)

where F_e could change significantly between samples, the model could lose accuracy. Verification of our method for systems where the FRVF is located at or below the surface of a compliant environment is left as a topic for future research, but preliminary experiments indicate that simply assuming no environment in the analysis will result in conservative stability predictions when a dissipative environment is present.

For completeness, let us briefly consider some of the limitations of our method. In particular, system models generally will have high-frequency inaccuracies, and as the models become less accurate, the analytical predictions will lose accuracy as well. The finger model loses accuracy at combinations of high sampling rate and high FRVF stiffness. The properties of the finger pad may be important here [62], but they are unmodeled in [32], which is the source for our finger data. The unmodeled effects of the finger pad are likely to make the finger more dissipative. Another possible inaccuracy is that the actuators (including their amplifiers) could deviate from the ideal actuator assumed in the model. Because of inductance in the motors and voltage limits in the current amplifiers, the actual rate of change in current through the motors is limited (although very fast). This effect would be most noticed with high sampling rate and high FRVF stiffness, and it would tend to make the effective FRVF stiffness slightly lower than what is expected. Finally, for small movements, unmodeled friction (such as Coulomb friction) tends to dominate, and the viscous friction tends to underestimate the actual dissipation. All of the above effects would tend to make the method predict in a conservative (safe) way.

However, our result was shown to be less conservative than that obtained using FRVF passivity as a sufficient condition for closed-loop stability, as shown in Fig. 2.21.

We also did not consider the effects of mechanical compliance. Our experimental telemanipulator is very rigid, with the compliance occurring in the controlled joints. Consequently, we were able to accurately model our system as a rigid bodies. This will not be the case with all systems; structural resonances are often important limitation in robot design [22]. Structural dynamics could be incorporated into a state-space analysis like that presented here – this would increase the dimension of the model.

2.4.4 Conclusions for Stability

This work presents a method to predict and prevent unstable vibrations of the master and slave manipulators of a bilateral telemanipulation system against FRVFs, implemented as virtual walls, through appropriate choice of control system gains and FRVF stiffness. With an understanding of the bounds of their stability, FRVFs can be safely overlaid on existing bilateral telemanipulation systems. FRVFs can be applied to robot-assisted minimally invasive surgical procedures to prevent the manipulator from entering into forbidden regions of the workspace – preventing unwanted and potentially dangerous interactions with delicate tissues.

We found that a telemanipulator with FRVFs can be rewritten around an equilibrium position, creating a dual system that can be analyzed using methods already

available for linear systems. Then we developed a discrete state-space model for a class of bilateral telemanipulators that includes many common telemanipulator control systems. The algorithm for generating this model is given as Appendix B. We then used the eigenvalues of this model to analyze the stability of the system. The eigenvalues also provide insight into transient response in the system, which is not available using some other stability methods (such as passivity).

Our method uses a worst-case LTI mass-spring-damper model of the human user (rather than a complicated nonlinear time-varying model or a general passive model), and a simple mass-damper model for the master and slave devices, but explicitly considers the sampling rate of the system. Experimental results show agreement with analytical predictions of stability in real non-ideal systems. Results indicate that unwanted vibration of the slave manipulator against a slave-side FRVF is independent of the type of user (*i.e.*, large or small hand), but is dependent on the impedance properties adopted by the user. It was found that the type of user is important in generating sustained vibrations of the master manipulandum against a master-side FRVF. Our result was also shown to be less conservative than requiring passivity of a master FRVF.

2.5 Conclusions

In this chapter we explored the design of stable forbidden-region virtual fixtures for bilateral telemanipulators of the impedance type. We developed three metrics to quantify the performance of forbidden-region virtual fixtures: tracking, safety,

and submittance. Using these metrics, a human-factors experiment was conducted to quantify the performance of various combinations of virtual fixtures and bilateral telemanipulation controller. The experiment showed that, while the design of virtual fixtures will likely be highly task dependent, there are a few rules of thumb that can be employed when choosing a virtual-fixture architecture. We analyzed the stability of impedance-type forbidden-region virtual fixtures using a sampled-data model of the closed-loop system. An algorithm was developed to predict potential instability; the algorithm requires a model of the telemanipulator, as well as simple bounds on the parameters of human users. This stability method was experimentally verified, and shown to be an effective predictor of stability in a real non-ideal system.

The research in this chapter explicitly considered a telemanipulation systems where both the master and slave are impedance-type robots. The stability results apply to a system implementing impedance-type forbidden-region virtual fixtures. In the next two chapters we use an alternative method for analysis of system stability – passivity. The passivity technique of Chapter 3 also considers impedance-type forbidden-region virtual fixtures (“virtual walls”). However, the passivity techniques of Chapter 4 generalize to systems where the master and slave devices are of either the impedance or admittance type, and the master and slave virtual fixtures are of either the impedance or admittance type. It also generalizes to both forbidden-region virtual fixtures and guidance virtual fixtures.

Chapter 3

Effects of Position Quantization and Sampling Rate on Virtual-Wall Passivity

The main result of this chapter is a virtual-wall passivity condition that considers friction, sampling rate, and sensor quantization effects. The research in this chapter is particularly relevant to the community researching the stability/passivity of haptic virtual environments. In the next chapter, we show how stability of telemanipulators with virtual fixtures can be assured through the coupling of passive virtual environments with unconditionally stable telemanipulators. Consequently, the passive virtual wall developed here can be employed as a stable forbidden-region virtual fixture.

3.1 Introduction

Many haptic virtual environments are created from fundamental building blocks known as “virtual walls.” A virtual wall is typically an impedance surface accompanied by a unilateral constraint, where the impedance surface (spring, spring-damper, *etc.*) displays a force that is a function of the position (and its time derivatives) of the haptic device, and the unilateral constraint is a nonlinear switching condition that determines if the user is or is not in contact with the virtual wall. It is desirable to make virtual environments feel like real ones, but it is common for the user to feel an active behavior (often described as “vibration” or “rumble”) that destroys the illusion of reality. This behavior is often associated with passivity, or the lack thereof; a passive system is incapable of generating the energy needed to sustain any active behavior.

Of all the prior work on virtual-wall stability and passivity discussed in Section 1.3.3, only [25] explicitly models quantization effects that occur from measuring position with an optical encoder, which is typical of haptic displays. In addition, much of the previous research mentioned uses some form of velocity measurement, without explicitly accounting for the fact that a quantized position measurement is typically used to compute the velocity estimate, introducing noise into the system. Adaptive velocity estimation techniques can help to mitigate this problem [44], but not alleviate it completely. Sensor quantization effects often impact on system performance, although they are almost never explicitly modeled. Explicit modeling of quantization effects is needed for improved accuracy of analytical results.

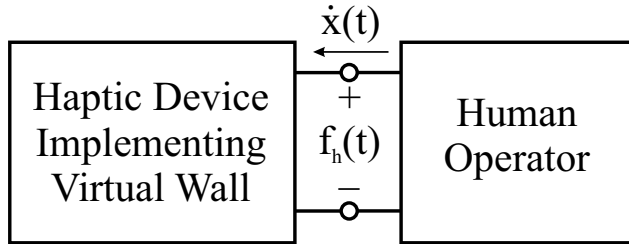


Figure 3.1: Closed-loop system consisting of a human coupled with a virtual-wall system. Passivity of the individual blocks is sufficient for coupled stability.

There are two motivations for designing virtual environments that appear passive at the driving point (that is, at the point where the user exchanges energy with the haptic device). The first, as previously discussed, is to eliminate the active tactile sensation that destroys the illusion of reality. Second, when a human interacts with a haptic device implementing a virtual wall, a closed loop is formed, as shown in Fig. 3.1. A sufficient condition for the coupled system to be stable is that each of the components in the system is passive [24, 104]. This relies on the assumption of human passivity for closed-loop stability, but there is evidence that humans can behave passively when they choose to do so [40]. Therefore, our second motivation for this research is to create systems with which humans can stably interact.

The current work is inspired by the philosophy of Colgate *et al.* [18, 20], in that we find a stiffness that is a simple function of the system parameters and is guaranteed to result in a virtual wall that appears passive to the user at the driving point. As in [20], the system is shown to be passive in that any “energy leaks” [29] from the virtual wall are dissipated by the friction in the haptic device.

This work differs from previously reported results in the following four ways. First, we explicitly consider sensor quantization. Second, we do not assume that

the sampling rate of the computer is significantly faster than the bandwidth of the system, nor that the zero-order hold (ZOH) elements can be modeled as linear time-invariant (LTI). Third, we make no assumptions about the human user. An assumption that is often made is that the sampling rate of the system is significantly faster than the human bandwidth. Under this assumption, human voluntary action is often neglected from the system stability analysis. In our analysis, the human may implement the most malicious strategy possible in an attempt to extract energy from the wall (including generating trajectories with significant aliasing). Finally, we assume a more realistic friction model than simple viscous friction. The most significant difference in our analysis from most literature in this field is that we make no assumptions about the sampling rate of the computer, or the resolution of the encoder, except that they are constant. We consider an arbitrarily slow computer, as well as an encoder with arbitrarily poor resolution.

Our main result is a simple necessary and sufficient condition on virtual-wall passivity that is a function of the friction present in the device, the sampling rate of the system, and the resolution of the position sensor. The result is given in Section 3.4, and passivity is proven by showing that our nonlinear sampled-data system is always more dissipative than an ideal lossless system. The condition is validated experimentally in Section 3.5, and found to be a good predictor of system behavior. The experiments also yield insight into the modes of non-passive behavior exhibited by these systems. The research in this chapter will appear in [5], and was presented in part in [4].

3.2 Passivity

A passive system is incapable of generating a net amount of energy, and is defined by:

$$\int_0^t (f(\tau) \cdot v(\tau)) d\tau + E(0) \geq 0, \quad \forall t \geq 0 \quad (3.1)$$

where f and v are conjugate power variables that describe the energy flow into the system, and $E(0)$ is any energy stored in the system at time $t = 0$ [24]. For the systems to be considered passive, (3.1) must hold for all possible $f(t)$, $v(t)$ pairs. If the system has more than one port for power exchange, then f and v are vector quantities, where the i th entry corresponds to the i th port, and the \cdot in (3.1) represents the vector dot product.

3.3 System Model

The system we consider is given as Fig. 3.2. It is a one-degree-of-freedom haptic device, modeled as a mass being acted upon by three forces: the force applied by the human user $f_h(t)$, the force applied by the actuator $f_a(t)$, and the force due to friction $f_f(t)$:

$$f_h(t) - f_a(t) - f_f(t) = m\ddot{x}(t) \quad (3.2)$$

The human force $f_h(t)$ is defined as positive when it tends to move the haptic device forward into the virtual wall. The actuator force $f_a(t)$ and friction force $f_f(t)$ are both defined as positive when they tend to move the device out of the virtual wall.

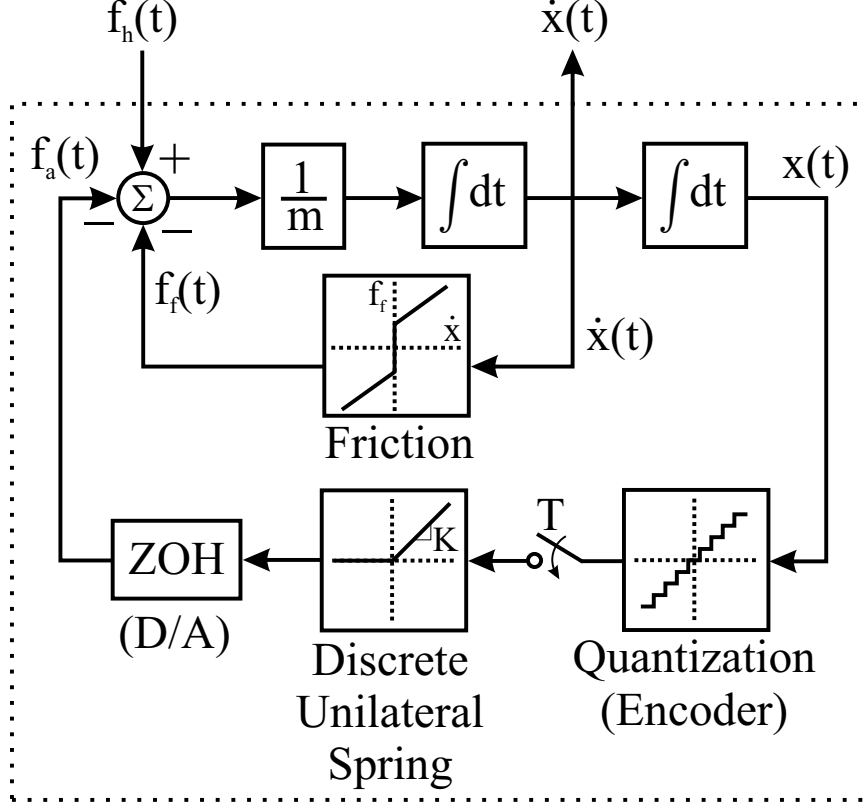


Figure 3.2: Haptic device implementing a virtual wall. This is a sampled-data system, with device dynamics, sensor quantization, sampling, and zero-order hold considered explicitly.

We adopt a Coulomb-plus-viscous friction model [10]:

$$f_f(t) = \begin{cases} f_c \text{sgn}(\dot{x}(t)) + b\dot{x}(t) & : \dot{x} \neq 0 \\ \min(f_c, |f_e(t)|) \text{sgn}(f_e(t)) & : \dot{x} = 0 \end{cases} \quad (3.3)$$

where f_c and b are the positive constant Coulomb and viscous friction parameters of the haptic device, and $f_e(t) = f_h(t) - f_a(t)$ is the net external force on the mass.

The quantized position signal is sampled with a constant sampling period of T .

The quantized and sampled position measurement from the encoder is used as the measured penetration into the virtual wall, which is implemented, at sample k , as

a simple discrete spring with a unilateral constraint:

$$f_a(k) = \begin{cases} Kx_{\text{enc}}(k) & : x_{\text{enc}}(k) > 0 \\ 0 & : x_{\text{enc}}(k) \leq 0 \end{cases} \quad (3.4)$$

where K is the stiffness of the virtual wall, and $x_{\text{enc}}(k)$ is the measured position at sample k . The quantization is due to measuring position with an incremental optical encoder with a resolution of Δ . We focus on encoders due to their ubiquity in haptic devices, but the analysis that follows applies to any position quantization (such as discretizing an analog signal with an A/D converter). The output of the discrete unilateral spring is held constant for the duration of the sampling period with a ZOH, resulting in a continuous-time staircase actuator force $f_a(t)$. It is clear that this simple virtual wall results in $f_a(t) \geq 0 \forall t$. We will exploit this property in our virtual-wall passivity analysis.

Sensor quantization is difficult to analyze accurately. It is a problem that exists independent of computer sampling, in that there is a fundamental loss of information, no matter how fast the sampling rate of the system. The mapping from the true position x to the measured position x_{enc} will exist somewhere between the two mappings shown in Fig. 3.3, for a given initialization, but where it lies is impossible to know. The quantization mapping will be time invariant, though, until the system is reinitialized. We will assume, without loss of generality, that the solid line represents the quantization of the sensor. This assumption can be made because the true zero position of the device with respect to the encoder has no bearing on the problem. The only effect of this assumption will be to possibly change the value of $E(0)$ in (3.1), which does not affect the system passivity.

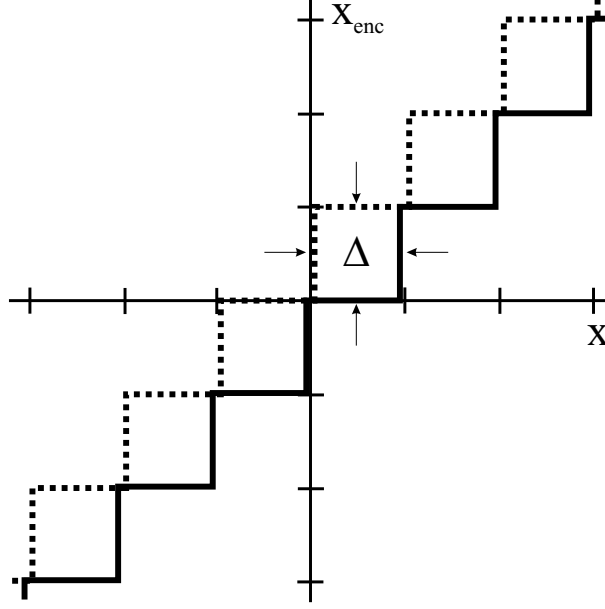


Figure 3.3: Quantization mapping of encoder with resolution Δ falls somewhere between two extremes. Assume without loss of generality that the solid line represents quantization mapping.

3.4 Virtual-Wall Passivity

We now develop a virtual-wall passivity proof that uses a time-domain energy analysis. The proof makes use of a known passive (lossless) system as a reference system. If a haptic device implementing a virtual wall can be shown to be more dissipative than this lossless system in all cases, then the haptic device implementing the virtual wall is itself passive. The main result of the passivity proof is summarized as follows:

A haptic device implementing a virtual wall, as described in Section 3.3, is guaranteed to be passive if and only if a simple condition is met:

$$K \leq \min \left(\frac{2b}{T}, \frac{2f_c}{\Delta} \right) \quad (3.5)$$

This condition on the maximum allowable virtual-wall stiffness involves two sim-

ple ratios – one between the viscous friction in the haptic device and the sampling period of the system, and one between the Coulomb friction in the haptic device and encoder resolution. We show later (in Section 3.5.2) that violating this condition physically results in systems that exhibit at least one of two types of non-passive behavior: closed-loop instability and active-tactile sensations.

3.4.1 Approach

Consider an ideal mass-spring system, defined in compression when $x > 0$, and the only force acting on the system is that input by a human, f_h . This system is passive and lossless, since the total energy of the system at each instant in time (which includes kinetic energy of the mass and potential energy of the spring) is equal to the total work input by the human:

$$W_h(t) = \int_0^t f_h(\tau)\dot{x}(\tau)d\tau \quad (3.6)$$

Now, consider the haptic device implementing the virtual wall shown in Fig. 3.2, with a mass equal to that in the ideal mass-spring system described above, and with a virtual spring constant equal to that of the spring described above. Previous work shows that a virtual wall (independent of the haptic device) is inherently non-passive [19, 29]. In this section we show that, below some critical virtual-wall stiffness, the friction present in a haptic device (which is not present in the ideal mass-spring system) will completely dissipate the energy generated by the discrete unilateral spring, making the system that contains both the virtual wall and the haptic device appear passive (or even dissipative) at the driving point.

We will conclude that a haptic device implementing a virtual wall is passive if and only if $W_h(t) \geq 0 \forall t \geq 0$. This will be accomplished by comparing the total energy (kinetic plus potential) in the haptic device implementing a virtual wall to that of the lossless ideal mass-spring system for all possible trajectories. The notion of kinetic energy translates easily between the physical mass-spring system and the haptic device; they are both simply $\frac{1}{2}m\dot{x}^2$. The notion of potential energy does not translate so trivially between an ideal spring and a virtual spring. This motivates Section 3.4.2.

We now proceed by proving that (3.5) is the necessary and sufficient condition for passivity of the system of Section 3.3. For sufficiency, we show that (3.5) guarantees that the system is incapable of generating any net energy. We then demonstrate the necessity of (3.5) by constructing counterexamples that result in net energy generation. For use in the remainder of this paper, we define the terms $x_0 = x(0)$, $\dot{x}_0 = \dot{x}(0)$, $x_T = x(T)$, and $\dot{x}_T = \dot{x}(T)$.

3.4.2 Sufficiency

We now consider four cases that span all possible scenarios encountered with the virtual wall: 1) starting inside the wall, and ending (one sample later) less deep or outside the wall, 2) starting inside the wall, and ending deeper inside, 3) starting outside the wall, and ending inside, and 4) starting and ending outside the wall. The result is a sufficient condition for virtual-wall passivity.

Moving Out Of The Wall ($x_0 \geq 0, x_T \leq x_0$)

Consider an ideal mass-spring-damper system with a relaxed position at $x = 0$. The potential energy of this system at any given time is calculated as $\frac{1}{2}Kx^2$, even though this amount of energy could never practically be reclaimed from the system because of the viscous friction losses associated with any movement. In this way, the potential energy is actually a supremum on the amount of latent energy in the system, and this upper-bound is approached (but never reached) the slower the spring is released. We use this same notion to define the potential energy of the virtual wall. In this section we determine what conditions must be met to use $\frac{1}{2}Kx^2$ as a measurement of potential energy of a virtual wall.

For any initial state condition (x_0, \dot{x}_0) , with $x_0 \geq 0$, consider the set of all possible trajectories, defined on the time interval $t \in [0, T]$, that move the device to some final state (x_T, \dot{x}_T) with $x_T \leq x_0$. This includes both the case of leaving the wall, and the case of a final position that is less deep, but still within the wall. The energy balance for this scenario is

$$f_a(x_0 - x_T) + W_h = \frac{1}{2}m(\dot{x}_T^2 - \dot{x}_0^2) + W_f \quad (3.7)$$

where W_h is the work input by the human (see (3.6)), W_f is a nonnegative quantity that includes all energy losses due to friction over the time interval, and f_a is the constant nonnegative actuator force. Rearranging terms gives the work done on the human $W_1 = -W_h$ as

$$W_1 = f_a(x_0 - x_T) + \frac{1}{2}m(\dot{x}_0^2 - \dot{x}_T^2) - W_f \quad (3.8)$$

An ideal mass-spring system is conservative, so the energy extracted from it, for the same initial and final states considered above, is found simply as the sum of the losses in potential and kinetic energy

$$W_2 = \frac{1}{2}K(x_0^2 - x_T^2) + \frac{1}{2}m(\dot{x}_0^2 - \dot{x}_T^2) \quad (3.9)$$

Consider the quantity $J = W_2 - W_1$, which represents the difference in the amount of energy extracted from the virtual wall and the ideal mass-spring for the same trajectory. If we can determine that J has a nonnegative lower bound, we can conclude that the potential energy of the virtual wall is no greater than the potential energy of the ideal mass-spring system, which is simply $\frac{1}{2}Kx^2$.

The problem of finding a lower bound on J , for a given set of initial and final state conditions, essentially becomes the problem of finding a lower bound on W_f in (3.8). It can be shown that the trajectory that minimizes friction losses is a monotonic trajectory with no stops of finite time (see Appendix C). This allows us to conclude that, in the trajectory that minimizes J , the effects of Coulomb friction can be modeled as a constant retarding force f_c . This removes the nonlinear switching nature of Coulomb friction for the purposes of finding a lower bound on J . The performance index described above is then written as

$$J = \frac{1}{2}K(x_0^2 - x_T^2) + (f_a - f_c)(x_T - x_0) + \int_0^T b\dot{x}^2(t)dt \quad (3.10)$$

The problem of finding a lower bound on J simply becomes the problem of finding a lower bound on the viscous losses. We can use the Cauchy-Schwarz Inequality [100]

to find the lower bound on the viscous losses:

$$\left(\int_0^T \dot{x}(t)dt\right)^2 \leq T \int_0^T \dot{x}^2(t)dt \quad (3.11)$$

Using a result from Appendix C, we see that the left-hand side of the above equation is simply the square of the trajectory length. From this, we get an explicit lower bound on J :

$$J \geq \frac{K}{2}(x_0^2 - x_T^2) + (f_a - f_c)(x_T - x_0) + \frac{b}{T}(x_T - x_0)^2 \quad (3.12)$$

We now need to ensure that $J \geq 0$. The actuator force, defined in (3.4), can be rewritten as

$$f_a = K(x_0 - \delta) \quad (3.13)$$

where $0 \leq \delta \leq \Delta$, but δ is otherwise unknown. The value of δ that minimizes the right-hand side of (3.12) is $\delta = 0$. Therefore, we can substitute $f_a = Kx_0$ into (3.12), and the worst-case J^* can be written as a function of initial and final states:

$$J^* = \alpha(x_0 - x_T)^2 + f_c(x_0 - x_T) \quad (3.14)$$

$$\alpha = \frac{b}{T} - \frac{K}{2} \quad (3.15)$$

It is interesting to note that J^* is only a function of the relative positions of the device, but not the velocities, at the endpoints. This should not be surprising, since we can instantaneously input or extract finite amounts of kinetic energy (in the limit) through impulsive forces. Examination of the quadratic nature of (3.14) reveals that $J^* \geq 0$ whenever $x_0 - x_T \geq 0$, if $\alpha \geq 0$. This condition can be rewritten

as a simple condition on the virtual-wall stiffness that may be implemented:

$$K \leq \frac{2b}{T} \quad (3.16)$$

If this condition is met, then the energy extracted from the virtual wall is always bounded from above by the energy extracted from an ideal mass-spring system with the same spring constant, mass, and initial conditions, and therefore $\frac{1}{2}Kx^2$ can be used as a conservative estimate of potential energy in our virtual wall.

It should be noted that the equation used for W_2 (3.9) did not consider the unilateral constraint associated with an ideal mass-spring wall. Incorporating a unilateral constraint would only tend to increase W_2 , and in turn increase J . Therefore, (3.14) is a conservative measure of the worst-case J when the user leaves the wall.

Moving Further Into The Wall ($x_0 \geq 0, x_T > x_0$)

In this section, we consider the case where the device starts within the wall ($x_0 \geq 0$), and the user moves deeper into the wall ($x_T > x_0$). Now that we are equipped with a simple representation of potential energy in the virtual wall, we want to guarantee that it is impossible to get free potential energy, which is the typical problem associated with implementing virtual walls [29]. In other words, we want to guarantee that any potential energy in the virtual wall that is gained during one sampling period is accompanied by at least as much prior work input by the human operator at the driving point.

For any initial condition (x_0, \dot{x}_0) , with $x_0 \geq 0$, consider the set of all possible trajectories, defined on the time interval $t \in [0, T]$, that move the device to some

final state (x_T, \dot{x}_T) deeper in the wall ($x_T > x_0$). In this case W_h , the work done by the human, is still found from the relationship in (3.7). An ideal mass-spring system is lossless, so the work done on it, for the same initial and final states considered above, is found simply as $W_3 = -W_2$ from (3.9). We now consider the quantity $J = W_h - W_3$, which represents the difference in the amount of work needed to compress the virtual wall and the ideal mass-spring along the same trajectory. A nonnegative value of J indicates that at least as much work is required to compress our virtual wall as it would have taken to compress an ideal mass-spring system along the same trajectory. If we can be assured that J has a nonnegative lower bound, we can conclude that it is impossible to get free potential energy from the virtual wall.

Again, the problem of finding a lower bound for J , for a given set of initial and final state conditions, becomes the problem of finding a lower bound for W_f . The performance index described above becomes

$$J = \frac{1}{2}K(x_0^2 - x_T^2) + (f_a + f_c)(x_T - x_0) + \int_0^T b\dot{x}_2^2(t)dt \quad (3.17)$$

Note that the only difference between this equation and (3.10) is a sign change on f_c . The Cauchy-Schwarz Inequality results in

$$J \geq \frac{K}{2}(x_0^2 - x_T^2) + (f_a + f_c)(x_T - x_0) + \frac{b}{T}(x_T - x_0)^2 \quad (3.18)$$

Again, note the sign change in f_c and also in $x_T - x_0$ between this and the previous section. Using the actuator force of (3.13), the value of δ that minimizes J is $\delta = \Delta$. Therefore, we can substitute $f_a = K(x_0 - \Delta)$ into (3.18), and after some

manipulation the worst-case J^* can be written as a function of initial and final states

$$J^* = \alpha(x_0 - x_T)^2 + \beta(x_0 - x_T) \quad (3.19)$$

$$\beta = K\Delta - f_c \quad (3.20)$$

with α defined in (3.15). Analyzing the quadratic nature of (3.19) reveals that J^* has a minimum when $\alpha > 0$, and this minimum is nonnegative for $x_T > x_0$ when $\beta \leq 0$. This results in two simple conditions: that of (3.16), and

$$K \leq \frac{f_c}{\Delta} \quad (3.21)$$

If these two conditions are met, we can be assured that the work required to compress the virtual wall is at least as large as the work required to compress a (passive) ideal mass-spring system with equivalent parameters.

The conditions of (3.16) and (3.21) form a sufficient condition for virtual-wall passivity, because we can construct a known passive device (the ideal mass-spring) that is less dissipative than the virtual wall in both compression and release. However, this result is overly conservative, because the virtual wall need not necessarily be more dissipative than the (lossless) ideal mass-spring in compression, if the virtual wall is significantly more dissipative than the ideal mass-spring during release. This is due to the virtual wall only being able to push, so that it can only generate energy during the release phase.

We find a less conservative sufficient condition if we replace (3.21) by

$$K \leq \frac{2f_c}{\Delta} \quad (3.22)$$

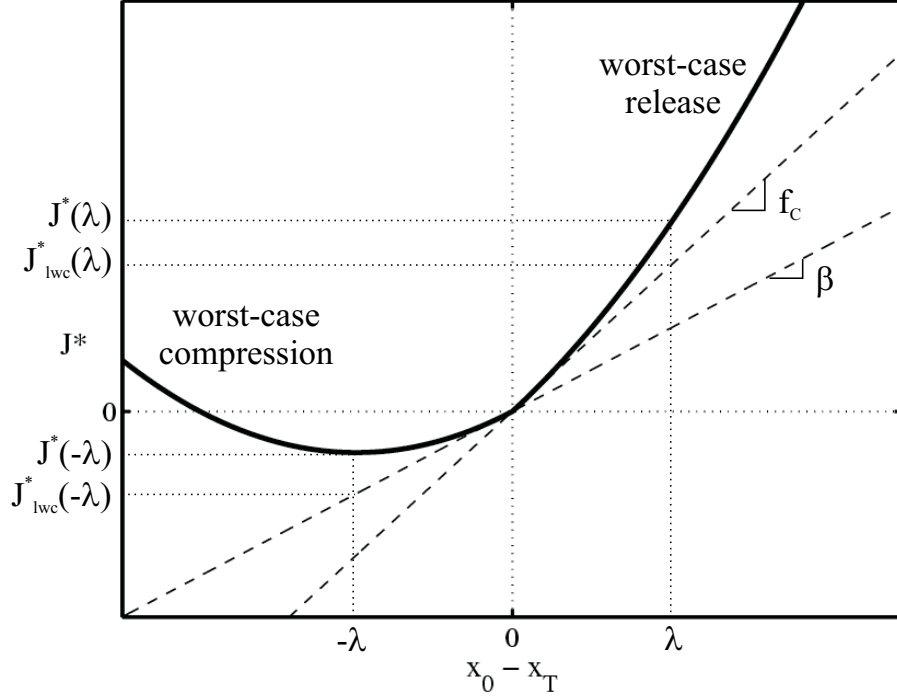


Figure 3.4: Worst-case J^* for virtual-wall compression and release for a nominal system, with $\alpha > 0$ and $f_c \geq \beta$. Linear-worst-case lines are shown. $|J^*(\lambda)| \geq |J^*(-\lambda)|$ and $|J_{lwc}^*(\lambda)| \geq |J_{lwc}^*(-\lambda)| \forall \lambda$.

This condition is equivalent to $\beta \leq f_c$. The sufficiency of (3.22), along with that of (3.16), is shown by considering Fig. 3.4. The left half of the plot shows J^* for compression (see (3.19)). J^* can take on negative values, which would never be the case with (3.21). This worst-case J^* is lower-bounded by the function $\beta(x_0 - x_T)$, which we will refer to as the linear-worst-case J^* for compression. It is clear that this function is always less than or equal to the worst-case J^* , therefore, it is even worse (in the sense of passivity). The right half of the plot shows the J^* for release (see (3.14)), which is lower-bounded by the function $f_c(x_0 - x_T)$, which we call the linear-worst-case J^* for release. Again, this linear-worst-case is even worse than J^* in a passivity sense. Because the virtual wall can only push, and not pull, it is impossible

to extract energy during a compression, and we know from consideration of the linear-worst-case functions for compression and release that any energy extracted during a release is guaranteed to be less than the amount required to compress the wall. In other words, it is alright if it takes less energy to compress the virtual wall than it would to compress an ideal mass-spring along the same trajectory, as long as the virtual wall is sufficiently dissipative during the release. Because of the linearity of the two linear-worst-case J^* functions, the conclusions hold for any combination of compressions and releases. We can therefore conclude that it is impossible to extract a net amount of energy from the virtual wall, regardless of the trajectory.

Crossing Into The Wall ($x_0 < 0, x_T \geq 0$)

The third case considered is when the device begins outside the wall ($x_0 < 0$) and ends inside the wall ($x_T \geq 0$), corresponding to a wall crossing between samples. Any trajectory $x_c(t)$ that accomplishes this will have some time $T_c \in (0, T]$ when the device crosses the wall boundary, after which the device never leaves the wall (*i.e.*, $x_c(t) \geq 0 \quad \forall t \in [T_c, T]$). We can conclude from Section 3.4.2 that any trajectory starting from the initial state ($x_0 = x_c(T_c), \dot{x}_0 = \dot{x}_c(T_c)$) and going to the final state ($x_T = x_c(T), \dot{x}_T = \dot{x}_c(T)$), which includes a trajectory that simply sits at the wall boundary for $0 \leq t \leq T_c$, would require at least as much work as the amount of potential energy gained. The trajectory we consider in this section requires this much work, in addition to the amount of work lost to friction just getting to the wall ($0 \leq t \leq T_c$), with no gains in potential energy (because they end in the same location).

Staying Outside The Wall ($x_0 < 0, x_T < 0$)

This trivial final case is when the device starts outside of the wall, and the user moves the device along a trajectory that also ends outside of the wall. This case is obviously passive (dissipative if any movement occurs). Beginning outside of the wall results in no actuator force, but friction still dissipates energy if any movement happens during the sampling period. Because the device will begin the next period outside of the wall, the actuator will remain off, therefore no potential energy will be created.

3.4.3 Necessity

In the previous section we showed that (3.16) and (3.22) together form a sufficient condition for system of Section 3.3 to be passive. In this section, we show that this condition is also necessary for passivity. We accomplish this by constructing two simple examples to show that violating either (3.16) or (3.22) will result in a non-passive system. The two examples also provide physical insight into the mode of non-passive behavior that may be expected if either (3.16) or (3.22) is violated.

Consider a system with $K > 2b/T$ ($\alpha < 0$). Figure 3.5 shows the worst-case J^* values for compression and release of the virtual wall for a nominal system. Recall that the worst-case J^* for compression occurs when x_0 lies just on the negative side of an encoder pulse, and the worst-case J^* for release occurs when x_0 lies just on the positive side of an encoder pulse. From the figure, it is easy to see that, due to the quadratic nature of J^* , and regardless of the value of β , there will exist some

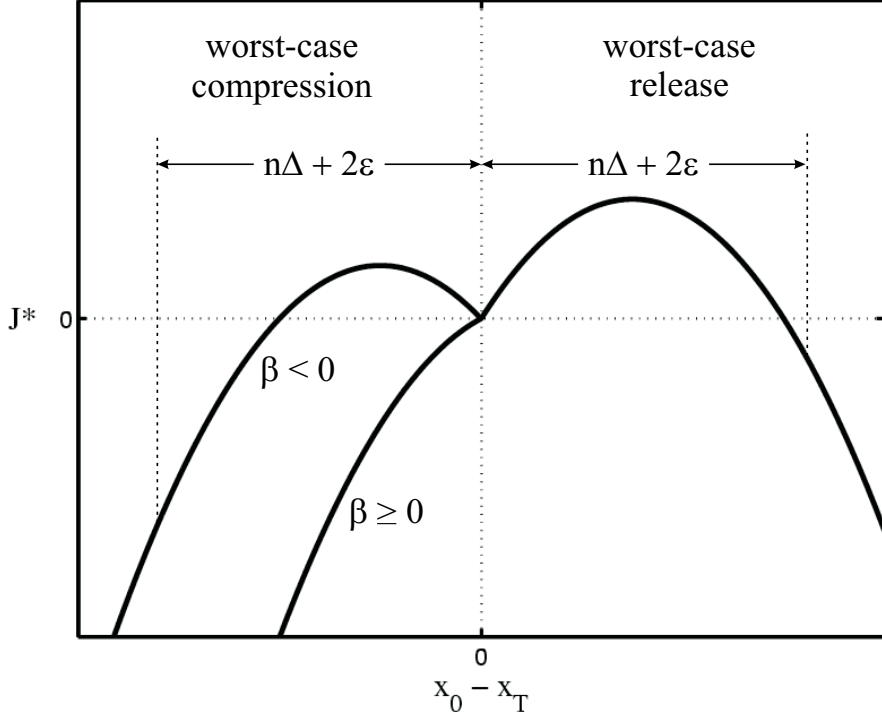


Figure 3.5: Worst-case J^* for virtual-wall compression and release for a nominal system, with $\alpha < 0$. Due to the quadratic nature of the curves, regardless of the sign of β , there will exist a closed kinematic trajectory that will result in net energy generation ($J^* < 0$ for compression and release).

(possibly large) integer n such that if the device is moved at a constant velocity in one sample period to a depth of $x_T = n\Delta + \epsilon$ (for some infinitesimal positive ϵ) from $x_0 = -\epsilon$, and then the device is withdrawn at a constant velocity back to $x = -\epsilon$ in the next sample period, the result is a net generation of energy. The net generation of energy is seen from the negative value of J^* in both compression and release of the wall. It is also easy to verify this generation of energy numerically. From this example of non-passive behavior, it is evident that (3.16) is a necessary condition for passivity.

Next, consider a system with $K > 2f_c/\Delta$. This is equivalent to $\beta > f_c$. The

previous necessary condition exploited arbitrarily large movements; we will now exploit arbitrarily small movements (for visualization, imagine Fig. 3.4 when $\beta > f_c$). We again make use of some very small positive quantity $\epsilon < \Delta$. Consider a haptic device that starts from rest at a position $x_0 = \Delta - \epsilon/2$, and is then brought impulsively to a velocity $\dot{x} = \epsilon/T$. This velocity is held constant for one sample period, and then the device is brought to rest impulsively at a position $x_T = \Delta + \epsilon/2$. This movement requires a net input of energy from the human user of $W_{in} = (f_c + b\epsilon/T)\epsilon$. At this point, the virtual wall switches on, with a value of $f_a = K\Delta$. Next, the velocity is brought impulsively to a velocity $\dot{x} = -\epsilon/T$, is held constant for one sampling period, and is then brought to rest impulsively at the original position $x = \Delta - \epsilon/2$. This movement extracts an amount of energy from the wall equal to $W_{out} = (K\Delta - f_c - b\epsilon/T)\epsilon$. The question is whether $W_{out} > W_{in}$. This would indicate a net extraction of energy, indicating a non-passive wall. $W_{out} - W_{in} > 0$ can be rewritten, after some manipulation, as

$$\beta - f_c > \frac{2b\epsilon}{T} \quad (3.23)$$

Because $\beta - f_c$ is some finite positive quantity, there will exist some (arbitrarily small) ϵ such that the above statement is true. Therefore, by repeating this simple motion, the user can extract an unlimited amount of energy from the virtual wall. From this example, it is evident that (3.22) is a necessary condition for passivity.

3.4.4 Discussion

The result of the previous sections is that the satisfaction of both (3.16) and (3.22) (written compactly as (3.5)) is necessary and sufficient for the system of Section 3.3 to be passive. The bound on virtual-wall stiffness in (3.5) indicates the importance of the relationship between viscous friction and sampling rate, and between Coulomb friction and encoder resolution. It also indicates a lack of coupling between the two sets of parameters. It seems intuitively obvious that increasing sampling rate, encoder resolution, and friction in the device would tend toward passivity, but it is not obvious that the relationships between these parameters would be so simple. A consequence of (3.5) is that, at some point, increasing the system sampling rate leads to no additional ability to increase passive wall stiffness without first increasing encoder resolution. Likewise, at some point, increasing encoder resolution leads to no additional improvement without first increasing computer speeds. There is no reason to believe that, in general, the two bounds contained in (3.5) would even be of the same order of magnitude. It will likely be the case that the stiffness allowed (for guaranteed passivity) on a given nominal system will be sensitive to changes in either $2b/T$ or $2f_c/\Delta$, but not both.

The passivity proof presented shows that a haptic display implementing a virtual wall that satisfies (3.5) is guaranteed to satisfy (3.1) at every sample, but it is easy to show that this system actually satisfies (3.1) for all time (which is needed to truly claim passivity). To verify this, consider a system where (3.1) is violated at some instant between samples. A simple malicious user strategy would be to bring the

device instantly to a stop at that instant (extracting even more energy from the virtual wall) and then to hold the device still until the next sample, resulting in a violation of (3.1) at that sample. Thus, by contrapositive, a guarantee of passivity at the samples implies passivity for all time.

One of the most important contributions of this research is the knowledge that no system that can be modeled as in Section 3.3 can be passive if $f_c = 0$. Note that the part of our condition represented by (3.16) is very similar to the main result of [20] (which states that a virtual-wall system is passive if and only if $K < 2b/T$ if no virtual damping is implemented). We have shown here that a system modeled as a mass-damper (*i.e.*, only viscous friction) is not passive once quantization effects are considered.

The requirement that the friction in the haptic device can be modeled as Coulomb-plus-viscous friction may at first seem to be unrealistic (but surely less prohibitive than the common assumption of only viscous friction). But, increasing friction can only increase energy losses for a given kinematic trajectory. Therefore, if the magnitude of the friction of the device is always at least as large as the friction predicted by the Coulomb-plus-viscous model, then the device will still be guaranteed passive (*i.e.*, sufficiency holds). Consider Fig. 3.6, where the friction in the device includes nonlinear viscosity, as well as stiction [10] (resulting from static friction that is larger than the dynamic friction). A device with this friction pattern could be modeled conservatively with the Coulomb-plus-viscous friction model shown; the bound on stiffness from (3.5) will simply be more conservative than it would be otherwise. It is

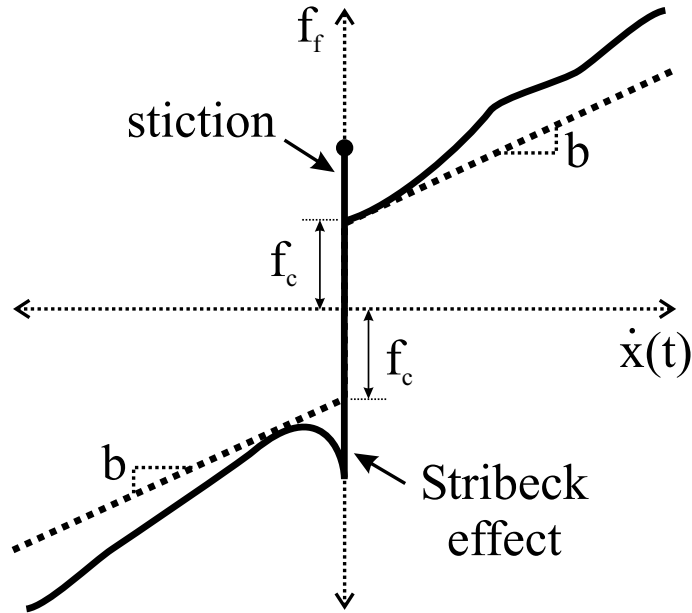


Figure 3.6: Friction containing stiction and nonlinear viscous friction, modeled as Coulomb-plus-viscous friction.

easy to verify that if the friction in the device can be modeled as stiction plus linear viscosity, then the necessity of the condition holds as well (the static friction can simply be overcome by impulsive input forces). Limitations in the friction model are discussed further in Section 3.5.2.

There is another factor that appears to contribute to (3.5) being conservative. The assumption that a human operator is capable of applying impulsive forces to the haptic device, leading to instantaneous changes in velocity, is obviously incorrect. Allowing these impulses appears to lead to a conservative model. Also, note that (3.5) says that the maximum allowable wall stiffness depends on every parameter in the model except the mass of the device. The mass of the device does come into play, though, in the conservative nature of the model. In this paper, impulsive forces can be thought of as a construct – a limiting behavior of real continuous bounded

forces. For haptic devices with very low mass, the human operator will be able to create nearly instantaneous changes in velocity, while the inertia of devices with higher mass will prohibit rapid changes in velocity. Therefore, the model becomes more conservative as mass is increased. However, this conservative assumption of allowing impulsive forces at the input does not reflect on the passivity of the virtual wall, but rather on the stability of the closed-loop system containing the human operator. The passivity of the virtual wall is independent of the type of inputs it experiences – the system is either passive or it is not. That said, requiring a virtual wall to be passive may be an overly conservative criterion if the actual desired result is stable human/wall interaction.

Another factor that led to the conservative nature of the proof is the use of the worst-case J^* in all of the analysis. The worst-case J^* must be considered to truly show passivity, but in practice it only occurs under special circumstances. This assumption leads to a system that is actually dissipative (rather than just passive), meaning the system will lose any initial energy, making sustained oscillations impossible. It should be noted that the passivity proof of Section 3.4 only applies directly to the model of Section 3.3. Real haptic devices may be thought of as fitting this model, with additional modeling noise present in the system. Because the virtual wall is dissipative, system passivity will be robust to some level of modeling error, provided the energy content of the modeling noise is relatively small. This robustness to modeling errors is verified experimentally in Section 3.5. Quantifying the amount of dissipativity in the virtual wall (*i.e.*, the acceptable level of modeling

errors) is left as an exercise for future work.

Possibly the largest drawback of the model used in this paper is the assumption that the actuator is an ideal force source that can apply any desired force instantaneously. This is a common assumption; in fact, none of the previous research discussed in Section 3.1 considers this problem, but in practice, an actuator will be limited by its own dynamics. Practically, the bandwidth of the actuator will likely be much higher than the bandwidth of the device being controlled. Current amplifiers can also be used in place of traditional voltage amplifiers to mitigate the effects of actuator dynamics. In addition, the D/A card communicating desired forces to the actuator will have limited resolution. The implicit assumption is that the resolution of the D/A will be relatively small (we also do not consider resolution of floating-point numbers in the computer, which will have even better resolution). Also, actuator saturation was not considered in our analysis, and this could affect the necessity of (3.5). Our methodology is very different from that used in previous work, and could be used to address actuator limitations and D/A resolution. The assumptions surrounding the actuator are addressed in more detail in Appendix A.3, where it is shown that actuator quantization and bandwidth effects for our system are significantly less important than the modeled effects. Still, it may be desirable to consider an improved actuator model in future work.

Finally, it would be very desirable to include a virtual damping term, in an analysis similar to that considered here. It has been shown that adding virtual damping makes a virtual wall feel stiffer to the user, without an actual increase in

stiffness. The problems inherent with measuring velocity from an encoder signal make the inclusion of virtual damping in a guaranteed-passive virtual wall difficult. Salcudean and Vlaar [87] show that implementing a “braking pulse” when entering a virtual wall is an alternative way of improving the perceived stiffness of the wall. This approach may fit in better with the methods presented here, as may other forms of event-driven “open-loop” velocity feedback [42]. Inclusion of some form of active damping is an important problem for future work.

3.5 Experimental Verification

For a general nonlinear system, it is impossible to prove passivity experimentally (because it would require us to move the device along all possible trajectories), but it is possible to prove that a system is not passive, through energy generation. In this section, we attempt to demonstrate passive and non-passive behaviors in an experimental system, and the resulting behaviors supports (3.5) as a useful measure of passivity in real systems.

3.5.1 Experimental Haptic Device

The haptic device used in the experimental verification is a simple 1-DOF haptic device known as the Haptic Paddle [74]. The Haptic Paddle considered here has been modified for higher performance – details of the system can be found in Appendix A. The Haptic Paddle is shown in Fig. 3.7.

The Haptic Paddle is modeled as a mass with Coulomb-plus-viscous friction

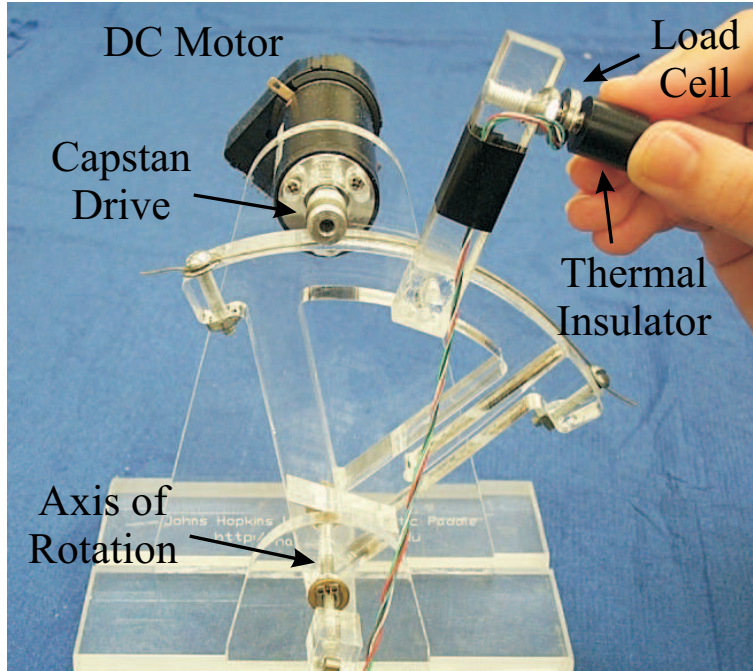


Figure 3.7: The modified Haptic Paddle used for virtual-wall passivity experiments.

in Appendix A, and the resulting parameters are $m = 0.037$ kg, $b = 0.15$ Ns/m, and $f_c = 0.12$ N ($r^2 = 0.95$). Using these parameter values, we compute $2b/T = 300$ N/m and $2f_c/\Delta = 10700$ N/m. Therefore, for our Haptic Paddle, the stiffest passive virtual wall that can be implemented is $K = 300$ N/m. For our system, the term based on viscous friction and sampling rate dominates over the term based on Coulomb friction and encoder resolution. Practically, we must increase the sampling rate of our system for any additional gains in wall stiffness.

It is interesting to note that, if we were to attempt to model our system as mass-damper system as in [20], the resulting least-squares fit would give $m = 0.036$ kg and $b = 0.41$ Ns/m, which would indicate that $K = 2b/T = 820$ N/m would be passive. But this stiffness is nearly three times too large, indicating that fitting a mass-damper model to our system could be detrimental in this setting. An r^2 value

of 0.92 verifies a poorer fit for the mass-damper model.

3.5.2 Experimental Results

In this section, we demonstrate that the passivity condition given in (3.5) is a good predictor of passive behavior in real systems. Specifically, violation of (3.16) is shown to result in unstable closed-loop systems, while violation of (3.22) is shown to generate active-tactile sensations.

We begin by exploring the physical implications of (3.16). Figure 3.8 shows interactions with a virtual wall with stiffness $K = 300$ N/m, which was predicted to be the stiffest possible passive wall for our system. The figure shows a *typical* touch, where the user holds the device at the load cell, moves at a moderate speed towards the wall, and then attempts to press against the wall with a constant force. The figure also shows a *malicious* touch, where the user learned how best to make the device vibrate against the wall. This was done by pressing much lower on the device, moving very quickly towards the wall, and matching the resonance frequency of the finger with that of the wall. Note that the user was attempting to touch the wall with a constant force; the oscillations seen are not the result of voluntary movement. At this wall stiffness, the user was unable to create sustained vibrations. This is evidence supporting the claim of passivity.

Virtual-wall passivity is only a sufficient condition for closed-loop stability, so requiring passivity of the virtual wall may potentially lead to conservative results – that is, the wall may be more compliant than is necessary for stability. With the

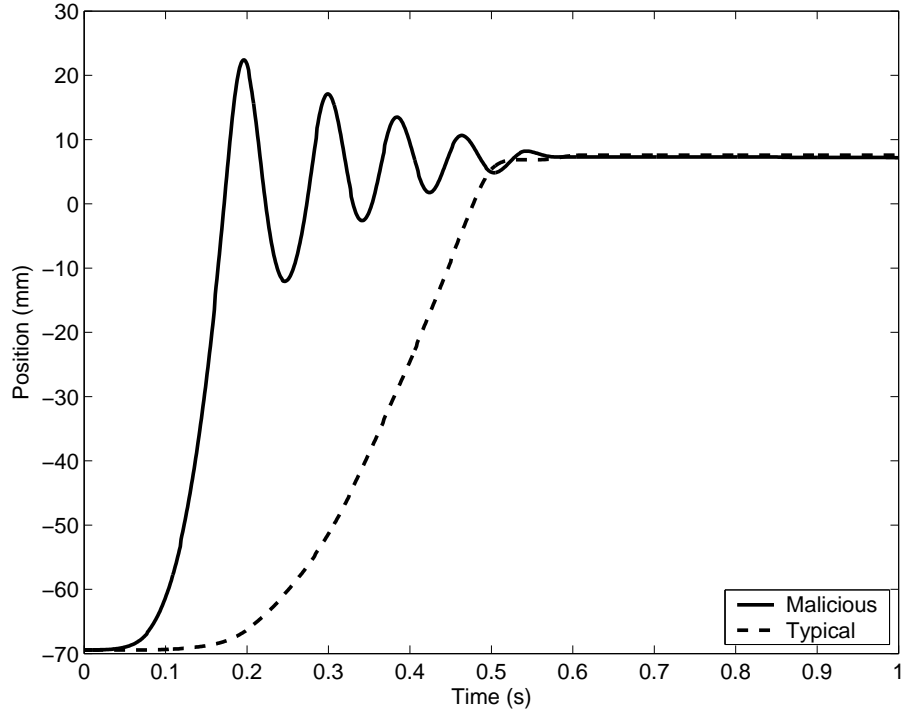


Figure 3.8: Experimental data resulting from typical and malicious touch with $K = 300$ N/m. Positive values correspond to virtual-wall penetration. This plot supports passivity.

malicious touch in Fig. 3.8, it took multiple bounces before the initial kinetic energy was dissipated. The virtual wall is clearly underdamped for some user actions. This is evidence supporting the condition on virtual-wall passivity as a useful measure of system stability (*i.e.*, it is not overly conservative).

Figure 3.9 shows interactions with a virtual wall with $K = 770$ N/m. The user was unable to create sustained oscillations by using the malicious strategy discussed above, but the response is more underdamped than that seen in Fig. 3.8. It appears, though, that more typical interactions with this wall are well behaved (as well behaved as the typical touch seen in Fig. 3.8). But when the user interacts with the haptic device through a wooden dowel, the the lower plot of Fig. 3.9

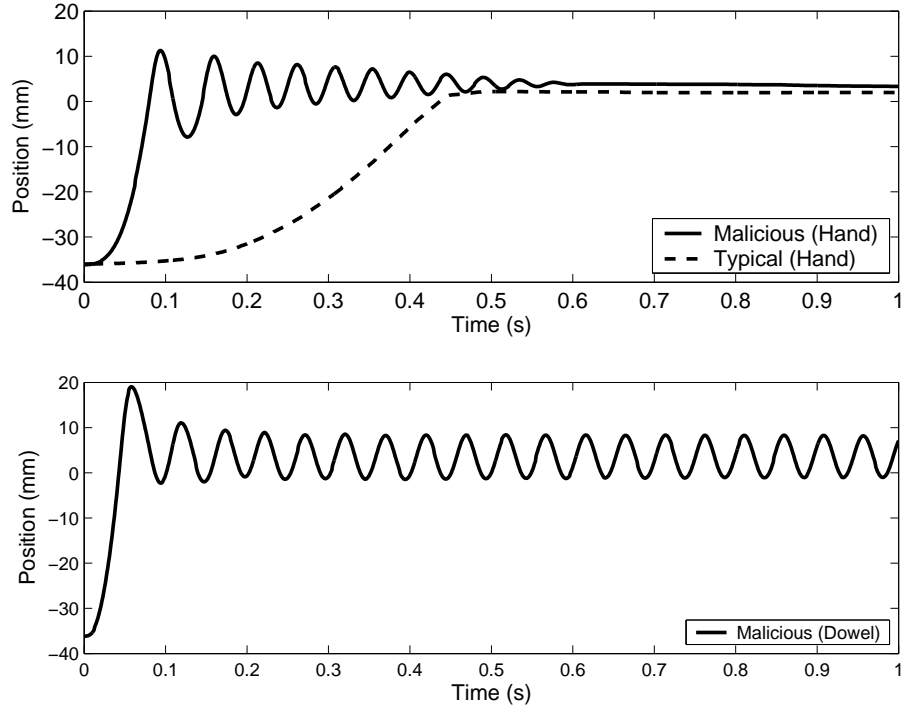


Figure 3.9: Experimental data resulting from typical and malicious touch with $K = 770$ N/m, and from a malicious touch with a wooden dowel for the same stiffness. Positive values correspond to virtual-wall penetration. The human finger can not exploit the active behavior at this stiffness.

clearly displays active behavior. This active behavior shows that this wall is not passive. The wooden dowel embodies an impedance that the human finger is unable to achieve. This stiffness is over twice as large as that predicted for passivity, but it is conceivable (even likely) that interacting with the virtual wall through other tools would push the difference between the predicted and experimentally validated passive stiffness values even lower. In Section 3.5.1, we found that modeling our device as a mass-damper, and then applying the passivity condition of [20], would result in a predicted passive stiffness of $K = 820$ N/m. It is clear that the upper-bound on passive virtual-wall stiffness for our system is below this value.

It is unlikely that any real interaction would ever create the conditions needed to generate energy (see Section 3.4.3) at stiffness just slightly greater than the upper bound for passivity, but Fig. 3.8 shows that system passivity may be a good predictor of possible undesirable behavior.

Next, we consider the physical implications of (3.22). For our system, we found that $2b/T$ was the limiting quantity, so our sampling rate must be increased to implement stiffer passive walls. But this may not be the case for other systems. To explore this notion, we now artificially lower the resolution of our encoder by a factor of 100, resulting in a maximum passive stiffness of $2f_c/\Delta = 107$ N/m.

The second necessary condition of Section 3.4.3 provides insight into the mode that the system will exhibit non-passivity. That necessary condition exploited very small movements that straddled an encoder pulse. In fact, we find that this is exactly how the system becomes non-passive, and the resulting active feeling destroys the illusion of reality during interaction with the virtual wall. Figure 3.10 shows a user interacting maliciously with three different virtual walls. In this case, a *malicious* interaction (that which most exploits non-passive behavior) is simply touching the wall very softly. For stiffness values of $K = 240$ N/m and $K = 120$ N/m, the user feels a buzzing sensation – an active behavior than no real (passive) environment would exhibit. For a stiffness of $K = 80$ N/m, the user was unable to create this phenomenon; the variance seen for this stiffness is simply due to the imprecision in human force control. In general, the energy content of the active behavior increases with increasing stiffness, as seen in the first two plots. Figure 3.11 shows experimen-

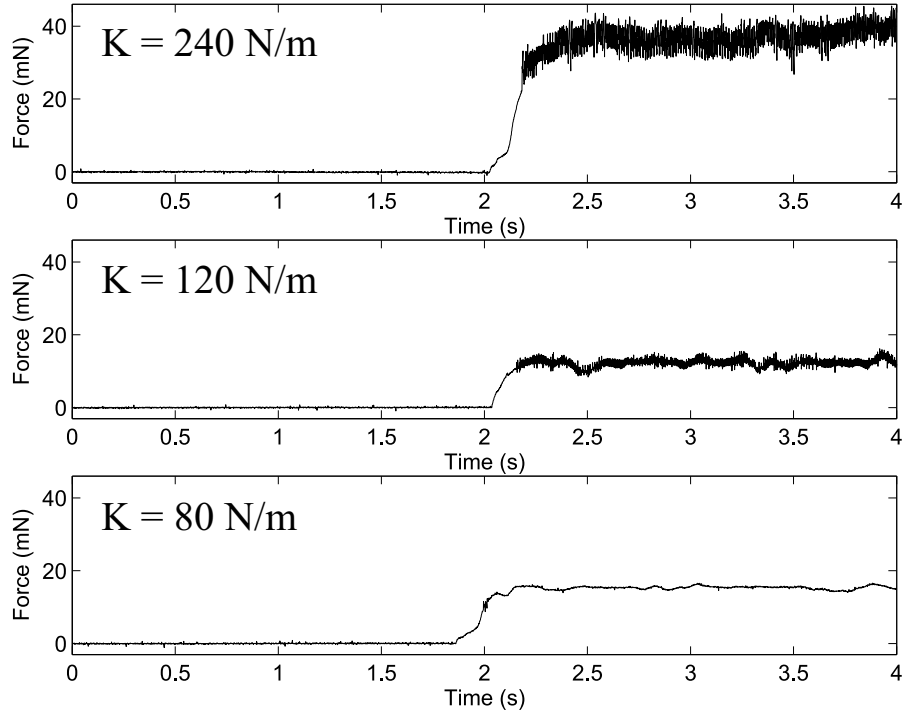


Figure 3.10: Experimental force data, measured by the load cell, resulting from malicious touch with three virtual-wall stiffness values. The user touched the virtual wall very softly at approximately the 2-second mark. This virtual wall behaves passively only for $K = 80 \text{ N/m}$.

tal data of a malicious touch for a stiffness of $K = 90 \text{ N/m}$. For our system, this appears to be near the limits of passive behavior. The user had to consciously work to exploit the non-passivity, as is evident in the plot. The corresponding position data confirms that the active behavior felt by the user is, in fact, due to straddling an encoder pulse.

The stiffness predicted by (3.5) is a good predictor of the limits on passivity due to quantization, but it slightly overestimated the actual boundary of passivity found experimentally. This is likely due to inaccuracies in our friction model. More comprehensive friction models than the Coulomb-plus-viscous friction model, such

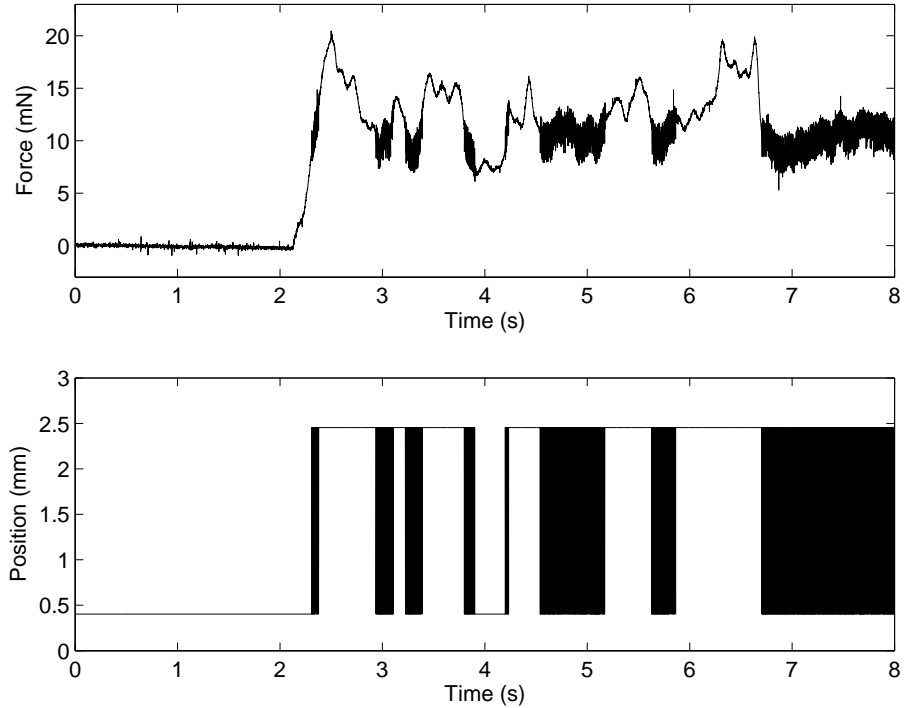


Figure 3.11: Experimental force data, measured by the load cell, resulting from malicious touch with $K = 90$ N/m. The user touched the virtual wall very softly at approximately the 2-second mark. This stiffness value appears to be the passivity limit for our system – it is difficult for the user to generate non-passive behavior. Position data confirms that non-passive behavior occurs when straddling an encoder pulse.

as that in [7], include hysteresis loops, due largely to potential energy stored at the asperity level. This can make friction appear to generate small amounts of energy when the device changes direction, although it is actually just the release of stored potential energy. The small periodic movements used to exploit non-passivity due to quantization may also be exploiting the inaccuracies in the model, making (3.5) slightly over-predict the achievable passive stiffness. It is also possible that obtaining an estimate of f_c through a method other than the pseudoinverse method would result in a more accurate model.

It is interesting to note that the two modes in which the system can become non-

passive experimentally appear to be largely decoupled. For the system with reduced encoder resolution, we repeated the experiment shown in Fig. 3.9, and we observed almost no change from the previous experiment (approximately 5%), even with a substantial difference in encoder resolution. This experiment was accompanied, though, by a high-frequency vibration, due to quantization, that was not felt in the experiment of Fig. 3.9. We performed an additional experiment where, for the system with reduced encoder resolution, we slowed down the sampling rate to $T = 0.003$ seconds, and repeated the experiment of Fig. 3.11. We observed a very small change in the boundary of passive behavior (approximately 10%), but the active behavior felt different – the vibrations were of lower frequency and larger magnitude.

The result of this experimental verification is that the passivity condition given in (3.5) is a good predictor of the limit in virtual-wall stiffness for desirable behavior in real systems. In addition, the two modes in which the system can behave non-passively correspond directly to the two motivations for passivity research that were introduced in Section 3.1 – creating stable coupled systems, and creating virtual environments that feel realistic. Physically, violation of (3.16) corresponds to non-passivity in a closed-loop-stability sense, while violation of (3.22) corresponds to non-passivity in an active-tactile sense.

3.6 Conclusions

We have given a simple explicit upper bound on virtual-wall stiffness that is necessary and sufficient for virtual-wall passivity. A passive user, interacting with such a wall, is incapable of generating sustained vibration. We considered a haptic display that can be modeled as an actuated mass with Coulomb-plus-viscous friction, but the condition also applies directly to a larger class of friction models that consider stiction. In addition, the sufficiency of the condition applies to an even larger class of friction models that consider nonlinear viscous friction. We explicitly considered the effects of a quantized position measurement. We also removed common assumptions about the human user and the sampling rate of the system. The results presented here show a decoupling of the effects of sampling rate and encoder resolution, and give useful design criteria for generating stiffer passive virtual walls. A simple experiment provided evidence that the results presented are applicable to real systems, and lead to a significant new (quantifiable) understanding of non-passive behavior in haptic devices implementing virtual walls.

In the next chapter, we show how passive virtual environments, such as the virtual wall developed here, can act as stable forbidden-region virtual fixtures for bilateral telemanipulation.

Chapter 4

Passively Combining Bilateral Telemanipulators and Virtual Environments

4.1 Introduction

In Chapter 2, we found that unwanted and potentially dangerous vibrations can occur as master and/or slave telemanipulator devices come into contact with virtual fixtures. We also found that the stability of the interaction is dependent on the human user's mechanical properties. As an alternative to the methods introduced in Chapter 2, in this chapter we consider passivity techniques. Passivity has become a popular analytical tool in the development of stable bilateral telemanipulators. Passivity techniques are based on energy concepts – a telemanipulator that is incapable

of generating energy is also incapable of sustained vibrations against a dissipative environment. Designing telemanipulators to be passive also avoids explicit modeling of the human user or slave environment – passivity of the user and environment is sufficient for closed-loop stability.

The use of virtual fixtures as task-assistance tools for telemanipulation is a nascent field of research. However, virtual fixtures are, in most cases, simply haptic virtual environments (VEs) overlaid on telemanipulators, and a large body of work exists considering haptic VEs, particularly their stability/passivity. This prior work was reviewed in Section 1.3.3. The result of Chapter 3 can be included here as well. One of the benefits of using passivity techniques in control system design is their modular nature – certain combinations of passive objects are known to be passive as well. In this chapter, we discuss stability issues involved with combining passive VEs with unconditionally stable bilateral telemanipulators, and we develop a framework in which we can synthesize and apply previous results in these two fields of research.

In Section 4.2 we discuss the implementation of passive haptic VEs. In Section 4.3 we discuss passivity and unconditional stability of bilateral telemanipulators. In Section 4.4, we discuss how to combine passive VEs and unconditionally stable bilateral telemanipulators to create a stable bilateral telemanipulator with virtual fixtures. This method generalizes to all VE/telemanipulator causalities (described below). In Section 4.5, we experimentally verify that the methods presented here result in systems that exhibit passive behavior. Finally, in Section 4.6, we discuss

the limitations of using passivity techniques for stability analysis, mainly their conservative nature, and we propose a method to improve system performance while still satisfying analytical passivity conditions.

4.2 Passive Virtual Environments

Many researchers have investigated the stability of haptic VEs, and the vast majority of stability techniques developed consider passivity of the VE – avoiding explicit modeling of the nonlinear and time-varying human operator. A summary of these passivity methods can be found in Section 1.3.3. Inanimate objects in the natural world are passive. When humans interact with a passive object in the natural world, active behavior never results. This makes it easy to distinguish between real environments and non-passive virtual environments. As discussed in Section 1.3.3, virtual environments that are designed as passive in a continuous-time framework can become non-passive once implemented as a sampled-data system [19, 29].

In general, there are four possible causality structures for a haptic device implementing a VE: the haptic device (*i.e.*, the robot) can be either of the impedance type (backdrivable, force-source actuator) or the admittance type (nonbackdrivable, velocity-source actuator), as discussed in Section 1.3.1, and the VE can be either of the impedance type (input velocity, output force) or the admittance type (input force, output velocity). To implement a mixed device/VE causality (*i.e.*, impedance/admittance or admittance/impedance), a virtual coupling must be used [6].

Most of the previous research on VE passivity has relied on the physical energy dissipation in the haptic device, so that the device implementing the VE appears passive at the driving point [4, 5, 6, 18, 20, 25, 64, 67, 68, 97]. Other researchers have designed the VE itself to be passive, without relying on the dissipation in the haptic device [30, 36, 84, 85]. The vast majority of previous work in VE passivity only considers the impedance/impedance causality.

Many researchers of VE and telemanipulator passivity have considered sampling effects, but few have explicitly considered sensor quantization effects in the passivity analysis [4, 5, 25]. This is an important topic for research, since velocity signals are typically constructed from quantized and sampled position signals, potentially leading to large amounts of noise [18]. This causes actual systems to behave differently from analytical predictions. In Chapter 3 we developed a virtual-wall passivity condition that accounts for sampling and quantization effects, and uses the dissipation in the haptic device to guarantee passivity at the driving point. In Section 4.6, we propose a new method to account for these sampled-data effects in a system passivity analysis.

4.3 Unconditionally Stable Bilateral Telemanipulators

In parallel to work on the stability of VEs, many researchers have investigated the stability of bilateral telemanipulators, as discussed in Section 1.3.2. Good results are

obtained using passivity techniques here as well – again, avoiding explicit modeling of the nonlinear and time-varying human operator and telemanipulated environment [8, 56, 73, 79, 86, 90, 91, 98, 110]. It can be shown that a passive telemanipulator, coupled to any passive human and passive environment, results in a stable closed-loop system, in an \mathcal{L}_2 sense [104]. That is, the force and velocity signals that define the power flow through the system do not grow unbounded.

In general, there are four possible causality structures for bilateral telemanipulators, as a consequence of the four combinations of impedance-type and admittance-type master and slave devices [37] (discussed in Section 1.3.1). The majority of the previous work in telemanipulation considers only the impedance/impedance causality. Most previous work includes the master and slave devices (and consequently, their dissipation) into the passivity analysis. One exception to this is [86], which considers passivity of the telemanipulator control system alone.

Requiring passivity of the telemanipulator may be too conservative, especially when power scaling is actually desired between the master and the slave devices. Requiring only *unconditional stability* generalizes, for telemanipulators with power scaling, the desirable closed-loop stability results obtained from requiring passivity [37]. A bilateral telemanipulator can be thought of as a two-port network, as shown in Fig. 4.1, where there are two distinct ports for energy exchange. Passivity of a two-port network is the necessary and sufficient condition for guaranteed stability of the closed-loop system resulting from terminating the two ports with any passive two-port network. Alternatively, *unconditional stability* of a two-port network is

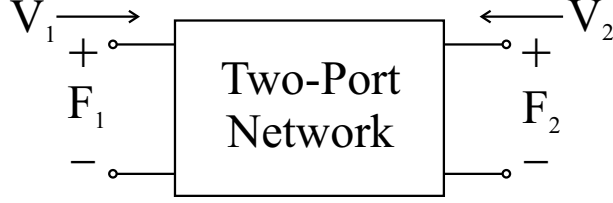


Figure 4.1: Two-port network. The instantaneous power flow into the network is given by $F_1V_1 + F_2V_2$.

the necessary and sufficient condition for guaranteed stability of the closed-loop system resulting from terminating the two ports with any two passive one-port networks [6, 37, 39]. Unconditional stability is sometimes referred to as “absolute stability,” but we use “unconditional stability” here to avoid confusion with an unrelated use of absolute stability in nonlinear system theory [48].

The two-port network of Fig. 4.1 can be written in at least one of four immittance matrices $\mathcal{P} = [p_{ij}]$ ($i, j \in \{1, 2\}$), such that the output vector \mathcal{O} is related to the input vector \mathcal{I} by $\mathcal{O} = \mathcal{P}\mathcal{I}$, and $\mathcal{O}^T\mathcal{I} = F_1V_1 + F_2V_2$ describes the instantaneous power flow into the two-port network. The four immittance matrices are the impedance, admittance, hybrid, and inverse hybrid matrices, respectively:

$$\begin{bmatrix} F_1 \\ F_2 \end{bmatrix} = \begin{bmatrix} z_{11} & z_{12} \\ z_{21} & z_{22} \end{bmatrix} \begin{bmatrix} V_1 \\ V_2 \end{bmatrix} \quad (4.1)$$

$$\begin{bmatrix} V_1 \\ V_2 \end{bmatrix} = \begin{bmatrix} y_{11} & y_{12} \\ y_{21} & y_{22} \end{bmatrix} \begin{bmatrix} F_1 \\ F_2 \end{bmatrix} \quad (4.2)$$

$$\begin{bmatrix} F_1 \\ V_2 \end{bmatrix} = \begin{bmatrix} h_{11} & h_{12} \\ h_{21} & h_{22} \end{bmatrix} \begin{bmatrix} V_1 \\ F_2 \end{bmatrix} \quad (4.3)$$

$$\begin{bmatrix} V_1 \\ F_2 \end{bmatrix} = \begin{bmatrix} g_{11} & g_{12} \\ g_{21} & g_{22} \end{bmatrix} \begin{bmatrix} F_1 \\ V_2 \end{bmatrix} \quad (4.4)$$

We now summarize the criteria for unconditional stability of a linear time-invariant (LTI) two-port network: an LTI two-port network is unconditionally stable if and only if

- the parameters p_{11} and p_{22} have no poles in the open right half plane,
- any poles of p_{11} and p_{22} on the imaginary axis are simple with real and positive residues, and
- the inequalities

$$\Re\{p_{11}\} \geq 0 \quad (4.5)$$

$$\Re\{p_{22}\} \geq 0 \quad (4.6)$$

$$2\Re\{p_{11}\}\Re\{p_{22}\} - \Re\{p_{12}p_{21}\} - |p_{12}p_{21}| \geq 0 \quad (4.7)$$

hold on the $j\omega$ axis for all $\omega \geq 0$.

The unconditional-stability criteria provide a powerful stability analysis tool for bilateral telemanipulation systems with any master/slave device causality, but the two-port network must be accurately modeled as LTI. Much of the previous work considers pure time delays in the communication channels (which can be modeled as LTI if they are constant), but very little research has been conducted that explicitly considers nonlinear time-varying (NLTV) sampling and quantization effects in bilateral telemanipulation [90, 91], though other methods could potentially be modified

to include these effects [86]. As previously noted, in Section 4.6, we propose a new method to account for these effects.

4.4 Combining Bilateral Telemanipulation and Virtual Environments

Virtual environments and telemanipulators have been combined in prior work, appearing under the name of “virtual fixtures,” “synthetic fixtures,” “virtual mechanisms,” and “haptically augmented telemanipulation,” as described in Section 1.3.4. This research considers various device/VE causalities: impedance/impedance [54, 78, 80], impedance/admittance [45, 66, 75, 102], admittance/admittance [1, 76], and admittance/impedance [43, 89] (in Section 2.3 we considered impedance/impedance and impedance/admittance). Sometimes the VE was implemented on the master side, and sometimes it was implemented on the slave side. From the different possible causality structures of the telemanipulator and VEs described above, there exist 16 possible causality structures for telemanipulators combined with VEs. Previous control implementations have been *ad hoc*, and without rigorous (if any) stability analysis. It is desirable to create an analytical stability method that generalizes to all 16 causality structures, so the method will not be as system-specific as prior work.

4.4.1 Impedance-Type Devices

The majority of previous work on system passivity considers impedance-type devices, so that is how we begin our discussion. It is logical that any passivity analysis should account for physical dissipation in the hardware. As discussed in Section 4.2, some current passivity techniques for VEs rely on physical dissipation in the haptic device, and some do not. Most passivity techniques for bilateral telemanipulation rely on physical dissipation in the master and slave manipulators. As we combine currently available passive systems, we must take care not to double count the dissipation in the hardware. Consequently, it is natural to think about combining an unconditionally stable telemanipulator (which includes the master and slave devices) with passive VEs, or combining passive haptic devices implementing VEs with an unconditionally stable telemanipulation controller.

First, we consider overlaying passive VEs on an unconditionally stable telemanipulator. We use the impedance device models:

$$F_h(s) - F_{am}(s) = F_h(s) - F_{tm}(s) - F_{mve}(s) = Z_m(s)V_m(s) \quad (4.8)$$

$$F_{as}(s) - F_e(s) = F_{ts}(s) - F_{sve}(s) - F_e(s) = Z_s(s)V_s(s) \quad (4.9)$$

where the master and slave actuator forces are separated into components due to the telemanipulator and the VEs, as shown in Fig. 4.2. Figure 4.2(a) demonstrates how passive VEs can easily be overlaid on an unconditionally stable telemanipulator. It makes use of an equivalent notation shown in Fig. 4.3, and the fact that a parallel combination of passive blocks (as in Fig. 4.3(a)) is itself passive [48]. Note that the VEs may be moved outside the telemanipulator for the purpose of analysis, although

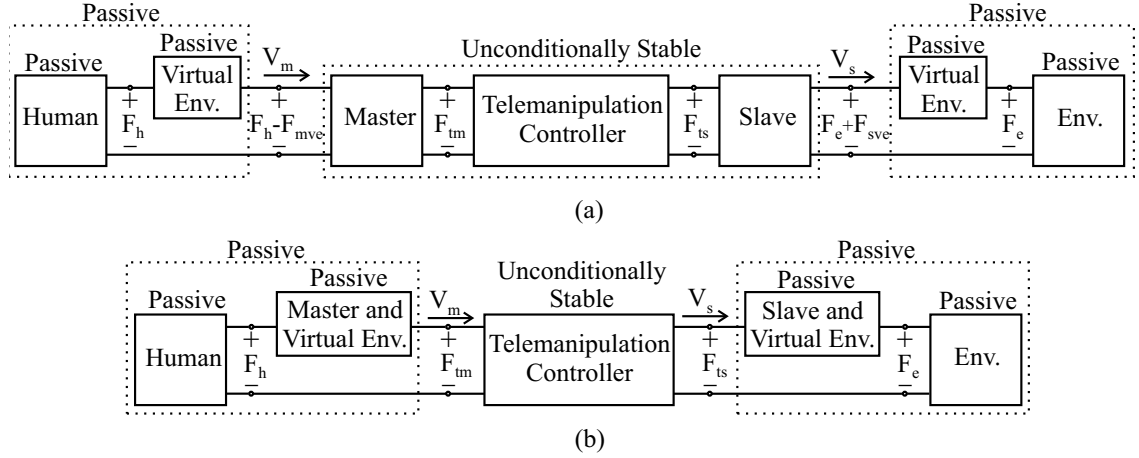


Figure 4.2: Network models for (a) passive VEs overlaid on an unconditionally stable telemanipulator, and (b) passive device/VEs combined with an unconditionally stable telemanipulation controller. These models assume impedance-type ports.

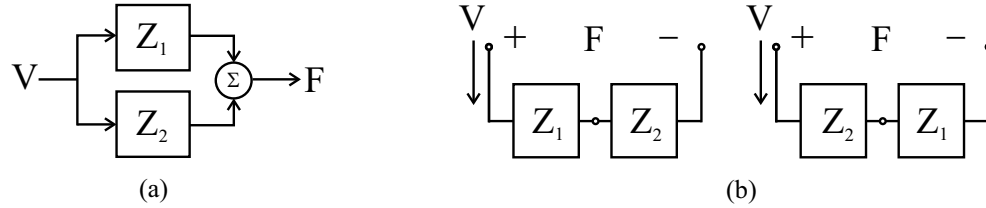


Figure 4.3: Parallel connection of impedance elements in (a) block diagram and (b) equivalent circuit notations.

they are physically implemented at the actuator.

Next we consider haptic devices implementing VEs, which are designed to be passive at the driving point, such as the system of Chapter 3. These are passively combined with an unconditionally stable telemanipulation controller as shown in Fig. 4.2(b). To rearrange the system in this way, we take advantage of the fact that we may consider the master and slave devices as either one-port networks or (constrained) two-port networks.

It is also possible to implement one type of passive VE on the master, and another on the slave. Additionally, one may implement admittance-type VEs on

one or both of the master and slave devices; this simply requires a virtual coupling to be included as part of the VE [6]. This idea is pursued in Chapter 5.

4.4.2 Admittance-Type Devices

Admittance-type devices must be considered differently than the impedance-type devices of the previous section. Because of the assumptions of the admittance model, it no longer makes sense to think about the manipulators being separate from, and acted upon by, the telemanipulation controller. We also may not simply sum the forces due to the telemanipulator and the VE. When implemented, the VE admittance and the telemanipulator admittance (which is really just another programmed VE) are combined in parallel. As with impedance-type devices, the device velocity is still the common variable shared between the telemanipulator and the VE, but now the velocity is the output of the controller, and is completely controlled under the assumptions of admittance control.

Figure 4.4 shows how we can think about admittance-type telemanipulators implementing VEs. We design the entire two-port network, consisting of the telemanipulator and any VEs, to be unconditionally stable. The two ports for energy exchange are the force sensors on the master and the slave. It is also possible to implement a telemanipulator with an admittance-type master (slave) and an impedance-type slave (master). In this case, the VE on the impedance-type device can still be considered in either of the two ways discussed in Section 4.4.1.

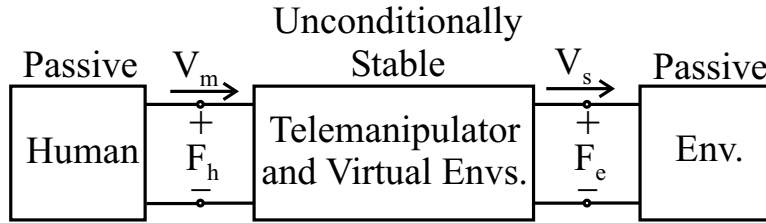


Figure 4.4: Under the assumptions of admittance control, the telemanipulator and the virtual environments are considered as one system. Unconditional stability of the entire admittance-type system is the appropriate design goal.

4.5 Experimental Demonstration

In this section, we apply the method discussed above to the 1-DOF bilateral telemanipulation system based on modified Haptic Paddles (Fig. 2.5). This is the same experimental system used in Chapters 2 and 3, and it is described in detail in Appendix A.

Let us consider the application of a forbidden-region virtual fixture (FRVF) to the master side of the telemanipulator. The FRVF will be implemented as a passive virtual wall, using the methods of Chapter 3. This technique will make the master device implementing the virtual wall passive. We will then design the two-port system consisting of the telemanipulation controller and the slave device to be unconditionally stable. As discussed above, this will result in a stable closed-loop system when combined with any passive human and environment. Figure 4.5 illustrates our design approach.

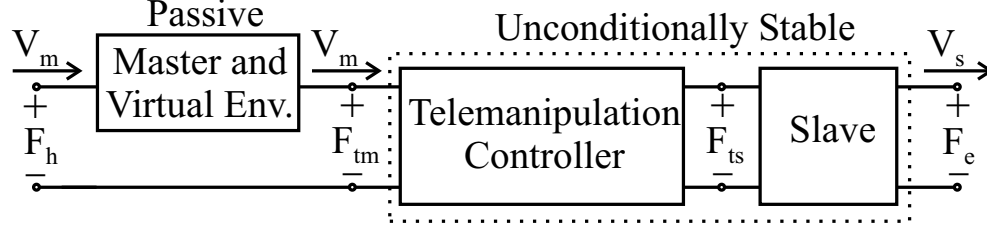


Figure 4.5: A master device passively implementing a virtual wall, coupled to an unconditionally stable two-port network consisting of the slave device and the telemanipulation controller. This system is stable when coupled to any passive human and environment.

4.5.1 Unconditional Stability

We begin by ensuring the unconditional stability of the two-port network consisting of the telemanipulation controller and the slave device. We model the slave as a mass-damper system being acted upon by the slave actuator force due to the telemanipulation controller, F_{ts} , as well as an external environmental force F_e :

$$F_{ts}(s) - F_e(s) = (m_s s + b_s) V_s(s) \quad (4.10)$$

We will implement a control law where the slave servos to the master with a PD controller, and the master servos to the slave with an identical PD controller. The telemanipulation controller forces applied to the slave and master, respectively, are:

$$F_{ts}(s) = \left(\frac{\frac{2}{T}}{s + \frac{2}{T}} \right) (K_{ds} s + K_{ps}) \left(\frac{V_m(s) - V_s(s)}{s} \right) \quad (4.11)$$

$$F_{tm}(s) = \left(\frac{\frac{2}{T}}{s + \frac{2}{T}} \right) (K_{dm} s + K_{pm}) \left(\frac{V_m(s) - V_s(s)}{s} \right) \quad (4.12)$$

We have included a low-pass filter approximation for the ZOH associated with these two controller forces:

$$G_{ZOH}(s) = \frac{\frac{2}{T}}{s + \frac{2}{T}} \quad (4.13)$$

where T is the sampling period of the system. This approximation captures the lagging effects of the ZOH, assuming that the sampling rate of the system is sufficiently fast [27].

We use the hybrid matrix to represent our two-port network of interest (Fig. 4.5):

$$\begin{bmatrix} F_{tm} \\ -V_s \end{bmatrix} = \begin{bmatrix} h_{11} & h_{12} \\ h_{21} & h_{22} \end{bmatrix} \begin{bmatrix} V_m \\ F_e \end{bmatrix} \quad (4.14)$$

The four hybrid matrix transfer functions are found as:

$$h_{11}(s) = \frac{\frac{2}{T}(K_{dm}s + K_{pm})(s^2 + \alpha_1s + \alpha_2 + \beta_1)}{(s + \frac{2}{T})(s^3 + \alpha_1s^2 + \alpha_2s + \alpha_3)} \quad (4.15)$$

$$h_{12}(s) = \frac{\frac{2}{T}(K_{dm}s + K_{pm})(\gamma_1s + \gamma_2)}{(s + \frac{2}{T})(s^3 + \alpha_1s^2 + \alpha_2s + \alpha_3)} \quad (4.16)$$

$$h_{21}(s) = \frac{\beta_1s + \beta_2}{s^3 + \alpha_1s^2 + \alpha_2s + \alpha_3} \quad (4.17)$$

$$h_{22}(s) = \frac{\gamma_1s^2 + \gamma_2s}{s^3 + \alpha_1s^2 + \alpha_2s + \alpha_3} \quad (4.18)$$

where

$$\alpha_1 = \frac{2}{T} + \frac{b_s}{m_s} \quad (4.19)$$

$$\alpha_2 = \frac{2b_s}{m_sT} + \frac{2K_{ds}}{m_sT} \quad (4.20)$$

$$\alpha_3 = \frac{2K_{ps}}{m_sT} \quad (4.21)$$

$$\beta_1 = -\frac{2K_{ps}}{m_sT} \quad (4.22)$$

$$\beta_2 = -\frac{2K_{ds}}{m_sT} \quad (4.23)$$

$$\gamma_1 = \frac{1}{m_s} \quad (4.24)$$

$$\gamma_2 = \frac{2}{m_sT} \quad (4.25)$$

We can now apply the unconditional stability criteria. We first must ensure that $h_{11}(s)$ and $h_{22}(s)$ have no poles in the right half plane. To accomplish this, we use Routh's stability criterion [27] on the denominators of $h_{11}(s)$ and $h_{22}(s)$, resulting in four conditions:

$$K_{ps} > 0 \quad (4.26)$$

$$K_{ps} < (b_s + K_{ds}) \left(\frac{2}{T} + \frac{b_s}{m_s} \right) \quad (4.27)$$

$$K_{ps} < \frac{b_s}{m_s} \left(2b_s + K_{ds} + \frac{2m_s}{T} \right) + \frac{2}{T} \left(3b_s + K_{ds} + \frac{4m_s}{T} \right) \quad (4.28)$$

$$0 < \left(\left(\frac{4}{T} + \frac{b_s}{m_s} \right) \left(2b_s + K_{ds} + \frac{2m_s}{T} \right) - \left(K_{ps} + \frac{2b_s}{T} + \frac{2K_{ds}}{T} \right) \right) \cdot \left(K_{ps} + \frac{2b_s}{T} + \frac{2K_{ds}}{T} \right) - m_s K_{ps} \left(\frac{4}{T} - \frac{b_s}{m_s} \right)^2 \quad (4.29)$$

The last equation is quadratic in K_{ps} , and is easily solved numerically. We also assure that there are no poles of $h_{11}(s)$ or $h_{22}(s)$ on the imaginary axis by our use of strict inequalities in (4.26)-(4.29).

The slave mass and damping are $m_s = 0.036$ kg and $b_s = 0.49$ Ns/m (Appendix A). To generate an illustrative example, we will only consider a sampling period $T = 0.001$ seconds and derivative gains $K_{ds} = K_{dm} = 2$ Ns/m, and then find the stiffest possible $K_{ps} = K_{pm}$ for unconditional stability. Using these values, (4.26)-(4.29) result in necessary bounds on K_{ps} : $0 < K_{ps} < 5013$ N/m.

Finally, we must verify that (4.5)-(4.7) hold. This is also accomplished by numerically evaluating these quantities for $0 < K_{ps} < 5013$ N/m, and determining what proportional-gain values violate any of the three conditions. For our system, this limit is $K_{ps} = K_{pm} = 3990$ N/m. Figure 4.6 shows the numerical results of the unconditional stability criteria (4.5)-(4.7) for $K_{ps} = K_{pm} = 3990$ N/m. All three

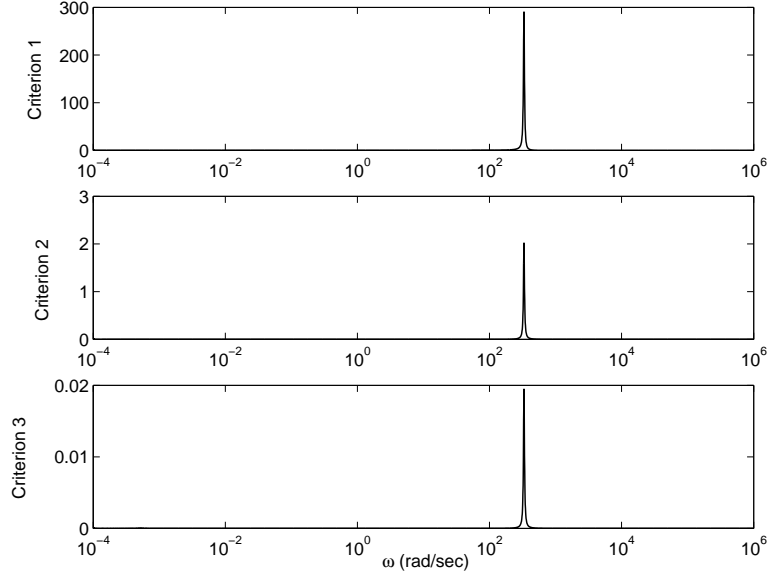


Figure 4.6: Unconditional stability criteria for two-port network consisting of slave device and telemanipulation controller with $K_{ds} = K_{dm} = 2$ Ns/m, $K_{ps} = K_{pm} = 3990$ N/m, and $T = 0.001$ seconds. Criteria 1-3 correspond to (4.5)-(4.7), respectively. This system is unconditionally stable.

criteria remain positive for all positive ω values. Thus, $K_{ds} = K_{dm} = 2$ Ns/m and $K_{ps} = K_{pm} = 3990$ N/m result in unconditional stability for our system. Qualitatively, these plots are typical of this method. As seen, it is not actually necessary to evaluate the criteria numerically up to $\omega = \infty$; the value of the quantities asymptote to zero if the conditions are not violated. Figure 4.7 shows the numerical results for (4.5)-(4.7) after increasing the proportional gains to $K_{ps} = K_{pm} = 4000$ N/m. It is clear that the third criterion is violated, indicating that this system is not unconditionally stable.

Now that we are equipped with an unconditionally stable telemanipulation controller/slave, we can design a passive master/FRVF using the method of Chapter 3. From Chapter 3, we know that the stiffest passive virtual wall that we can implement on our master device is $K_{mVF} = 300$ N/m. We can combine this FRVF

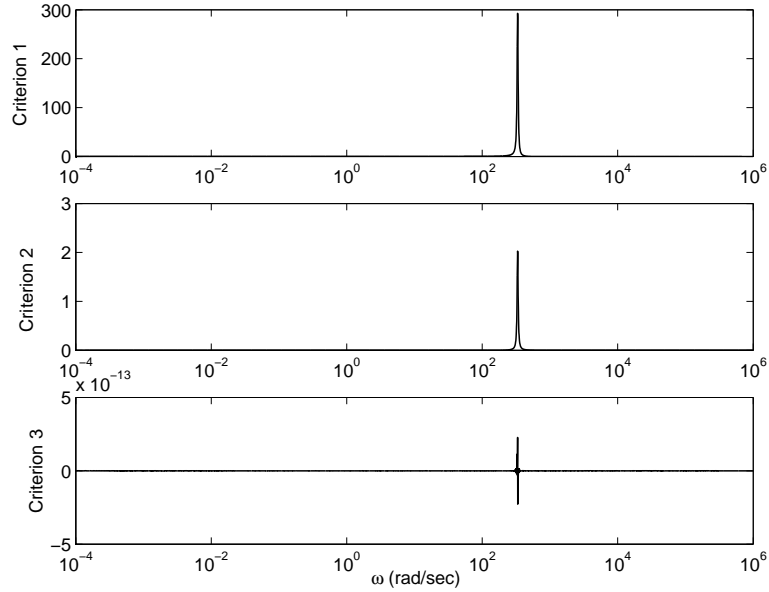


Figure 4.7: Unconditional stability criteria for two-port network consisting of slave device and telemanipulation controller with $K_{ds} = K_{dm} = 2$ Ns/m, $K_{ps} = K_{pm} = 4000$ N/m, and $T = 0.001$ seconds. Criteria 1-3 correspond to (4.5)-(4.7), respectively. This system is not unconditionally stable.

with the telemanipulation controller designed above to create a telemanipulator with virtual fixtures that is guaranteed to be stable when interacting with any passive environment (whenever the human behaves passively).

4.5.2 Results

Figure 4.8 shows evidence of passivity for a user interacting with the unconditionally stable system of Fig. 4.6. As discussed in Chapter 3, it is impossible to prove passivity experimentally, but it is possible to demonstrate non-passive behavior. Figure 4.8 shows three interactions with the FRVF with stiffness $K_{mVF} = 300$ N/m. In the first plot, the user moves the master device towards the FRVF at a moderate speed, and then applies a moderate force, with his index finger through

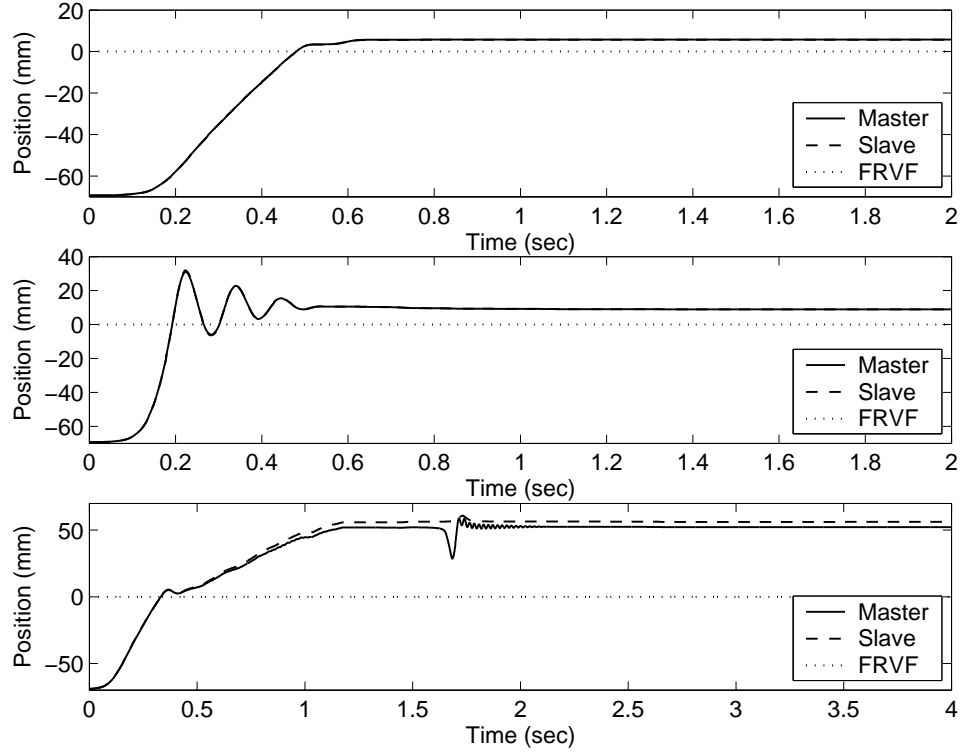


Figure 4.8: Interaction with a master-side FRVF with $K_{mVF} = 300$ N/m, $K_{ds} = K_{dm} = 2$ Ns/m, $K_{ps} = K_{pm} = 3990$ N/m, and $T = 0.001$ seconds. (top) A typical interaction where the user applies a moderate force to the FRVF with a finger through the finger loop. (middle) A malicious interaction where the user attempts to create non-passive behavior by applying a force low on the master device. (bottom) A malicious interaction where the slave is pulled into the forbidden region, saturating the slave actuators, and the master is then impulsively disturbed at approximately the 1.7-second mark. No non-passive behavior was demonstrated with this system.

the Velcro finger loop. In the second plot, the user attempts to make the system exhibit non-passive behavior. This data was recorded after the user had ample time to practice with the system, and determine what malicious strategy would make the system behave in the most oscillatory way. In this case, the malicious forcing strategy was to move the master quickly towards the FRVF, while applying a force low on the master device, and then attempting to match the impedance of the finger with the impedance of the FRVF. In the third plot, the hand was completely

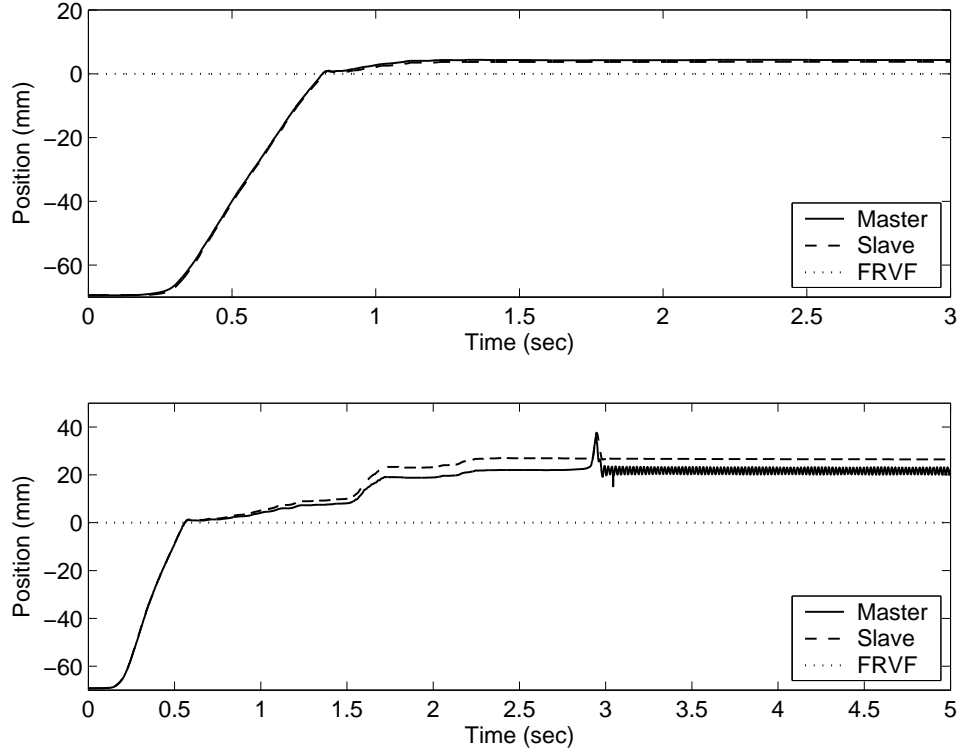


Figure 4.9: Interaction with a master-side FRVF with $K_{mVF} = 900$ N/m, $K_{ds} = K_{dm} = 2$ Ns/m, $K_{ps} = K_{pm} = 3990$ N/m, and $T = 0.001$ seconds. (top) A typical interaction where the user applies a moderate force to the FRVF with a finger through the finger loop. (bottom) A malicious interaction where the slave is pulled into the forbidden region, saturating the slave actuators, and the master is then impulsively disturbed at approximately the 2.9-second mark. This disturbance results in a demonstration of non-passive behavior.

removed from the master, and the slave was pulled into the forbidden region so far as to saturate the slave actuator. The master was then impulsively disturbed. In all three cases, the system demonstrated dissipative behavior; this is evidence supporting the passivity of the system as seen by the user.

Figure 4.9 shows the effect of increasing the FRVF stiffness to $K_{mVF} = 900$ N/m, with all other system parameters constant. The forcing methods applied by the user for these two plots correspond to the first and third plots in Fig. 4.8, respectively. With a typical touch, this system behaves much like one with a lower value of K_{mVF} .

However, saturating the slave actuator by pulling it into the forbidden region and then impulsively disturbing the master device is a malicious strategy that does invoke non-passive behavior in this system. Thus, we can definitely say that the true limit for the stability of our system with $K_{ds} = K_{dm} = 2$ Ns/m and $K_{ps} = K_{pm} = 3990$ N/m is $K_{mVF} < 900$ N/m. This means that the value $K_{mVF} = 300$ N/m may be conservative by as much as a factor of three, but it is impossible to experimentally determine where the exact stability limit is.

It may at first seem that saturating the actuators of our system violates the model used in our analysis, but this is not the case. Since the system must stably interact with any passive environment, we may also include a vise which passively prohibits any slave motion. From the point of view of the master, it is indistinguishable if the slave loses control authority due to actuator saturation or externally applied loads. In both cases, master movements have no effect on the slave, and are therefore not fed back to the master through the closed-loop. Thus, saturating the slave actuator simulates the slave coupled with an infinitely stiff passive environment.

4.6 Discussion

We demonstrated that notions of passivity and unconditional stability can be used to design telemanipulators and virtual environments in a modular way, such that their combination will result in a stable system. The method appears to be conservative, based on observations of our experimental system. This is not surprising; analytical stability methods that rely on passivity are typically only sufficient

for stability, and are therefore conservative.

The design process using the methods presented in this chapter is slightly different than the way we might typically like to think about virtual fixture design. In Section 2.4, we began with an existing well-designed telemanipulator, and then overlaid the stiffest possible stable FRVF on the existing system. We found that the FRVFs could be made significantly stiffer than the underlying telemanipulator. However, that is not the case with the passivity method presented here. If we were to consider our experimental telemanipulator above, but lower the proportional gains to $K_{ps} = K_{pm} = 1000$ N/m, we would find that the telemanipulation controller/slave two-port is unconditionally stable (note that this is a binary test), but we would still require that our master FRVF have a stiffness of only $K_{mVF} = 300$ N/m. This is counter-intuitive, and in fact, we find that we can increase the FRVF to $K_{mVF} = 3800$ N/m before a malicious strategy creates a non-passive behavior like that seen in Fig. 4.9 (bottom). It is interesting to note that by decreasing the telemanipulator stiffness by approximately 3000 N/m, we experimentally find that we can increase the FRVF stiffness by approximately 3000 N/m. This agrees with the model of Section 2.4, where the maximum stable FRVF stiffness was a function of the sum of the telemanipulator stiffness and the FRVF stiffness. This indicates that the unconditionally stable system with $K_{ps} = K_{pm} = 1000$ N/m actually has excess dissipation that can be utilized by the master implementing the FRVF.

We must account for this excess dissipation in order to design systems that simultaneously provide good performance and guaranteed stability. It is possible to

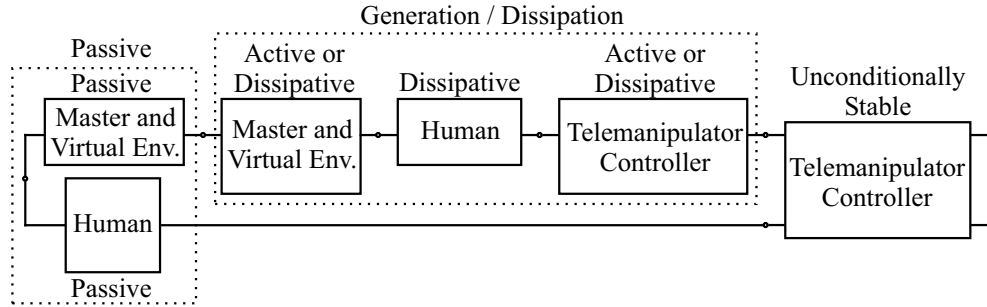


Figure 4.10: Master side of Fig. 4.2(b), with energy generation/dissipation explicitly considered.

separate passive system elements – such as the human, master device, *etc.* – into two components: a dissipative component, and a passive (and possibly lossless) component [64, 68]. Equivalently, we can separate an active element into two components: an active component, and a passive (and possibly lossless) component. Figure 4.10 shows the master side of Fig. 4.2(b), after rewriting the system with these considerations. By using the equivalent notations shown in Fig. 4.3, we are able to rearrange the system elements so that all of the possible energy generation and dissipation blocks are together, each with a defined impedance. Passivity of the Generation/Dissipation element (there will be one at each port) is sufficient for system stability. Also, note that failure to account for the dissipation in the human will lead to conservative results, but performance will almost certainly suffer, as discussed in Section 2.4, and shown in Fig. 2.21. From the index finger data of Fig. 2.11, we find that a minimum dissipation of 1.4 Ns/m could safely be assumed for the user’s index finger; this could be incorporated into our system passivity analysis if the system was only active when the user’s finger was in the finger loop.

As shown, passively combining telemanipulators and VEs is straightforward in

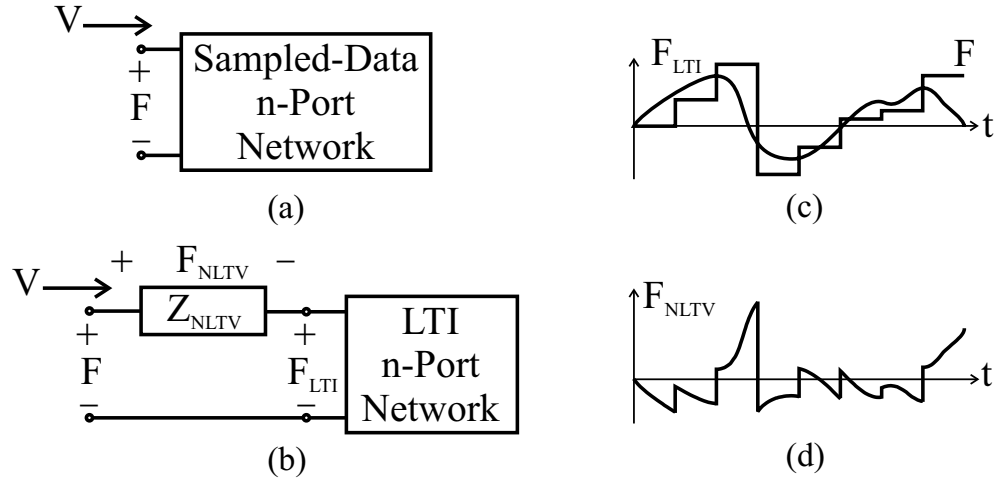


Figure 4.11: (a) An impedance-type port of a sampled-data n-port network, (b) separated into its (passive-by-design) LTI n-port network, and an NLTV impedance that captures the difference between the LTI force F_{LTI} expected from the velocity V , and the actual sampled-data force F . Plot (c) shows an F associated with a typical F_{LTI} , and (d) shows F_{NLTV} . The instantaneous power entering the NLTV impedance is found by the inner product of F_{NLTV} and V .

the continuous-time case. One tends to design VEs and bilateral telemanipulation controllers as continuous-time LTI systems (because of ties to physical intuition), but then actually implement them as sampled-data systems. In Section 4.5, we did not account for quantization effects in the telemanipulation controller (though we did account for them in the passive virtual wall), and we modeled the effect of the ZOH as a low-pass filter in the unconditional stability analysis. As demands on system performance increase, we must accurately account for sampling and quantization effects in our passivity analysis.

We propose a method to accomplish this as follows. As shown in Fig. 4.11, an impedance-type port of a sampled-data n-port network can be separated into two components: the desired LTI system seen at the port, and an NLTV component that captures every discrepancy between the actual system and the desired LTI system.

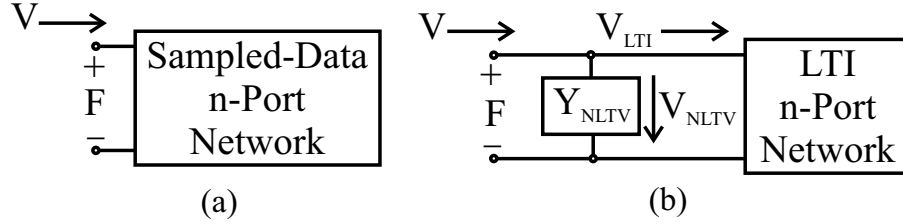


Figure 4.12: (a) An admittance-type port of a sampled-data n-port network, (b) separated into its (passive-by-design) LTI n-port network, and an NLTV admittance that captures the difference between the LTI velocity V_{LTI} expected from the applied force F , and the actual velocity V .

While it does not make sense to separate the VE from other control systems acting on an admittance-type device, we may still handle sampling and quantization effects as described above. Consider Fig. 4.12, where an admittance-type port is separated into its LTI model and an NLTV element that captures any discrepancies between the actual and predicted velocities.

This leads us to an interesting problem for future research: quantifying the energetic behavior of the NLTV elements associated with a sampled-data n-port network. This may be as simple as bounding the behavior. Figure 4.11(d) shows the type of forces that may be generated across the NLTV impedance for a typical continuous-time velocity. For the admittance system, we could construct a plot of V_{NLTV} much like that of Fig. 4.11(d). Understanding the energetic behavior of these NLTV system elements could be the key to using passivity methods to create stable systems, combining telemanipulators and VEs, that provide optimal performance.

It is also interesting to note that, under the passivity considerations above, the maximum stiffness of the telemanipulator allowed (*i.e.*, K_{ps}) is significantly stiffer than the provably passive FRVF stiffness. In fact, for our system, the telemanipu-

lator is an order of magnitude stiffer than the FRVF. This may make proxy-based FRVFs (that is, admittance-type FRVFs) a desirable alternative to impedance-type FRVFs (*i.e.*, virtual walls). Under proxy-based FRVFs, K_{ps} is the stiffness of the FRVF, which we are allowed to make relatively high for our system while maintaining stability robustness.

4.7 Conclusions

In this chapter, we presented a framework in which the problem of stably combining bilateral telemanipulators and virtual environments can be approached, using notions of passivity and unconditional stability. It was shown that we can design complicated systems in a modular way, allowing rigorous analysis of virtual environment/telemanipulator systems with various underlying physical properties and control methods (*i.e.*, impedance or admittance). We experimentally verified that the method presented works on a real system with unmodeled effects, and noted that the method is conservative. Finally, we proposed a technique to quantify (bound) the energetic difference between the LTI system elements that are designed and the actual sampled-data system elements that are implemented. Stability can be ensured with less degradation of performance if these energetic differences are understood. This approach to system modeling and analysis provides a needed and well-defined future research direction for those interested in creating robustly stable, high-performance systems that contain both bilateral telemanipulation and virtual environments.

Chapter 5

Pseudo-admittance Bilateral

Telemanipulation with Guidance

Virtual Fixtures

5.1 Introduction

In this chapter, we present a novel bilateral telemanipulation scheme that we call Pseudo-admittance Bilateral Telemanipulation, or simply Pseudo-admittance control. Pseudo-admittance control mimics admittance control, where the velocity of the robot is proportional to the applied force, on a telemanipulation system with an impedance-type master device. The method generalizes to systems with slave manipulators of either the impedance or admittance type. Pseudo-admittance control is designed to have asymmetries that provide desirable steady-hand characteristics

– in that high-frequency movements of the master are attenuated at the slave – but still allow for high-fidelity force feedback from the slave to the master. Pseudo-admittance control also exhibits quasi-static transparency. That is, the system has static equilibrium points if and only if there is perfect position correspondence between the master and the slave, and the (possibly scaled) slave/environment interaction force is perfectly reflected to the user. In addition, this property is closely approximated when the system is moving slowly. The structure of the Pseudo-admittance controller also lends itself to the implementation of so-called passive guidance virtual fixtures (introduced in Section 1.3.4). When implementing guidance virtual fixtures via Pseudo-admittance control, we retain quasi-static transparency in both the constrained and the unconstrained directions. This property is unique amongst previous implementations of guidance virtual fixtures.

Because Pseudo-admittance control does not require admittance-type hardware, one benefit of this controller is the ability to overlay it on existing impedance-type telemanipulators that have been designed for stability and transparency, as discussed in Section 1.3.2; the Pseudo-admittance controller can then be turned on and off as desired. Pseudo-admittance control has potential benefits on tasks that require better-than-human levels of precision. It also has potential benefits on systems that are traditionally run under rate control because either the workspace of the slave is much larger than the workspace of the master or the slave device has restrictive velocity saturation limits.

One of the potential uses of guidance virtual fixtures under Pseudo-admittance

control is as task-specific macros that would allow a user to quickly and safely conduct structured tasks. Some research has investigated autonomous macros for surgical tasks, but guidance virtual fixtures provide an additional degree of operator control. For example, a virtual ruler could be used to move the slave in a straight line or on a flat plane. Guidance virtual fixtures could also potentially assist in suturing tasks for minimally-invasive surgery (MIS) [46]. For bone drilling tasks, to avoid damage to the bit, the drill should only be moved axially once the drilling begins [26]; guidance virtual fixtures could be used in this application. Researchers have investigated remote-center-of-motion robotic movements for needle placement [13]; guidance virtual fixtures could be used for this type of task as well. Another guidance virtual fixture could then be used to assist in the needle insertion after the alignment.

We present Pseudo-admittance Bilateral Telemanipulation in Section 5.2, and detail its defining characteristics. In Section 5.3, we explain how guidance virtual fixtures can be incorporated into the Pseudo-admittance controller. We verify the properties of Pseudo-admittance control with and without guidance virtual fixtures through experiment and simulation in Section 5.4. For the duration of this chapter, scalar quantities are represented by lower-case letters, and matrix quantities (including vectors) are represented by upper-case letters.

5.2 Pseudo-admittance Bilateral Telemanipulation

In this section we present a novel bilateral telemanipulation control method called “Pseudo-admittance.” Pseudo-admittance control is designed to mimic the following admittance-type control system:

$$\dot{X}_s = \dot{X}_m = K_a(F_h + \gamma_f F_e) \quad (5.1)$$

where \dot{X}_m and \dot{X}_s are the master and slave velocities, respectively, F_h and F_e are the applied human and slave/environment forces, respectively, γ_f is a force scaling gain, and K_a is a user-defined diagonal admittance gain matrix that relates the applied forces to the resulting robot velocity. This type of admittance control law (also known as proportional-velocity control) has previously been explored with the Johns Hopkins University Steady Hand Robot [81, 82] – a human-machine cooperative system – as well as with an admittance-type haptic device known as the HapticMaster [103]. The admittance control of (5.1) can be accomplished directly if both the master and slave devices are of the admittance type, but many telemanipulators (particularly those designed for MIS) are of the impedance type – this motivates our work.

Pseudo-admittance bilateral telemanipulation is proxy-based controller that works as follows: a proxy exists in software, the slave robot servos to the proxy, the master servos to the slave, the measured environmental force F_e is scaled and fed directly to the master, and the proxy moves as a function of the error between the master and the slave positions. Pseudo-admittance control has some very desirable system properties:

- it mimics admittance control on impedance-type devices, and can be overlaid on existing telemanipulation systems with impedance-type masters
- it exhibits quasi-static transparency
- stability is maintained even with tight servo loops on the master and slave
- it can generate large slave/environment interaction forces regardless of gains in the slave servo loop
- it exhibits steady-hand properties that attenuate user hand tremor
- it is easily modified to include guidance virtual fixtures

5.2.1 Control System

We begin with the system model. The master and slave devices we consider are assumed to be serial-link robots with dynamics

$$M_m(\Theta_m)\ddot{\Theta}_m + N_m(\Theta_m, \dot{\Theta}_m) = \Upsilon_{am} + J_m^T(\Theta_m)F_h \quad (5.2)$$

$$M_s(\Theta_s)\ddot{\Theta}_s + N_s(\Theta_s, \dot{\Theta}_s) = \Upsilon_{as} + J_s^T(\Theta_s)F_e \quad (5.3)$$

where Θ_m and Θ_s are the master and slave joint variables, M_m and M_s are the positive-definite master and slave inertia matrices, N_m and N_s are vectors containing Coriolis and centrifugal terms, as well as gravity effects and joint friction, Υ_{am} and Υ_{as} are the master and slave joint actuator forces/torques, F_h is the force applied by the human to the master end effector, F_e is the environmental force applied to the slave end effector (expressed in the same frame as F_h), and J_m and J_s are the

master and slave velocity Jacobians (expressed in the same frame as the applied forces).

Using the linearizing and decoupling control law described in the Appendix D, we assume a model

$$\ddot{X}_m = F_{cm} + M_{xm}^{-1}(\Theta_m)F_h \quad (5.4)$$

$$\ddot{X}_s = F_{cs} + M_{xs}^{-1}(\Theta_s)F_e \quad (5.5)$$

where X_m and X_s are the Cartesian positions of the master and slave end effectors, M_{xm} and M_{xs} are the master and slave Cartesian inertia matrices, and F_{cm} and F_{cs} are the Cartesian master and slave controller forces.

For the slave controller, we command the slave to servo to the proxy, using proportional control with velocity feedback:

$$F_{cs} = K_{ps}(X_p - X_s) - K_{ds}\dot{X}_s \quad (5.6)$$

X_p is the position of the proxy (more details about the proxy will soon follow). K_{ps} and K_{ds} are the positive-definite proportional and derivative control matrices. In fact, we will assume an isotropic servo controller that can be written in the form

$$K_{ps} = k_{ps}I \quad (5.7)$$

$$K_{ds} = k_{ds}I \quad (5.8)$$

where k_{ps} and k_{ds} are scalar gains, and I is the identity matrix.

For the master controller, we command the master to servo to the slave using proportional-derivative control (PD) control. In addition, we feed forward a scaled

version of the measured environmental force:

$$F_{cm} = K_{pm}(X_s - X_m) + K_{dm}(\dot{X}_s - \dot{X}_m) + M_{xm}^{-1}(\Theta_m)\gamma_f F_e \quad (5.9)$$

where γ_f is the scalar force-scaling gain, and K_{pm} and K_{dm} are isotropic as in (5.7) and (5.8). The appearance of the Cartesian inertia matrix in (5.9) is an artifact of the linearizing and decoupling control law of Appendix D.

The proxy moves with the (programmed) dynamics

$$\dot{X}_p = K_a F_{PDm} \quad (5.10)$$

where K_a is the positive-definite diagonal admittance gain matrix, and F_{PDm} is the component of the user's applied force due to the master's PD servo controller:

$$F_{PDm} = \hat{M}_{xm}(\Theta_m)(K_{pm}(X_m - X_s) + K_{dm}(\dot{X}_m - \dot{X}_s)) \quad (5.11)$$

where \hat{M}_{xm} is the estimate of M_{xm} . There may be cases where different admittance gains are desired in different directions of the workspace, but typically the admittance gain matrix will be chosen to be isotropic:

$$K_a = k_a I \quad (5.12)$$

We are also particularly interested in two error variables: the position error between the slave and the proxy

$$E_s = X_s - X_p \quad (5.13)$$

and the position error between the master and slave

$$E_m = X_s - X_m \quad (5.14)$$

The system dynamic equations, in terms of these error variables, are given by:

$$\ddot{X}_m = K_{pm}E_m + K_{dm}\dot{E}_m + M_{xm}^{-1}(\Theta_m)(F_h + \gamma_f F_e) \quad (5.15)$$

$$\ddot{X}_s = -K_{ps}E_s - K_{ds}\dot{X}_s + M_{xs}^{-1}(\Theta_s)F_e \quad (5.16)$$

$$\dot{X}_p = -K_a\hat{M}_{xm}(\Theta_m)(K_{pm}E_m + K_{dm}\dot{E}_m) \quad (5.17)$$

We will assume that \hat{M}_{xm} is updated continuously for the purposes of the linearizing and decoupling controller, but in the proxy dynamics of (5.17) it will be updated at a rate that is slow relative to the other system dynamics. This is done for the purposes of ensuring stability (this topic is discussed in detail in Section 5.2.2). It is reasonable to wonder if a switch between controllers will create an impulse that will add noise to the system that is possibly felt by the user. An update in $\hat{M}_{xm}(\Theta_m)$ causes a discontinuity in the proxy velocity of (5.17), but it does not cause a discontinuity in the proxy position X_p . The slave controller of (5.6) does not rely on \dot{X}_p , so the slave's actuator does not display a discontinuity. The master servos to the slave (see (5.9)), so it does not experience a discontinuity either. Thus, the user does not feel the switching event.

Unlike previous chapter, here we choose to neglect sample-and-hold effects. The Pseudo-admittance controller is designed for systems that are intended to move relatively slowly (*i.e.*, low-bandwidth). In practice, the local master and slave servo gains will be limited by sampling and quantization effects, but we assume here that those local controllers are suitably designed to be robust to sampled-data effects.

For the purpose of analysis, we are interested in expressing our system with respect to the variables \dot{E}_m , E_m , \dot{X}_s , E_s , and X_p . The system written in this state-

space form is given as:

$$\begin{aligned}
\begin{bmatrix} \ddot{E}_m \\ \dot{E}_m \\ \ddot{X}_s \\ \dot{E}_s \\ \dot{X}_p \end{bmatrix} &= \begin{bmatrix} -K_{dm} & -K_{pm} & -K_{ds} & -K_{ps} & 0 \\ I & 0 & 0 & 0 & 0 \\ 0 & 0 & -K_{ds} & -K_{ps} & 0 \\ K_a \hat{M}_{xm}(\Theta_m) K_{dm} & K_a \hat{M}_{xm}(\Theta_m) K_{pm} & I & 0 & 0 \\ -K_a \hat{M}_{xm}(\Theta_m) K_{dm} & -K_a \hat{M}_{xm}(\Theta_m) K_{pm} & 0 & 0 & 0 \end{bmatrix} \begin{bmatrix} \dot{E}_m \\ E_m \\ \dot{X}_s \\ E_s \\ X_p \end{bmatrix} \\
&+ \begin{bmatrix} -M_{xm}^{-1}(\Theta_m) & M_{xs}^{-1}(\Theta_s) - \gamma_f M_{xm}^{-1}(\Theta_m) \\ 0 & 0 \\ 0 & M_{xs}^{-1}(\Theta_s) \\ 0 & 0 \\ 0 & 0 \end{bmatrix} \begin{bmatrix} F_h \\ F_e \end{bmatrix} \quad (5.18)
\end{aligned}$$

5.2.2 Stability

To analyze the stability of (5.18), we must first begin by defining what *stability* means for our system. From an arbitrary initial condition, we would like the unforced system ($F_h = F_e = 0$) to come to rest ($\dot{X}_m, \dot{X}_s, \dot{X}_p \rightarrow 0$) with no position error between the master and the slave ($E_m \rightarrow 0$). We cannot characterize the stability of our system by the stability of some equilibrium state vector. For our system, the position of the proxy X_p (and consequently the master and slave position) should move around the workspace in an unbounded fashion; there is no zero position to which we would like the unforced system to return.

The block diagonal structure of the state matrix in (5.18) allows us to consider

the stability of the error system independently from X_p :

$$\begin{aligned}
\begin{bmatrix} \ddot{E}_m \\ \dot{E}_m \\ \ddot{X}_s \\ \dot{E}_s \end{bmatrix} &= \begin{bmatrix} -K_{dm} & -K_{pm} & -K_{ds} & -K_{ps} \\ I & 0 & 0 & 0 \\ 0 & 0 & -K_{ds} & -K_{ps} \\ K_a \hat{M}_{xm}(\Theta_m) K_{dm} & K_a \hat{M}_{xm}(\Theta_m) K_{pm} & I & 0 \end{bmatrix} \begin{bmatrix} \dot{E}_m \\ E_m \\ \dot{X}_s \\ E_s \end{bmatrix} \\
&+ \begin{bmatrix} -M_{xm}^{-1}(\Theta_m) & M_{xs}^{-1}(\Theta_s) - \gamma_f M_{xm}^{-1}(\Theta_m) \\ 0 & 0 \\ 0 & M_{xs}^{-1}(\Theta_s) \\ 0 & 0 \end{bmatrix} \begin{bmatrix} F_h \\ F_e \end{bmatrix} \quad (5.19)
\end{aligned}$$

We would like this system (when unforced) to have a stable equilibrium at the zero state vector. We would also like this system to be bounded-input/bounded-output (BIBO) stable; that is, we would like bounded external forces to lead to bounded master and slave velocities and bounded position errors in the system. While X_p does not explicitly enter into the error dynamics, it does affect the value of the Cartesian inertia matrices. For example, the joint position of the the master Θ_m is related to the Cartesian position X_m through the robot kinematics, and $X_m = E_s - E_m + X_p$. From (5.18), it is clear that a bounded \dot{E}_m and E_m result in a bounded \dot{X}_p .

For simplicity, we will refer to (5.19) with the notation

$$\dot{Y}(t) = A(t)Y(t) + B(t)U(t) \quad (5.20)$$

We begin by considering the unforced system $\dot{Y}(t) = A(t)Y(t)$. If we consider the

$A(t)$ matrix when $K_a = 0$:

$$A_0 = \begin{bmatrix} -K_{dm} & -K_{pm} & -K_{ds} & -K_{ps} \\ I & 0 & 0 & 0 \\ 0 & 0 & -K_{ds} & -K_{ps} \\ 0 & 0 & I & 0 \end{bmatrix} \quad (5.21)$$

it is clear from the block diagonal structure of A_0 that the system eigenvalues are those of the master and slave servo controllers. A_0 is also LTI. The PD gains can be chosen to place the eigenvalues where desired; if they are chosen such that A_0 is Hurwitz, the system $\dot{Y}(t) = A_0 Y(t)$ will be *uniformly exponentially stable* [83].

We now return to the original $A(t)$ matrix. The matrix $M_{xm}(\Theta_m)$ is bounded, assuming that the robot is bounded away from any singular configurations. From the continuity of matrix eigenvalues, we know that $A(t)$ will be Hurwitz for $\|K_a\|$ sufficiently small.

We can rewrite $A(t)$ as:

$$A(t) = A_0 + \tilde{A}(t)$$

where A_0 is defined in (5.21) and

$$\tilde{A}(t) = \begin{bmatrix} 0 & 0 & 0 & 0 \\ 0 & 0 & 0 & 0 \\ 0 & 0 & 0 & 0 \\ K_a \hat{M}_{xm}(t) K_{dm} & K_a \hat{M}_{xm}(t) K_{pm} & 0 & 0 \end{bmatrix} \quad (5.22)$$

Because A_0 is uniformly exponentially stable and bounded ($\|A_0\| \leq \alpha$), there exists a positive constant β such that $\dot{Y}(t) = A(t)Y(t)$ is uniformly exponentially stable if

$\|\tilde{A}(t)\| \leq \beta \forall t$ [83]. For a given master device, this is essentially a small-gain result limiting $\|K_a\|$.

To develop a more constructive stability condition, we consider the system where the matrix $\hat{M}_{xm}(\Theta_m)$ is updated at a constant rate with a period of τ seconds. We assume that $\|K_a\|$ has been chosen small enough such that all of the LTI systems that may potentially be switched to are exponentially stable. For each LTI A_i matrix in this bounded set, the system response is

$$Y(t) = e^{A_i t} Y(0) \quad (5.23)$$

We are interested in the evolution of the state vector from one switching event to the next:

$$Y(k+1) = e^{A_i \tau} Y(k) \quad (5.24)$$

By making use of an induced matrix norm [41], we find that:

$$\|Y(k+1)\| \leq \|e^{A_i \tau}\| \|Y(k)\| \quad (5.25)$$

We can be assured that the norm of the state vector exponentially decreases to zero at the switching times by requiring

$$\|e^{A_i \tau}\| < 1 \quad \forall A_i \quad (5.26)$$

Also note that the induced matrix norm is equal to the maximum singular value of the matrix ($\bar{\sigma}(\cdot) = \|\cdot\|$). We know that for all Hurwitz A_i , $\|e^{A_i \tau}\| \rightarrow 0$ as $\tau \rightarrow \infty$.

If we implement an update period of τ such that $\|e^{A_i \tau}\| < 1 \quad \forall A_i, \forall \tau \geq \tau$, we can be

assured that the norm of the state vector, sampled at the switches, exponentially decreases to zero.

Each of the LTI A_i systems are uniformly exponentially stable [83]; that is, there exist positive constants γ_i and λ_i such that for any t_0 and $Y(t_0)$:

$$\|Y(t)\| \leq \gamma_i e^{-\lambda_i(t-t_0)} \|Y(t_0)\| \quad (5.27)$$

The exponential convergence of the state vector norm at the switching times (described above) can also be bounded by a continuous-time exponential decay:

$$\|Y(t)\| \leq e^{-\tilde{\lambda}t} \|Y(t_0)\| \quad (5.28)$$

where

$$\tilde{\lambda} = -\frac{\ln(\max_i \|e^{A_i\tau}\|)}{\tau} \quad (5.29)$$

for the specific value of τ chosen. Synthesizing these two facts, the unforced system $\dot{Y}(t) = A(t)Y(t)$ is found to be uniformly exponentially stable:

$$\|Y(t)\| \leq \bar{\gamma} e^{-\underline{\lambda}(t-t_0)} \|Y(t_0)\| \quad (5.30)$$

where $\bar{\gamma} \geq \max\{\gamma_i\}$ and $\underline{\lambda} \leq \min\{\{\lambda_i\}, \tilde{\lambda}\}$.

We now return to the forced system, and consider BIBO stability. The output we are concerned with is the entire state vector $Y(t)$. Assuming that both the master and slave robots are bounded away from any singular configurations, we know that $B(t)$ is bounded. That is, there exists a finite constant β such that $\|B(t)\| \leq \beta \forall t$. This, in addition to the uniform exponential stability of the unforced system, is sufficient for BIBO stability of our system [83].

The constructive stability condition of (5.26) is sufficient for system stability (assuming the stability of the individual LTI controllers), but will be conservative. The stability condition assumes that the worst-case switching conditions consistently occur. In practice, we find that the matrix $\hat{M}_{xm}(\Theta_m)$ can be updated continuously with stable performance (as shown in Section 5.4). An interesting topic for future work is a stability proof that does not rely on the slowly-updated $\hat{M}_{xm}(\Theta_m)$ in the proxy controller.

5.2.3 System Characteristics

In this section we analytically explore some of the distinguishing characteristics of this control system – namely, quasi-static transparency, pseudo-admittance, and steady-hand behavior. Recall that quasi-static transparency refers to the position and force correspondence between the master and slave at static equilibria, which is closely approximated at slow velocities, pseudo-admittance refers to the mimicking of the admittance control of (5.1), and steady-hand behavior refers to the attenuation of user hand tremor at the slave. These properties are shown through experiment and simulation in Section 5.4.2.

We begin by considering the static equilibrium points for our system. Let us for a moment assume that we implement a perfect estimate of the master’s Cartesian inertia matrix ($\hat{M}_{xm}(\Theta_m) = M_{xm}(\Theta_m)$) in the proxy dynamics. A static equilibrium

is reached when

$$\begin{bmatrix} \ddot{E}_m \\ \dot{E}_m \\ \ddot{X}_s \\ \dot{E}_s \\ \dot{X}_p \end{bmatrix} = \begin{bmatrix} 0 \\ 0 \\ 0 \\ 0 \\ 0 \end{bmatrix} \quad (5.31)$$

Assuming K_a is invertible, static equilibrium only occurs when $F_h = -\gamma_f F_e$, and the associated static equilibrium state vector is

$$\begin{bmatrix} \dot{E}_m \\ E_m \\ \dot{X}_s \\ E_s \\ X_p \end{bmatrix} = \begin{bmatrix} 0 \\ 0 \\ 0 \\ K_{ps}^{-1} M_{xs}^{-1}(\Theta_s) F_e \\ X_p \end{bmatrix} \quad (5.32)$$

Thus, there is a unique static equilibrium associated with each slave position. At this static equilibrium, the proxy is at a position such that the human exactly feels the scaled slave/environment force ($F_h = -\gamma_f F_e$) and there is perfect position correspondence between the master and the slave ($E_m = 0$). These two properties define the first component of quasi-static transparency. The existence of these static equilibria assumes that the applied forces are not greater than those that the robots are capable of applying. If the actuators saturate, the system loses control authority to drive $E_m \rightarrow 0$; in this case, the proxy position could grow unbounded as well.

To gain additional insight into the system's performance, let us consider the system moving so slowly that $\dot{M}_{xm}(\Theta_m)$ and $\dot{M}_{xs}(\Theta_s)$ are negligible. For a given

constant input vector, the equilibrium state is found to be

$$\begin{bmatrix} \dot{E}_m \\ E_m \\ \dot{X}_s \\ E_s \\ X_p \end{bmatrix} = \begin{bmatrix} 0 \\ -K_{pm}^{-1}M_{xm}^{-1}(\Theta_m)(F_h + \gamma_f F_e) \\ K_a(F_h + \gamma_f F_e) \\ K_{ps}^{-1}(-K_{ds}K_a(F_h + \gamma_f F_e) + M_{xs}^{-1}(\Theta_s)F_e) \\ X_p \end{bmatrix} \quad (5.33)$$

For a given set of input forces, (5.33) represents the local equilibrium state associated with a given master and slave position. The values of E_m and E_s vary across the workspace for the same input forces, due to the effects of the underlying linearizing and decoupling controller. The velocity of the slave tends to move under the admittance-control paradigm $\dot{X}_s = K_a(F_h + \gamma_f F_e)$ as we move slowly across the workspace, giving the desired system property introduced in (5.1). $\dot{E}_m = 0 \Leftrightarrow \dot{X}_m = \dot{X}_s$, so the master tends to move under the admittance-control paradigm $\dot{X}_m = K_a(F_h + \gamma_f F_e)$ as well, as we move slowly across the workspace.

We found above that $E_m = 0$ at static equilibrium. This is not the case when the system is moving. In fact, the position error E_m is used to drive the movement of the system (see (5.10,5.11)). The position error E_m is related to the applied forces, and consequently, the velocity of the system. As we apply small forces (that is, when the difference between F_h and $-\gamma_f F_e$ is small), E_m becomes small, and the system moves slowly across the workspace. This in turn leads to the steady-state velocity properties discussed above. This is the second component of quasi-static transparency: as the velocity of the system is reduced, the system approaches perfect transparency.

By including an \dot{X}_s term in the master controller (5.9), as well as direct force feedback, we have provided a means for high-bandwidth haptic information to be relayed to the user. The slave does not servo to the proxy with PD control, but rather, with proportional control plus velocity feedback. By excluding \dot{X}_p in (5.6), we create a well-damped slave without the ability to track high-frequency inputs. In addition, the integrating nature of the proxy dynamics tends to attenuate and average high-bandwidth movements of the master relative to the slave. This creates a steady-hand behavior in the system.

In the preceding analysis, we considered a perfect estimate of the master's Cartesian inertia matrix ($\hat{M}_{xm}(\Theta_m) = M_{xm}(\Theta_m)$). In practice this estimate will not be perfect – possibly because of errors in the model, and possibly because of the slow update rate discussed in Section 5.2.2. If we consider static equilibrium points of the system, as in (5.32), we find that the static equilibrium state values are unchanged with an error in $\hat{M}_{xm}(\Theta_m)$. However, the dynamic properties of the controller are affected. If we again assume that the system is moving so slowly that $\dot{M}_{xm}(\Theta_m)$ and $\dot{M}_{xs}(\Theta_s)$ are negligible, the local equilibrium state values are found as:

$$\begin{bmatrix} \dot{E}_m \\ E_m \\ \dot{X}_s \\ E_s \\ X_p \end{bmatrix} = \begin{bmatrix} 0 \\ -K_{pm}^{-1}M_{xm}^{-1}(\Theta_m)(F_h + \gamma_f F_e) \\ K_a \hat{M}_{xm}(\Theta_m)M_{xm}^{-1}(\Theta_m)(F_h + \gamma_f F_e) \\ K_{ps}^{-1}(-K_{ds}K_a \hat{M}_{xm}(\Theta_m)M_{xm}^{-1}(\Theta_m)(F_h + \gamma_f F_e) + M_{xs}^{-1}(\Theta_s)F_e) \\ X_p \end{bmatrix} \quad (5.34)$$

It is clear that the slave dynamics (and consequently the master dynamics) deviate from the ideal admittance control, even when moving slowly, because of the imperfect cancelling of the master's Cartesian inertia matrix ($\hat{M}_{xm}(\Theta_m)M_{xm}^{-1}(\Theta_m) \neq I$).

If we consider

$$\hat{M}_{xm}(\Theta_m) = M_{xm}(\Theta_m) + (\hat{M}_{xm}(\Theta_m) - M_{xm}(\Theta_m)) \quad (5.35)$$

we can write the slave velocity as

$$\dot{X}_s = K_a(F_h + \gamma_f F_e) + K_a(\hat{M}_{xm}(\Theta_m) - M_{xm}(\Theta_m))M_{xm}^{-1}(\Theta_m)(F_h + \gamma_f F_e) \quad (5.36)$$

The error in the slave velocity (*i.e.*, the deviation from quasi-static admittance control) is proportional to the error in $\hat{M}_{xm}(\Theta_m)$.

5.3 Guidance Virtual Fixtures

One of the things enabled by the Pseudo-admittance controller introduced of Section 5.2 is the ability to implement so-called *passive* guidance virtual fixtures (GVFs), which were introduced in Section 1.3.4. Recall that guidance virtual fixtures assist the user in guiding the slave along desired paths or surfaces in the workspace. One of the benefits of these admittance-type GVFs is that they do not typically exhibit instabilities like those confronted in Chapter 2. In this section, we extend the GVFs introduced by Bettini *et al.* [11] (originally designed for human-machine cooperative systems) to Pseudo-admittance Bilateral Telemanipulation. The construction of the the Pseudo-admittance controller, specifically the

use of a proxy, lends itself to this type of GVF.

All of the previous virtual-fixturing schemes for telemanipulation discussed in Section 1.3.4 put the virtual fixture on either the master or slave side – our method is different in that respect, in that the entire system is integrated into the implementation of the GVF. All of the previous proxy-based virtual-fixture methods have restricted the proxy to desired subsets of the workspace (described as “virtual fixtures,” “virtual mechanisms,” *etc.*). But why restrict the proxy to the desired path or surface, if our actual goal is to move the slave along the desired path or surface? If the slave robot experiences a disturbance load, it could actually keep the slave off of the desired path or surface, leading to problems with submittance like those discussed in Section 2.3.3. Our method is different from previous work in this respect as well; the proxy has the potential to move anywhere in the workspace, in an attempt to keep the slave moving on the desired path or surface. Allowing the proxy to move anywhere in the workspace also lends itself to GVFs that act as guidance in the truest sense of the word. Our GVFs allow the user to maintain ultimate control of the system – the slave is allowed to potentially move anywhere in the workspace. Our GVF uses instantaneous preferred directions of motion to haptically assist the user in easily moving the slave along desired paths or surfaces, while imposing guarded motion when the user intentionally moves away from the desired path or surface.

5.3.1 Implementation

In general, the desired path or surface that we would like the slave to move along may have any continuous geometry. In this section we will refer to the desired path or surface as the VF for simplicity. We assume we can instantaneously find the point on the VF that is closest to the slave – we call this point X_{vf} . Finding this closest point constitutes its own field of research in computational geometry [94], and we will not address it here. We then define the VF error as the vector between the slave and the VF:

$$E_{vf} = X_{vf} - X_s \quad (5.37)$$

The VF may be instantaneously defined by linear subspace described by a $3 \times n$ matrix Δ_{vf} , where the n linearly-independent columns form an orthonormal basis for the VF space ($n = 1$ for a line, $n = 2$ for a plane). If the desired path or surface is not continuously differentiable, additional system intelligence will be required to define Δ_{vf} at any corners.

We will consider the force that the user applies to overcome the master's PD controller, F_{PDm} , as the input to the GVF. Recalling (5.9), if the user is perfectly balancing any reflected environmental force, we have $F_{PDm} = 0$, which is interpreted as no input to the GVF (*i.e.*, no velocity command). We find the projection of the input force into the VF space:

$$F_{\Delta} = \Delta_{vf} \Delta_{vf}^T F_{PDm} \quad (5.38)$$

We then construct the instantaneous unit tangent vector to the VF as:

$$\hat{T}_{vf} = \begin{cases} \frac{F_{\Delta}}{\|F_{\Delta}\|} & : \|F_{\Delta}\| > 0 \\ 0 & : \|F_{\Delta}\| = 0 \end{cases} \quad (5.39)$$

We now define the preferred direction of the GVF as

$$P_{vf} = k_{vf}E_{vf} + \hat{T}_{vf} \quad (5.40)$$

where k_{vf} is the user-defined VF stiffness. Though this term does not have traditional stiffness units, it does determine how much the preferred direction tries to influence movement back toward the VF, as a function of the VF error E_{vf} . We will make use of the normalized preferred direction:

$$\hat{P}_{vf} = \begin{cases} \frac{P_{vf}}{\|P_{vf}\|} & : \|P_{vf}\| > 0 \\ 0 & : \|P_{vf}\| = 0 \end{cases} \quad (5.41)$$

We next break the input force F_{PDm} into components in the preferred direction

$$F_P = \begin{cases} (\hat{P}_{vf} \cdot F_{PDm})\hat{P}_{vf} & : \hat{P}_{vf} \cdot F_{PDm} > 0 \\ 0 & : \hat{P}_{vf} \cdot F_{PDm} \leq 0 \end{cases} \quad (5.42)$$

and in the nonpreferred directions

$$F_{\bar{P}} = F_{PDm} - F_P \quad (5.43)$$

We then construct the GVF force by combining the force in the preferred direction with an attenuation of the force in the nonpreferred directions:

$$F_{vf} = F_P + \gamma_{vf}F_{\bar{P}} \quad (5.44)$$

where $\gamma_{vf} \in [0, 1]$ is the user-defined GVF attenuation gain. To implement the GVF, we modify the proxy dynamics of (5.10) to

$$\dot{X}_p = k_a F_{vf} \quad (5.45)$$

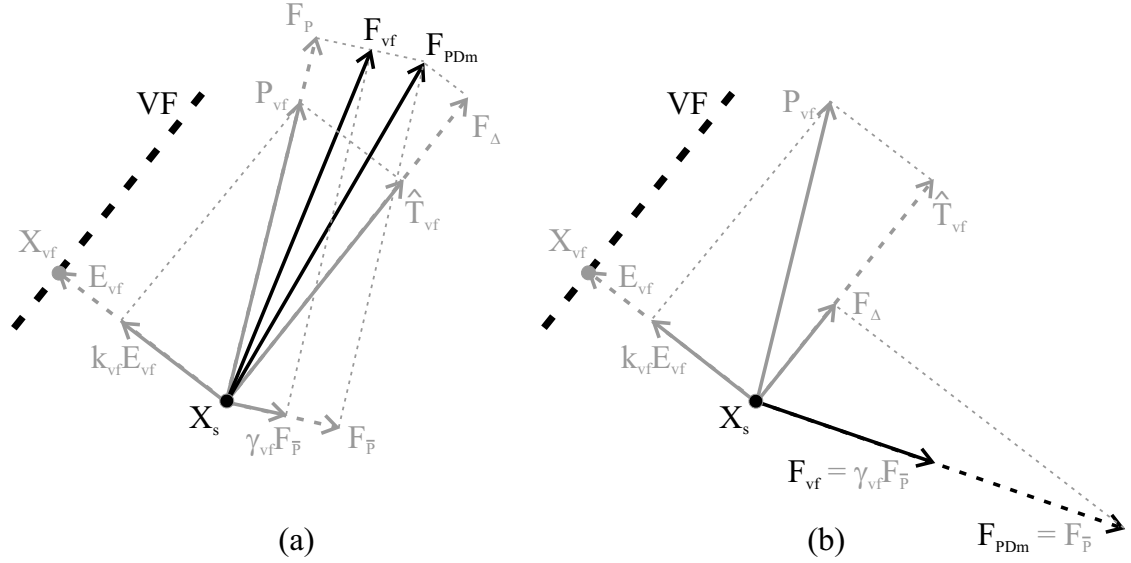


Figure 5.1: A geometrical view of guidance virtual fixtures when (a) there is a component of the applied force in the preferred direction, and (b) when there is no component of the applied force in the preferred direction. The virtual fixture maps the input force F_{PDm} into the virtual fixture force F_{vf} , which is then used as a command to the proxy.

The procedure we use to implement GVFs is shown in Fig. 5.1. In Fig. 5.1(a), we see a case when there is a component of the applied force F_{PDm} in the preferred direction. The algorithm maps the applied force into the GVF force F_{vf} , which points more in the direction of the VF than the original. This moves the proxy in a direction that will tend to move the slave (which is servoing to the proxy) towards the VF. It is also evident that the applied force is slightly attenuated in magnitude in creating F_{vf} . In Fig. 5.1(b), we see a case when there is no component of the applied force F_{PDm} in the preferred direction. In this case, the GVF does not change the direction of the applied force at all, but the magnitude is greatly attenuated. In this sense, if the user commands a force that is intentionally moving away from the VF, the algorithm does not guide the user towards the VF, but rather, it forces the

user to move in a more guarded fashion.

In Section 5.2.2, we determined that for guaranteed stability, we should restrict the $A(t)$ matrix to be LTI for sufficient durations of time. This was accomplished by updating time-varying elements in the proxy dynamics at a slower rate. Though the implementation is slightly different, the GVFs introduced in this section are simply a state-dependent adaptation of the proxy dynamics. For the guaranteed stability result of Section 5.2.2, we must ensure that $A(t)$ is still LTI for sufficient durations of time. To accomplish this, the \hat{M}_{xm} matrix should still be updated with period τ , and in addition, the preferred direction of the GVF (5.40) should also be updated with a period τ .

5.3.2 Attractivity

The purpose of the GVF is to guide the user along desired paths or surfaces, but we have designed a GVF method that allows the user to potentially move the slave anywhere in the workspace. It is reasonable to wonder how well our GVF works in serving its intended purpose. In this section, this concern is addressed and quantified. If, with some initial error E_{vf} , the user attempts to move the slave along the VF, we would hope that the slave either converges to the VF, or at least moves parallel to it; it would be undesirable if the slave actually diverged from the VF. But humans are imprecise, and the actual commanded force F_h could be in a different direction than the intended commanded force/velocity. In this section we quantify the robustness of GVF attractivity to errors in the direction of the commanded

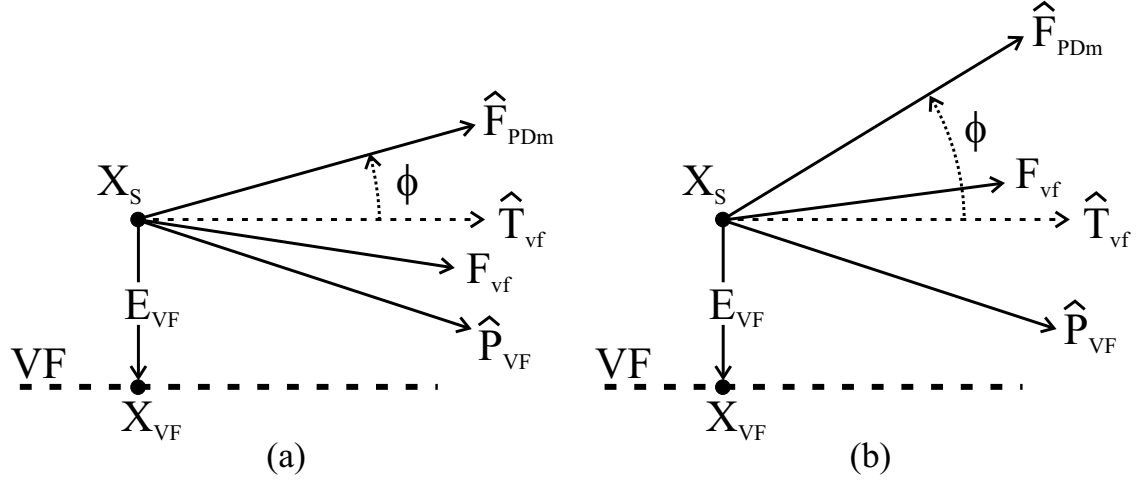


Figure 5.2: The user applies a unit-magnitude force \hat{F}_{PDm} , and the VF maps the applied force into the force F_{vf} . (a) If the angle ϕ is sufficiently small, the VF tends to be attractive. (b) If the angle ϕ is too large, the proxy is commanded away from the VF.

force.

Consider Fig. 5.2, where the user applies a unit-magnitude force that is ϕ radians away from parallel to the VF. For simplicity, we only consider the 2-D case, but the extension to higher dimensions (*i.e.*, when the VF is a plane) is clear. In this section, we explicitly consider linear VFs (lines and planes). We would like to quantify for what angles ϕ the resulting F_{vf} would actually tend to increase $\|E_{vf}\|$ by pointing away from the VF. For this section, we use the notation $s\phi = \sin(\phi)$, $c\phi = \cos(\phi)$, $t\phi = \tan(\phi)$.

We are particularly interested in the sign of the vertical component of the force F_{vf} resulting from the force F_{PDm} in Fig. 5.2. If this vertical component is negative, the proxy will be commanded to move towards the VF; if the vertical component is positive, the proxy will be commanded to move away from the VF. We begin by

writing (5.44) as

$$F_{vf} = (F_{PDm}^T \hat{P}_{vf}) \hat{P}_{vf} + \gamma_{vf} (F_{PDm} - (F_{PDm}^T \hat{P}_{vf}) \hat{P}_{vf}) \quad (5.46)$$

where \hat{F}_{PDm} can be rewritten as

$$\hat{F}_{PDm} = \begin{bmatrix} c\phi \\ s\phi \end{bmatrix} \quad (5.47)$$

and from the previous section we know that

$$P_{vf} = \begin{bmatrix} 1 \\ -k_{vf} e_{vf} \end{bmatrix} \quad (5.48)$$

and, after some manipulation, we have

$$F'_{vf} = (1 - \gamma_{vf})(c\phi - k_{vf} e_{vf} s\phi) \begin{bmatrix} 1 \\ -k_{vf} e_{vf} \end{bmatrix} + \gamma_{vf}(1 + k_{vf}^2 e_{vf}^2) \begin{bmatrix} c\phi \\ s\phi \end{bmatrix} \quad (5.49)$$

where

$$e_{vf} = \|E_{vf}\| \quad (5.50)$$

and

$$F'_{vf} = \|P_{vf}\|^2 F_{vf} \quad (5.51)$$

is simply a positively scaled version of F_{vf} . Since the sign of the vertical component of F_{vf} indicates whether it points toward or away from the VF, we consider the vertical component of F'_{vf} :

$$f'_{vf} = k_{vf}^2 e_{vf}^2 s\phi + (\gamma_{vf} - 1)k_{vf} e_{vf} c\phi + \gamma_{vf} s\phi \quad (5.52)$$

If $\phi = 0$, then

$$f'_{vf} = (\gamma_{vf} - 1)k_{vf}e_{vf} \quad (5.53)$$

is always negative. In other words, the VF is always attractive if the commanded force does not point away from it, which comes as no surprise. If $\phi > 0$, then $c\phi > 0$ and we can divide (5.52) by $c\phi$ to get a positively scaled version of f'_{vf} :

$$f''_{vf} = k_{vf}^2 t \phi e_{vf}^2 + (\gamma_{vf} - 1)k_{vf}e_{vf} + \gamma_{vf} t \phi \quad (5.54)$$

This is a quadratic function in e_{vf} , and because of the positive scalings in the preceding derivation, the sign of f''_{vf} is the same as the sign of the vertical component of F_{vf} .

Figure 5.3 shows a visualization of the quadratic function (5.54). The roots of (5.54) are found as

$$e_{1,2} = \frac{1 - \gamma_{vf}}{2k_{vf}t\phi} \pm \frac{((1 - \gamma_{vf})^2 - 4\gamma_{vf}t^2\phi)^{\frac{1}{2}}}{2k_{vf}t\phi} \quad (5.55)$$

where the “+” corresponds to e_{crit} in Fig. 5.3(b), and the “−” corresponds to e_{conv} in Fig. 5.3(b). If

$$(1 - \gamma_{vf})^2 - 4\gamma_{vf}t^2\phi < 0 \quad (5.56)$$

then the roots of (5.55) are imaginary, and we have curve of Fig. 5.3(a), indicating that e_{vf} will continue to grow (*i.e.*, divergence from the VF). This equation can be rewritten as a condition on ϕ for a given γ_{vf} :

$$\phi > \text{atan} \left(\frac{1 - \gamma_{vf}}{2} \left(\frac{1}{\gamma_{vf}} \right)^{\frac{1}{2}} \right) \quad (5.57)$$

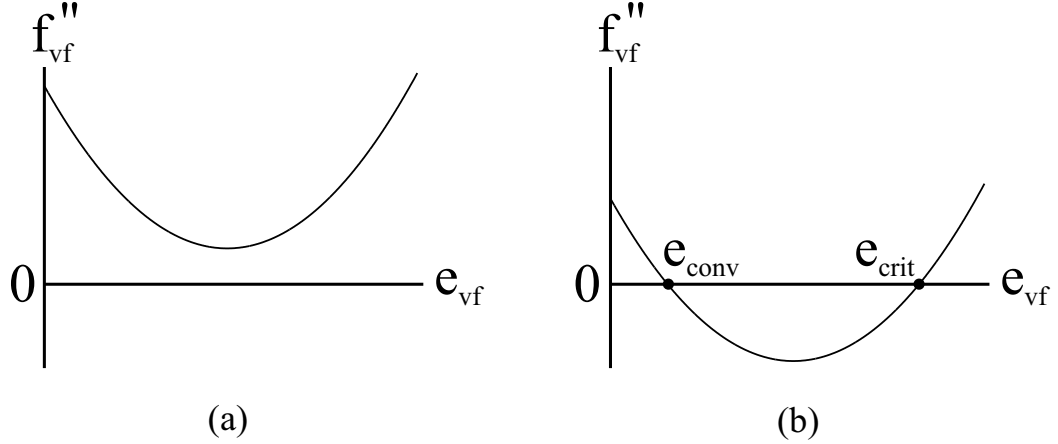


Figure 5.3: Visualization of the quadratic function (5.54), when (a) $(1 - \gamma_{vf})^2 - 4\gamma_{vf}t^2\phi < 0$, and when (b) $(1 - \gamma_{vf})^2 - 4\gamma_{vf}t^2\phi \geq 0$. A positive f''_{vf} tends to increase e_{vf} .

Thus, for each value of γ_{vf} there exists some ϕ above which the proxy will diverge from the VF (regardless of the value of k_{vf} or e_{vf}). When the roots of (5.55) are real, we have curve of Fig. 5.3(b). For a given set of k_{vf} , γ_{vf} , and ϕ , if $e_{vf} > e_{crit}$ then the proxy will diverge from the VF, and if $0 \leq e_{vf} < e_{crit}$ then e_{vf} will converge on e_{conv} .

From the preceding analysis, we find that given a set of k_{vf} and γ_{vf} , as well as a bound on the possible valued that ϕ might take, we can find a bounded region of magnitude e_{conv} such that if we begin within this region, then we are assured to stay within this region.

5.3.3 Parameter Selection

With so many user-defined parameters, choosing them in some sort of optimal way may at first seem daunting. The user-defined parameters are actually fairly decoupled, and they should be designed in a prescribed order:

1. Choose the desired admittance felt if the system begins on the VF ($E_{vf} = 0$), and the user commands the slave to move along the VF; this value is k_a . This should be chosen to give the desired velocity/force relationship when moving through free space.
2. Choose the force-scaling gain γ_f . This gain should be chosen specifically with static equilibria in mind.
3. Choose the master and slave PD gains. These gains should probably be chosen for critical damping, and should be chosen to be as large as is possible to implement on a real system with sampling and quantization effects. These parameters should be chosen with consideration of the stability issues discussed in Section 5.2.2.
4. Choose the desired admittance to be felt if leaving the VF perpendicularly. This admittance should make the system move in a slow, guarded way. γ_{vf} is then chosen as the ratio of this admittance and the previously selected k_a .
5. Choose the GVF return gain k_{vf} . The selection of this parameter is more art than science. Choosing k_{vf} too low gives a preferred direction that is essentially parallel to the VF, which results in little guidance back to the VF if $E_{vf} \neq 0$. Choosing k_{vf} too high makes the system feel sluggish when trying to move along the VF, since the preferred direction is nearly perpendicular to the VF if $E_{vf} \neq 0$. One rule of thumb is to determine for what error magnitude $\|E_{vf}\|$ one wants the preferred direction to be past 45 degrees from parallel to

the VF (pointing more towards the VF than parallel to it). k_{vf} is then chosen as the inverse of $\|E_{vf}\|$.

5.4 Experimental Verification

In this section we verify the properties of Pseudo-admittance control and the guidance virtual fixtures introduced in the previous sections. This is accomplished through both experiments and simulations.

5.4.1 System

The experimental system that we consider is constructed of two PHANToM robots from SensAble Technologies. The master device is a PHANToM Premium 1.0, and the slave device is a PHANToM Premium 1.5; in general, either robot can act as the master or the slave. These are nearly identical robots, but the workspace of the PHANToM 1.5 is 50% larger than that of the PHANToM 1.0, and the other robot parameters are scaled accordingly. The PHANToMs are run on a single computer, at a sampling rate of 500 Hz. In addition to the experimental system, we have constructed an accurate MATLAB simulation of our system. This allows us to explore certain aspects of system performance in a more controlled setting.

The Pseudo-admittance control algorithm, as well as our simulation, requires an accurate model of the robotic devices. To obtain these models, we synthesized two prior works [15, 23] to implement an adaptive parameter estimator of the robot

properties. This adaptive algorithm was run off-line from the Pseudo-admittance controller to obtain the 20 robot inertial and frictional parameter values needed to describe the system. The details of the PHANToM kinematic and dynamic model, as well as the adaptive parameter identification algorithm, are given in Appendix E.

For our system, the servo gains for the linearizing and decoupling controller were chosen empirically. The values chosen are $k_{dm} = k_{ds} = 150$ and $k_{pm} = k_{ps} = 5625$. Recall that these are the servo gains that act on a linear and decoupled unit-mass system. These gains were chosen such that the individual systems are critically damped (assuming a stationary proxy), and they were chosen to be as high as possible before sampling and quantization effects start to noticeably affect the system’s behavior. These gains are used throughout the experiments and simulations to follow.

After choosing the PD servo gains, the next step is to find the fastest rate at which we may update our proxy dynamics and still guarantee stability of the nonlinear, time-varying system. To quantify the bounds of (5.26), we numerically evaluated the norm of the matrix $A(t)$ at hundreds of locations across the workspace of the master device, for the largest values of k_a to be used in this section, and it was determined that an update rate of 10 Hz ($\tau = 0.1$ seconds) of the parameter $\hat{M}_{xm}(\Theta_m)$ in the proxy dynamics will result in a guaranteed stable system. This value was used in the experiments and the simulations to follow. We found that the location in the robot workspace actually had little effect on the value of τ needed to

satisfy (5.26); the norm of $A(t)$ was dominated by the servo gains. Also, in practice we find that we can update $\hat{M}_{xm}(\Theta_m)$ in the proxy dynamics continuously (that is, at every sample) with no perceived degradation in stability. The condition of (5.26) is simply a sufficient condition; a nonlinear stability proof that does not rely on (5.26) is left as a topic for future consideration.

To obtain our measurement of the environmental force F_e in our experimental setup, we use the force generated at the tool tip by the slave’s actuators as an approximation of the true force, thus a force sensor is not required. For our slow-moving, low-inertia, low-friction PHANToms, this is a good approximation for the purposes of this section. We begin by considering the behavior of Pseudo-admittance Bilateral Telemanipulation on its own, and then we incorporate guidance virtual fixtures.

5.4.2 Pseudo-admittance Bilateral Telemanipulation

We begin by demonstrating the steady-hand properties of Pseudo-admittance. Figure 5.4 shows the master and proxy positions in the three coordinate axes as the user moves the telemanipulator across the workspace. The slave is moving in free space, and it closely follows the proxy. The user displays hand tremor that is greatly attenuated in the proxy. Also, at approximately the 5-second mark, the user releases the master, and the system stays in place, confirming the stability of the system.

Ideally, the proxy velocity is, by definition, proportional to the applied force

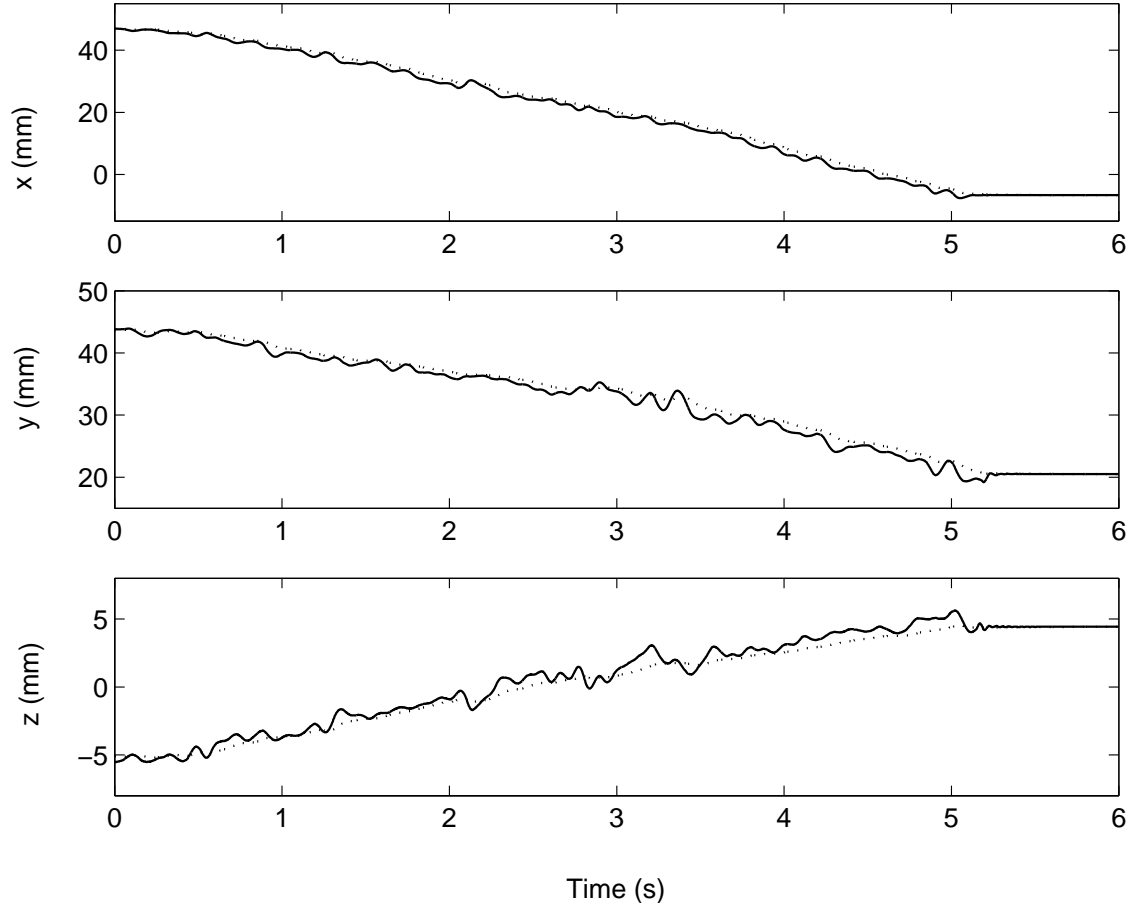


Figure 5.4: An experimental demonstration of the steady-hand behavior seen in Pseudo-admittance control ($k_a = 30 \text{ mm}/(\text{Ns})$). Master (—) and proxy (\cdots) trajectories are shown. At approximately the 5-second mark, the user releases the master, and the system stays in place.

F_{PDm} through (5.10). But to guarantee stability, we choose to update the proxy dynamics at a slower rate. Figure 5.5 shows that this does not significantly impact on the performance of the system. In the figure, we see the proxy velocity along the three coordinated axes, plotted against the applied force F_{PDm} normalized by the admittance gain k_a . If the proxy dynamics were updated continuously, these two values would perfectly coincide. In this figure we see that the proxy velocity shows very little differences with the commanded velocity. In fact, every 0.1 seconds (that

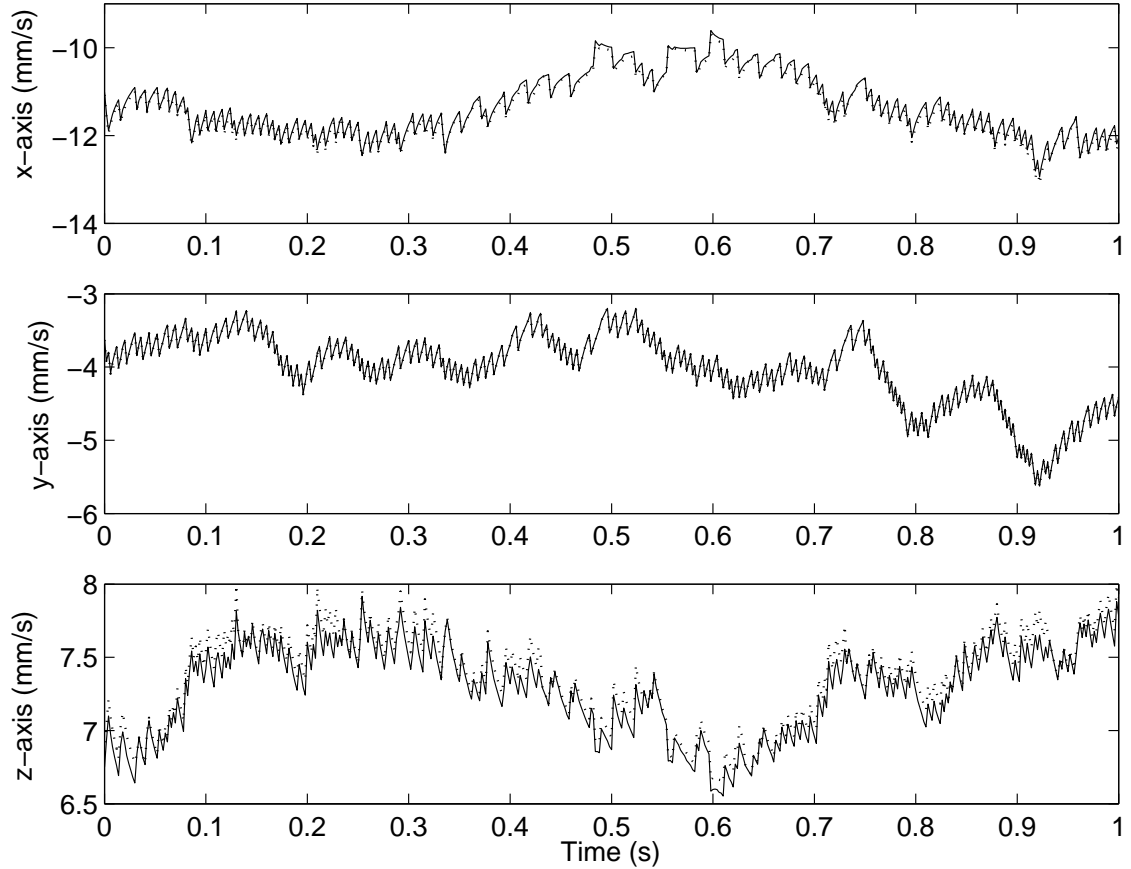


Figure 5.5: Effects of slow update rate in proxy dynamics ($k_a = 30 \text{ mm}/(\text{Ns})$). Normalized force F_{PDm}/k_a (—) and proxy velocity (\cdots) are shown.

is, at every update of the proxy dynamics), the two variables coincide. Figure 5.4 is also evidence that the proxy velocity does not show any signs of strange variation because of the slower update rate.

Qualitatively, this system feels very stable – it feels almost like a pure, high viscosity. The system interacts well with every environment (including steel) for a large range of admittance gain values. While the control system does not exhibit transparency in the traditional sense, it does provide the user with a rich set of haptic information.

The human user is an integral component in this human-machine collaborative

system, but human motions and physical parameters are also very variable. We have created a simulation for our PHANToM telemanipulation system that allows us to obtain less anecdotal results than we would obtain from experiments alone. We make use of our simulation now to consider, in a controlled fashion, the behaviors of the Pseudo-admittance Bilateral Telemanipulation system when interacting with various types of environments. Figures 5.6 and 5.7 show how our system interacts with purely viscous environments with damping b_e . We include $b_e = 0$ Ns/m, which is the slave moving freely in space. For each simulation, the user applies a constant force F_h in the x direction (see Appendix E.1) for the first three seconds, and then releases the device ($F_h = 0$) for the last second. The plots show the position in the x direction. Figures 5.6 and 5.7 are meant to be considered together; we can observe changes in any one of the parameters k_a , F_h , or γ_f with all the others held constant, by moving side-to-side, up-and-down, and back-and-forth, respectively, between the plots in these two figures.

From these plots, the nature of the Pseudo-admittance controller becomes clear. The slave moves with a velocity that is almost perfectly linearly proportional to the applied forces. The position error between the master and slave is used to drive that movement. When the master is released, the position error disappears, and the system stays where it was released by the user.

As the value of the admittance gain k_a is increased, the system moves faster, and it is easier to distinguish the two different viscosities, since the environmental force is proportional to the speed of the slave. The position error generated between

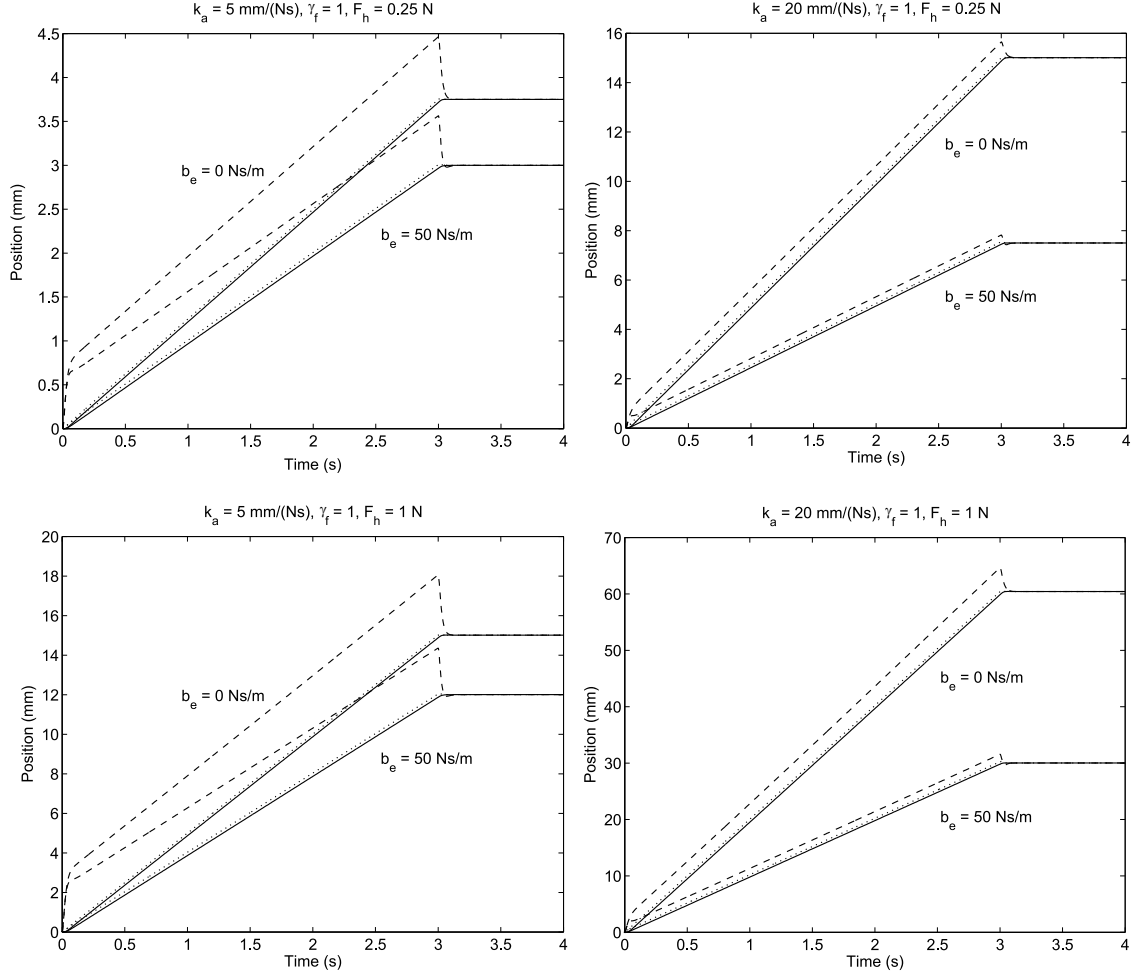


Figure 5.6: Simulated interactions with viscous environments with damping b_e , $\gamma_f = 1$, and varying values of admittance gain k_a . Master (---), slave (—), and proxy (\cdots) trajectories are shown. The user applies a constant force F_h for the first three seconds, and then releases the master.

the master and slave by the user's applied force is unchanged, but it appears to be reduced because it is smaller relative to the total distance travelled.

Increasing the force feedback gain γ_f has no effect when the slave is moving in free space, but does result in slower velocities when the slave is moving through a viscous environment. Increasing γ_f also has the effect of reducing the position error between the master and the slave while moving. This makes sense – a larger portion of the applied force F_h is going towards balancing the force $\gamma_f F_e$, leaving less force

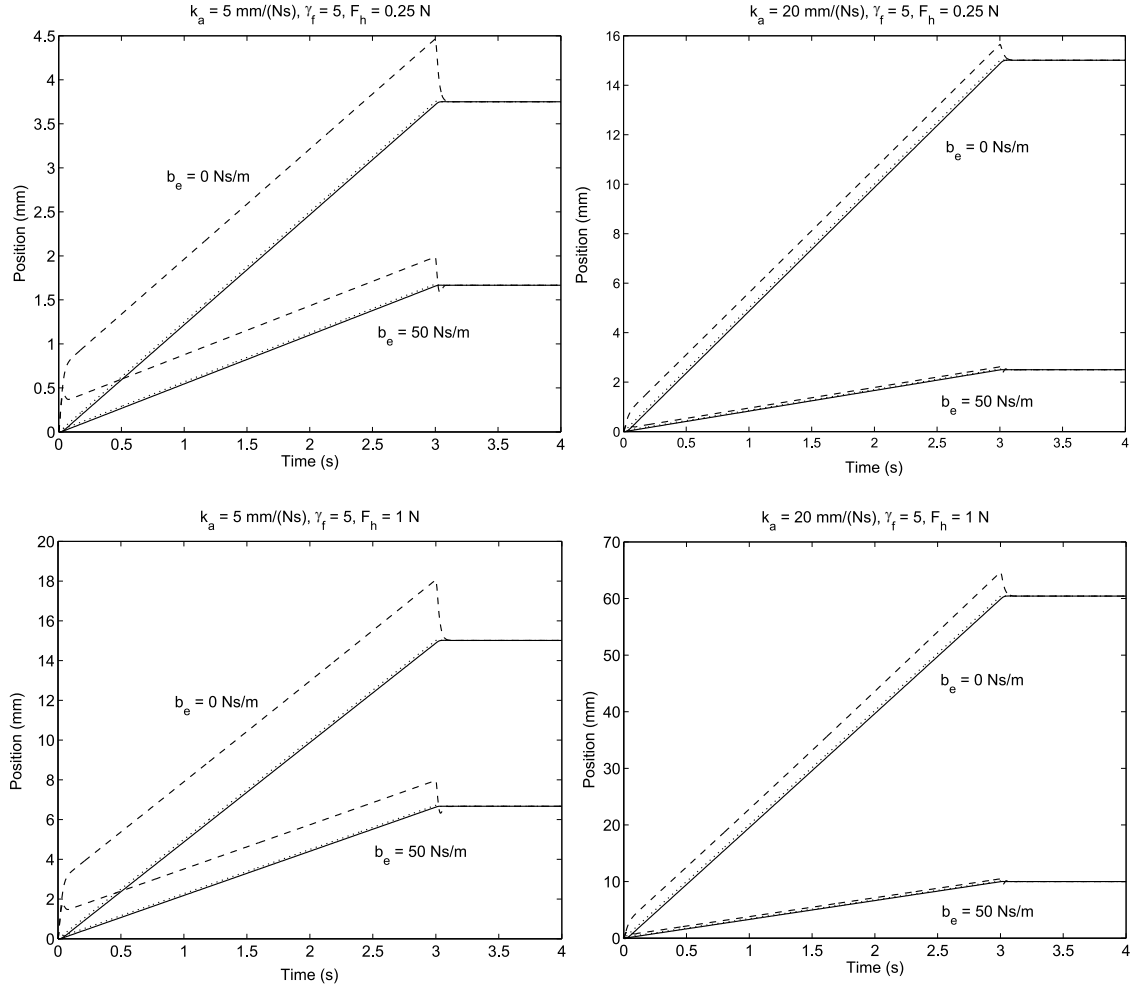


Figure 5.7: Simulated interactions with viscous environments with damping b_e , $\gamma_f = 5$, and varying values of admittance gain k_a . Master (---), slave (—), and proxy (⋯) trajectories are shown. The user applies a constant force F_h for the first three seconds, and then releases the master.

for generating a position error in the master's servo controller.

The effect of pushing harder (increasing F_h) is faster movement, with larger associated position errors between the master and the slave. However, from the plots it is evident that the increase in position error is proportional to the increase in velocity, so that the relative behavior of the system is essentially unchanged by a change in the applied force.

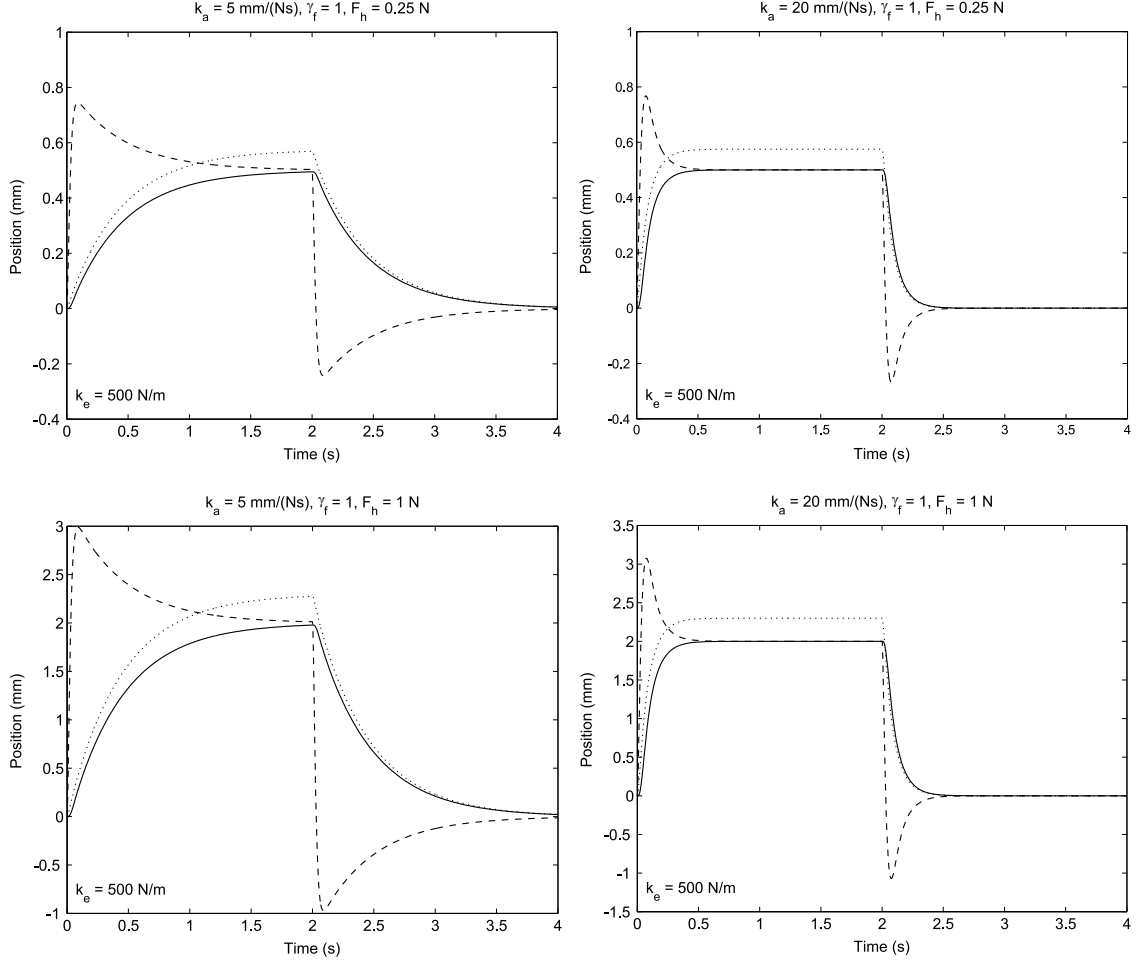


Figure 5.8: Simulated interactions with an elastic environment with spring constant $k_e = 500$ N/m, with $\gamma_f = 1$ and varying values of admittance gain k_a . Master (---), slave (—), and proxy (\cdots) trajectories are shown. The user applies a constant force F_h for the first two seconds, and then releases the master.

Figures 5.8 and 5.9 show how our system interacts with purely elastic environments. We simulate a unilateral spring surface that pushes in the $-x$ direction, with a spring constant k_e , when the slave enters the $+x$ half-space. For each simulation, the user applies a constant force F_h in the x direction (see the PHANToM frame description in Appendix E.1) for the first two seconds, and then releases the device ($F_h = 0$) for the last two seconds. The plots show the position in the x direction. Again, Figs. 5.8 and 5.9 are meant to be considered together; we can observe

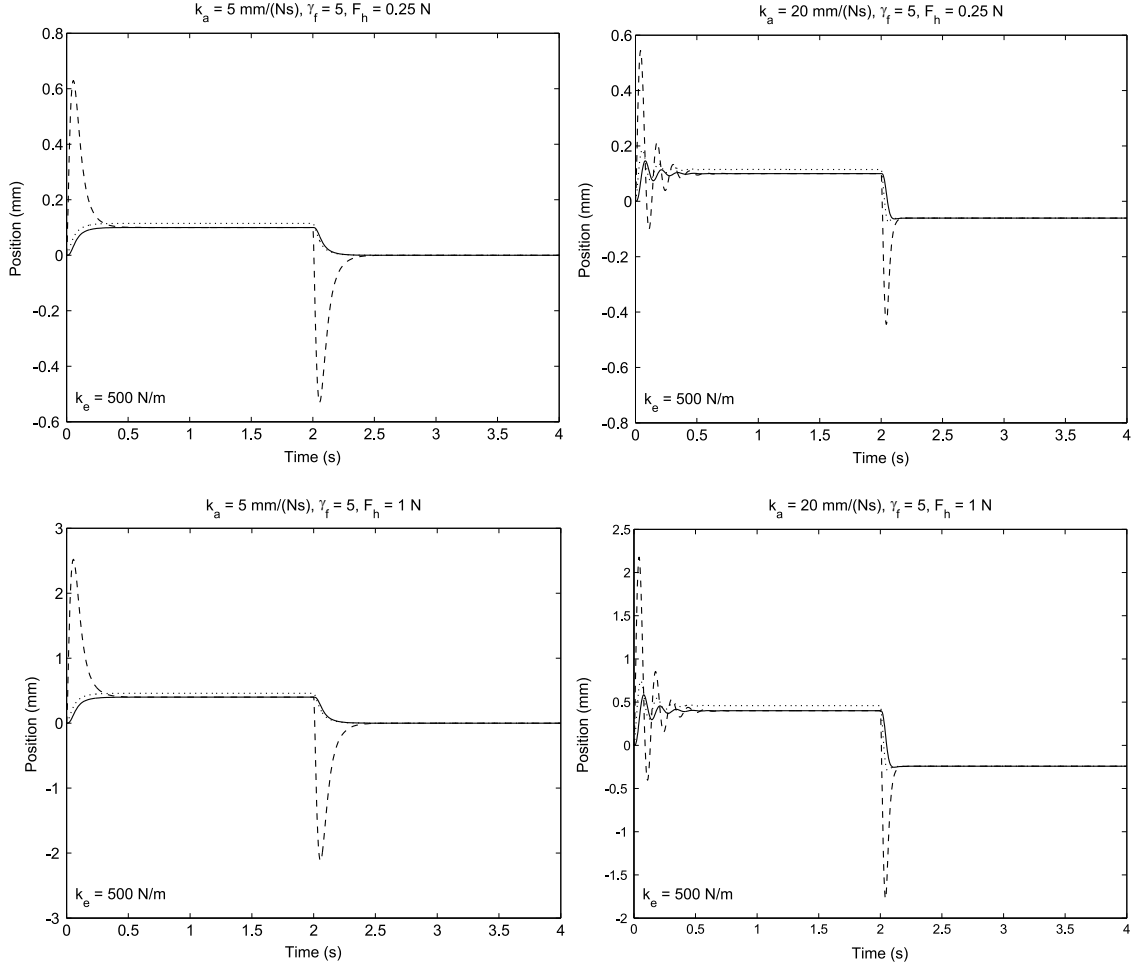


Figure 5.9: Simulated interactions with an elastic environment with spring constant $k_e = 500 \text{ N/m}$, with $\gamma_f = 5$ and varying values of admittance gain k_a . Master (---), slave (—), and proxy (\cdots) trajectories are shown. The user applies a constant force F_h for the first two seconds, and then releases the master.

changes in any one of the parameters k_a , F_h , or γ_f with all the others held constant, by moving side-to-side, up-and-down, and back-and-forth, respectively, between the plots in these two figures.

From each of the plots, it is evident that a constant input force F_h does result in a static equilibrium with an elastic environment. In addition, the position error between the master and the slave does vanish. The proxy reaches into the environment, pulling the slave behind it, until the force generated is large enough to

drive the master back into static equilibrium. When the master device is released with potential energy stored in the environment, the environment pushes the slave out to the surface. The master is temporarily pushed well outside the boundaries of the environment by the force-feedforward term, but the position error between the master and the slave eventually vanishes, with the system coming to rest just outside the elastic environment.

It is clear that the static equilibrium position is independent from the admittance gain k_a ; the admittance gain simply governs how quickly static equilibrium is reached. In fact, increasing either k_a or γ_f decreases the rise time of the system. Changing the magnitude of the input force F_h results in a change in equilibrium position, but the relative time response is unchanged. Changing γ_f also changes the equilibrium point; changing γ_f effectively changes the stiffness of the environment.

An interesting behavior is seen for combinations of large k_a and large γ_f . An underdamped ringing happens when the user pushes into the environment; it is of relatively large magnitude on the master, and it is attenuated at the slave. This behavior was not anticipated by the analytical results of Section 5.2.3. It may warrant further analysis if Pseudo-admittance control is applied to fast moving systems with large levels of force feedback.

5.4.3 Guidance Virtual Fixtures

In this section we consider the implementation of a basic GVF – a vertical plane – on our experimental system. The desired surface is a vertical plane defined by

$x = 0$ (see the PHANToM frame description in Appendix E). We describe the VF surface by:

$$\Delta_{vf} = \begin{bmatrix} 0 & 0 \\ 1 & 0 \\ 0 & 1 \end{bmatrix} \quad (5.58)$$

We implement the GVF on a Pseudo-admittance telemanipulator with admittance gain $k_a = 40 \text{ mm}/(\text{Ns})$.

Figure 5.10 shows GVFs resulting from four combinations of k_{vf} and γ_{vf} values. Note that the desired plane is $x = 0$, which is the line that divides each of these plots down the center. In each plot, we start at rest (at four different initial conditions) towards the bottom of the plot. Then the human user simply applies a gentle force in the positive y direction. The plot shows the resulting movement of the master device, as well as the proxy (to which the slave servos).

It is evident from the figure how increasing k_{vf} points the preferred direction more towards the desired plane than parallel to it. Reducing γ_{vf} has a similar but smaller effect, by attenuating the component of the input force in the the non-preferred directions. The benefits of these GVFs are evident when $\gamma_{vf} \approx 0$; the device closely approaches the desired surface with essentially no cognitive effort on the part of the user. Recall that the user has complete control to move the device away from the plane at all times; these are simply the paths that the robots favor. Decreasing γ_{vf} has a larger effect on the system than is evident from the figure. In the process of creating this figure, the device was moved to its initial position off of the desired plane. For the system with $\gamma_{vf} = 0.05$, this movement away from the

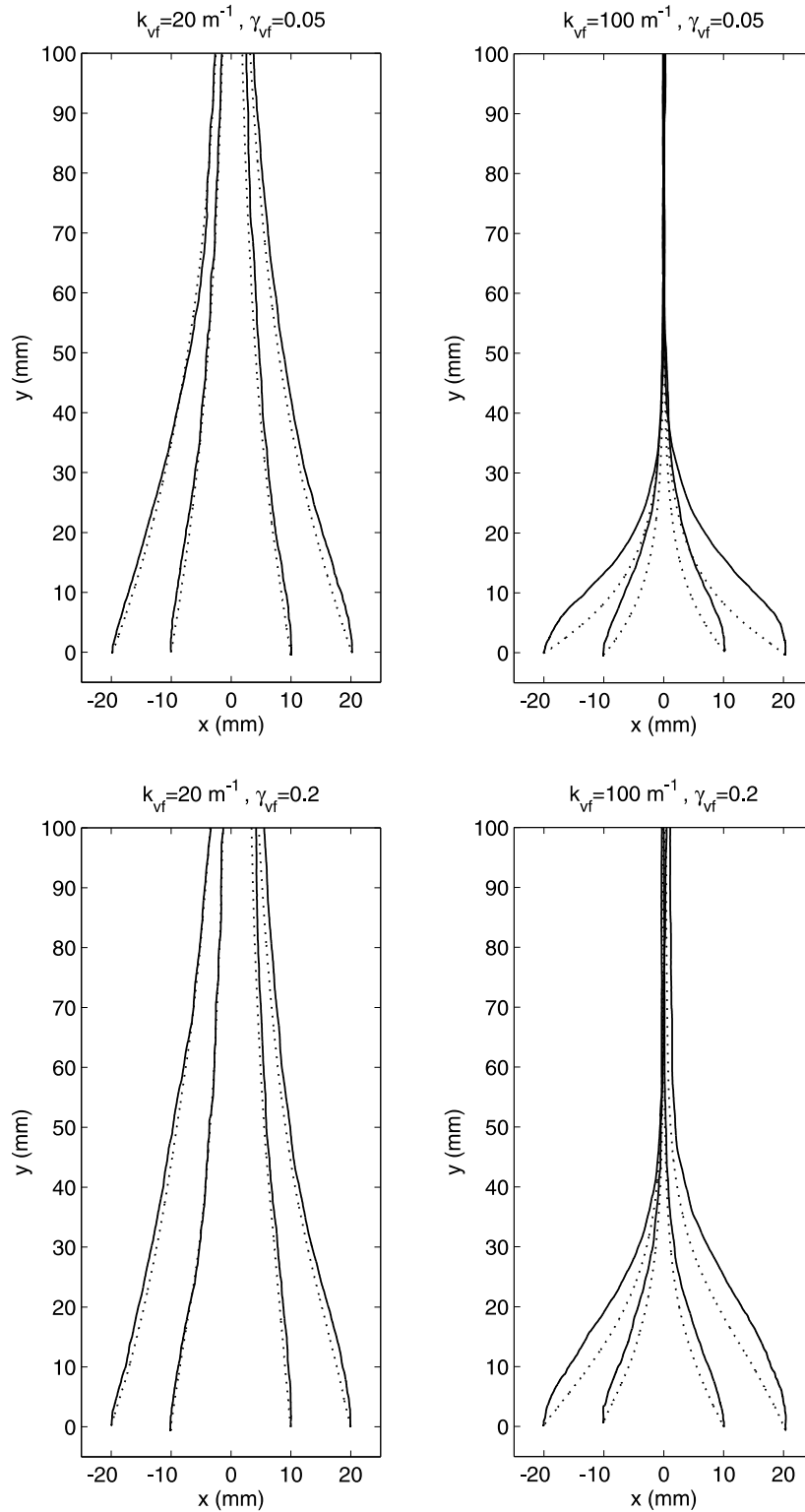


Figure 5.10: Guidance virtual fixtures for the vertical plane defined by $x = 0$. Master (—) and proxy (\cdots) trajectories are shown. All data is shown for $k_a = 40$ mm/(Ns), with other GFV parameters varying.

plane (*i.e.*, in a non-preferred direction) was very slow (four times slower than for $\gamma_{vf} = 0.2$).

From the figure, it appears that increasing k_{vf} tends to increase the position error between the master and the proxy (and consequently between the master and the slave). But recall that the position error is proportional to the applied force, under the quasi-static assumption of the slow-moving proxy. The position error seen in this figure is simply due to the large components of the applied force in the non-preferred direction. The lower values of k_{vf} have similar position errors – they are simply more aligned with the direction of motion.

5.5 Conclusions

In this chapter we presented a novel, provably-stable bilateral telemanipulation system called Pseudo-admittance. This system is designed to mimic admittance control on systems where the master is an impedance-type robot. It has many desirable properties, such as steady-hand tremor attenuation, quasi-static transparency, and the ability to include guidance virtual fixtures. A novel guidance virtual fixture method was presented that builds upon a method previously developed [11] for human-machine cooperative systems. The properties of Pseudo-admittance Bilateral Telemanipulation, with and without guidance virtual fixtures, were verified through experiment and simulation on a system where both the master and slave are of the impedance-type. Pseudo-admittance has potential benefits for systems that are designed for stability and transparency, but that require better-than-human

levels of precision during the execution of certain tasks. It could also be applied to systems with large motion scaling or velocity limits at the slave. Guidance virtual fixtures could be used as task macros – potentially increasing both speed and precision on structured tasks that still require direct human control.

Chapter 6

Conclusions and Future Work

This dissertation explored the application of virtual fixtures to bilateral telemanipulators. Virtual fixtures show great promise for use in telemanipulated tasks that require better-than-human levels of accuracy and precision, but also require the intelligence provided by a human directly in the control loop. While telemanipulation can be thought of as making up for the limitations in autonomous robotics (*i.e.*, in artificial intelligence, sensor-data interpretation, and environment modeling), virtual fixtures can be thought of as making up for the limitations imposed by including a human directly in the control loop. Virtual fixtures can be used to find an optimal balance between autonomy and direct human control. Virtual fixtures can act as a safety constraint – keeping the telemanipulator from entering into potentially dangerous regions of the workspace. Virtual fixtures can also be used as macros that assist a human user in carrying out a structured task. Some of the potential applications for virtual fixtures are robot-assisted surgery, difficult

assembly tasks, and inspection and manipulation tasks in dangerous environments.

Previous work in virtual fixtures has been largely *ad hoc*; virtual fixtures have been shown to improve performance of certain tasks, but the results have been specific to the system and task considered. In addition, previous work has rarely considered the limitations confronted in the stable implementation of virtual fixtures. In this dissertation, we considered issues that apply to virtual fixtures implemented on broad classes of telemanipulation systems and tasks. Much of the dissertation focused on different methods to accurately analyze the stability of systems with virtual fixtures, ensuring that virtual fixtures can be designed for high performance and safety. We also presented a novel telemanipulation controller that can be overlaid on a broad class of existing systems, providing a means for improved control. Each of the previous chapters contains its own discussion and conclusions, so the major results of each chapter are only summarized here. In addition, we present interesting topics for future research that build upon the results in this dissertation.

In Chapter 2, we explored the design of stable forbidden-region virtual fixtures (FRVFs) for bilateral telemanipulators where the master and slave robots are of the impedance type. We developed three metrics to quantify the performance of FRVFs: tracking, safety, and submittance. Using these metrics, a human-factors experiment was conducted to quantify the performance of various combinations of FRVF and bilateral telemanipulation controller. The experiment showed that, while FRVF design will likely be highly task dependent, there are a few rules of thumb that can be employed when choosing a FRVF architecture. We analyzed the stability of

impedance-type FRVFs using a sampled-data model of the closed-loop system. An algorithm was developed to predict potential instability; the algorithm requires a model of the telemanipulator, as well as simple bounds on the parameters of human users. This stability method was experimentally verified, and shown to be a good predictor of stability behavior in a real, non-ideal system.

The human-factors experiment we conducted simulated a scenario where the human user knows where the forbidden region is, and is trying to work near it without entering into it. The subjects were able to use visual feedback for assistance. Another experiment that should be conducted in the future is to examine the case where the user is unaware of the exact position of the forbidden region with respect to the slave, possibly due to an obstruction of visual feedback. In this case, it is likely that the benefits of FRVFs will be even more pronounced.

We did not consider FRVFs on telemanipulation systems where one or both of the master and slave devices is of the admittance type. There is reason to believe that this could lead to systems with desirable characteristics; nearly perfect position tracking may be possible for a large range of environmental impedances. This is left as a topic for future work.

The topics explored in this chapter should be extended to higher degrees of freedom than 1-DOF. The stability results are likely to have analogies in higher degrees of freedom for impedance-type robots where the flexibility in the robot is largely in the controlled (backdrivable) joints. In a 1-DOF system the master and slave movements are always normal to the FRVF, but with higher degrees of freedom this

will not be the case. It is known from research in haptic virtual environments that virtual environments with higher degrees of freedom are considerably more complicated than those in 1-DOF, especially when the geometry of the virtual environment is complicated. In fact, this is the very reason for the advent of the proxy in [113]. Proxy-based forbidden-region virtual fixtures were only briefly considered in Chapter 2, and their stability was not considered at all, but the Pseudo-admittance controller of Chapter 5 is an example of a very stable proxy-based control system. The design of stable and functional proxy-based FRVFs is an interesting topic for future research.

In Chapter 3, we gave a simple explicit condition on virtual-wall stiffness that is necessary and sufficient for virtual-wall passivity. We considered a haptic display that can be modeled as an actuated mass with Coulomb-plus-viscous friction, with both sampling and sensor quantization explicitly considered. The condition also applies directly to a larger class of friction models that consider stiction. The results show a decoupling of the effects of sampling rate and encoder resolution, and give useful design criteria for generating stiffer passive virtual walls. A simple experiment provided evidence that the results presented are applicable to real systems, and lead to a significant new (quantifiable) understanding of non-passive behavior in haptic devices implementing virtual walls. These passive virtual walls can be stably incorporated as virtual fixtures for telemanipulation using the method described in Chapter 4.

We discussed that there are mainly two potential weaknesses in the model used

above: inaccuracies in the friction model, and not considering actuator dynamics. We showed that actuator dynamics are likely to be significantly less important than the parameters considered in the model. Improving the friction model is an interesting topic for future work. Specifically, improving the model near zero velocity. Many more detailed models than Coulomb-plus-viscous friction exist, and it is conceivable that one of these could be incorporated in a rigorous passivity condition.

Another interesting topic for future research in this area is the inclusion of some form of virtual damping in a way that still guarantees passivity. This is a daunting prospect, because the fundamental loss of information due to sampling a quantized position measurement makes knowledge of instantaneous velocity essentially unattainable. However, with some reasonable assumptions about the system, it may be possible to add virtual damping in a passive way. It also may be possible to include physical (passive) damping in way that does not compromise fidelity.

In Chapter 4, we discussed how virtual fixtures are often nothing more than haptic virtual environments (about which there is a large body of prior work) overlaid on telemanipulators. We presented a framework in which the problem of passively combining bilateral telemanipulators and virtual environments can be approached. It was shown that we can design complicated systems in a modular way, allowing rigorous analysis of telemanipulators with virtual fixtures with various underlying physical properties and control methods (*i.e.*, impedance or admittance). We experimentally demonstrated that this method does result in stable systems, but the results are conservative.

We discussed how if one can quantify (bound) the difference between the LTI system elements that are designed and the actual sampled-data system elements that are implemented, stability can be ensured in a way that is not so conservative as to be prohibitive for use in real applications. This approach to system modeling and analysis provides a well-defined future research direction for those interested in creating stable high-performance systems that contain both bilateral telemanipulation and virtual fixtures. In Chapter 2, we showed how accounting for the dissipation in human users leads to much more accurate (nonconservative) stability results than simply requiring passivity of the virtual fixture. Simply modeling the human as passive, which is typical of research in the stability of both bilateral telemanipulators and haptic virtual environments, is likely to lead to conservative results – creating systems with performance that is not optimized. Modeling the human body (hand, arm, *etc.*) as it pertains to haptic devices should continue to be an active area of research. In addition, existing passive virtual environments could be reexamined to quantify their level of dissipativity or activity.

The model used in Chapter 3 also provides an ideal proving ground for the method presented in Chapter 4. In this model, we have a provably passive system that is actually dissipative in all practical situations, and quantifying this dissipativity is an interesting problem.

In Chapter 5 we presented a novel, provably stable bilateral telemanipulation system called Pseudo-admittance. This system is designed to mimic admittance control on systems where the master is an impedance-type robot. It was shown to

have many desirable properties, such as steady-hand tremor attenuation, quasi-static transparency, and the ability to include guidance virtual fixtures. A novel guidance virtual fixture method was presented. The properties of Pseudo-admittance Bilateral Telemanipulation, with and without guidance virtual fixtures, were verified through experiment and simulation. Pseudo-admittance has potential benefits on systems that are designed for stability and transparency, but that require better-than-human levels of precision on certain tasks. Guidance virtual fixtures could be used as task macros – potentially increasing both speed and precision on structured tasks that still require direct human control. These macros could be particularly useful in robot-assisted surgical tasks.

We quantified the attractivity of desired lines and planes using guidance virtual fixtures, but what about when the desired path or surface is curved? Simply locally moving tangent to curved path will result in movement away from the path. The consideration of path and surface curvature as they pertain to guidance virtual fixtures is left as a topic for future work.

We did not explicitly consider orientation in our Pseudo-admittance controller. It was assumed that orientation was handled by a traditional control method. But the benefits of Pseudo-admittance could potentially translate to orientation, though it is not clear. The notion of the proxy reaching into an environment to generate large slave forces may not translate to orientation – the noncommuting nature of rotation complicates any but the most trivial rotations. However, position doesn't scale with orientation like it does with rectilinear motion; a full turn of a joint

is 2π radians, no matter the size of the robot. It may be possible to exploit this property. In certain cases, it may also be desirable to use Pseudo-admittance control on end-effector position, while implementing another control scheme for orientation.

A promising application for Pseudo-admittance control is with systems with bandwidth limitations, providing for a system with less lag between the master and the slave than might otherwise be achieved with position control. Systems with large motion scaling and velocity limits at the slave, such as heavy hydraulic equipment, are often controlled with rate control, but may potentially be controlled more intuitively with Pseudo-admittance control. This may also be an application where Pseudo-admittance could be used to control end-effector position (because of the large position scaling), but not end-effector orientation (since the lack of position scaling in rotation may not require the steady-hand properties of Pseudo-admittance control). Slow-moving parallel robots with compact workspaces could also potentially be controlled with a Pseudo-admittance control scheme implemented on a simple impedance-type haptic device; the method should be extended to systems where one or both of the robots is not a serial link robot.

In conclusion, while significant advances were made in this dissertation regarding virtual fixtures for bilateral telemanipulation, there are many interesting problems that remain in this field of research. Once one starts to visualize the world in terms of virtual fixtures, it is hard to imagine a task where virtual fixtures couldn't lead to improvements. They provide the creative engineer with tools to push the boundary of what is possible with human-machine systems.

Appendix A

Haptic Paddles

We have constructed a 1-DOF bilateral telemanipulator based on a haptic device known as the Haptic Paddle [74]. This system is used as a bilateral telemanipulator in Chapters 2 and 4, and the master device is used as a haptic display in Chapter 3. In this appendix we present the details of the electromechanical system, and develop the device models used in Chapters 2-4.

A.1 Electromechanical Device

The master and slave Haptic Paddles are geometrically identical, with a paddle rotation of one radian corresponding to a motion at the load cell with an arclength of 115 mm. The Haptic Paddles considered here have been modified from their original design [74] with Maxon DC motors (model 118754) with 500-counts-per-turn Hewlett Packard encoders. We have also added Entran ± 10 -N load cells (model ELFS-T3E-10N) to measure the applied user and environment forces. Delrin caps

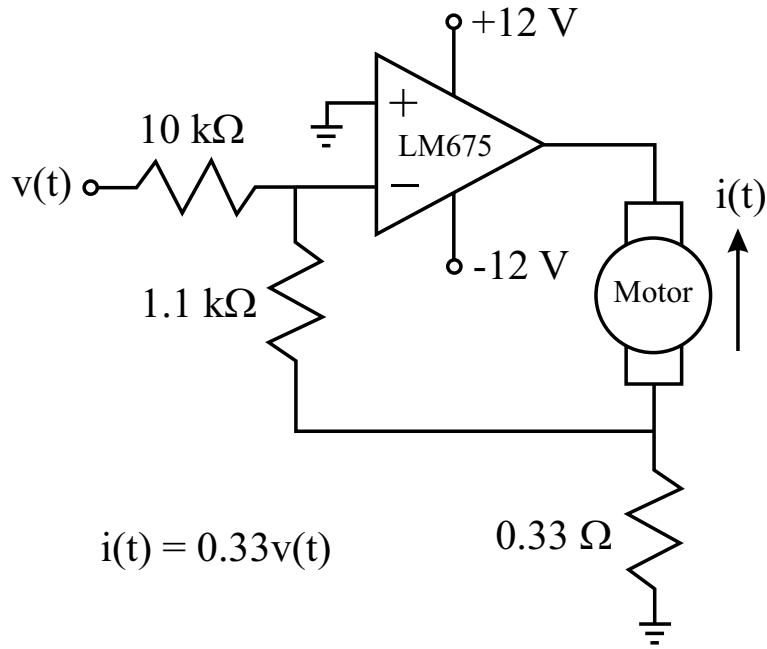


Figure A.1: Current amplifier.

were added to thermally insulate each load cell. The telemanipulation system is shown in Fig. 2.5. The device properties are typical of haptic displays (backdrivable, low friction, low inertia, low backlash). We use the PCI-DAS6402 data acquisition card from Measurement Computing Inc. to output voltages to the motor amplifiers and to input voltages from the load cells. The 16-bit D/A is configured for ± 10 V, and the 16-bit A/D is configured for ± 1.25 V. The output of the D/A is passed through current amplifiers that give a current through the motor that is proportional to the D/A voltage ($i = 0.33v$); the current amplifiers are built around the National Semiconductor LM675 power op-amp; the current amplifier is shown in Fig. A.1. This gives us direct control of applied torque on the motor. The resulting system has a force felt at the driving point that is proportional to the output voltage (1.65

N/V) statically. The signal from the load cells are passed through instrumentation amplifiers (Burr-Brown INA103) with a gain of 5 before they are read by the A/D. We use the PCI-Quad04, also from Measurement Computing, to interface with the encoders. The virtual-wall control loop is implemented at a maximum rate of 1000 Hz ($T = 0.001$ seconds), and the highest position resolution at the driving point is $\Delta = 2.24 \times 10^{-5}$ meters. A Velcro finger loop is included on the master device, similar to those found on the daVinci™Surgical System [31].

A.2 Device Models

In the bilateral telemanipulation system of Chapter 2, the master and slave devices are modeled as masses with viscous friction. In Chapter 3, the master device is used as a haptic display – it is modeled as a mass with Coulomb-plus-viscous friction. In Chapter 4, the slave is modeled as in Chapter 2, and the master is modeled as in Chapter 3.

A.2.1 Mass with Viscous Friction

We begin by modeling our telemanipulator master and slave as masses with viscous friction. The Haptic Paddle is a rotational system, but we can find the equivalent linear system felt at the load cell as it moves along an arc. At every instant in time, when in motion, the unactuated device should follow

$$m\ddot{x}(t) = f(t) - b\dot{x}(t) \tag{A.1}$$

where m is the effective mass of the device (kg), b is the effective damping in the device (Ns/m), x is the position of the device along the arc (m), and f is the externally applied force along the arc (N). By sampling the system at many instances, we may construct the matrix equation

$$[\ddot{\mathbf{x}} \quad \dot{\mathbf{x}}][m \quad b]^T = \mathbf{f}$$

This system can be written compactly with a data matrix \mathbf{D} and a parameter vector \mathbf{p} :

$$\mathbf{D}\mathbf{p} = \mathbf{f}$$

The best estimate of the parameter vector, in a least-squares sense, is found using a pseudoinverse based on the singular value decomposition of \mathbf{D} [99] (also known as the Moore-Penrose generalized inverse [41]):

$$\mathbf{p} = \mathbf{D}^\dagger \mathbf{f}$$

To construct the \mathbf{D} matrix, we “randomly” forced the device while holding the Velcro finger loop on the load cell, mitigating the effect of torques on the load cell (the Velcro finger loop was attached to the slave device as well for modeling purposes). Four runs of data were taken, with the load cell unloaded and recalibrated between each run – this was done to mitigate the effects of drift in the force measurement. Position and force data were recorded at each sample, and the position data was then used to construct the velocity and acceleration data. Because of the “staircase” discontinuous position measurement, the position data was smoothed

off-line using a multiple-pass 3-point moving-average filter [95] before differentiation. The velocity data was also smoothed before differentiation. The data sets were finally stacked to create the \mathbf{D} matrix and the \mathbf{f} vector, with a total of nearly 100,000 samples.

The resulting best-fit parameters are $m_m = 0.035$ kg and $b_m = 0.41$ Ns/m ($r^2 = 0.92$), and $m_s = 0.034$ kg and $b_s = 0.49$ Ns/m ($r^2 = 0.91$), indicating a good fit of the model [51]. The damping parameters indicate the actual differences in these devices that were designed to be identical. The mass and friction values given above are for the devices without the Delrin cap or Velcro finger loop (note the location of the Delrin cap with respect to the load cell). Once the Delrin caps are included, and the Velcro finger loop is included on the master, the resulting masses are $m_m = 0.040$ kg and $m_s = 0.036$ kg. The distribution of the data indicated that the r^2 metric is appropriate as a measure of how well the model fits the data. Note that a perfect fit ($r^2 = 1$) is essentially unattainable because of the noisy force and position measurements. Figure A.2 shows the fit of the data for the master device.

A.2.2 Mass with Coulomb-Plus-Viscous Friction

Next, we model our master device as a mass with Coulomb-plus-viscous friction. We use the same data gathered above. At every instant in time, when the device is in motion, the unactuated system should follow

$$m\ddot{x}(t) = f_h(t) - b\dot{x}(t) - f_c\text{sgn}(\dot{x}(t))$$

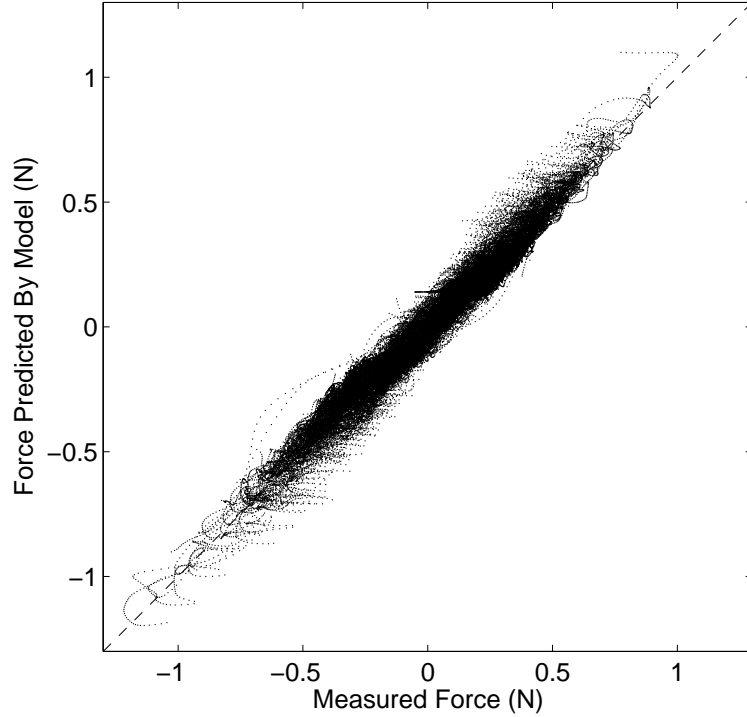


Figure A.2: Plot showing that the r^2 metric is appropriate for a mass-damper model of the Haptic Paddle. Data is shown for master device.

where f_c is the Coulomb friction in the device (N). By sampling the system at many instances, we may construct the matrix equation

$$\begin{bmatrix} \ddot{\mathbf{x}} & \dot{\mathbf{x}} & \text{sgn}(\dot{\mathbf{x}}) \end{bmatrix} \begin{bmatrix} m & b & f_c \end{bmatrix}^T = \mathbf{f}$$

This equation is then solved using the pseudoinverse technique described above. Note that the force $f_c \text{sgn}(\dot{x}(t))$ is only valid when $\dot{x}(t) \neq 0$. Because we never allowed the device to stay at rest while taking data, the samples occurring at zero velocity are few, and should have little effect on the resulting least-squares solution.

The resulting best-fit parameters are $m = 0.035$ kg, $b = 0.15$ Ns/m, and $f_c = 0.12$ N, with $r^2 = 0.95$, indicating a very good fit of the model. Again, the distribution of the data indicated that the r^2 metric is appropriate as a measure of how well

the model fits the data. Once the Delrin cap is added (the Velcro finger loop is not used in Chapter 3), the resulting mass is $m = 0.037$ kg. The slave device was also modeled as a mass with Coulomb-plus-viscous friction, though the results are not used in this dissertation. The resulting best-fit parameters for the slave are $m = 0.034$ kg, $b = 0.23$ Ns/m, and $f_c = 0.12$ N, with $r^2 = 0.94$. After the addition of the Delrin cap, the mass of the slave increases to $m = 0.036$ kg.

A.3 Ideal Actuator Assumptions

In Section 3.4.4, we discussed the assumptions surrounding the ideal actuator in our model – that is, that the quantization in the actuator signal is small relative to the quantization effects of the position measurement, and that the bandwidth of the actuator is much faster than the sampling rate of the computer. It only makes sense to compare the force (D/A) resolution to the position resolution for a given virtual-wall stiffness, so we compute the force resolution for the virtual wall with a stiffness of 300 N/m, using the information provided in Section A.1. We find that the force resolution is 13 times finer than the position resolution for this stiffness – an order of magnitude better. For stiffer virtual walls, the force resolution will only improve relative to the position resolution (since a single step in quantized position corresponds to many steps in quantized force).

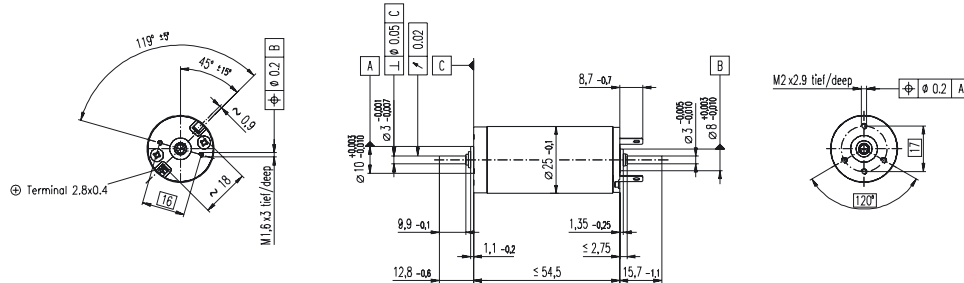
Next, we consider the rise time of the power amplifier. The bandwidth of the op-amp itself is many orders of magnitude faster than the other time constants in the system, so it will not be considered explicitly. For our system, the factors

limiting the actuator rise time are the inductance in the motor, and the saturation limits of the amplifier. Ideally, the inductance in the motor would have no effect when using a current amplifier, but this would require voltages that are well beyond the ± 12 -volt output limit of the amplifier. Therefore, when a constant current is commanded from the amplifier, the inductance in the motor forces the amplifier to saturate to its maximum achievable voltage, and the maximum rate of change in current is given by

$$\left(\frac{di}{dt}\right)_{\max} = \frac{v_{\max}}{L}$$

For our motor, the inductance is $L = 0.55$ mH, resulting in a maximum rate of change in current of 21800 A/s. For the longest rise time possible, we consider an instantaneous change in current command from 0 A to 3.3 A, the largest current we can command to our motor. For this scenario, the rise time would be 0.15 ms, which is 15% of the sampling period. In any practical application, we will not experience this worst-case scenario, and the rise time of the amplifier will be much faster, making the amplifier speed an order of magnitude faster than the sampling rate of the system. Increasing the supply voltage to the op-amp would also help to mitigate this effect. With the above considerations, we conclude that the modeling assumption of an ideal actuator is safe with respect to the other modeled elements in the system.

RE 25 Ø25 mm, Graphite Brushes, 20 Watt



M 1:2

- Stock program
- Standard program
- Special program (on request!)

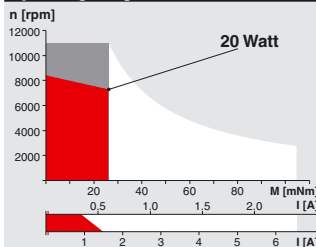
Order Number

		118749	118750	118751	118752	118753	118754	118755	118756	118757
according to dimensional drawing		302002	302003	302004	302005	302006	302007	302001	302008	302009
Shaft length 15.7 shortened to 4 mm										
Motor Data										
1	Assigned power rating	W	20	20	20	20	20	20	20	20
2	Nominal voltage	Volt	9.0	15.0	18.0	24.0	30.0	42.0	48.0	48.0
3	No load speed	rpm	10000	9650	10200	9550	9850	11100	10300	8230
4	Stall torque	mNm	232	225	220	243	249	283	264	210
5	Speed / torque gradient	rpm / mNm	46.5	44.7	47.9	40.2	40.3	39.7	39.6	39.7
6	No load current	mA	110	61	54	37	31	25	20	15
7	Starting current	mA	29100	15700	13500	10400	8720	7940	6030	3910
8	Terminal resistance	Ohm	0.309	0.953	1.33	2.32	3.44	5.29	7.96	12.6
9	Max. permissible speed	rpm	11000	11000	11000	11000	11000	11000	11000	11000
10	Max. continuous current	mA	1500	1500	1500	1210	992	800	652	519
11	Max. continuous torque	mNm	11.8	20.6	23.5	26.1	26.1	26.3	26.3	26.3
12	Max. power output at nominal voltage	mW	52000	52800	55500	58300	62200	80400	70200	44400
13	Max. efficiency	%	77	82	83	85	86	87	87	84
14	Torque constant	mNm / A	7.97	14.3	16.3	23.4	28.5	35.7	43.8	55
15	Speed constant	rpm / V	1200	669	585	407	335	268	218	173
16	Mechanical time constant	ms	5	5	5	4	4	4	4	4
17	Rotor inertia	gcm ²	11.3	10.0	9.11	10.3	10.1	10.1	10.0	9.96
18	Terminal inductance	mH	0.03	0.09	0.12	0.24	0.35	0.55	0.83	1.31
19	Thermal resistance housing-ambient	K / W	14	14	14	14	14	14	14	14
20	Thermal resistance rotor-housing	K / W	3.1	3.1	3.1	3.1	3.1	3.1	3.1	3.1
21	Thermal time constant winding	s	13	12	10	12	12	12	11	11

Specifications

- Axial play 0.05 - 0.15 mm
- Max. ball bearing loads
 - axial (dynamic) not preloaded 3.2 N
 - preloaded 16 N
 - radial (5 mm from flange) 64 N
 - Force for press fits (static) (static, shaft supported) 270 N
- Radial play ball bearing 0.025 mm
- Ambient temperature range -20 ... +100°C
- Max. rotor temperature +125°C
- Number of commutator segments 11
- Weight of motor 130 g
- 2 pole permanent magnet
- Values listed in the table are nominal. For applicable tolerances see page 43. For additional details please use the maxon selection program on the enclosed CD-ROM.

Operating Range



Comments

- Recommended operating range
 - Continuous operation
In observation of above listed thermal resistances (lines 19 and 20) the maximum permissible rotor temperature will be reached during continuous operation at 25°C ambient.
= Thermal limit.
 - Short term operation
The motor may be briefly overloaded (recurring).
- 118757 Motor with high resistance winding
118749 Motor with low resistance winding

Details on page 49

maxon Modular System

Overview on page 17 - 21

Planetary Gearhead
Ø26 mm
0.5 - 2.0 Nm
Details page 216

Planetary Gearhead
Ø32 mm
0.75 - 6.0 Nm
Details page 218 / 220

Planetary Gearhead
Ø32 mm
0.4 - 2.0 Nm
Details page 222

Recommended Electronics:
LSC 30/2 page 257
ADS 50/5 259
ADS_E 50/5 260
EPOS 24/5 271
MIP 10 273
Notes 17

Encoder MR
128 - 1000 CPT,
3 channels
Details page 238

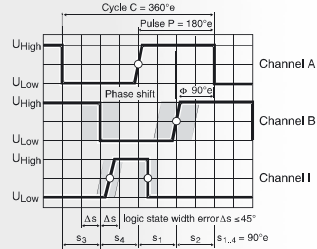
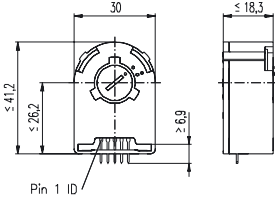
Encoder Enc
Ø22 mm
100 CPT, 2 channels
Details page 240

Encoder HED_ 5540
500 CPT,
3 channels
Details page 242 / 244

DC-Tacho DCT
Ø22 mm, 0.52 V
Details page 252

Brake AB
Ø40 mm
24 VDC, 0.4 Nm
Details page 279

Encoder HEDS 5540, 500 Counts per turn, 3 Channels



- Stock program
- Standard program
- Special program (on request!)

Order Number

110511	110513	110515	110517
--------	--------	--------	--------

Type

Counts per turn	500	500	500	500
Number of channels	3	3	3	3
Max. operating frequency (kHz)	100	100	100	100
Shaft diameter (mm)	3	4	6	8



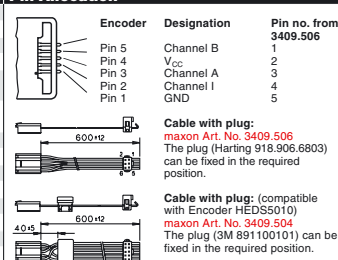
Combination

+ Motor	Page	+ Gearhead	Page	+ Brake	Page	Overall length [mm] / see: + Gearhead
RE 25, 10 W	77					75.3
RE 25, 10 W	77	GP 26, 0.5 - 2.0 Nm	216			•
RE 25, 10 W	77	GP 32, 0.75 - 6.0 Nm	218/220			•
RE 25, 10 W	77	GP 32, 0.4 - 2.0 Nm	222			•
RE 25, 20 W	78					75.3
RE 25, 20 W	78	GP 26, 0.5 - 2.0 Nm	216			•
RE 25, 20 W	78	GP 32, 0.75 - 6.0 Nm	218/220			•
RE 25, 20 W	78	GP 32, 0.4 - 2.0 Nm	222			•
RE 26, 18 W	79					77.2
RE 26, 18 W	79	GP 26, 0.5 - 2.0 Nm	216			•
RE 26, 18 W	79	GP 32, 0.75 - 6.0 Nm	218/220			•
RE 26, 18 W	79	GP 32, 0.4 - 2.0 Nm	222			•
RE 35, 90 W	81					91.9
RE 35, 90 W	81	GP 32, 0.75 - 6.0 Nm	219/220			•
RE 35, 90 W	81	GP 42, 3.0 - 15 Nm	224			•
RE 35, 90 W	81			AB 40	279	124.1
RE 35, 90 W	81	GP 32, 0.75 - 6.0 Nm	219/220	AB 40	279	•
RE 35, 90 W	81	GP 42, 3.0 - 15 Nm	224	AB 40	279	•
RE 36, 70 W	82					92.2
RE 36, 70 W	82	GP 32, 0.75 - 6.0 Nm	219/220			•
RE 36, 70 W	82	GP 32, 0.4 - 2.0 Nm	222			•
RE 36, 70 W	82	GP 42, 3.0 - 15 Nm	224			•
RE 40, 150 W	83					91.7
RE 40, 150 W	83	GP 42, 3.0 - 15 Nm	224			•
RE 40, 150 W	83	GP 52, 4.0 - 30 Nm	227			•
RE 40, 150 W	83			AB 40	279	124.2
RE 40, 150 W	83	GP 42, 3.0 - 15 Nm	224	AB 40	279	•
RE 40, 150 W	83	GP 52, 4.0 - 30 Nm	227	AB 40	279	•
RE 75, 250 W	84					241.5
RE 75, 250 W	84	GP 81, 20 - 120 Nm	230			•
RE 75, 250 W	84			AB 75	282	281.4
RE 75, 250 W	84	GP 81, 20 - 120 Nm	230	AB 75	282	•

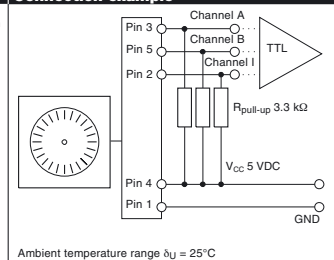
Technical Data

Supply voltage	5 V ± 10 %
Output signal	TTL compatible
Phase shift Φ (nominal)	90°e
Logic state width s	min. 45°e
Signal rise time (typical at $C_L = 25$ pF, $R_L = 2.7$ k Ω , 25°C)	180 ns
Signal fall time (typical at $C_L = 25$ pF, $R_L = 2.7$ k Ω , 25°C)	40 ns
Index pulse width (nominal)	90°e
Operating temperature range	-40 ... +100°C
Moment of inertia of code wheel	≤ 0.6 gcm ²
Max. angular acceleration	250 000 rad s ⁻²
Output current per channel	min. -1 mA, max. 5 mA

Pin Allocation



Connection example

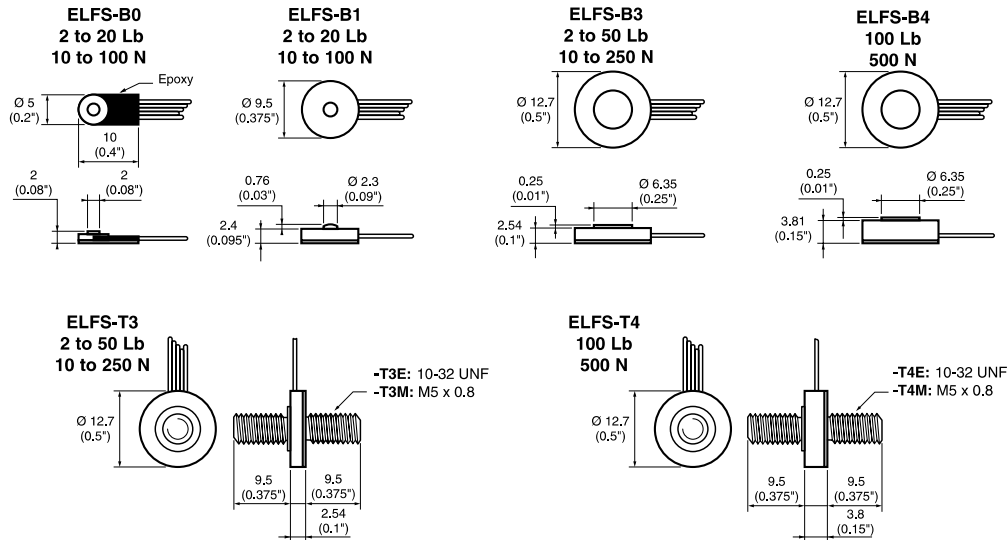


ELFS Series Load Cells

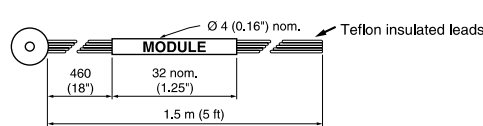


Subminiature - High Output

ELFS-B0, -B1, -B3, -B4, -T3 & -T4



WIRING



Dim: mm (inches)

ELFS Series

BODY STYLES	Lb RANGES "FS" (\pm for -T)	N RANGES "FS" (\pm for -T)	OVERRANGE LIMIT	OUTPUT "FSO" nom. type B0	OUTPUT "FSO" nom. types B1, B3, T3, T4 (\pm for -T)
ELFS-B0, -B1, -B3 & -T3	2	10	2x FS	100 mV	100 mV
ELFS-B0, -B1, -B3 & -T3	5	25	2x FS	100 mV	200 mV
ELFS-B0, -B1, -B3 & -T3	10	50	1.5x FS	100 mV	250 mV
ELFS-B0, -B1, -B3 & -T3	20	100	1.5x FS	100 mV	250 mV
ELFS-B3 & -T3	50	250	1.5x FS	not available	250 mV
ELFS-B4 & -T4	100	500	1.2x FS	not available	250 mV

EXCITATION: 15VDC
IMPEDANCE IN: 2000 Ω nom. (1500 Ω nom. for ELFS-B0)
IMPEDANCE OUT: 1000 Ω nom. (500 Ω nom. for ELFS-B0)
SENSING TECHNOLOGY: Semiconductor
NON-LINEARITY: $\pm 1\%$ FSO ($\pm 2\%$ FS for ELFS-B0)
HYSTERESIS: $\pm 1\%$ FSO
DEFLECTION AT "FS": $< 0.013\text{mm}$ ($< 0.0005\text{"}\text{) nom.}$
THERMAL ZERO SHIFT: $\pm 2.5\text{mV}/50^\circ\text{C}$ ($\pm 2.5\text{mV}/100^\circ\text{F}$)
THERMAL SENSITIVITY SHIFT (TSS): $\pm 2.5\%/50^\circ\text{C}$ ($\pm 2.5\%/100^\circ\text{F}$)
OPERATING TEMPERATURE: -40°C to 120°C (-40°F to 250°F)
COMPENSATED TEMPERATURE: 20°C to 80°C (70°F to 170°F)
ZERO OFFSET AT 20°C (70°F): $\pm 15\text{mV}$ typ.
MODE: -B: Compression (+Signal Output for Compression)
 -T: Tension/Compression (+Signal Output for Tension)
 -B: In Compression -T: In Tension
CALIBRATION: Stainless Steel
BODY MATERIAL:

"Off-the-Shelf" Stocking Program

<p>www.entran.com</p>	<p>ELFS LOAD CELLS Subminiature - High Output Smallest Size & Profile</p>	<p>Entran Sensors & Electronics USA: Fairfield, NJ UK: Garston, Watford, Herts, England Europe: Les Clayes-sous-Bois, France</p>		
		SPECIFICATION	ISSUE	PAGE
		ELFSS001U	PC0	1 of 2

ELFS specifications continued ...

Options and Accessories:

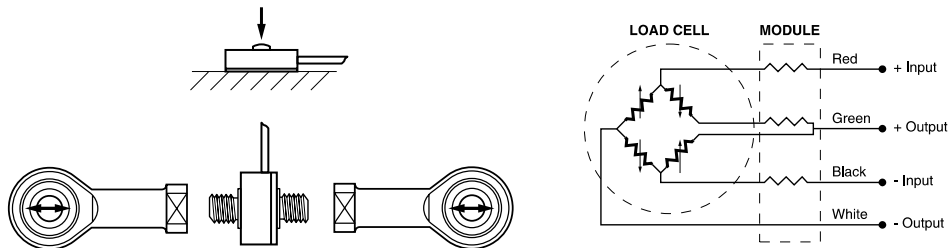
COMPENSATED TEMPERATURE RANGES:	STANDARD	= 20°C to 80°C (70°F to 170°F)
	Z1	= -20°C to 40°C (0°F to 100°F)
	Z2	= 0°C to 60°C (32°F to 140°F)
	Z4	= 40°C to 90°C (100°F to 200°F)
	Z*	= Non-standard, contact Entran
5 WIRE BRIDGE WIRING FOR ADJUSTABLE ZERO OFFSET:	5	= 5 Wire
EXCITATION VOLTAGE:	STANDARD	= 15VDC
	V00	= Replace "00" with Excitation between 1 and 15. If less than 15, Sensitivity (FSO) will decrease accordingly.
	V*	= Non-standard Excitation with standard FSO and non-standard TSS, contact Entran
SPECIAL LEAD LENGTH:	L00F	= Replace "00" with total length in feet.
	L00M	= Replace "00" with total length in meters.
SPECIAL MODULE LOCATION:	M00F	= Replace "00" with distance between sensor and module in feet.
	M00M	= Replace "00" with distance between sensor and module in meters.
WATERPROOFING LEAD EXIT	X	= Short term waterproofing. Limited to 105°C (220°F).
CONNECTOR WIRED TO LEADS:	C	= Microtech type male or equivalent (w/o mate)
	R	= RJ Telephone type male (w/o mate)
	RQ	= Pins to mate with MM50 screw terminals
MATING CONNECTORS FOR CONNECTOR OPTIONS:	See Cable and Connector Bulletin	
CALIBRATION:	STANDARD	-B: Compression -T: Tension
	Available	Tension & Compression calibration for -T body

Model Number construction:

ELFS Series	-	B1 Bodies	-	100 Range	N Units	-	/Z1/L2M/R Options
		B0 B1 B3 B4 T3E, T3M T4E, T4M		(K used for 1000 Ex.: 1K)	N=Newtons L=Pounds		C, R or RQ L00F or L00M M00F or M00M V1 thru V15 or V* X Z1, Z2, Z4, or Z* 5

Off-the-Shelf Stocking Program

Mounting & Wiring:



Entran®	ELFS LOAD CELLS	SPECIFICATION	ISSUE	PAGE
		ELFSS001U	PC0	2 of 2

Appendix B

Discrete State-Space Model

Here we generate the discrete state-space system of Section 2.4.1. The sampled-data system that contains the bilateral telemanipulator, the virtual fixtures, and the human user, can be modeled as a discrete system, under the assumption that the external inputs to the system can be modeled as constant throughout one sampling period. The model assumes a constant sampling period of T . It assumes the master and slave devices can both be modeled as mass-damper systems with masses m_m and m_s , and dampers b_m and b_s , respectively. It also assumes the human can be modeled as a mass-spring-damper, as in (2.2). The control system gains used in this model are defined in (2.25) and (2.26). All units are assumed to be in *S.I.*

The system is of the form

$$\mathbf{x}(k+1) = \mathbf{A}\mathbf{x}(k) + \mathbf{B}\mathbf{u}(k) \tag{B.1}$$

where the state vector and input vector of the system are given by

$$\mathbf{x}(k) = \begin{bmatrix} X_m(k) \\ X_m(k-1) \\ X_m(k-2) \\ X_s(k) \\ X_s(k-1) \\ X_s(k-2) \\ F_h^*(k-1) \\ F_e(k-1) \end{bmatrix}, \quad \mathbf{u}(k) = \begin{bmatrix} F_h^*(k) \\ F_e(k) \end{bmatrix} \quad (\text{B.2})$$

The A and B matrices are given as:

$$A = \begin{bmatrix} A_{11} & A_{12} & A_{13} & A_{14} & A_{15} & A_{16} & A_{17} & A_{18} \\ 1 & 0 & 0 & 0 & 0 & 0 & 0 & 0 \\ 0 & 1 & 0 & 0 & 0 & 0 & 0 & 0 \\ A_{41} & A_{42} & A_{43} & A_{44} & A_{45} & A_{46} & A_{47} & A_{48} \\ 0 & 0 & 0 & 1 & 0 & 0 & 0 & 0 \\ 0 & 0 & 0 & 0 & 1 & 0 & 0 & 0 \\ 0 & 0 & 0 & 0 & 0 & 0 & 0 & 0 \\ 0 & 0 & 0 & 0 & 0 & 0 & 0 & 0 \end{bmatrix}, \quad B = \begin{bmatrix} B_{11} & B_{12} \\ 0 & 0 \\ 0 & 0 \\ B_{41} & B_{42} \\ 0 & 0 \\ 0 & 0 \\ 1 & 0 \\ 0 & 1 \end{bmatrix} \quad (\text{B.3})$$

We now present the algorithm to numerically generate the A and B matrix values. It is to be implemented sequentially, as given in (B.4)-(B.46).

$$m_{hm} = m_h + m_m \quad (\text{B.4})$$

$$b_{hm} = b_h + b_m \quad (\text{B.5})$$

$$\phi_1 = \frac{b_{hm}}{2m_{hm}} \quad (\text{B.6})$$

$$\phi_2 = \sqrt{\frac{k_h}{m_{hm}} - \phi_1^2} \quad (\text{B.7})$$

In the case where $\phi_2 = 0$, ϕ_3 and ϕ_4 are computed with the equations

$$\phi_3 = 1 - e^{-\phi_1 T}(1 + \phi_1 T) \quad (\text{B.8})$$

$$\phi_4 = e^{-2\phi_1 T} + e^{-\phi_1 T}(\phi_1 T - 1) \quad (\text{B.9})$$

Otherwise, they are computed as

$$\phi_3 = 1 - e^{-\phi_1 T} \cos(\phi_2 T) - \frac{\phi_1}{\phi_2} e^{-\phi_1 T} \sin(\phi_2 T) \quad (\text{B.10})$$

$$\phi_4 = e^{-2\phi_1 T} + \frac{\phi_1}{\phi_2} e^{-\phi_1 T} \sin(\phi_2 T) - e^{-\phi_1 T} \cos(\phi_2 T) \quad (\text{B.11})$$

Continuing,

$$\phi_5 = -2e^{-\phi_1 T} \cos(\phi_2 T) \quad (\text{B.12})$$

$$\phi_6 = e^{-2\phi_1 T} \quad (\text{B.13})$$

$$\phi_7 = \frac{\phi_3}{k_h} \quad (\text{B.14})$$

$$\phi_8 = \frac{\phi_4}{k_h} \quad (\text{B.15})$$

$$\theta_1 = \frac{b_s}{m_s} \quad (\text{B.16})$$

$$\theta_2 = -e^{-\theta_1 T} - 1 \quad (\text{B.17})$$

$$\theta_3 = e^{-\theta_1 T} \quad (\text{B.18})$$

$$\theta_4 = \frac{\theta_1 T - 1 + e^{-\theta_1 T}}{b_s \theta_1} \quad (\text{B.19})$$

$$\theta_5 = \frac{1 - e^{-\theta_1 T} - \theta_1 T e^{-\theta_1 T}}{b_s \theta_1} \quad (\text{B.20})$$

$$\eta_1 = \frac{K_{dm} + K_{vm}}{T} + K_{pmm} \quad (\text{B.21})$$

$$\eta_2 = -\frac{K_{dm} + K_{vm}}{T} \quad (\text{B.22})$$

$$\eta_3 = -\frac{K_{dm}}{T} - K_{pm3} \quad (\text{B.23})$$

$$\eta_4 = \frac{K_{dm}}{T} \quad (\text{B.24})$$

$$\rho_1 = -\frac{K_{ds} + K_{vs}}{T} - K_{pss} \quad (\text{B.25})$$

$$\rho_2 = \frac{K_{ds} + K_{vs}}{T} \quad (\text{B.26})$$

$$\rho_3 = \frac{K_{ds}}{T} + K_{ps1} \quad (\text{B.27})$$

$$\rho_4 = -\frac{K_{ds}}{T} \quad (\text{B.28})$$

$$A_{11} = -\phi_7\eta_1 - \phi_5 \quad (\text{B.29})$$

$$A_{12} = -\phi_7\eta_2 - \phi_8\eta_1 - \phi_6 \quad (\text{B.30})$$

$$A_{13} = -\phi_8\eta_2 \quad (\text{B.31})$$

$$A_{14} = -\phi_7\eta_3 \quad (\text{B.32})$$

$$A_{15} = -\phi_7\eta_4 - \phi_8\eta_3 \quad (\text{B.33})$$

$$A_{16} = -\phi_8\eta_4 \quad (\text{B.34})$$

$$A_{17} = \phi_8 \quad (\text{B.35})$$

$$A_{18} = -\phi_8 K_{fm} \quad (\text{B.36})$$

$$A_{41} = \theta_4\rho_3 \quad (\text{B.37})$$

$$A_{42} = \theta_4\rho_4 + \theta_5\rho_3 \quad (\text{B.38})$$

$$A_{43} = \theta_5\rho_4 \quad (\text{B.39})$$

$$A_{44} = \theta_4\rho_1 - \theta_2 \quad (\text{B.40})$$

$$A_{45} = \theta_4 \rho_2 + \theta_5 \rho_1 - \theta_3 \quad (\text{B.41})$$

$$A_{46} = \theta_5 \rho_2 \quad (\text{B.42})$$

$$A_{47} = 0 \quad (\text{B.43})$$

$$A_{48} = -\theta_5 \quad (\text{B.44})$$

$$B_{41} = 0 \quad (\text{B.45})$$

$$B_{42} = -\theta_4 \quad (\text{B.46})$$

This algorithm requires both $m_{hm} \neq 0$ and $m_s \neq 0$, which will never be violated for a real system. Careful inspection of the equations for ϕ_7 and ϕ_8 reveals the condition that $k_h \neq 0$. This is a representational singularity, and setting these stiffness values to a negligible nonzero value will avoid the singularity and have no effect on the total system response.

Appendix C

Trajectories That Minimize Energy Losses Due to Friction

We present two intuitive energy concepts used in the analysis in Chapter 3. These concepts increase our knowledge about trajectories that minimize friction losses over one sampling period. The result is that, for the trajectory (with fixed starting and ending states) that minimizes energy losses due to friction, the component of friction due to Coulomb friction will be constant in magnitude and direction.

C.1 Monotonic Trajectories

We first show that when moving the unactuated haptic device of Section 3.3 from any given initial state $(x(0), \dot{x}(0))$ consisting of position and velocity to any given final state $(x(T), \dot{x}(T))$, the trajectory $x(t)$ that minimizes energy losses due to friction is monotonic. We assume without loss of generality that $x(T) \geq x(0)$,

and the monotonic trajectory is therefore nondecreasing, *i.e.* $\dot{x}(t) \geq 0 \forall t \in [0, T]$.

The energy losses for the trajectory $x(t)$ due to Coulomb friction are found by

$$W_{cf} = \int_0^T f_c |\dot{x}(t)| dt$$

A lower bound on the Coulomb losses is found with

$$f_c \int_0^T |\dot{x}(t)| dt \geq f_c \left| \int_0^T \dot{x}(t) dt \right| \quad (\text{C.1})$$

where equality is reached only when $x(t)$ is monotonic [100].

The energy losses due to viscous friction are also minimized when $x(t)$ is nondecreasing. The argument to prove this is simple: given any continuous but otherwise arbitrarily complicated trajectory $x_1(t)$, in which $\exists t \in [0, T]$ such that $\dot{x}_1(t) < 0$, we can easily construct a nondecreasing trajectory $x_2(t)$ with smaller viscous friction losses than those due to $x_1(t)$. We will construct $x_2(t)$ by parameterizing $x_1(t)$ along the trajectory:

$$x_2(t) = \frac{x_1(T) - x_1(0)}{\int_0^T |\dot{x}_1(s)| ds} \int_0^t |\dot{x}_1(s)| ds \quad (\text{C.2})$$

The losses due to viscous friction are found by

$$W_{vf_i} = \int_0^T b \dot{x}_i^2(t) dt \quad (\text{C.3})$$

To show that the viscous friction losses in $x_2(t)$ are smaller than those in $x_1(t)$, it follows from (C.3) that it is sufficient to show that $\dot{x}_2^2(t) < \dot{x}_1^2(t) \forall t$. Differentiating (C.2) and squaring gives

$$\dot{x}_2^2(t) = \left(\frac{x_1(T) - x_1(0)}{\int_0^T |\dot{x}_1(s)| ds} \right)^2 \dot{x}_1^2(t)$$

resulting in

$$\frac{W_{vf_2}}{W_{vf_1}} < 1$$

It should be noted that creating $x_2(t)$ as a parametrization of $x_1(t)$ in this way results in a discontinuity in $\dot{x}_2(t)$ at the endpoints. That is to say, $\dot{x}_2(0) \neq \dot{x}_2(0^+)$ and $\dot{x}_2(T) \neq \dot{x}_2(T^-)$. This is not a problem if impulsive forces, which create this type of discontinuity in velocity, are considered. The impulses needed to create $x_2(t)$ occur over infinitesimal distances, so they result in no energy losses due to either Coulomb or viscous friction. These impulses represent the limiting behavior of bounded continuous forces.

C.2 No Resting

The previous result shows that when moving the unactuated haptic display from any initial state to any final state, the trajectory that minimizes energy losses due to friction is monotonic. This essentially means the mass may not turn around, but it could potentially stop for some duration of time. In this section we prove that the trajectory that minimizes energy losses due to friction is one that contains no finite periods of zero velocity (*i.e.*, any stops that the trajectory may contain are of infinitesimal duration). We show this by taking any arbitrary trajectory that contains periods of rest, and constructing a trajectory with no resting that results in less frictional losses than the original.

Consider Fig. C.1. The trajectory $x_1(t)$ has zero velocity for time $t = T'$ to $t = T$, and is monotonic but otherwise arbitrary before $t = T'$. No Coulomb or

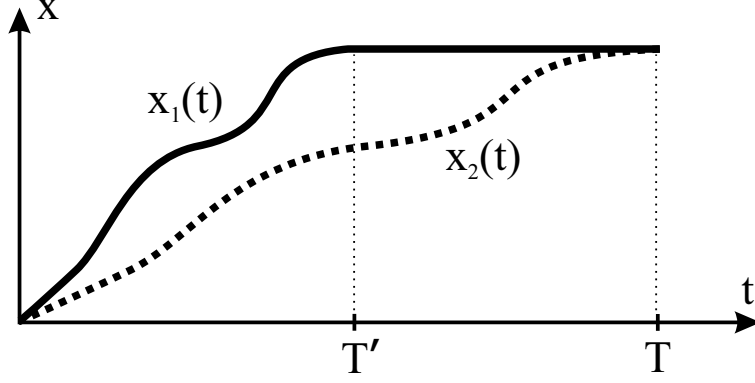


Figure C.1: The dynamic portion of $x_1(t)$ is stretched in time to create $x_2(t)$, containing no resting region.

viscous frictional losses are experienced during the rest phase, so the two losses can be expressed, respectively, as

$$W_{cf1} = \int_0^{T'} f_c |\dot{x}_1(t)| dt$$

$$W_{vf1} = \int_0^{T'} b \dot{x}_1^2(t) dt$$

Now construct the trajectory $x_2(t)$ by stretching the dynamic portion of $x_1(t)$ in time:

$$x_2(t) = x_1\left(\frac{T'}{T}t\right) \quad (\text{C.4})$$

Because both trajectories have the same length (given by $|x_1(T') - x_1(0)|$), their energy losses due to Coulomb friction are equal ($W_{cf2} = W_{cf1}$). The viscous losses in $x_2(t)$ are found by

$$W_{vf2} = \int_0^T b \left(\frac{d}{dt}x_2(t)\right)^2 dt \quad (\text{C.5})$$

This is simply a restatement of (C.3). We will consider the change of variables

$$s = \frac{T'}{T}t$$

which, when combined with (C.4) and (C.5), results in

$$W_{vf2} = \frac{T'}{T} \int_0^{T'} b \left(\frac{d}{ds} x_1(s) \right)^2 ds$$

Therefore, we can conclude that the viscous losses in $x_2(t)$ are less than those of $x_1(t)$, since

$$\frac{W_{vf2}}{W_{vf1}} = \frac{T'}{T} < 1$$

Now that the total friction losses in $x_2(t)$ are found to be less than those in $x_1(t)$, we can apply this result to a monotonic but otherwise arbitrary trajectory with more than one period of rest: simply break the trajectory into segments that contain only one period of rest, and then stretch each segment in time as described above. We also note that including the resting region of $x_1(t)$ at the beginning rather than end would not change the result.

Appendix D

Linearizing and Decoupling

Control

A linearizing and decoupling control law, also known as the computed-torque method, is used in Chapter 5. The details of the following linearizing and decoupling control scheme are found in Craig [22].

A general serial-link robot is described by the dynamic equation

$$M(\Theta)\ddot{\Theta} + Q(\Theta, \dot{\Theta}) = \Upsilon_a + J^T(\Theta)F_{\text{ext}} \quad (\text{D.1})$$

where Θ is the vector of generalized joint variables, $M(\Theta)$ is the positive-definite mass matrix, and $Q(\Theta, \dot{\Theta})$ is a vector containing Coriolis and centrifugal terms, as well as gravity effects and joint friction. The vector Υ_a represents the generalized joint actuator torques, the vector F_{ext} represents the force that is externally applied to the end effector, and $J(\Theta)$ is the manipulator Jacobian, expressed in the same frame as F_{ext} .

The robot always has a defined Jacobian matrix mapping the joint velocities to the Cartesian velocity of the end-effector:

$$\dot{X} = J(\Theta)\dot{\Theta} \quad (\text{D.2})$$

where the Jacobian is written in the same frame as X . This Jacobian (when square) is invertible whenever the robot is not in a singular configuration. We use the product rule to obtain

$$\ddot{X} = J(\Theta)\ddot{\Theta} + \dot{J}(\Theta)\dot{\Theta} \quad (\text{D.3})$$

which is needed in the development.

We can express the robot dynamics as a Cartesian robot of the form

$$M_x(\Theta)\ddot{X} + Q_x(\Theta, \dot{\Theta}) = F_a + F_{\text{ext}} \quad (\text{D.4})$$

where F_a is the effective controller force vector at the end-effector, which is converted to joint actuator torques using

$$\Upsilon_a = J^T(\Theta)F_a \quad (\text{D.5})$$

The Cartesian matrices are constructed as

$$M_x(\Theta) = J^{-T}(\Theta)M(\Theta)J^{-1}(\Theta) \quad (\text{D.6})$$

$$Q_x(\Theta, \dot{\Theta}) = J^{-T}(\Theta)(Q(\Theta, \dot{\Theta}) - M(\Theta)J^{-1}(\Theta)\dot{J}(\Theta)\dot{\Theta}) \quad (\text{D.7})$$

Note this Cartesian formulation requires an invertible Jacobian.

A serial link Cartesian robot of (D.4) can be made to appear (to the controller) like a unit-mass linear and decoupled Cartesian robot:

$$\ddot{X} = F_c + M_x^{-1}(\Theta)F_{\text{ext}} \quad (\text{D.8})$$

where F_c is the controller force that is designed assuming a linear and decoupled unit-mass robot. This is accomplished by applying an actuator force of the form:

$$F_a = M_x(\Theta)F_c + Q_x(\Theta, \dot{\Theta}) \quad (\text{D.9})$$

Note that this linearizing and decoupling control law does not cancel the dynamics of the robot; this is evident from the presence of the Cartesian inertia matrix in (D.8). It does allow any additional controller to be designed for a unit-mass, decoupled system – that is, in (D.8), F_c controls \ddot{X} directly in the absence of any external disturbances.

Appendix E

Adaptive Identification of PHANToM Parameters

To obtain accurate models of the PHANToM Premium 1.5 and PHANToM Premium 1.0 robots used in Chapter 5, we synthesized two prior works. Çavuşoğlu *et al.* [15] give a kinematic and dynamic model of the PHANToM 1.5 robot, and they give estimates of the parameter values in the model. The PHANToM 1.0 robot has the same kinematic and dynamic model as the PHANToM 1.5, but it is a smaller robot, with different parameter values. Craig *et al.* [23] give an adaptive parameter-identification algorithm for a serial-link robot. The estimates of the robot parameters asymptotically converge to the true values, provided the initial guesses for the parameters are sufficiently close to their true values, and provided the system receives persistent excitation.

We incorporated the model of [15] into the algorithm of [23]; we also included

a friction estimate for each joint, which was not done in [15]. Using the parameter estimates from [15] as initial guesses, the parameters for our PHANToM 1.5 robot were found with the adaptive algorithm. The algorithm was then used to find the parameters for the PHANToM 1.0, for which we did not have accurate initial guesses. For both devices, the parameters obtained from the adaptive algorithm provide for effective gravity compensation throughout the workspace, as well as making the system dynamics consistent throughout the workspace, supporting the validity of the parameters obtained.

For the duration of this appendix, we use the notation $s\theta = \sin(\theta)$, $c\theta = \cos(\theta)$, $t\theta = \tan(\theta)$.

E.1 PHANToM Model

This section is provided as a supplement to the work of Çavuşoğlu *et al.* [15]. The equations from that work that are relevant to the experiments and simulations of Chapter 5 are presented and expanded upon here.

Figure E.1 shows the kinematic model used for the PHANToM robots in this section. The homogeneous transformation relating a point in the tool frame to a point in the world frame is

$${}^w_tT(\Theta) = \begin{bmatrix} c\theta_1 & -s\theta_1s\theta_3 & c\theta_3s\theta_1 & s\theta_1(l_1c\theta_2 + l_2s\theta_3) \\ 0 & c\theta_3 & s\theta_3 & l_2(1 - c\theta_3) + l_1s\theta_2 \\ -s\theta_1 & -c\theta_1s\theta_3 & c\theta_1c\theta_3 & -l_1 + c\theta_1(l_1c\theta_2 + l_2s\theta_3) \\ 0 & 0 & 0 & 1 \end{bmatrix} \quad (\text{E.1})$$

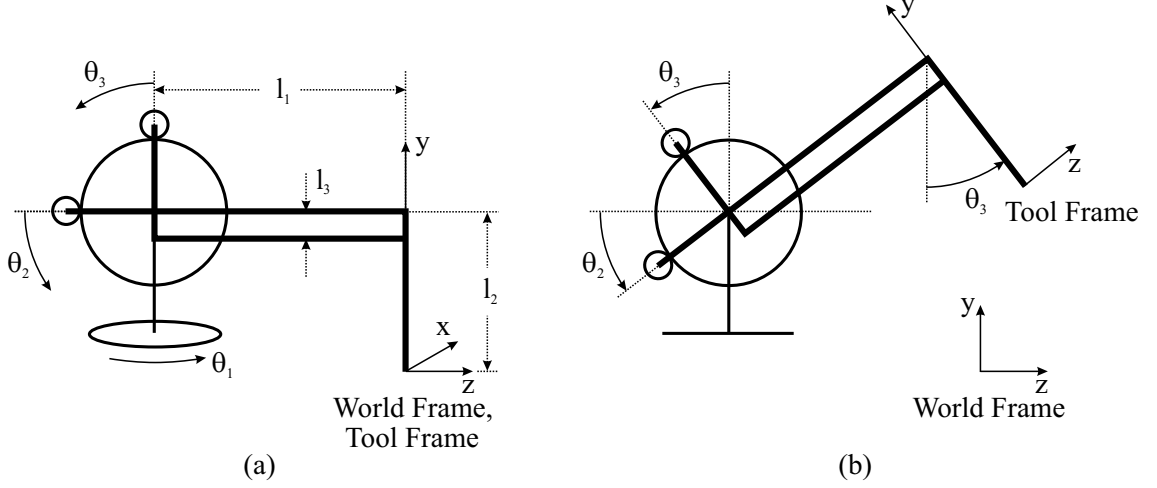


Figure E.1: Kinematic model of PHANToM robot. (a) Zero configuration. (b) Definition of angles and frames.

The Jacobian, expressed in the world frame, is computed as:

$$J(\Theta) = R(\Theta)J^b(\Theta) \quad (\text{E.2})$$

where

$$R(\Theta) = \begin{bmatrix} c\theta_1 & -s\theta_1 s\theta_3 & c\theta_3 s\theta_1 \\ 0 & c\theta_3 & s\theta_3 \\ -s\theta_1 & -c\theta_1 s\theta_3 & c\theta_1 c\theta_3 \end{bmatrix} \quad (\text{E.3})$$

$$J^b(\Theta) = \begin{bmatrix} l_1 c\theta_2 + l_2 s\theta_3 & 0 & 0 \\ 0 & l_1 \cos(\theta_2 - \theta_3) & 0 \\ 0 & -l_1 \sin(\theta_2 - \theta_3) & l_2 \end{bmatrix} \quad (\text{E.4})$$

and after multiplication:

$$J(\Theta) = \begin{bmatrix} c\theta_1(l_1 c\theta_2 + l_2 s\theta_3) & -l_1 s\theta_1 s\theta_2 & l_2 s\theta_1 c\theta_3 \\ 0 & l_1 c\theta_2 & l_2 s\theta_3 \\ -s\theta_1(l_1 c\theta_2 + l_2 s\theta_3) & -l_1 c\theta_1 s\theta_2 & l_2 c\theta_1 c\theta_3 \end{bmatrix} \quad (\text{E.5})$$

The time derivative of the Jacobian is needed for the linearizing and decoupling controller of Appendix D. We differentiate the Jacobian term-by-term to obtain $\dot{J}(\Theta, \dot{\Theta}) = [\dot{J}_{ij}(\Theta, \dot{\Theta})]$ ($i, j = (1, 2, 3)$):

$$\dot{J}_{11}(\Theta) = -l_1(\dot{\theta}_1 s\theta_1 c\theta_2 + \dot{\theta}_2 c\theta_1 s\theta_2) - l_2(\dot{\theta}_1 s\theta_1 s\theta_3 - \dot{\theta}_3 c\theta_1 c\theta_3) \quad (\text{E.6})$$

$$\dot{J}_{12}(\Theta) = -l_1(\dot{\theta}_1 c\theta_1 s\theta_2 + \dot{\theta}_2 s\theta_1 c\theta_2) \quad (\text{E.7})$$

$$\dot{J}_{13}(\Theta) = l_2(\dot{\theta}_1 c\theta_1 c\theta_3 - \dot{\theta}_3 s\theta_1 s\theta_3) \quad (\text{E.8})$$

$$\dot{J}_{21}(\Theta) = 0 \quad (\text{E.9})$$

$$\dot{J}_{22}(\Theta) = -l_1 \dot{\theta}_2 s\theta_2 \quad (\text{E.10})$$

$$\dot{J}_{23}(\Theta) = l_2 \dot{\theta}_3 c\theta_3 \quad (\text{E.11})$$

$$\dot{J}_{31}(\Theta) = -l_1(\dot{\theta}_1 c\theta_1 c\theta_2 - \dot{\theta}_2 s\theta_1 s\theta_2) - l_2(\dot{\theta}_1 c\theta_1 s\theta_3 + \dot{\theta}_3 s\theta_1 c\theta_3) \quad (\text{E.12})$$

$$\dot{J}_{32}(\Theta) = l_1(\dot{\theta}_1 s\theta_1 s\theta_2 - \dot{\theta}_2 c\theta_1 c\theta_2) \quad (\text{E.13})$$

$$\dot{J}_{33}(\Theta) = -l_2(\dot{\theta}_1 s\theta_1 c\theta_3 + \dot{\theta}_3 c\theta_1 s\theta_3) \quad (\text{E.14})$$

The PHANToM is built with mechanical joint limits, giving it unique inverse kinematics. For a given tool position $P = [p_x \ p_y \ p_z]$ in world coordinates, the joint values (in radians) are found as

$$\theta_1 = \text{atan2}(p_x, p_z + l_1) \quad (\text{E.15})$$

$$\theta_2 = \cos^{-1} \left(\frac{l_1^2 + r^2 - l_2^2}{2l_1 r} \right) + \text{atan2}(p_y - l_2, d) \quad (\text{E.16})$$

$$\theta_3 = \theta_2 + \cos^{-1} \left(\frac{l_1^2 + l_2^2 - r^2}{2l_1 l_2} \right) - \frac{\pi}{2} \quad (\text{E.17})$$

making use of the intermediate variables

$$d = \sqrt{p_x^2 + (p_z + l_1)^2} \quad (\text{E.18})$$

$$r = \sqrt{p_x^2 + (p_y - l_2)^2 + (p_z + l_1)^2} \quad (\text{E.19})$$

We use the dynamic model given in [15], plus we include additional joint friction parameters B_i ($i = (1, 2, 3)$) not found in [15]:

$$\begin{aligned} \begin{bmatrix} \tau_1 \\ \tau_2 \\ \tau_3 \end{bmatrix} &= \begin{bmatrix} M_{11} & 0 & 0 \\ 0 & M_{22} & M_{23} \\ 0 & M_{32} & M_{33} \end{bmatrix} \begin{bmatrix} \ddot{\theta}_1 \\ \ddot{\theta}_2 \\ \ddot{\theta}_3 \end{bmatrix} \\ &+ \begin{bmatrix} C_{11} + B_1 & C_{12} & C_{13} \\ C_{21} & B_2 & C_{23} \\ C_{31} & C_{32} & B_3 \end{bmatrix} \begin{bmatrix} \dot{\theta}_1 \\ \dot{\theta}_2 \\ \dot{\theta}_3 \end{bmatrix} + \begin{bmatrix} 0 \\ N_2 \\ N_3 \end{bmatrix} \end{aligned} \quad (\text{E.20})$$

where

$$\begin{aligned} M_{11} &= \frac{1}{8}(4I_{ayy} + 4I_{azz} + 8I_{baseyy} + 4I_{beyy} + 4I_{bezz} + 4I_{cyy} + 4I_{czz} + 4I_{dfyy} \\ &+ 4I_{dfzz} + 4l_1^2m_a + l_2^2m_a + l_1^2m_c + 4l_3^2m_c) + \frac{1}{8}(4I_{beyy} - 4I_{bezz} + 4I_{cyy} \\ &- 4I_{czz} + l_1^2(4m_a + m_c))\cos(2\theta_2) + \frac{1}{8}(4I_{ayy} - 4I_{azz} + 4I_{dfyy} - 4I_{dfzz} \\ &- l_2^2m_a - 4l_3^2m_c)\cos(2\theta_3) + l_1(l_2m_a + l_3m_c)c\theta_2s\theta_3 \end{aligned} \quad (\text{E.21})$$

$$M_{22} = I_{bexx} + I_{cexx} + l_1^2m_a + \frac{1}{4}l_1^2m_c \quad (\text{E.22})$$

$$M_{23} = -\frac{1}{2}l_1(l_2m_a + l_3m_c)\sin(\theta_2 - \theta_3) \quad (\text{E.23})$$

$$M_{32} = M_{23} \quad (\text{E.24})$$

$$M_{33} = I_{axx} + I_{dfxx} + \frac{1}{4}l_2^2m_a + l_3^2m_c \quad (\text{E.25})$$

$$\begin{aligned} C_{11} &= \frac{1}{8}(-2s\theta_2((4I_{beyy} - 4I_{bezz} + 4I_{cyy} - 4I_{czz} + 4l_1^2m_a + l_1^2m_c)c\theta_2 \\ &+ 2l_1(l_2m_a + l_3m_c)s\theta_3)\dot{\theta}_2 + 2c\theta_3(2l_1(l_2m_a + l_3m_c)c\theta_2 \\ &+ (-4I_{ayy} + 4I_{azz} - 4I_{dfyy} + 4I_{dfzz} + l_2^2m_a + 4l_3^2m_c)s\theta_3)\dot{\theta}_3) \end{aligned} \quad (\text{E.26})$$

$$\begin{aligned}
C_{12} &= -\frac{1}{8}((4I_{beyy} - 4I_{bezz} + 4I_{cyy} - 4I_{czz} + l_1^2(4m_a + m_c))\sin(2\theta_2) \\
&\quad + 4l_1(l_2m_a + l_3m_c)s\theta_2s\theta_3)\dot{\theta}_1
\end{aligned} \tag{E.27}$$

$$\begin{aligned}
C_{13} &= -\frac{1}{8}(-4l_1(l_2m_a + l_3m_c)c\theta_2c\theta_3 - (-4I_{ayy} + 4I_{azz} - 4I_{dfyy} \\
&\quad + 4I_{dfzz} + l_2^2m_a + 4l_3^2m_c)\sin(2\theta_3))\dot{\theta}_1
\end{aligned} \tag{E.28}$$

$$C_{21} = -C_{12} \tag{E.29}$$

$$C_{23} = \frac{1}{2}l_1(l_2m_a + l_3m_c)\cos(\theta_2 - \theta_3)\dot{\theta}_3 \tag{E.30}$$

$$C_{31} = -C_{13} \tag{E.31}$$

$$C_{32} = \frac{1}{2}l_1(l_2m_a + l_3m_c)\cos(\theta_2 - \theta_3)\dot{\theta}_2 \tag{E.32}$$

$$N_2 = \frac{1}{2}g(2l_1m_a + 2l_5m_{be} + l_1m_c)c\theta_2 \tag{E.33}$$

$$N_3 = \frac{1}{2}g(l_2m_a + 2l_3m_c - 2l_6m_{df})s\theta_3 \tag{E.34}$$

τ_i is the actuator torque on joint i , g is the acceleration due to gravity, assumed to be in the $-y$ direction, and the individual inertial parameters and centers of mass are defined in Fig. E.2.

E.2 Adaptive Algorithm

This section is provided as a supplement to the work by Craig *et al.* [23]. The pertinent equations from that work are presented and expanded upon here. We begin with a serial-link robot, which can be modeled as

$$\Upsilon = M(\Theta)\ddot{\Theta} + Q(\Theta, \dot{\Theta}) \tag{E.35}$$

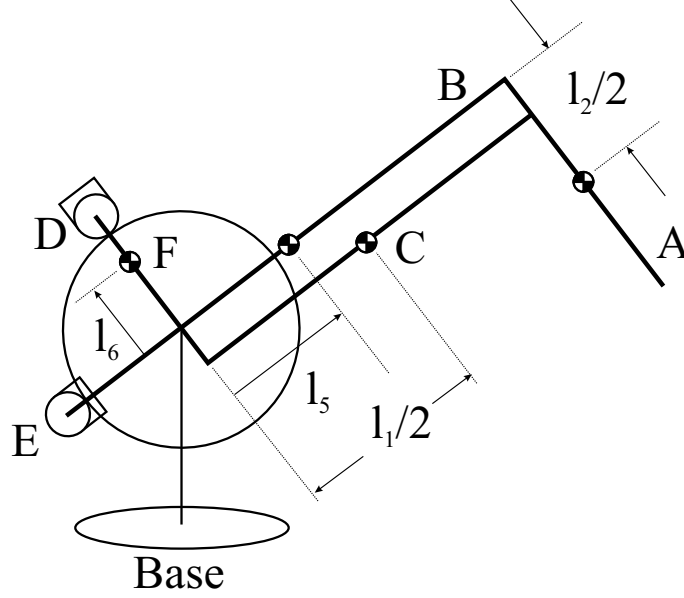


Figure E.2: Inertial model of the PHANToM.

where Υ is the $n \times 1$ vector of generalized joint torques, Θ is the $n \times 1$ vector of generalized joint positions, $M(\Theta)$ is the $n \times n$ manipulator mass matrix, and $Q(\Theta, \dot{\Theta})$ is the $n \times 1$ vector containing all other torques due to centrifugal, Coriolis, gravitational, and frictional forces. We assume that we have a kinematic and dynamic model of the robot. We also assume that we know all of the parameter values necessary for the kinematic model, but do not know all of the parameters in the dynamic model. This system is linear in the unknown parameters, and can be rewritten as

$$\Upsilon = W(\Theta, \dot{\Theta}, \ddot{\Theta})P \quad (\text{E.36})$$

where P is the $r \times 1$ vector of unknown parameters, and $W(\Theta, \dot{\Theta}, \ddot{\Theta})$ is an $n \times r$ matrix that has no dependence on the parameter vector P .

We will construct an estimate of the unknown parameters, and then design an

adaptive controller to asymptotically converge on the true parameter value. We will refer to our estimate of P at each instant in time as \hat{P} . Because we have a dynamic model, at each instant in time we can construct an estimate of the dynamic matrices as $\hat{M}(\Theta)$ and $\hat{Q}(\Theta, \dot{\Theta})$.

We use a control law

$$\Upsilon = \hat{M}(\Theta)\ddot{\Theta}^* + \hat{Q}(\Theta, \dot{\Theta}) \quad (\text{E.37})$$

where

$$\ddot{\Theta}^* = \ddot{\Theta}_d + K_v\dot{E} + K_pE \quad (\text{E.38})$$

$$E = \Theta_d - \Theta, \quad (\text{E.39})$$

Θ_d is a desired joint trajectory, and K_v and K_p are $n \times n$ constant, diagonal matrices with k_{vi} and k_{pi} on the diagonals.

We define a “filtered servo error” E_1 as

$$E_1 = \dot{E} + \Psi E \quad (\text{E.40})$$

where $\Psi = \text{diag}(\psi_1 \dots \psi_n)$ with $\psi_i > 0$. There is an additional constraint that ψ_i is chosen such that the transfer function

$$\frac{s + \psi_i}{s^2 + k_{vi}s + k_{pi}} \quad (\text{E.41})$$

is strictly positive real. This condition is equivalent to $\psi_i < k_{vi}$. We then implement the adaptation law

$$\dot{\hat{P}} = \Gamma W^T \hat{M}^{-1} E_1 \quad (\text{E.42})$$

where $\Gamma = \text{diag}(\gamma_1 \dots \gamma_r)$ and $\gamma_i > 0$. It is shown in [23] that this adaptive control algorithm has guaranteed parameter convergence under persistent excitation conditions.

E.3 Adaptive Algorithm Applied to PHANToMs

We now explain how the algorithm was applied to estimate the dynamic parameters of the PHANToM robots. In practice, convergence of the adaptive algorithm proved to be sensitive to the values assigned to K_v , K_p , Ψ , and Γ .

Using the dynamic model of Section E.1, we measured the three link lengths for the two robots. For the PHANToM 1.5:

$$l_1 = 0.210 \text{ m} \tag{E.43}$$

$$l_2 = 0.170 \text{ m} \tag{E.44}$$

$$l_3 = 0.032 \text{ m} \tag{E.45}$$

and for the PHANToM 1.0:

$$l_1 = 0.140 \text{ m} \tag{E.46}$$

$$l_2 = 0.100 \text{ m} \tag{E.47}$$

$$l_3 = 0.032 \text{ m} \tag{E.48}$$

We estimated the remaining $r = 20$ parameters. Our parameter vector $P \in \mathbb{R}^{20}$ is built as $P = [m_a \ I_{axx} \ I_{ayy} \ I_{azz} \ m_c \ I_{cxx} \ I_{cyy} \ I_{czz} \ l_5 m_{be} \ I_{bexx} \ I_{beyy} \ I_{bez z} \ l_6 m_{df} \ I_{dfxx} \ I_{dfyy} \ I_{dfzz} \ I_{baseyy} \ B_1 \ B_2 \ B_3]^T$, using the parameters defined in Section E.1. Note that we

have combined parameters as $l_5 m_{be}$ and $l_6 m_{df}$, since those variables only enter into the model in a coupled way.

To choose the $r = 20$ values for Γ , which determine the parameter convergence rates, we set

$$\gamma_i = c_\gamma P_i(0) \quad (\text{E.49})$$

where $P_i(0)$ is the initial guess of parameter P_i , and c_γ is the single user-set convergence gain. Because we had good initial guesses $P(0)$ from [15], this allowed the parameters to evolve at rates that were proportional to their size.

To construct the W matrix of (E.36), we use the PHANToM dynamics of (E.20,E.35), and take the partial derivatives of the joint torques with respect to the parameters:

$$W_{i,j} = \frac{\partial \tau_i}{\partial P_j} \quad (\text{E.50})$$

This formulation is correct because the parameters enter into the model linearly.

Using Mathematica for the symbolic differentiation, the W values are found as:

$$\begin{aligned} W_{1,1} &= \frac{1}{8}(4l_1^2 + l_2^2)\ddot{\theta}_1 - \frac{1}{2}\dot{\theta}_1\dot{\theta}_2\dot{\theta}_3c\theta_3s\theta_2(2l_1l_2c\theta_2 + l_2^2s\theta_3) \\ &\quad \cdot ((4I_{beyy} - 4I_{bezz} + 4I_{cyy} - 4I_{czz} + 4l_1^2m_a + l_1^2m_c)c\theta_2 \\ &\quad + 2l_1(l_2m_a + l_3m_c)s\theta_3) - \frac{1}{2}\dot{\theta}_1\dot{\theta}_2\dot{\theta}_3c\theta_3s\theta_2(4l_1^2c\theta_2 + 2l_1l_2s\theta_3) \\ &\quad \cdot (2l_1(l_2m_a + l_3m_c)c\theta_2 + (-4I_{ayy} + 4I_{azz} - 4I_{dfyy} + 4I_{dfzz} \\ &\quad + l_2^2m_a + 4l_3^2m_c)s\theta_3) - \frac{1}{8}\dot{\theta}_1\dot{\theta}_2(4l_1^2\sin(2\theta_2) + 4l_1l_2s\theta_2s\theta_3) \\ &\quad - \frac{1}{8}\dot{\theta}_1\dot{\theta}_3(-4l_1l_2c\theta_2c\theta_3 - l_2^2\sin(2\theta_3)) \quad (\text{E.51}) \\ W_{2,1} &= l_1^2\ddot{\theta}_2 + gl_1c\theta_2 + \frac{1}{2}l_1l_2\dot{\theta}_3^2\cos(\theta_2 - \theta_3) - \frac{1}{2}l_1l_2\ddot{\theta}_3\sin(\theta_2 - \theta_3) \end{aligned}$$

$$+\frac{1}{8}\dot{\theta}_1^2(4l_1^2\sin(2\theta_2) + 4l_1l_2s\theta_2s\theta_3) \quad (\text{E.52})$$

$$\begin{aligned} W_{3,1} &= \frac{1}{4}l_2^2\ddot{\theta}_3 - \frac{1}{2}l_1l_2\ddot{\theta}_2\sin(\theta_2 - \theta_3) \\ &+ \frac{1}{2}gl_2s\theta_3 + \frac{1}{8}\dot{\theta}_1^2(-4l_1l_2c\theta_2c\theta_3 - l_2^2\sin(2\theta_3)) \end{aligned} \quad (\text{E.53})$$

$$W_{3,2} = \ddot{\theta}_3 \quad (\text{E.54})$$

$$\begin{aligned} W_{1,3} &= \frac{1}{2}\ddot{\theta}_1 + 2\dot{\theta}_1\dot{\theta}_2\dot{\theta}_3c\theta_3s\theta_2s\theta_3((4I_{beyy} - 4I_{bezz} + 4I_{cyy} - 4I_{czz} + 4l_1^2m_a \\ &+ l_1^2m_c)c\theta_2 + 2l_1(l_2m_a + l_3m_c)s\theta_3) - \frac{1}{2}\dot{\theta}_1\dot{\theta}_3\sin(2\theta_3) \end{aligned}$$

$$W_{3,3} = \frac{1}{2}\dot{\theta}_1^2\sin(2\theta_3) \quad (\text{E.55})$$

$$\begin{aligned} W_{1,4} &= \frac{1}{2}\ddot{\theta}_1 - 2\dot{\theta}_1\dot{\theta}_2\dot{\theta}_3c\theta_3s\theta_2s\theta_3((4I_{beyy} - 4I_{bezz} + 4I_{cyy} - 4I_{czz} + 4l_1^2m_a \\ &+ l_1^2m_c)c\theta_2 + 2l_1(l_2m_a + l_3m_c)s\theta_3) + \frac{1}{2}\dot{\theta}_1\dot{\theta}_3\sin(2\theta_3) \end{aligned}$$

$$W_{3,4} = -W_{3,3} \quad (\text{E.56})$$

$$\begin{aligned} W_{1,5} &= \frac{1}{8}(l_1^2 + 4l_3^2)\ddot{\theta}_1 - \frac{1}{2}\dot{\theta}_1\dot{\theta}_2\dot{\theta}_3c\theta_3s\theta_2(2l_1l_3c\theta_2 + 4l_3^2s\theta_3) \\ &\cdot((4I_{beyy} - 4I_{bezz} + 4I_{cyy} - 4I_{czz} + 4l_1^2m_a + l_1^2m_c)c\theta_2 \\ &+ 2l_1(l_2m_a + l_3m_c)s\theta_3) - \frac{1}{2}\dot{\theta}_1\dot{\theta}_2\dot{\theta}_3c\theta_3s\theta_2(l_1^2c\theta_2 + 2l_1l_3s\theta_3) \\ &\cdot(2l_1(l_2m_a + l_3m_c)c\theta_2 + (-4I_{ayy} + 4I_{azz} - 4I_{dfyy} + 4I_{dfzz} \\ &+ l_2^2m_a + 4l_3^2m_c)s\theta_3) - \frac{1}{8}\dot{\theta}_1\dot{\theta}_2(l_1^2\sin(2\theta_2) + 4l_1l_3s\theta_2s\theta_3) \\ &- \frac{1}{8}\dot{\theta}_1\dot{\theta}_3(-4l_1l_3c\theta_2c\theta_3 - 4l_3^2\sin(2\theta_3)) \end{aligned} \quad (\text{E.57})$$

$$\begin{aligned} W_{2,5} &= \frac{1}{4}l_1^2\ddot{\theta}_2 + \frac{1}{2}gl_1c\theta_2 + \frac{1}{2}l_1l_3\dot{\theta}_3^2\cos(\theta_2 - \theta_3) - \frac{1}{2}l_1l_3\ddot{\theta}_3\sin(\theta_2 - \theta_3) \\ &+ \frac{1}{8}\dot{\theta}_1^2(l_1^2\sin(2\theta_2) + 4l_1l_3s\theta_2s\theta_3) \end{aligned} \quad (\text{E.58})$$

$$\begin{aligned} W_{3,5} &= l_3^2\ddot{\theta}_3 - \frac{1}{2}l_1l_3\ddot{\theta}_2\sin(\theta_2 - \theta_3) + gl_3s\theta_3 \\ &+ \frac{1}{8}\dot{\theta}_1^2(-4l_1l_3c\theta_2c\theta_3 - 4l_3^2\sin(2\theta_3)) \end{aligned} \quad (\text{E.59})$$

$$W_{2,6} = \ddot{\theta}_2 \quad (\text{E.60})$$

$$W_{1,7} = \frac{1}{2}\ddot{\theta}_1 - \frac{1}{2}\dot{\theta}_1\dot{\theta}_2\sin(2\theta_2) - 2\dot{\theta}_1\dot{\theta}_2\dot{\theta}_3c\theta_2c\theta_3s\theta_2(2l_1(l_2m_a + l_3m_c)c\theta_2) \\ + (-4I_{ayy} + 4I_{azz} - 4I_{dfyy} + 4I_{dfzz} + l_2^2m_a + 4l_3^2m_c)s\theta_3 \quad (\text{E.61})$$

$$W_{2,7} = \frac{1}{2}\dot{\theta}_1^2\sin(2\theta_2) \quad (\text{E.62})$$

$$W_{1,8} = \frac{1}{2}\ddot{\theta}_1 + \frac{1}{2}\dot{\theta}_1\dot{\theta}_2\sin(2\theta_2) + 2\dot{\theta}_1\dot{\theta}_2\dot{\theta}_3c\theta_2c\theta_3s\theta_2(2l_1(l_2m_a + l_3m_c)c\theta_2) \\ + (-4I_{ayy} + 4I_{azz} - 4I_{dfyy} + 4I_{dfzz} + l_2^2m_a + 4l_3^2m_c)s\theta_3 \quad (\text{E.63})$$

$$W_{2,8} = -W_{2,7} \quad (\text{E.64})$$

$$W_{2,9} = gc\theta_2 \quad (\text{E.65})$$

$$W_{2,10} = \ddot{\theta}_2 \quad (\text{E.66})$$

$$W_{1,11} = W_{1,7} \quad (\text{E.67})$$

$$W_{2,11} = W_{2,7} \quad (\text{E.68})$$

$$W_{1,12} = W_{1,8} \quad (\text{E.69})$$

$$W_{2,12} = W_{2,8} \quad (\text{E.70})$$

$$W_{3,13} = -gs\theta_3 \quad (\text{E.71})$$

$$W_{3,14} = \ddot{\theta}_3 \quad (\text{E.72})$$

$$W_{1,15} = W_{1,3} \quad (\text{E.73})$$

$$W_{3,15} = W_{3,3} \quad (\text{E.74})$$

$$W_{1,16} = W_{1,4} \quad (\text{E.75})$$

$$W_{3,16} = W_{3,4} \quad (\text{E.76})$$

$$W_{1,17} = \ddot{\theta}_1 \quad (\text{E.77})$$

$$W_{1,18} = \dot{\theta}_1 \quad (\text{E.78})$$

$$W_{2,19} = \dot{\theta}_2 \quad (\text{E.79})$$

$$W_{3,20} = \dot{\theta}_3 \quad (\text{E.80})$$

and $W_{i,j} = 0$ if not explicitly defined above.

The parameter update law of (E.42) requires the inverse of the estimate of the PHANToM mass matrix. The PHANToM mass-matrix inverse can be computed efficiently (see (E.20)) as:

$$M^{-1} = \begin{bmatrix} \frac{1}{M_{11}} & 0 & 0 \\ 0 & \frac{M_{33}}{\det} & \frac{-M_{23}}{\det} \\ 0 & \frac{-M_{23}}{\det} & \frac{M_{22}}{\det} \end{bmatrix} \quad (\text{E.81})$$

where $\det = M_{22}M_{33} - M_{23}^2$.

We ran our algorithm on a digital computer with a sampling period of $T = 0.002$ seconds. Because no velocity sensors are available on the PHANToM, an estimate of velocity must be computed from the position measurement obtained with an incremental optical encoder. The velocity estimate at sample k was computed with a backwards-difference approximation:

$$\dot{\theta}_i(k) = \frac{\theta_i(k) - \theta_i(k-1)}{T} \quad (\text{E.82})$$

and then passed through a digital first-order low-pass filter with a time constant of $5T$. The acceleration measurements were generated by taking a backwards-difference of these filtered velocity estimates. It was determined that very little filtering was required (or desirable) in the system. We found that the integrating nature of the

adaptive algorithm is robust to the noise in the velocity and acceleration measurements, but not to the phase lag incurred from filtering.

The gains that were used in the final implementation of this algorithm were $c_\gamma = 0.00002$, and $\psi_i = 10$, $k_{vi} = 60$ Nms/rad, $k_{pi} = 900$ Nm/rad $\forall i$. The servo gains were chosen for critical damping of the joints after dynamic compensation. As suggested in [15], bounds were put on the parameter evolution, such that they were not permitted to change by more than 50% from their initial guesses. This enforced stable operation throughout the run of the algorithm. If parameter convergence was not achieved, the initial guesses were changed in the (perceived) correct direction, and the algorithm was rerun. For persistent excitation, each of the joints was commanded to follow sinusoids whose magnitudes were chosen such that the robot moved throughout the workspace, and whose frequencies were chosen such that the overall robot trajectory was not periodic.

It was determined that the parameters had converged sufficiently when three criteria were met:

1. Plots of the individual parameters appeared to have asymptotically converged to a value. Continued local variations around some value did not preclude determination of convergence.
2. The joints appeared to have roughly critically damped behavior throughout the workspace.
3. The gravity compensation worked throughout the workspace; in the absence of any position control, the robot starting at rest would remain at rest.

The converged values for the PHANToM 1.0 and 1.5 models are given below, along with the values for the PHANToM 1.5 reported in [15]. The three length parameters, measured by hand, are also given. All units are in the meter-kilogram-second system. Note that the values for the viscous-friction parameters are sensitive to the system velocities experienced during the adaptive algorithm. This is due to pure viscous friction being an incomplete friction model for actual joint friction. Also note that the inertial parameters are sensitive to the alignment of the encoders. The motors should be rotated (see Fig. E.2) such that the centers of mass of the encoders lie along the line that defines the link, which is assumed in the model of [15].

Parameter	PHANToM 1.0	PHANToM 1.5	PHANToM 1.5 [15]
l_1	1.40×10^{-1}	2.10×10^{-1}	2.15×10^{-1}
l_2	1.00×10^{-1}	1.70×10^{-1}	1.70×10^{-1}
l_3	3.20×10^{-2}	3.20×10^{-2}	3.25×10^{-2}
m_a	6.17×10^{-3}	1.92×10^{-2}	2.02×10^{-2}
I_{axx}	1.99×10^{-5}	4.39×10^{-5}	4.864×10^{-5}
I_{ayy}	4.30×10^{-8}	1.77×10^{-7}	1.843×10^{-7}
I_{azz}	1.98×10^{-5}	4.12×10^{-5}	4.864×10^{-5}
m_c	7.38×10^{-3}	2.47×10^{-2}	2.49×10^{-2}
I_{cxx}	3.32×10^{-5}	3.45×10^{-5}	9.59×10^{-5}
I_{cyy}	3.38×10^{-5}	8.66×10^{-5}	9.59×10^{-5}
I_{czz}	4.40×10^{-7}	4.47×10^{-7}	5.1×10^{-7}
$l_5 m_{be}$	-4.36×10^{-3}	-8.15×10^{-3}	-8.681×10^{-3}
I_{bexx}	4.25×10^{-4}	3.96×10^{-4}	1.109×10^{-3}
I_{beyy}	3.72×10^{-4}	9.02×10^{-4}	1.006×10^{-3}
$I_{bez z}$	5.78×10^{-5}	5.22×10^{-5}	5.91×10^{-5}
$l_6 m_{df}$	6.95×10^{-3}	1.08×10^{-2}	1.004×10^{-2}
I_{dfxx}	2.80×10^{-4}	6.45×10^{-4}	7.11×10^{-4}
I_{dfyy}	1.40×10^{-5}	6.18×10^{-5}	6.29×10^{-5}
I_{dfzz}	2.51×10^{-4}	5.13×10^{-4}	6.246×10^{-4}
I_{baseyy}	4.96×10^{-4}	9.24×10^{-4}	1.187×10^{-3}
B_1	1.67×10^{-2}	1.57×10^{-2}	NA
B_2	5.54×10^{-3}	1.12×10^{-2}	NA
B_3	3.64×10^{-3}	1.18×10^{-2}	NA

Bibliography

- [1] D. Aarno, S. Ekvall, and D. Kragić. Adaptive virtual fixtures for machine-assisted teleoperation tasks. In *Proc. IEEE Int'l. Conf. on Robotics and Automation*, pages 1151–1156, 2005.
- [2] J. J. Abbott and A. M. Okamura. Steady-hand teleoperation with virtual fixtures. In *Proc. 12th IEEE Int'l. Workshop on Robot and Human Interactive Communication (RO-MAN)*, pages 145–151, 2003.
- [3] J. J. Abbott and A. M. Okamura. Virtual fixture architectures for telemanipulation. In *Proc. IEEE Int'l. Conf. on Robotics and Automation*, pages 2798–2805, 2003.
- [4] J. J. Abbott and A. M. Okamura. A sufficient condition for virtual wall passivity with quantization effects. In *Proc. ASME Int'l. Mechanical Engineering Congress and Exposition*, pages 1065–1073, 2004.
- [5] J. J. Abbott and A. M. Okamura. Effects of position quantization and sampling rate on virtual-wall passivity. *IEEE Trans. Robotics*, 2005.

- [6] R. J. Adams and B. Hannaford. Stable haptic interaction with virtual environments. *IEEE Trans. Robotics and Automation*, 15(3):465–474, 1999.
- [7] F. Al-Bender, V. Lampaert, and J. Swevers. A novel generic model at asperity level for dry friction force dynamics. *Tribology Letters*, 16(1-2):81–93, 2004.
- [8] R. J. Anderson and M. W. Spong. Bilateral control of teleoperators with time delay. *IEEE Trans. Automatic Control*, 34(5):494–501, 1989.
- [9] R. J. Anderson and M. W. Spong. Asymptotic stability for force reflecting teleoperators with time delay. *Int'l. J. Robotics Research*, 11(2):135–149, 1992.
- [10] B. Armstrong-Helouvry, P. DuPont, and C. Canudas de Wit. Survey of models, analysis tools and compensation methods for the control of machines with friction. *Automatica*, 30(7):1083–1138, 1994.
- [11] A. Bettini, P. Marayong, S. Lang, A. M. Okamura, and G. D. Hager. Vision-assisted control for manipulation using virtual fixtures. *IEEE Trans. Robotics*, 20(6):953–966, 2004.
- [12] E. Bizzi, N. Hogan, F. A. Mussa-Ivaldi, and S Giszter. Does the nervous system use equilibrium-point control to guide single and multiple joint mevements? *Behavioral and Brain Sciences*, 15:603–613, 1992.
- [13] E. Boctor, R. J. Webster III, H. Mathieu, A. M. Okamura, and G. Fichtinger. Virtual remote center of motion control for needle placement robots. *Computer-Aided Surgery*, In Press.

- [14] A. Casals, L. Munoz, and J. Amat. Workspace deformation based teleoperation for the increase of movement precision. In *Proc. IEEE Int'l. Conf. on Robotics and Automation*, pages 2824–2829, 2003.
- [15] M. C. Çavuşoğlu, D. Feygin, and F. Tendick. A critical study of the mechanical and electrical properties of the phantom haptic interface and improvements for high-performance control. *Presence*, 11(6):555–568, 2002.
- [16] M. C. Çavuşoğlu, A. Sherman, and F. Tendick. Bilateral controller design for telemanipulation in soft environments. In *Proc. IEEE Int'l. Conf. on Robotics and Automation*, pages 1045–1052, 2001.
- [17] J. E. Colgate. Robust impedance shaping telemanipulation. *IEEE Trans. Robotics and Automation*, 9(4):374–384, 1993.
- [18] J. E. Colgate and J. M. Brown. Factors affecting the Z-Width of a haptic display. In *Proc. IEEE Int'l. Conf. on Robotics and Automation*, pages 3205–3210, 1994.
- [19] J. E. Colgate, P. E. Grafing, M. C. Stanley, and G. Schenkel. Implementation of stiff virtual walls in force-reflecting interfaces. In *Proc. IEEE Annual Virtual Reality Int'l. Symposium*, pages 202–208, 1993.
- [20] J. E. Colgate and G. G. Schenkel. Passivity of a class of sampled-data systems: Application to haptic interfaces. *J. Robotic Systems*, 14(1):37–47, 1997.
- [21] J. E. Colgate, M. C. Stanley, and J. M. Brown. Issues in the haptic display of

- tool use. In *Proc. IEEE/RSJ Int'l. Conf. on Intelligent Robots and Systems*, pages 140–145, 1995.
- [22] J. J. Craig. *Introduction to Robotics: Mechanics and Control*. Addison Wesley, Reading, Massachusetts, second edition, 1989.
- [23] J. J. Craig, P. Hsu, and S. S. Sastry. Adaptive control of mechanical manipulators. *Int'l. J. Robotics Research*, 6(2):16–28, 1987.
- [24] C. A. Desoer and M. Vidyasagar. *Feedback Systems: Input-Output Properties*. Academic Press, New York, 1975.
- [25] N. Diolaiti, G. Niemeyer, F. Barbagli, J. K. Salisbury, and C. Melchiorri. The effect of quantization and coulomb friction on the stability of haptic rendering. In *Proc. World Haptics Conf.*, 2005.
- [26] H. Esen, K. Yano, and M. Buss. A control algorithm and preliminary user studies for a bone drilling medical training system. In *Proc. 12th IEEE Int'l. Workshop on Robot and Human Interactive Communication (RO-MAN)*, pages 153–158, 2003.
- [27] G. F. Franklin, J. D. Powell, and A. Emami-Naeini. *Feedback Control of Dynamic Systems*. Addison Wesley, Reading, Massachusetts, third edition, 1994.
- [28] G. F. Franklin, J. D. Powell, and M. L. Workman. *Digital Control of Dynamic Systems*. Addison Wesley, Reading, Massachusetts, second edition, 1994.

- [29] R. B. Gillespie and M. R. Cutkosky. Stable user-specific haptic rendering of the virtual wall. In *Proc. ASME Dynamic Systems and Control Division*, volume 58, pages 397–406, 1996.
- [30] M. Goldfarb and J. Wang. Passive stiffness simulation with rate-independent hysteresis. In *Proc. ASME Dynamic Systems and Control Division*, volume 67, pages 345–350, 1999.
- [31] G. S. Guthart and J. K. Salisbury. The IntuitiveTM telesurgery system: Overview and application. In *Proc. IEEE Int'l. Conf. on Robotics and Automation*, pages 618–621, 2000.
- [32] A. Z. Hajian and R. D. Howe. Identification of the mechanical impedance at the human finger tip. *ASME J. Biomechanical Engineering*, 119:109–114, 1997.
- [33] B. Hannaford. A design framework for teleoperators with kinesthetic feedback. *IEEE Trans. Robotics and Automation*, 5(4):426–434, 1989.
- [34] B. Hannaford. Stability and performance tradeoffs in bi-lateral telemanipulation. In *Proc. IEEE Int'l. Conf. on Robotics and Automation*, pages 1764–1767, 1989.
- [35] B. Hannaford and R. Anderson. Experimental and simulation studies of hard contact in force reflecting teleoperation. In *Proc. IEEE Int'l. Conf. on Robotics and Automation*, pages 584–589, 1988.

- [36] B. Hannaford and J.-H. Ryu. Time-domain passivity control of haptic interfaces. *IEEE Trans. Robotics and Automation*, 18(1):1–10, 2002.
- [37] K. Hashtrudi-Zaad and S. E. Salcudean. Analysis of control architectures for teleoperation systems with impedance/admittance master and slave manipulators. *Int'l. J. Robotics Research*, 20(6):419–445, 2001.
- [38] K. Hashtrudi-Zaad and S. E. Salcudean. Transparency in time-delayed systems and the effect of local force feedback for transparent teleoperation. *IEEE Trans. Robotics and Automation*, 18(1):108–114, 2002.
- [39] S. S. Haykin. *Active Network Theory*. Addison-Wesley, 1970.
- [40] N. Hogan. Controlling impedance at the man/machine interface. In *Proc. IEEE Int'l. Conf. on Robotics and Automation*, pages 1626–1631, 1989.
- [41] R. Horn and C. R. Johnson. *Matrix Analysis*. Cambridge University Press, Cambridge, United Kingdom, 1985.
- [42] J. D. Hwang, M. D. Williams, and G. Niemeyer. Toward event-based haptics: Rendering contact using open-loop force pulses. In *Proc. 12th Symposium on Haptic Interfaces for Virtual Environments and Teleoperator Systems*, pages 24–31, 2004.
- [43] T. Itoh, K. Kosuge, and T. Fukuda. Human-machine cooperative telemanipulation with motion and force scaling using task-oriented virtual tool dynamics. *IEEE Trans. Robotics and Automation*, 16(5):505–516, 2000.

- [44] F. Janabi-Sharifi, V. Hayward, and C.-S. J. Chen. Discrete-time adaptive windowing for velocity estimation. *IEEE Trans. Control Systems Technology*, 8(6):1003–1009, 2000.
- [45] L. D. Joly and C. Andriot. Imposing motion constraints to a force reflecting telerobot through real-time simulation of a virtual mechanism. In *Proc. IEEE Int'l. Conf. on Robotics and Automation*, pages 357–362, 1995.
- [46] H. Kang and J. T. Wen. Autonomous suturing using minimally invasive surgical robots. In *Proc. IEEE Int'l. Conf. on Robotics and Automation*, pages 742–747, 2000.
- [47] H. Kazerooni and J. Guo. Human extenders. *ASME J. Dynamic Systems, Measurement, and Control*, 115(2(B)):281–289, 1993.
- [48] H. K. Khalil. *Nonlinear Systems*. Prentice Hall, third edition, 2001.
- [49] W. S. Kim, B. Hannaford, and A. K. Bejczy. Force-reflecting and shared compliant control in operating telemanipulators with time delay. *IEEE Trans. Robotics and Automation*, 8(2):176–185, 1992.
- [50] W. S. Kim, F. Tendick, S. R. Ellis, and L. W. Stark. A comparison of position and rate control for telemanipulators with consideration of manipulator system dynamics. *IEEE J. Robotics and Automation*, RA-3(5):426–436, 1987.
- [51] D. G. Kleinbaum, L. L. Kupper, K. E. Muller, and A. Nizam. *Applied Regres-*

sion Analysis and Other Multivariable Methods. Duxbury Press, Pacific Cove, California, third edition, 1998.

- [52] M. E. Kontz and W. J. Book. Position/rate haptic control of a hydraulic fork-lift. In *Proc. ASME Int'l. Mechanical Engineering Congress and Exposition*, pages 801–808, 2003.
- [53] D. Kragic, P. Marayong, M. Li, A. M. Okamura, and G. D. Hager. Human-machine collaborative systems for microsurgical applications. In *Proc. Int'l. Symposium of Robotics Research*, 2003.
- [54] A. B. Kuang, S. Payandeh, B. Zheng, F. Henigman, and C. L. MacKenzie. Assembling virtual fixtures for guidance in training environments. In *Proc. 12th Symposium on Haptic Interfaces for Virtual Environments and Teleoperator Systems*, 2004.
- [55] K. J. Kuchenbecker, J. G. Park, and G. Niemeyer. Characterizing the human wrist for improved haptic interaction. In *Proc. ASME Int'l. Mechanical Engineering Congress and Exposition*, 2003.
- [56] D. A. Lawrence. Stability and transparency in bilateral teleoperation. *IEEE Trans. Robotics and Automation*, 9(5):624–637, 1993.
- [57] P. D. Lawrence, S. E. Salcudean, N. Sepehri, D. Chan, S. Bachmann, N. Parker, M. Zhu, and R. Frenette. Coordinated and force-feedback control of hydraulic excavators. In *Proc. 4th Int'l. Symposium on Experimental Robotics*, pages 181–194, 1995.

- [58] G. M. H. Leung, B. A. Francis, and J. Apkarian. Bilateral controller for teleoperators with time delay via μ -synthesis. *IEEE Trans. Robotics and Automation*, 11(1):105–116, 1995.
- [59] M. Li and A. M. Okamura. Recognition of operator motions for real-time assistance using virtual fixtures. In *Proc. 11th Symposium on Haptic Interfaces for Virtual Environments and Teleoperator Systems*, pages 125–131, 2003.
- [60] P. Y. Li and R. Horowitz. Passive velocity field control of mechanical manipulators. *IEEE Trans. Robotics and Automation*, 15(4):751–763, 1999.
- [61] L. Love and W. Book. Contact stability analysis of virtual walls. In *Proc. ASME Dynamic Systems and Control Division*, volume 57, pages 689–694, 1995.
- [62] R. Lundström. Local vibrations – mechanical impedance of the human hand’s glabrous skin. *J. Biomechanics*, 17(2):137–144, 1984.
- [63] D. R. Madill, D. W. L. Wang, and M. C. Ching. A nonlinear observer for minimizing quantization effects in virtual walls. In *Proc. ASME Dynamic Systems and Control Division*, volume 67, pages 335–343, 1999.
- [64] M. Mahvash and V. Hayward. High-fidelity passive force-reflecting virtual environments. *IEEE Trans. Robotics*, 21(1):38–46, 2005.
- [65] P. Marayong and A. M. Okamura. Speed-accuracy characteristics of human-

- machine cooperative manipulation using virtual fixtures with variable admittance. *Human Factors*, 46(3):518–532, 2004.
- [66] A. Micaelli, C. Bidard, and C. Andriot. Decoupling control based on virtual mechanisms for telemanipulation. In *Proc. IEEE Int'l. Conf. on Robotics and Automation*, pages 1924–1931, 1998.
- [67] B. E. Miller, J. E. Colgate, and R. A. Freeman. Guaranteed stability of haptic systems with nonlinear virtual environments. *IEEE Trans. Robotics and Automation*, 16(6):712–719, 2000.
- [68] B. E. Miller, J. E. Colgate, and R. A. Freeman. On the role of dissipation in haptic systems. *IEEE Trans. Robotics*, 20(4):768–771, 2004.
- [69] F. Mobasser and K. Hashtrudi-Zaad. Implementation of a rate mode impedance reflecting teleoperation controller on a haptic simulations system. In *Proc. IEEE Int'l. Conf. on Robotics and Automation*, pages 1974–1979, 2004.
- [70] F. Mobasser, K. Hashtrudi-Zaad, and S. E. Salcudean. Impedance reflecting rate mode teleoperation. In *Proc. IEEE Int'l. Conf. on Robotics and Automation*, pages 3296–3302, 2003.
- [71] C. A. Moore, M. A. Peshkin, and J. E. Colgate. Cobot implementation of virtual paths and 3-D virtual surfaces. *IEEE Trans. Robotics and Automation*, 19(2):347–351, 2003.

- [72] G. Niemeyer and J.-J. E. Slotine. Stable adaptive teleoperation. *IEEE J. Oceanic Engineering*, 16(1):152–162, 1991.
- [73] G. Niemeyer and J.-J. E. Slotine. Designing force reflecting teleoperators with large time delays to appear as virtual tools. In *Proc. IEEE Int'l. Conf. on Robotics and Automation*, pages 2212–2218, 1997.
- [74] A. M. Okamura, C. Richard, and M. R. Cutkosky. Feeling is believing: Using a force-feedback joystick to teach dynamic systems. *ASEE J. Engineering Education*, 92(3):345–349, 2002.
- [75] S. Park, R. D. Howe, and D. F. Torchiana. Virtual fixtures for robotic cardiac surgery. In *Proc. 4th Int'l. Conf. on Medical Image Computing and Computer-Assisted Intervention*, pages 1419–1420, 2001.
- [76] Y. S. Park, H. Kang, T. F. Ewing, E. L. Faulring, J. E. Colgate, and M. A. Peshkin. Enhanced teleoperation for D & D. In *Proc. IEEE Int'l. Conf. on Robotics and Automation*, pages 3702–3707, 2004.
- [77] N. R. Parker, S. E. Salcudean, and P. D. Lawrence. Application of force feedback to heavy duty hydraulic machines. In *Proc. IEEE Int'l. Conf. on Robotics and Automation*, pages 375–381, 1993.
- [78] S. Payandeh and Z. Stanisic. On application of virtual fixtures as an aid for telemanipulation and training. In *Proc. 10th Symposium on Haptic Interfaces for Virtual Environments and Teleoperator Systems*, pages 18–23, 2002.

- [79] G. J. Raju, G. C. Verghese, and T. B. Sheridan. Design issues in 2-port network models of bilateral remote manipulation. In *Proc. IEEE Int'l. Conf. on Robotics and Automation*, pages 1316–1321, 1989.
- [80] L. Rosenberg. Virtual fixtures: Perceptual tools for telerobotic manipulation. In *Proc. IEEE Virtual Reality Int'l. Symposium*, pages 76–82, 1993.
- [81] J. Roy, D. L. Rothbaum, and L. L. Whitcomb. Haptic feedback augmentation through position based adaptive force scaling: Theory and experiment. In *Proc. IEEE/RSJ Int'l. Conf. on Intelligent Robots and Systems*, pages 2911–2919, 2002.
- [82] J. Roy and L. L. Whitcomb. Adaptive force control of position/velocity controlled robots: Theory and experiment. *IEEE Trans. Robotics and Automation*, 18(2):121–137, 2002.
- [83] W. J. Rugh. *Linear Systems Theory*. Prentice-Hall, Upper Saddle River, New Jersey, second edition, 1996.
- [84] J.-H. Ryu, B. Hannaford, C. Preusche, and G. Hirzinger. Time domain passivity control with reference energy behavior. In *Proc. IEEE/RSJ Int'l. Conf. on Intelligent Robots and Systems*, pages 2932–2937, 2003.
- [85] J.-H. Ryu, Y. S. Kim, and B. Hannaford. Sampled- and continuous-time passivity and stability of virtual environments. *IEEE Trans. Robotics*, 20(4):772–776, 2004.

- [86] J.-H. Ryu, D.-S. Kwon, and B. Hannaford. Stable teleoperation with time-domain passivity control. *IEEE Trans. Robotics*, 20(2):365–373, 2004.
- [87] S. E. Salcudean and T. D. Vlaar. On the emulation of stiff walls and static friction with a magnetically levitated input/output device. *ASME J. Dynamic Systems, Measurement, and Control*, 119:127–132, 1997.
- [88] S. E. Salcudean, M. Zhu, W.-H. Zhu, and K. Hashtrudi-Zaad. Transparent bilateral teleoperation under position and rate control. *Int'l. J. Robotics Research*, 19(12):1185–1202, 2000.
- [89] C. Sayers. *Remote Control Robotics*. Springer-Verlag, New York, 1999.
- [90] C. Secchi, S. Stramigioli, and C. Fantuzzi. Dealing with unreliabilities in digital passive geometric telemanipulation. In *Proc. IEEE/RSJ Int'l. Conf. on Intelligent Robots and Systems*, pages 2823–2828, 2003.
- [91] C. Secchi, S. Stramigioli, and C. Fantuzzi. Digital passive geometric telemanipulation. In *Proc. IEEE Int'l. Conf. on Robotics and Automation*, pages 3290–3295, 2003.
- [92] T. B. Sheridan. *Telerobotics, Automation, and Human Supervisory Control*. The MIT Press, Cambridge, Massachusetts, 1992.
- [93] A. Sherman, M. C. Çavuşoğlu, and F. Tendick. Comparison of teleoperator control architectures for palpation task. In *Proc. ASME Dynamic Systems and Control Division*, pages 1261–1268, 2000.

- [94] M. Smid. *Handbook of Computational Geometry*. Elsevier, 2000.
- [95] S. W. Smith. *The Scientist and Engineer's Guide to Digital Signal Processing*. California Technical Publishing, San Diego, California, 1997.
- [96] J. E. Speich, K. Fite, and M. Goldfarb. A method for simultaneously increasing transparency and stability robustness in bilateral telemanipulation. In *Proc. IEEE Int'l. Conf. on Robotics and Automation*, pages 2671–2676, 2000.
- [97] S. Stramigioli, C. Secchi, A. J. van der Schaft, and C. Fantuzzi. A novel theory for sample data system passivity. In *Proc. IEEE/RSJ Int'l. Conf. on Intelligent Robots and Systems*, pages 1936–1941, 2002.
- [98] S. Stramigioli, A. van der Schaft, B. Maschke, and C. Melchiorri. Geometric scattering in robotic telemanipulation. *IEEE Trans. Robotics and Automation*, 18(4):588–596, 2002.
- [99] G. Strang. *Linear Algebra and its Applications*. Harcourt Brace Jovanovich, Fort Worth, Texas, third edition, 1988.
- [100] R. S. Strichartz. *The Way of Analysis*. Jones and Bartlett, Boston, Massachusetts, 2000.
- [101] R. Taylor, P. Jensen, L. Whitcomb, A. Barnes, R. Kumar, D. Stoianovici, P. Gupta, Z. Wang, E. deJuan, and L. Kavoussi. Steady-hand robotic system for microsurgical augmentation. *Int'l. J. Robotics Research*, 18(12):1201–1210, 1999.

- [102] N. Turro and O. Khatib. Haptically augmented teleoperation. In *Proc. 7th Int'l. Symposium on Experimental Robotics*, pages 1–10, 2000.
- [103] R. Q. van der Linde, P. Lammerste, E. Frederiksen, and B. Ruiter. The HapticMaster, a new high-performance haptic interface. In *Proc. Eurohaptics Conf.*, 2002.
- [104] A. van der Schaft. *L₂-Gain and Passivity Techniques in Nonlinear Control*. Springer-Verlag, London, 2000.
- [105] C. R. Wagner, N. Stylopoulos, and R. D. Howe. The role of force feedback in surgery: Analysis of blunt dissection. In *Proc. 10th Symposium on Haptic Interfaces for Virtual Environments and Teleoperator Systems*, 2002.
- [106] C. D. Wickens. *Engineering Psychology and Human Performance*. Harper Collins, New York, 2000.
- [107] R. L. Williams II, J. M. Henry, M. A. Murphy, and D. W. Repperger. Free and constrained motion teleoperation via naturally-transitioning rate-to-force control. In *Proc. IEEE Int'l. Conf. on Robotics and Automation*, pages 225–230, 1999.
- [108] J. Yan and S. E. Salcudean. Teleoperation controller design using H_∞ -optimization with application to motion-scaling. *IEEE Trans. Control Systems Technology*, 4(3):244–258, 1996.
- [109] Y. Yokokohji, T. Imaida, and T. Yoshikawa. Bilateral teleoperation under

- time-varying communication delay. In *Proc. IEEE/RSJ Int'l. Conf. on Intelligent Robots and Systems*, pages 1854–1859, 1999.
- [110] Y. Yokokohji and T. Yoshikawa. Bilateral control of master-slave manipulators for ideal kinesthetic coupling – formulation and experiment. *IEEE Trans. Robotics and Automation*, 10(5):605–620, 1994.
- [111] S. Zhai. Investigation of feel for 6DOF inputs: Isometric and elastic rate control for manipulation in 3D environments. In *Proc. Human Factors and Ergonomics Society 37th Annual Meeting*, pages 323–327, 1993.
- [112] S. Zhai and P. Milgram. Human performance evaluation of manipulation schemes in virtual environments. In *Proc. First IEEE Virtual Reality Annual Int'l. Symposium*, pages 155–161, 1993.
- [113] C. B. Zilles and J. K. Salisbury. A constraint-based god-object method for haptic display. In *Proc. IEEE/RSJ Int'l. Conf. on Intelligent Robots and Systems*, pages 146–151, 1995.

Vita

Jake Abbott was born on June 28, 1977 in Salt Lake City, Utah, and raised in West Jordan, Utah. After graduating valedictorian of his class at West Jordan High School in 1995, Jake went on to earn his B.S. in Mechanical Engineering *magna cum laude* in 1999 at Utah State University in Logan, Utah. While there, he was awarded the Outstanding Senior award by the Department of Mechanical Engineering. Jake earned his M.S. in Mechanical Engineering in 2001 at the University of Utah in Salt Lake City, Utah. Jake's emphasis was in control systems and robotics, and he earned the Mechatronics Certificate from the College of Engineering. Since 2002, Jake has been working towards his Ph.D. in Mechanical Engineering at the Johns Hopkins University in Baltimore, Maryland, again with an emphasis in control systems and robotics. In 2005, he was awarded the Teaching Assistant Award by the Department of Mechanical Engineering. Jake is the author of a number of peer-reviewed conference and journal papers. Jake is a member of the American Society of Mechanical Engineers (ASME) and the Institute of Electrical and Electronics Engineers (IEEE).